MEASUREMENT AND RECONSTRUCTION OF WIND TURBINE INFLOW WITH GROUND AND NACELLE-BASED SCANNING LIDARS



Von der Fakultät für Mathematik und Naturwissenschaften der Carl von Ossietzky Universität Oldenburg angenommene Dissertation zur Erlangung des akademischen Grades und Titels eines Doktors der Ingenieurwissenschaften Dr.-Ing.

von

Anantha Padmanabhan KIDAMBI SEKAR, M.Sc.

geboren in Karamana, Indien

Keywords: lidar measurements, wind turbine inflow, wind field reconstruction, flow characterisation, lidar-assisted control

Gutachter: Prof. Dr. Martin Kühn Zweitgutachter: Prof. Dr. David Schlipf

Tag der Disputation: 13.12.2024

CONTENTS

Su	ımma	ıry		ix
Ζu	ıssam	nenfass	sung	хi
Ac	knov	wledgm	nents	xiii
Li	st of .	Abbrev	viations	xv
Li	st of	Symbo	ls	xvii
Li	st of	Figures	S	xxi
Li	st of	Tables		xxvi
1	Intr	oductio	on	1
	1.1	The n	eed for remote sensing in wind energy	1
	1.2	A brie	of introduction to lidar anemometery	3
	1.3	Lidar	scanning and mounting techniques for wind energy applications	5
	1.4	Applio	cations of lidar measured data in wind energy	6
		1.4.1	Wind resource assessment and power performance testing	6
		1.4.2	Flow characterisation	7
		1.4.3	Turbulence assessment	7
		1.4.4	Load validation	8
	1.5	Inflow	sensing lidars for optimising turbine operation	9
	1.6	Open	questions and challenges	11
		1.6.1	Evolution of scanning lidar technology	11
		1.6.2	Lidar wind field reconstruction	13
		1.6.3	Lidar measurement availability	15
		1.6.4	Flow evolution in the induction zone	16
	1.7	Resear	rch motivation and goals	17
	1.8	Struct	rure of the thesis	18
2		_	g Scanning and Fixed Beam Lidar Systems with High Fidelity	
	Sim	ulation	18	21
	2.1		luction	21
	2.2	The co	ontineous-wave lidar measurement principles	23
		2.2.1	Directional bias	23
		2.2.2	The volume averaging effect	24
		2.2.3	Wind evolution and blockage deceleration	25
		2.2.4	Spatio-temporal limitations	26

vi Contents

	2.3	Metho	ods	28
		2.3.1	Large-Eddy simulations	28
		2.3.2	The SpinnerLidar	30
		2.3.3	Lidar simulator (LiXim)	31
	2.4	Result	s	33
		2.4.1	Effect of temporal sampling rate on the time series moments	33
		2.4.2	The volume averaging effect	34
		2.4.3	Effect of directional bias	35
		2.4.4	Sampling the wind field in a stationary and rotating frame of refer-	
			ence	37
		2.4.5	The wind evolution and induction zone slowdown	39
	2.5		ating fixed beam and scanning lidar systems	41
		2.5.1	Estimation of optimum scan location based on REWS	41
		2.5.2	Effect of spatial sampling on three-parameter estimation	43
	2.6		ssions	45
		2.6.1	The limitations and capabilities of turbine-mounted lidars	45
		2.6.2	On the evaluation of fixed-beam and scanning lidars for lidar-	
			assisted control applications	46
		2.6.3	On the potential LCoE reductions	47
	2.7	Concli	usions	48
3	Low	er Ord	er Description and Reconstruction of Sparse Scanning Lidar	
			ents of Wind Turbine Inflow Using Proper Orthogonal Decom-	
	-	ition		49
	3.1		uction	50
	3.2		ods	52
		3.2.1	Proper Orthogonal Decomposition (POD)	53
		3.2.2	The Gappy-POD	54
		3.2.3	Turbine-mounted lidars for inflow scanning	56
		3.2.4	Large-Eddy simulations (LES) and the lidar simulator (LiXim) $\ . \ . \ .$	58
	3.3		8	60
		3.3.1	Application of the POD methodology to scanning lidar measure-	
			ments	60
		3.3.2	ments	60 62
			ments	
		3.3.2	ments	62
		3.3.2 3.3.3	ments	62 63
	3.4	3.3.2 3.3.3 3.3.4 3.3.5	ments	62 63 68
	3.4	3.3.2 3.3.3 3.3.4 3.3.5	ments	62 63 68 69
	3.4	3.3.2 3.3.3 3.3.4 3.3.5 Discus	ments	62 63 68 69 73

Contents

4	Ove	rcoming Blade Interference: A Gappy-POD Data Reconstruction	
	Met	hod for Nacelle-Mounted Lidar Measurements	79
	4.1	Introduction	80
	4.2	Methodology	80
		4.2.1 Large-eddy simulations and scanning lidar simulations	80
		4.2.2 SpinnerLidar velocity snapshots with gaps	81
		4.2.3 Proper Orthogonal Decomposition	82
		4.2.4 Gappy Proper Orthogonal Decomposition (Gappy-POD)	82
	4.3	Results and discussion	84
		4.3.1 Convergence of Gappy-POD	84
		4.3.2 Velocity field reconstruction	86
		4.3.3 Reconstruction of wind parameters for the undisturbed inflow case	87
		4.3.4 Reconstruction of turbulent spectra in fixed and rotating reference	0.0
		frames	88
	4.4		89 90
	4.4	Conclusions	90
5	Syn	chronised WindScanner Field Measurements of the Induction Zone	
	Betv	ween Two Closely Spaced Wind Turbines	93
	5.1	Introduction	94
	5.2	Methods	96
		5.2.1 Test site description and inflow characterisation	96
		5.2.2 WindScanners	98
		5.2.3 WindScanner measurement errors and uncertainties	
		5.2.4 Measurements	
		5.2.5 Numerical simulations of the experimental site	
	5.3	Results	
		5.3.1 Virtual WindScanner evaluation in LES	
	- 1	5.3.2 Measurement results	
	5.4 5.5	Discussion	
	5.5	Conclusions	121
6	Con	clusions and Outlook	12 3
	6.1	Conclusions	
		6.1.1 Lidar measurements of wind turbine inflow	123
		6.1.2 Development of wind field reconstruction methods for scanning	
		lidars	
		6.1.3 Characterising the induction zone with synchronised lidars	
	6.2	Outlook	126
Re	ferei	nces	129
Li	st of	Publications	149
Cı	ırricı	ılum Vitæ	15 3
Ei	desst	attliche Erklärung	155

SUMMARY

Remote sensing measurements of wind turbine inflow can be used to understand the interaction between the wind in the atmospheric boundary layer and the structural response of the wind turbine. Recent developments in optical and scanning technologies have enabled lidar systems capable of non-intrusive measurements of the wind inflow upstream of a turbine. Integrating this preview information of the inflow into the turbine operation creates opportunities for optimising power production and alleviating structural loads. This approach contrasts with traditional feed-back controllers, which can react to changes in the inflow state only after the impacts have already occurred.

Designing control systems that adequately utilise upstream lidar measurements requires a comprehensive understanding of the measurement principle and, therefore, the measurements themselves. Previously, simple lidar systems with just a few pointing directions were utilised to probe the wind field upstream of the turbine. Due to the limitations of the measurement principle and sparse scanning capabilities, wind field reconstruction strategies are required so that the measurements can be converted into turbine-relevant parameters. In addition, the upstream measurements do not represent the inflow experienced by the wind turbine due to the evolution of turbulent structures between the measurement location and the rotor plane and the deceleration in the rotor induction zone.

With the development of scanning technologies, lidar systems can now provide quasiinstantaneous measurements of the spatially distributed fluctuations of the wind with high
resolution. In this thesis, simulations and experiments were conducted to understand the
capabilities and limitations of scanning lidar systems in conducting inflow measurements.
Fully exploiting the high-resolution measurements requires the development of wind field
reconstruction methods that can express the spatio-temporal inflow dynamics relevant to
the wind turbine. As nacelle-based installations are preferred for inflow sensing due to ease
of installation, it is necessary to develop wind field reconstruction methods to reconstruct
measurements lost due to effects such as blade interference to increase data availability.
Finally, field measurements were performed in the scope of thesis with two synchronised
scanning lidars to characterise the wind turbine upstream induction zone and evaluate
engineering models that describe induction slowdown.

Based on simulations of scanning lidar measurements in a controlled high fidelity simulation environment, the ability of lidar systems to accurately capture the inflow dynamics is investigated. Due to the more extensive rotor area coverage, scanning lidars can capture the spatio-temporal inflow variations directly driving the turbine response compared to simpler fixed-beam devices. For example, scanning lidars can capture the vertical wind speed variation due to wind shear by a rotational sampling of the wind field, which could be exploited to attenuate the harmonic loading on the blades due to rotation.

A line-of-sight velocity field reconstruction methodology based on Proper Orthogonal Decomposition (POD) was developed to fully utilize scanning lidar measurements in two spatial dimensions within the scanning plane upstream of a wind turbine. An analysis x Summary

of LES simulations of varying inflow and stability conditions determined that the spatio-temporal variations in the wind field could be reconstructed with just ten modes, thereby providing data compression, which is advantageous for a wind turbine controller. POD also revealed the coherent motions in the inflow where the modes were highly correlated with parameters describing the inflow, such as vertical shear and yaw misalignment, even though the relationship differed on a case-to-case basis. Therefore, a fully 2D wind field could be reconstructed with very high accuracy by carefully selecting the dominant spatial modes. To overcome blade interference, a POD extension named Gappy-POD was applied to reconstruct the line-of-sight measurements from nacelle-mounted scanning lidar systems. Gappy-POD performs a space-time interpolation at the missing points by exploiting the correlations from the measurement time series. An evaluation of the method in a simulation environment indicates that the technique can successfully reconstruct sparse measurements of undisturbed and fully waked inflow even up to 90 % of missing data. This increased data availability reduces the uncertainty of estimating inflow parameters from lidar measurements allowing for more robust control.

To characterise the wind turbine induction zone, experiments were conducted with two synchronised WindScanner lidars. The highly temporally and spatially resolved induction zone measurements revealed the interaction of the atmospheric boundary layer, site orography and the wind turbine for no wake, partial and fully waked inflow scenarios. Under full and partial wake scenarios, an interaction between the upstream turbine wake and the downstream turbine induction zone was visible. Due to the measurement complexity and the highly dynamic nature of the atmospheric flow, a virtual lidar in wind simulation methodology to investigate the accuracy of measurements was employed to assess the impact of the measurement layout and the device uncertainties on the measurements. The limited capability of the dual-scanning system owing to the assumption of vanishing vertical velocity for the dual-Doppler reconstruction, especially in the highly turbulent wake, introduced larger uncertainties in the measurements and presented a challenge to the interpretation of results. The thesis concludes with recommendations for future research on the further capabilities of nacelle-lidars for characterising the wind turbine inflow, wind field reconstruction possibilities for nacelle-based scanning lidars and recommendations for a more thorough measurement setup with synchronised scanning lidars to measure turbine-turbine interactions.

ZUSAMMENFASSUNG

Fernerkundungsmessungen der Anströmung von Windenergieanlage (WEA) können genutzt werden, um die Wechselwirkung zwischen dem Wind in der atmosphärischen Grenzschicht und der strukturellen Reaktion der Windturbine zu verstehen. Entwicklungen im Bereich der optischen und scannenden Technologien ermöglichen Lidar-Systeme, die in der Lage sind, die Windanströmung stromaufwärts einer WEA nicht-intrusiv zu messen. Die Integration der Informationen über die Anströmung in den WEA-Regelung eröffnet Möglichkeiten zur Optimierung der Stromerzeugung und zur Verringerung der strukturellen Belastungen. Dieser Ansatz steht im Gegensatz zu herkömmlichen Feedbackreglern, die auf Änderungen des Anströmungszustands erst reagieren können, wenn die Auswirkungen bereits eingetreten sind.

Die Entwicklung von Regelungssystemen, die Lidar-Messungen der Anströmung angemessen nutzen, erfordert ein umfassendes Verständnis des Messprinzips und damit der Messungen selbst. Bisher wurden einfache Lidar-Systeme eingesetzt, welche das Windfeld stromaufwärts der Anlage entlang weniger vordefinierter Richtungen erfassen. Aufgrund der Einschränkungen des Messprinzips und der spärlichen Abtastung sind Strategien zur Rekonstruktion des Windfeldes erforderlich, um die Messungen in turbinenrelevante Parameter umzurechnen. Darüber hinaus repräsentieren die stromaufwärtigen Messungen nicht die Anströmung der Windenergieanlage, da sich zwischen dem Messort und der Rotorebene turbulente Strukturen entwickeln und der wind in der Induktionszone des Rotors abgebremst wird.

Mit der Entwicklung von Scanning-Technologien können Lidar-Systeme nun quasi-instantane Messungen der räumlich verteilten Fluktuationen des Windes mit hoher Auflösung liefern. In dieser Arbeit wurden Simulationen und Experimente durchgeführt, um die Möglichkeiten und Grenzen von scannenden Lidar-Systemen bei der Durchführung von Anströmungsmessungen zu verstehen. Die volle Nutzung der hochaufgelösten Messungen erfordert die Entwicklung von Methoden zur Windfeldrekonstruktion, die die für die Windenergieanlage relevante räumlich-zeitliche Anströmungsdynamik repräsentieren. Da gondelbasierte Lidar-Systeme aufgrund der, im Vergleich zu vor dem Rotor in der Nabe installierten Lidar-Systemen, einfachen Installation für die Messung der Anströmung bevorzugt werden, müssen Methoden zur Rekonstruktion des Windfelds entwickelt werden, um Datenlücken auszufüllen, welche durch Blattinterferenzen verloren gehen. Schließlich wurden im Rahmen dieser Arbeit Freifeldexperimente mit zwei synchronisierten Scanning-Lidar durchgeführt, um die Induktionszone der Windturbine zu charakterisieren und Induktionsmodelle zu bewerten.

Auf der Grundlage High-Fidelity-Simulationen wird die Fähigkeit von Lidar-Systemen zur genauen Erfassung der Anströmdynamik untersucht. Im Vergleich zu einfacheren Geräten mit festen Strahlrichtungen können Scanning-Lidar aufgrund der größeren Abdeckung der Rotoreinströmung die räumlich-zeitlichen Anströumngsvariationen, welche das Turbinenverhalten direkt beeinflussen, besser erefassen. Beispielsweise können Scanning-Lidar

xii Zussamenfassung

Lidar die vertikalen Windgeschwindigkeitsänderung durch die Rotationsabtastung des Windfeldes erfassen, was zur Abschwächung der harmonischen Belastung der Rotorblätter genutzt werden könnte.

Es wurde eine Methode zur Rekonstruktion des Geschwindigkeitsfeldes auf der Grundlage der Proper Orthogonal Decomposition (POD) entwickelt, um Scanning-Lidar-Messungen in zwei räumlichen Dimensionen innerhalb der Scanebene stromaufwärts einer Windenergieanlage vollständig nutzen zu konnen. Eine Analyse von LES-Simulationen unterschiedlicher Anströmungs- und Stabilitätsbedingungen ergab, dass die räumlich-zeitlichen Variationen des Windfeldes mit nur zehn Moden rekonstruiert werden können, was eine Datenkompression ermöglicht, die für die Regelung einer WEA von Vorteil ist. POD zeigte auch die kohärenten Bewegungen in der Anströmung auf, wobei die Moden in hohem Maße mit Parametern korrelierten, die die Anströmung beschreiben, wie vertikale Scherung und Gierversatz, auch wenn die Beziehung von Fall zu Fall unterschiedlich war. Mithilfe der dominanten räumlichen Moden konnte ein vollständiges 2D-Windfeld mit sehr hoher Genauigkeit rekonstruiert werden. Zur Überwindung von Blattinterferenzen wurde eine POD-Erweiterung namens Gappy-POD entwickelt, um die Sichtlinienmessungen von auf der Gondel montierten Scanning-Lidar-Systemen zu rekonstruieren. Gappy-POD führt eine Raum-Zeit-Interpolation an den fehlenden Punkten durch, indem es die Korrelationen der Messzeitreihen verwendet. Eine Evaluierung der Methode in einer Simulationsumgebung zeigt, dass die Technik erfolgreich bei bis zu 90 % fehlender Messdaten rekonstruieren kann. Dies verringert die Unsicherheit bei der Schätzung von Anströmungsparametern aus Lidar-Messungen und ermöglicht eine robustere Regelung.

Zur Charakterisierung der Induktionszone von Windenergieanlagen wurden Experimente mit zwei synchronisierten WindScanner-Lidaren durchgeführt. Die zeitlich und räumlich hoch aufgelösten Messungen der Induktionszone zeigten die Wechselwirkung zwischen der atmosphärischen Grenzschicht, der Orographie des Standorts und der Windturbine für Szenarien ohne Nachlauf, mit halb überlappendem und mit vollem Nachlauf. Dabei war eine Wechselwirkung zwischen der stromaufwärts gelegenen Turbinen-Nachlaufströmung und der stromabwärts gelegenen Turbinen-Induktionszone erkennbar. Aufgrund der Komplexität der Messungen und der hochdynamischen Natur der atmosphärischen Strömung wurde ein virtuelles Lidar in der Windsimulation eingesetzt, um die Genauigkeit der Messungen zu untersuchen und die Auswirkungen der Messanordnung und der Geräteunsicherheiten auf die Messungen zu bewerten. Die Annahme, dass die vertikale Geschwindigkeitskomponente des Windes Null ist, verursacht insbesondere in der hochturbulenten Nachlaufströmung größere Messunsicherheiten. Die Arbeit schließt mit Empfehlunngen für künftige Forschung zum Einsatz von gondelbasierten Scanning-Lidar-Systemen zur Charakterisierung und Rekonstruktion derr Einströmung. Darüber hinaus werden Empfehlungen für den Messaufbau von synchronisierten Scanning-Lidar-Systemen zur Messung von Turbinen-Interaktionen gegeben.

ACKNOWLEDGMENTS

Victoria concordia crescit

Without a doubt, the acknowledgements are the most widely and most eagerly read part of any thesis. This is the part where I have the opportunity to thank my family, friends, colleagues, scientists, and mentors who supported me throughout this journey.

Completing a PhD research is not just the work of one person alone. Special thanks to my colleagues Marijn, Stephan, Jörge, Arjun, Paul, Davide, Fredrick, David, Vlaho, Frauke, Mehdi, Langidis, Laura for many discussions on lidars and wind tunnels amongst other things. Thanks to my family for their invaluable support, for which I am forever grateful. The constant and invaluable support of the DTU WindScanner team (Prof. Torben Mikkelsen, Mikael Sjöholm, Nicolas Angelou, Claus Pederson) regarding the WindScanner lidars is gratefully acknowledged. Special mention to people I worked on field campaigns with, especially the "WindScanner crew", thanks for keeping the spirits high during many cold days out in the field.

I would like to thank Prof. Dr. Martin Kühn for providing the opportunity and financial support to conduct a PhD at the Wind Energy Systems Group at the University of Oldenburg. Many thanks go also to Prof. David Schlipf who took part with enthusiasm in the examination of the PhD.

This work was mainly funded by the Federal Ministry for Economic Affairs and Energy according to a resolution by the German Federal Parliament in the scope of research projects DFWind (Ref. Nr. 0325936C), SmartBlades2 (Ref. Nr. 0324032D), CompactWind II (Ref. Nr. 0325492H). I acknolwedge all project partners for their support.

Ananth October 12, 2025

LIST OF ABBREVIATIONS

AEP Annual Energy Production ABL Atmospheric Boundary Layer

ALM Actuator Line Model

CBL Convective Boundary Layer
CNR Carrier to Noise Ratio
CPC Collective Pitch Control
D Wind turbine rotor diameter
DBS Doppler Beam Swinging

FAST Fatigue, Aerodynamics, Structures and Turbulence code

FFT Fast Fourier Transform

FLORIS FLOw Redirection and Induction in Steady State

GPS Global Positioning System

HH Hub Height

IEC International Electrotechnical Commission

IRGASON integrated CO2/H2O open-path gas analyzer and 3D sonic anemometer

IPC Individual Pitch Control
LAC Lidar Assisted Control
LCOE Levelised Cost of Energy
LES Large Eddy Simulations
Lidar Light Detection and Ranging
LiXim Lidar Scanner Simulator

MM Met mast

PALM Parallelised Large Eddy Simulation Model

PIV Particle Image velocimetry
PTV Particle Tracking velocimetry
POD Proper Orthogonal Decomposition

Plan Position Indicator PPI **PSD** Power Spectral Density RHI Range Height Indicator **RMSE** Root Mean Square Error Reduced-Order Model ROM SBL Stable Boundary Layer SRWS Short Range WindScanner VAD Velocity Azimuth Display Wind Field Reconstruction WFR

WT Wind Turbine

LIST OF SYMBOLS

Common

Symbol	Meaning	Unit
a	Axial induction factor	-
f	Focus distance	m
$n_{\rm LOS}$	Line-of-sight direction unit vector	-
R	Goodness of fit of a linear regression	-
$S_{ m V}$	Vertical shear parameter	s^{-1}
TI	Turbulence intensity	-
U	Cumulative horizontal wind speed component	${\rm m}~{\rm s}^{-1}$
и	Wind speed vector	${\rm m}~{\rm s}^{-1}$
и	Wind speed component in <i>x</i> -direction	${\rm m}~{\rm s}^{-1}$
$u_{\text{projected}}$	Projected longitudinal wind speed in <i>x</i> -direction	${\rm m}~{\rm s}^{-1}$
$u_{ m eff}$	Lidar estimated rotor effective longitudinal wind speed	${\rm m}~{\rm s}^{-1}$
$u_{ m hub}$	Hub height wind speed	${\rm m}~{\rm s}^{-1}$
u_{∞}	Freestream wind speed	${\rm m}~{\rm s}^{-1}$
v	Wind speed component in <i>y</i> -direction	${\rm m}~{\rm s}^{-1}$
w	Wind speed component in <i>z</i> -direction	${\rm m}~{\rm s}^{-1}$
x	Domain longitudinal direction	m
y	Domain lateral direction	m
z	Domain vertical direction	m
α	Vertical wind shear exponent	-
β	Wind veer	0
Γ	Half Width Half Maximum of Lidar beam	m
δ	Lidar elevation angle	0
$\delta_{ m h}$	Lidar estimated yaw misalignment	0
θ	Relative horizontal wind inflow angle	۰
λ	Wavelength of Lidar laser beam	μ m
χ	Azimuth angle of line-of-sight direction	•
ω	Blade rotational speed	rad/s

CHAPTER 2

Symbol Meaning Unit

xviii 0 List of Symbols

a	Effective radius of the lidar's telescope	m
a_1, a_2, b_1, b_2	Wind evolution tuning parameters from LES	-
S	Distance from the focus point along the line-of-sight direction	m
$e_{ m eddy}$	Smallest detectable eddy size	m
ϵ_u	Error of projection estimation of the longitudinal wind speed.	${\rm m}~{\rm s}^{-1}$
f	Lidar upstream focus distance	m
$f b_{ m LES}$	Coherence bandwidth from LES	Hz
$f b_{ m unmod}$	Estimated Coherence bandwidth from Eq. 2.8	Hz
$fb_{ m mod}$	Estimated Coherence bandwidth from Eq. 2.9	Hz
$f_{ m opt}$	Optimal focus distance	m
$f \hat{b}_{ m opt}$	Optimal coherence bandwidth	0
û	projection estimation of the longitudinal wind speed.	${\rm m}~{\rm s}^{-1}$
$k_{ m opt}$	Optimal wave number	rad/m
$L_{\rm u}$	Integral length scale	m
u_{ind}	Induction zone wind velocity	$m s^{-1}$
γ	Wind coherence	(-)
2Γ	Full Width Half Maximum of Lidar beam	m
Δx	Horizontal separation between measurement locations	m
ϵ	Standard and dynamic error of lidar estimated wind parameters	-
$\theta_{ m up}$	Turbine uptilt	0
$\theta_{ m opt}$	Optimal opening angle	0
θ	Scanning lidar beam deflection angle	0
ξ	Upstream location factor	-
ρ	Correlation coefficient	-
$\sigma_{\rm m}$	Standard deviation of the longitudinal wind speed	${\rm m}~{\rm s}^{-1}$

CHAPTER 3, 4

Symbol	Meaning	Unit
G	Gappiness	-
L	Obhukov length	m
M	Dimensions of the reduced-order reconstructions	-
m	Masking matrix of the velocity snapshot matrix	-
N	Dimensions of the full reconstructions	-
n	Gappy-POD main iteration indices	-
R	Covariance matrix	-
S	Gappy-POD sub-iteration indices	-
${ m TI}_{spatial}$	Lidar estimated spatial turbulence intensity	-
$u_{\rm eff,wake}$	Wake effective wind speed	${\rm m}~{\rm s}^{-1}$
V	Velocity snapshot matrix	${\rm m}~{\rm s}^{-1}$
V'	Fluctuating velocity field	${\rm m}~{\rm s}^{-1}$
$\overline{V}_{n,s}$	Filled wind field	${\rm m}~{\rm s}^{-1}$
$\overline{V}_{n,s} \ ilde{V}_{n,s} \ ilde{V}_n$	POD approximation of filled wind field	$m\ s^{-1}$
\hat{V}_n	Gappy-POD reconstructed wind field at the end of n^{th} iteration	$m\ s^{-1}$

$\langle V \rangle$	Time averaged spatial velocity field	$\mathrm{m}\;\mathrm{s}^{-1}$
$v_{ m los,gappy}$	Converged Gappy-POD reconstruction	${\rm m}~{\rm s}^{-1}$
$v_{ m los,ref}$	Reference Gappy-POD reconstruction	${\rm m}~{\rm s}^{-1}$
$\hat{v}_{ m los}$	Fitted line-of-sight of the three-parameter model	${\rm m}~{\rm s}^{-1}$
$X_{d t}$	Location of valid measurement points	-
$X_{g t}$	Location of invalid points	-
z_0	Friction velocity	${\rm m}~{\rm s}^{-1}$
$y_{\rm c}$	Wake meandering position in the lateral direction	m
z_i	Modal temporal evolution	-
$z_{\rm c}$	Wake meandering position in the vertical direction	m
ϵ	Reconstruction errors	-
λ_i	POD eigenvalues	-
ϕ_i	POD spatial mode	-

CHAPTER 5

Symbol	Meaning	Unit
$e_{ m u,v}$	Dual-Doppler reconstruction error	-
k	von Karmen constant	-
g	Accleration due to gravity	$\mathrm{m}\;\mathrm{s}^{-2}$
L	Obhukov length	m
u_{\star}	Friction velocity	$\mathrm{m}~\mathrm{s}^{-1}$
$v_{ m los,i}$	Line-of-sight velocity measured by the <i>i</i> th lidar	$\mathrm{m}~\mathrm{s}^{-1}$
z/L	Monin-Obhukov stability parameter	-
γ	Wind veer	0
YWT1	Yaw misalignment of WT1	0
YWT2	Yaw misalignment of WT2	0
$\theta_{winddir}$	Wind direction measured at met mast hub height	0
$ heta_{ ext{GPS},1}$	GPS measured WT1 heading	0
$ heta_{ ext{GPS},2}$	GPS measured WT2 heading	0
$ heta_{ m s}$	Sonic temperature	K

LIST OF FIGURES

1.1	Generic coherent detection lidar system.	4
1.2	Lidar line-of-sight wind speed measurement strategies: [a] velocity azimuth display (VAD); [b] range height indicator (RHI) [van Dooren 2021]; [c] nacelle-mounted inflow scanning; [d] multiple synchronised scanning	6
1.3	Block diagram of a typical combined feedforward-feedback mechanism with inflow sensing lidars	10
1.4	[a] Visualisation of the scanning patterns of the SpinnerLidar along with the scanning trajectory of a simpler 2 and 4 beam lidar system. [b] The SpinnerLidar at the University of Oldenburg.	12
1.5	Wind field reconstruction ambiguity between a horizontal shear (left) and a misaligned direction (right).	13
1.6	Wind field reconstruction ambiguity between directional misalignment (left) and a partial wake scenario (right).	14
1.7	[a] A nacelle installation of the SpinnerLidar on the CART3 research turbine at the National Renewable Energy Laboratory. Photo credit: Marijn Floris van Dooren. [b] Distribution of the measured line-of-sight wind speeds from the SpinnerLidar for one minute.	15
2.1	The investigated lidar scan patterns.	28
2.2	The mean longitudinal component u at a vertical plan 1 D upstream of the reference turbine for the CBL and SBL cases at the beginning of the main run. The red circle indicates the area covered by the rotor.	29
2.3	The SpinnerLidar along with its mounting mechanism at the University of Oldenburg.	31
2.4	The visualisation of the rosette scan pattern performed by the SpinnerLidar seen in the <i>y-z</i> -plane	31
2.5	The variation of the measurement probe volume as a function of focus distance for the SpinnerLidar.	31
2.6	(a) Visualisation of the different scanning scenarios simulated for the study. The horizontal dotted lines indicate the width covered by the rotor. The black vertical lines show the different focus distances, and the coloured lines illustrate the different deflection angles of the SpinnerLidar, respectively. (b) The scatter plot between the LES u -component 1 D upstream of the turbine along the rotor axis against the corresponding SpinnerLidar $v_{\rm los}$	
	measurement for the CBL and SBL cases	32

xxii List of Figures

2.7	The first four standardised moments of the time series calculated at different upstream positions relative to the location of the turbine for the CBL and SBL cases. The dotted lines are the result of a lidar performing measuring with the influence of the probe volume and the circles are the results of the perfect lidar measurements without probe volume averaging. The solid lines are the results from the <i>u</i> -component velocity from the LES simulations at the nearest grid point	33
2.8	Time series of the line-of-sight wind velocities measured along the rotor axis for different focus distances compared against the longitudinal wind speed component from the reference LES at the same location. Only the CBL case is shown.	35
2.9	The ratio of the turbulent kinetic energy along the line-of-sight direction measured at the different upstream distances along the rotor axis for the lidar measurements with and without probe length averaging. Here $2\Gamma \leq \delta x$ indicates the region where the probe volume is smaller than the LES grid resolution	36
2.10	The error in estimation of the longitudinal component (ϵ_u) as a function of the elevation δ and azimuth χ angle for unity lateral and vertical wind speed in Eq. 2.4. The red circle indicates the \pm 30° opening angle of the SpinnerLidar	36
2.11	The non-rotating turbulent spectra of the line-of-sight velocities calculated from the SpinnerLidar simulations at a point located on the rotor axis at different upstream focus distances ($f=30\mathrm{m},60\mathrm{m},90\mathrm{m},126\mathrm{m}$ and 150 m). The solid lines show the results of a "perfect" lidar while the dotted lines show the results including the volume averaging effect while the dashed vertical line indicated the Nyquist cut-off frequency.	38
2.12	Power spectral density of the v_{los} and $u_{projected}$ velocities normalised with the PSD of the LES u velocity for the CBL and SBL cases. Points A, B, C, D lie are defined in Fig. 2.4	38
2.13	The rotational spectrum of the line-of-sight (dotted lines) and the projected velocities (solid lines) calculated by following a point located at 90% of the rotor radius for different upstream measurement distances following the legend in Fig. 2.11. The rotational speeds were $\omega_{\text{CBL}} = 11.8$ rpm and $\omega_{\text{SBL}} = 8.59$ rpm respectively. Legend similar to Figure 2.11	39
2.14	Coherence obtained between the reference upstream point located at $f = 150$ m in front of the turbine along the rotor axis from the LES simulations with ideal and real SpinnerLidar measurements at $f = 30$ m, 60 m and 90 m corresponding to $\Delta x = 120$ m, 60 m and 24 m for the CBL and SBL cases respectively	40
2.15	Coherence calculated between SpinnerLidar measurements for three different longitudinal separation distances along the rotor axis from the reference LES wind field and the coherence estimated by the unmodified longitudinal model and the modified coherence model taking into account the induction slowdown for the CBL and SBL cases.	40
	SIOWGOWH TOT THE CDL AND ODL CASES	40

List of Figures xxiii

2.16	Normalised mean square error between the rotor effective wind speed calculated from the turbine and the lidar measured rotor effective wind speed as a function of focus distance and opening angle for SpinnerLidar measurements for the CBL and SBL cases.	42
2.17	The standard and dynamic errors calculated for the different spatial samples	
	for the CBL case and the SBL case.	44
3.1	The SpinnerLidar with its mounting platform mounted on the nacelle of the research turbine CART3 at the National Renewable Energy Laboratory (NREL), Colorado, USA. Photo courtesy of Marijn Floris van Dooren	57
3.2	The rosette scanning pattern of the SpinnerLidar shown from two perpendicular perspectives	58
3.3	(a) Vertical profiles of the potential temperature, wind speed and wind veer at the end of the precursor run and (b) the averaged <i>u</i> -component at hub height extracted from the unstable LES wind field for the main run. The black vertical line indicates the position and size of the turbine rotor, and the red curve is the SpinnerLidar's measurement trajectory	59
3.4	Eigen value distributions (a) and the energy contribution of each mode (b)	
	for the unstable and stable cases	61
3.5	POD modes 1 to 4 of the line-of-sight ($v_{\rm los}$) measurements for the CBL case.	61
3.6	POD modes 1 to 4 of the line-of-sight ($v_{\rm los}$) measurements for the SBL case.	61
3.7	CBL case: Reconstruction of the line-of-sight (v_{los}) velocity snapshot at an arbitrary time instant $t = 256$ s with different numbers of modes ($M = 1,5,7$ and 10) and their corresponding errors with respect to full lidar	62
3.8	measurements (bottom right-hand plot captioned as lidar) The time series of the wind field parameters $u_{\rm eff}$, $s_{\rm v}$ and $\delta_{\rm h}$ extracted at a sampling rate of 1 Hz for a duration of 300 seconds for different POD	
3.9	reconstructions for the CBL and SBL cases	65
3.10	parameters; and the time evolution of the different POD modes $Z_j(t)$ (a) Fixed point spectra of the v_{los} velocity on the rotor axis at an upstream measurement distance of 126 m with $M=1,3,5$ and 10 modes. (b) Rotational spectra of the $u_{projected}$ velocities of the reduced-order reconstruction with	67
3.11	$M = 1, 3, 5$ and 10 modes. The results are shown only for the CBL case RMSE normalised with the hub height wind speed u_{hub} as a function of	68
	main iterations for the CBL case (solid lines) and the SBL case (dotted lines) for different gappiness percentages.	70
3.12	(a) Error comparison for the three methods. Solid and dotted lines indicate the CBL and SBL cases, respectively. (b) Comparison of the computational	
	time taken for the three methods to reconstruct missing points	71
3.13	Comparison of s_v , δ_h and $TI_{Spatial}$ calculated from the reconstructed data for the CBL case with $G = 30\%$	72

xxiv List of Figures

3.14	Comparison of s_v , δ_h and TI _{Spatial} calculated from the reconstructed data for the SBL case with $G = 30\%$	73
4.1	(a) The mean longitudinal wind velocity component (<i>u</i>) at a horizontal plane at hub height. The SpinnerLidar (red curve) is simulated at the hub height of the upstream turbine WT1 and the virtual downstream turbine WT2. (b) Exemplary instantaneous snapshot of the simulated SpinnerLidar measurement from WT1	81
4.2	(a) The main iteration convergence for the undisturbed inflow and the full wake inflow cases for different gappiness percentages <i>G</i> . The solid and dotted lines denote the undisturbed inflow and the full wake case respectively. (b) The RMS error calculated for the Gappy-POD with optimum number of main iterations and the spatial interpolation estimation at the missing points for different gappiness percentages	85
4.3	A snapshot of (a) the true reference wind field and (b) a gappy wind field with 66% gappiness at an arbitrary time $t = 2266$ s obtained from the undisturbed inflow case. The result of spatial interpolation of the gappy field is seen in (c) while (d) illustrates the reconstructed wind field obtained from the Gappy-POD algorithm after the optimum number of iterations	86
4.4	Time series of the three wind field parameters $u_{\rm eff}$, $s_{\rm v}$ and $\delta_{\rm h}$ at 1 Hz for a duration of 200 seconds	87
4.5	(a) Fixed point spectrum at the spatial point with lowest availability. Reference indicates the full lidar data with the volume averaging effect and Perfect refers to ideal lidar measurements without the volume averaging effect. Interpolated and Gappy refers to the spectra calculated from the missing point estimates through the Gappy-POD and spatial interpolation methods and $-5/3$ Kolmogorov slope is also indicated. (b) The rotational spectrum measured by following at point at 90% of the blade radius with a rotational speed of 0.19 Hz	88
4.6	Time series of the three wind field parameters $u_{\rm eff,wake}$, $y_{\rm c}$ and $z_{\rm c}$ at 1 Hz for a duration of 200 seconds	90
5.1	The wind park and measurement layout at Kirch Mulsow overlayed with elevation contours. A zoomed-out image of the site is shown in the top right corner illustrating the hills present upstream of the wind park. MM and VAD refer to the met mast and the inflow lidar while WS1 and WS2 refer to the two WindScanners. © Microsoft	97
5.2	(a) View of WS2 installed in a weatherproof container with WT1 in the background. The WindScanners were lifted through a hatch on the roof during operation using a hydraulic table. (b) The two laser beams from WS1 and WS2 simultaneously focused over a distance of approximately 200 m at WT2 onto a 5.3 cm by 8.6 cm laser beam detector card (white dots)	00
	after performing a steering calibration	98

List of Figures xxv

5.3	Illustration of the horizontal scanning pattern performed by the Wind-Scanners, indicating the relative position of the two turbines and the two WindScanner with and without an intentional misalignment. The coordinate system is centred at the bottom of WT2	100
5.4	(a) The variation of the lidar measurement volume with focus distance. The dashed lines indicate the minimum and maximum measurement ranges, and (b) the variation in the effective lidar measurement volume within the scanning area	102
5.5	The variation of the beam intersection angle $R_{\rm int}$ (a) and the elevation angles, $\delta_{\rm WS1}$ (b), $\delta_{\rm WS1}$ (c) in the scanning area. WT2 is represented by a black vertical line at $x/D=0$	103
5.6	Longitudinal (u) , lateral (v) and vertical (w) velocities on the horizontal plane from the LES (1 st row) and the results of 2D WindScanner reconstruction inside the LES (2 nd row) both averaged for the last 35 minutes of the simulation. The black vertical line at $x/D=0$ is the rotor of WT2	107
5.7	Statistical uncertainty estimated through the margin of error for the (a) u and (b) v components for the evaluated LES flow field	109
5.8	Dual-Doppler reconstruction error for (a) the longitudinal (e_u) and (b) the lateral (e_v) components for the evaluated LES flow field. The markers P1 - P6 indicate regions of interest	109
5.9	Quadratic contributions of the different error terms in the Standard Uncertainty Propagation (SUP) to the [a]] longitudinal (e_u) and [b] lateral (e_v) components at the marker	110
5.10	WindScanner estimated velocity profiles (red) of longitudinal (a) and lateral (b) velocities at six upstream cross sections compared against the reference LES (blue). The red shaded area indicate the total combined measurement uncertainty estimated through Eqn. 5.7 and Eqn. 5.8 using the local w velocity component.	111
5.11	Case 1: Longitudinal (a) and lateral (b) velocities measured while WT1 was not operating and WT2 was operational. In (c), the quiver plot is based on the measured horizontal velocities.	111
5.12	Case 1: Inflow longitudinal (a) and lateral (b) profiles extracted at various positions upstream of WT2. The shaded area represents the total combined measurement uncertainty calculated from the standard uncertainty propagation method (a) with $w = 0.2 \text{ m/s}$ or WT1 was not operational	112
5.13	propagation method (e_u) with $w = 0.2$ m/s, as WT1 was not operational Case 1: Comparison of the velocity deceleration along the rotor axis against the predictions from different induction zone models. The green shaded area represents the upper and lower bounds of the total measurement uncertainty	113 114
5.14	Case 2: Longitudinal (a) and lateral (b) velocities measured for the full wake case. The contour of the magnitude of the horizontal velocity and its vector field is plotted in (c).	

xxvi List of Figures

5.15	Case 2: Longitudinal and lateral velocities measured for the full wake case.	
	The shaded area represents the total combined uncertainty calculated from	
	the standard uncertainty propagation method (e_u) with $w = 1$ m/s, as WT1	
	was operational	116
5.16	Cases 3 and 4: Longitudinal and lateral velocities measured for positive yaw	
	offset (Case 3, 1st row) and negative yaw offset (Case 4, 2nd row). The red	
	dashed line represents the average wind direction during the measurement	
	period	117
5.17	Cases 3 and 4: Wake profiles of the normalised longitudinal component	
	(upper row) and the lateral velocity (lower row) extracted at various po-	
	sitions upstream of WT2 during active wake steering at WT1. The dots	
	correspond to the wake centre at each location. The shaded area represents	
	the total combined uncertainty calculated using the SUP method with $w =$	
	1 m/s	110

LIST OF TABLES

2.1	Overview of the scan patterns used to investigate the effects of spatial sampling.	27
2.2 2.3	The key parameters of the two PALM-FAST simulations Settings of the SpinnerLidar scenarios performed with the LiXim. The last	30
	row contains the normal operational parameters of the SpinnerLidar. The focus distance is normalised with the rotor diameter of the NREL 5 MW reference turbine.	32
2.4	Coherence bandwidth for the modified ($f b_{\text{mod}}$) and the unmodified ($f b_{\text{unmod}}$) coherence models and the results from the reference LES wind field for the CBL and SBL cases.	41
2.5	CBL Case: The optimal focus distance and opening angle for the highest coherence bandwidth and corresponding measurable wave number for the rotor effective wind speeds calculated for the different scans	43
2.6	SBL Case: The optimal focus distance and opening angle for the highest coherence bandwidth and corresponding measurable wave number for the rotor effective wind speeds calculated for the different scans	43
3.1	Setup of the two LES simulations and the results at the end of the precursor run	59
4.1	Root Mean Square Error (RMSE) for the calculated three inflow and wake parameters parameters for the Interpolated and gappy cases	88
5.1	Relative and normalised distances from the bottom of WT2 and WS1, WS2 and WT1. The height offsets for WS1 and WS2 are calculated from the middle of the outer prism at the highest jacked-up position of the hydraulic	404
5.2	table (Fig. 5.2 (a))	101101
5.3	Overview of the measurement cases acquired in the field. Each case is characterised by its freestream wind speed u_{∞} , turbulence intensity (TI), integral length scale (T_i) , mean θ_{wdir} and its standard deviation within the measurement period, stability parameter (z/L) , stability, wind veer (γ) , α_{shear} and the yaw offset of the turbines (γ_{WT}) . Here the following abbreviations are used: Strong Stable (SS), Weakly Stable (WS) and Near	
	Neutral (NN)	105

1

Introduction

The transition of energy infrastructure towards sustainable energy sources from fossil fuels represents one of the most challenging problems of the 21st century. Sustainable energy brings many economic and environmental benefits, including reduced greenhouse gas emissions by moving away from fossil fuels and diversifying energy supply while stimulating growth by increased economic activity. To this effect, many countries worldwide have set ambitious goals for this transition. The Paris Agreement within the United Nations Framework Convention on Climate Change is one measure. This agreement outlines a set of climate change mitigation, adaptation and financial policies to reduce global warming [Glanemann et al. 2020].

One of the more ambitious goals of the Paris accord is to maintain the global average temperature increase within 2 $^{\circ}$ C pre-industrial levels and to limit the rise to 1.5 $^{\circ}$ C preferably. Wind energy will play a vital role in shifting towards sustainable energy sources. According to data collected from Frauhofer ISE 2024, in Germany, renewable energy accounted for approximately 60 $^{\circ}$ 0 of the net power production in 2023, with onshore and offshore wind energy accounting for 32 $^{\circ}$ 0 of the net electricity production.

For the successful economic operation of wind farms and to maintain strong growth rates, it is necessary to accurately predict the energy yield of a wind park and reduce the levelised cost of energy (LCoE) over its operational period. Reductions in LCoE can be brought about in many ways, such as optimising energy production and extending operational lifetime by utilising technological innovations. With rotor diameters exceeding 200 m and growing, innovative solutions to optimise turbine performance are necessary, requiring advancements in wind turbine design, development of sensors and control strategies. With accurate predictions of energy yield during operation, the financial and operational risks of wind farms could be reduced. However, one of the main challenges of extracting power from wind is that wind field as an energy resource is unknown until it reaches the rotor. The turbine only reacts to changes in the inflow after the wind affects the rotor.

1.1 THE NEED FOR REMOTE SENSING IN WIND ENERGY

Wind energy science and engineering requires observations and understanding of the atmospheric flow, the fuel that drives wind turbines. The variability in the wind resource

that a turbine would experience during its lifetime directly impacts power production and creates a wide variety of mechanical responses. While wind observations during the resource assessment stage are useful for determining the wind energy potential at a site, wind observations during turbine operation can be used to optimise the turbine performance [Schlipf 2016].

There is a demand for accurate experimental data measured with high spatial and temporal resolutions for studying fluid flow problems, and wind energy is not different. The development of high fidelity flow modelling tools requires highly resolved experimental measurements capable of capturing very small scales with high accuracy to validate these models.

Wind observation has been performed for centuries since the development of the first mechanical anemometer by Leon Battista Alberti in Italy in 1450. His design consisted of a flat plate suspended perpendicular to the wind, which swung proportionally to the force exerted on it by the wind. The rotational or cup anemometer, first developed by John Robinson in 1846, works based on the pressure differences between its convex and concave surfaces. These devices are widely accepted in meteorology as reliable measurement devices. Anemometers based on temperature gradients (hot-wire anemometers) and sound waves (ultrasonic anemometers) also exist. All of these methods are *intrusive*: the measurement device needs to be physically present inside the flow they need to measure [Kaimal et al. 1968] and therefore can drastically influence the flow at the measurement location.

Cup anemometers constitute the traditional method of performing accredited measurements for wind energy applications such as resource assessments and power curve measurements. Aside from the device-induced flow perturbation, these devices' application is surmounted by many problems. With growing wind turbine sizes, traditional methods for wind measurements such as anemometers mounted on expensive tall masts are insufficient to measure the wind speed distribution over the rotor. The diameters of modern rotors regularly exceed 100 m and is pushing beyond 200 m¹. Accurate measurements of the flow around present-day wind turbines require multi-point and multi-height measurements in the rotor plane area to characterise the atmospheric flow variations over the rotor. For measuring vertical wind profiles, expensive tall met masts outfitted with anemometers at many heights are required. Such tall met masts are quite uneconomical, especially offshore. Optical methods for flow diagnostics have improved remarkably in the last decades and are irreplaceable tools for experimental research and routine diagnostics in the industry. Tools like Particle Image Velocimetery (PIV) [Adrian 2005], Particle Tracking Velocimetery (PTV) [Maas et al. 1993], Laser Doppler Anemometry (LDA) [Tropea 1995] have been developed and improved in the last decades and have consistently shown their value in measurement of fluid flows. PIV and PTV techniques, which use high-speed cameras to record a seeded flow illuminated by lasers, are indispensable when the size of the flow system is small, i.e., a small wind tunnel campaign or the measurements of biological flows. PIV methods have also been applied exceptionally also in field measurements around large turbines using snowflakes as tracer particles [Hong et al. 2014], but cannot be relied on as they only operate under particular atmospheric conditions.

 $^{^{1}}$ The Mingyang MySE 16-260 offshore turbine with a rotor diameter of 260 m respectively and rated up to 16 MW is the largest commissioned turbine as of March 2024.

1

3

Remote sensing methods based on Doppler anemometry provide an alternative method for wind measurements in wind energy applications. Doppler anemometers are *non-intrusive*: they can probe the wind remotely from a location far away from the measurement region of interest, paving a way to overcome flow perturbation due to sensing. The measurement principle of Doppler anemometry involves sending waves of different natures (radio, sound and light for Radars, Sodars and Lidars, respectively) into the atmosphere, where a portion gets scattered by aerosols in the wind. The aerosols impart a Doppler shift proportional to the velocity, which can be estimated by measuring the incident and the reflected frequencies of the wave beam through Detection And Ranging (DAR) techniques.

Even though laser an emometry has been used since the 1960s, the rise of high-powered diode lasers in the 1980s and the development of the modern 1.5 $\mu \rm m$ wavelength laser by the telecommunications industry has made laser an emometry with Doppler wind lidars a desirable proposition for wind energy applications [Hill 2018]. Modern lidars created for wind energy applications are compact and operate around the 1.5 $\mu \rm m$ wavelength due to these advancements.

1.2 A BRIEF INTRODUCTION TO LIDAR ANEMOMETERY

The measurement principle of lidar anemometry involves sending a laser beam of narrow bandwidth into the atmosphere where a portion is scattered by atmospheric aerosols. The laser beam illuminates the area around the target point and gets backscattered off the atmospheric aerosols assumed to be carried by the wind. The backscatter is measured by the receiver system from which the Doppler shift, and with prior knowledge of the emitted frequency, the corresponding velocity is estimated along the laser beam direction: the radial or the line-of-sight velocity $v_{\rm los}$.

$$f_r = f_e \left(1 + 2 \frac{v_{\text{los}}}{c} \right) \tag{1.1}$$

where $f_{\rm e}$, $f_{\rm r}$ are the incident and reflected laser beam frequencies and c is the speed of light. The measurement principle relies on the assumption that aerosols are transported at the same speed as the wind while the backscattered signal relies on good environmental conditions to reach the lidar again. Two detection concepts exist: direct and coherent detection methods.

In direct detection, the Doppler shift is directly estimated from the backscattered light using suitable optical frequency analysers, which detectors can measure. On the other hand, in coherent detection systems, the backscattered light from the atmosphere is mixed with a portion of emitted light to create a beat signal which can be detected by photodetectors and from which the Doppler shift is estimated. Coherent detection is further classified into homodyne and heterodyne detection. In homodyne detection, the local oscillator is unmodified; hence estimating the frequency shift's sign and thereby the sign of the line-of-sight wind velocity is impossible. In heterodyne detection, the local oscillator is shifted by a specific frequency allowing to determine the sign of the frequency shift and hence the measured velocities.

Wind lidars are subdivided into two major types depending on how the device emits the laser beam. In the continuous measurement type, referred to as continuous-wave (cw) lidars, the laser beam is focused at the target measurement point. The continuous operation

4 1 Introduction

enables a high intensity at the measurement location providing high sampling rates of up to 500 Hz. However, when focusing the laser beam at more considerable distances, the peak of the backscatter spectra is less defined as the return signal contains contributions of the reflected laser light over a large measurement length. Therefore, the length of the measurement volume limits the maximum range of cw lidars. In the pulsed systems (referred to as pulsed lidars), the laser beam is emitted in pulses while the pulse propagates through the atmosphere until its intensity decreases. As the pulse moves through the atmosphere in the desired direction, light is continuously emitted back by the aerosols. By carefully controlling the width of the emitted pulse and the accumulation time between pulses, these lidars can simultaneously estimate the radial wind speeds along the beam direction at multiple locations. The distances are calculated from the time-of-flight of the light collected from various range windows. Due to the accumulation time required for the laser pulses to travel back to the lidar and to provide a high enough signal-to-noise ratio to provide a reasonable velocity estimate, pulsed lidars sample at a substantially lower sampling rate, usually in the range of 0.1 Hz to 10 Hz but can measure at distances of tens of kilometres away.



Figure 1.1: Generic coherent detection lidar system.

Both cw and pulsed lidar measurements contain wind speed contributions from a volume of an air pocket in space rather than an infinitesimally small point where the measurement was intended. Since the dimensions of the measurement volume along the laser beam direction are much larger than the traverse dimensions, the measurement volume is modelled as an infinitely thin beam. The measured wind speeds along the infinitesimally narrow beam are integrated according to a weighting function from the detected line-of-sight wind speeds. Therefore, the line-of-sight measurement can mathematically represent a convolution of the projection along the laser beam direction and a weighing function. For cw lidars, the weighing function is approximated as a Lorentzian distribution as defined in Sonnenschein and Horrigan 1971, while for pulsed systems, the pulse shape is approximated as a Gaussian pulse [Sathe and Mann 2012].

Furthermore, any lidar system can only measure the projection of the wind velocity along the line-of-sight direction, the so-called *cyclops dilemma* [Schlipf and Kühn 2008]. Therefore, multiple beams or mechanical systems are required to steer the laser beam to different directions to obtain information about the wind vector rather than the lidar measured radial

wind speed component. However, as synchronised scanning strategies are quite complex, simplified wind profiles are obtained by assuming certain flow field characteristics and combining measurements over multiple spatial locations. This process is broadly termed wind field reconstruction, which van Dooren 2023 defines as "combining multiple line-of-sight measurements from one or multiple lidars to yield a specific wind field description suitable for a particular application." In this thesis, we focus on developing a spatially varying line-of-sight velocity field description from scanning lidar measurements. This differs from earlier, simpler reconstruction methods where lower spatial and temporal measurement resolutions limited applications to deriving only rotor-averaged quantities relevant for wind turbine inflow.

1.3 Lidar scanning and mounting techniques for wind energy applications

Doppler lidars continue to gain widespread acceptance in wind energy research and industrial communities in the last decade as a reliable tool for performing wind measurements for wind energy applications.

The Velocity Azimuth Display (VAD) and Doppler Beam Swinging (DBS) profiling lidars (Fig. 1.2 [a]) have applications in measuring vertical wind profiles and have large importance in the wind industry by replacing traditional and expensive meteorological masts. They are very robust instruments for site resource assessment due to their relatively cheap and easy installation. However, as a result of sampling many measurement volumes in various directions, the measured wind vector could be erroneous, especially during non-homogeneous flow situations.

Long-range pulsed lidars combined with an optical scanhead offer a spatial resolution of many kilometres with flexible scan trajectories. Scanning patterns such as Range Height Indicator (RHI) (Fig. 1.2 [b]) and Plane Position Indicator (PPI) scans are being used extensively to characterise prominent flow features and interactions between wind farms [Schneemann et al. 2020; Schneemann et al. 2021]. As a long-range lidar can sense the wind conditions at large distances in the order of many kilometres, they can also be used to forecast wind farm power output [Valldecabres et al. 2018; Würth et al. 2019]. Similar to VAD and DBS profilers, assumptions about the wind flow and the wind field models are required to calculate the wind profile from the radial measurements.

Turbine-mounted installations can also measure the flow directly upstream of a wind turbine. Such systems are useful for performing power performance measurements and assisting the turbine control system in corrective actions during unfavourable inflow situations by lidar-assisted feedforward control [Schlipf and Kühn 2008]. A typical turbine-based inflow scanning strategy is visualised in Fig. 1.2 [c]. Due to the lidar limitations of volumetric line-of-sight scanning, wind vector estimation requires assumptions about the incoming flow, such as homogeneity.

A minimum of three independent measurements at the target point are required to retrieve all three components of a wind vector at a measurement point. Synchronising multiple lidar systems in space and time allows for full 3D velocity reconstruction in the scanning area, providing unprecedented insights into flow around wind turbines in free field. By combining scanning and synchronisation strategies, multi-lidar systems are capable

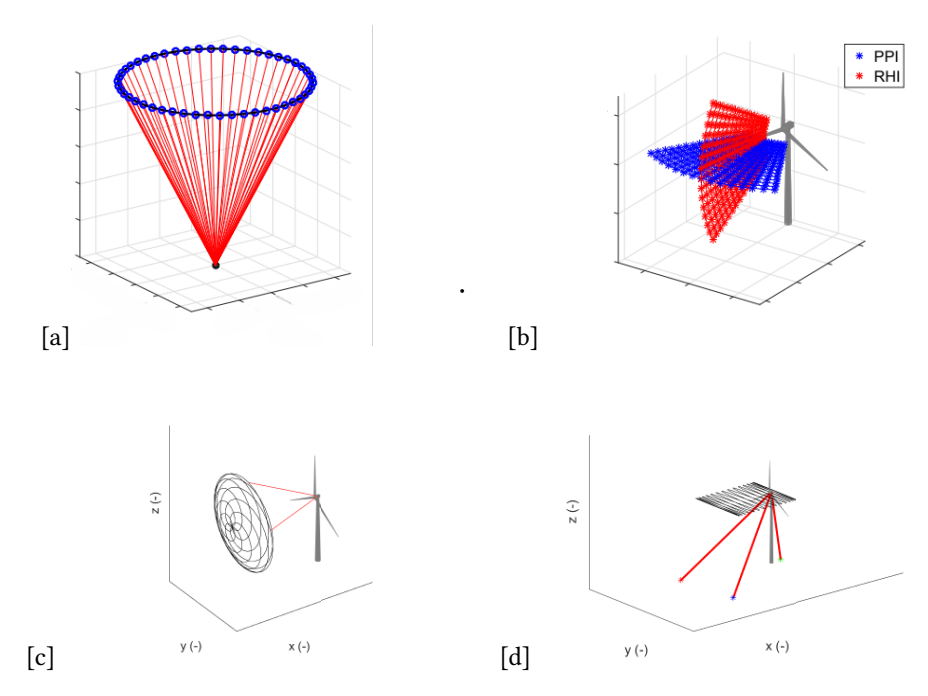


Figure 1.2: Lidar line-of-sight wind speed measurement strategies: [a] velocity azimuth display (VAD); [b] range height indicator (RHI) [van Dooren 2021]; [c] nacelle-mounted inflow scanning; [d] multiple synchronised scanning

of resolving and characterising complex flow events around wind turbines that can be subsequently used to validate numerical flow models (Fig. 1.2 [d]). However, these multilidar measurement strategies require careful installation and calibration of the mechanical systems steering the laser beams to the measurement locations.

1.4 Applications of lidar measured data in wind energy

As a result of their high measurement flexibility, lidars have found use cases in a variety of commercial and research applications.

1.4.1 WIND RESOURCE ASSESSMENT AND POWER PERFORMANCE TEST-ING

Lidar systems are now the *de-facto* source of wind measurements conducted to assess the wind resource potential for both onshore and offshore areas. For offshore sites, a lidar system is typically placed inside a buoy and attached to a mooring that is deployed at the site of interest. These so-called Floating Lidar Systems (FLS), offer an alternative to building expensive offshore met masts and can provide vertical wind profiles and measurement at hub heights for very large offshore turbines. Due to these reasons, profiling lidars have

made their way into the industry accepted standards such as the IEC 61400-50- series and are considered as *bankable* measurements. Bankable measurements refers to data that is considered reliable and accurate enough to be used by financial institutions for making investment decisions in wind farm projects.

During operational phase, turbine-mounted lidars performing upstream measurements can be used to assess the wind turbine power curve [Borraccino et al. 2017; Wagner et al. 2011; Wagner et al. 2014]. The purpose of a power performance test is to verify that a wind turbine's actual power output matches the warranted power curve provided by the manufacturer. In addition to ensuring that contractual obligations between the turbine provider and operators are fulfilled, these tests enable operators to identify any potential performance issues with the turbine that might be affecting its efficiency. Power performance testing with nacelle-mounted lidars is well established in the industry and accepted as best practise [*IEC 61400-50-3* 2022].

1.4.2 FLOW CHARACTERISATION

Both short-range and long-range lidar systems with beam scanning capabilities can be used to understand and characterise the flow around wind turbines in high resolution. The development of scanning lidar systems capable of synchronised scan trajectories can be utilised for multi-dimensional flow characterisation of the interaction between the wind turbine and the atmospheric boundary layer. Such measurements offer an insight into understanding complex flows around wind turbines, while the recorded data could be used to evaluate flow models of different complexities. While wind speed measurements performed by a turbine-mounted lidar can preview the wind inflow to the turbine allowing for control applications, ground-based scanning lidars can be utilised for characterising the flow development around wind turbines and wind farms.

For example, scanning lidars have been used to map the development of a wake of a wind turbine [Bromm et al. 2018; Brugger et al. 2020; Herges et al. 2017b; Iungo et al. 2013; Smalikho et al. 2013; Zhan et al. 2020a], wind farms [Krishnamurthy et al. 2013; Schneemann et al. 2020; Zhan et al. 2020b], wind turbine inflow [Bodini et al. 2017; Held and Mann 2019a; Mikkelsen et al. 2020; Pena et al. 2018; Simley et al. 2016]. In addition, scanning cw lidar systems can also be used to perform flow characterisation of model turbines and wind tunnels due to the highly customisable beam scanning strategies [Hulsman et al. 2022b; van Dooren et al. 2017]. In addition, these devices have also been applied to measure the flow around trees [Angelou et al. 2021] and helicopter downwash [Sjöholm et al. 2014], suspension bridges [Cheynet et al. 2017] and bluff bodies like fences [Peña et al. 2016].

1.4.3 TURBULENCE ASSESSMENT

In addition to the measurements of mean wind speeds and profiles, the measurement of turbulent fluctuations by lidar systems is relevant for wind turbines as they contribute to the structural fatigue of the turbine components. Therefore, accurate wind speed and turbulence estimations are crucial in designing and developing wind farms. However, estimating turbulence from lidars is tricky due to the large measurement volumes due to either focusing the laser beam in cw lidars or the pulse length for pulsed lidar systems. Turbulence measurements with lidars are still an ongoing research topic, and there is no

8 1 Introduction

1

established industry standard for estimating turbulence from lidar systems.

However, an extensive amount of literature is dedicated to extracting turbulence from lidar systems [Kelberlau et al. 2020; Newman and Clifton 2017; Sathe and Mann 2012]. Sathe and Mann 2013 presented a review of lidar-based turbulence estimation techniques over 30 years and pointed out that most works relied on combining isotropic turbulence models with raw lidar measurements. They concluded that the major challenge was estimating unfiltered turbulence from the volume-averaged lidar measurements. Branlard et al. 2013 experimentally demonstrated that the width of the Doppler spectrum of a cw lidar is proportional to the probability density function of the line-of-sight velocities, which opened possibilities of using cw lidars to estimate second-order turbulence statistics. Penã et al. 2017, presented two methods to characterise turbulence from nacelle-mounted lidars using a three-dimensional spectral velocity tensor model combined with a lidar spatial radial velocity averaging model. The first method provided lidar filtered turbulence estimates, while the second provided unfiltered turbulent variances and worked on both pulsed and cw systems. Fu et al. 2022, presented a method to estimate unfiltered Reynolds stress components from the measurements of a nacelle-mounted SpinnerLidar. The method considered the turbulence-induced spectral broadening reduced the error in the turbulence estimation compared to a sonic anemometer. Other methods to model the spectral broadening have been investigated by Angelou et al. 2012, who proposed a direct transfer function based on the attenuation of the power spectral density using measurements from a sonic anemometer as reference. van Dooren 2021, presented a theoretical model for the turbulence spectrum measured by a cw lidar and validated it using hot wire anemometry in an experimental wind tunnel campaign.

1.4.4 LOAD VALIDATION

Mechanical loads on the different parts of a wind turbine are driven by the stochastic turbulent fluctuations that occur in the atmosphere. Previously, due to the large rotor sizes and the sizes of large turbulent structures, it was not possible to fully characterise the inflow based on field measurements without erecting expensive meteorological masts. Therefore, in numerical simulations, the wind fields were modelled as a random three-dimensional Gaussian field while the wind turbulence was modelled through models such as the Kaimal [Veers 1988] or Mann model [Mann 1994; Mann 1998]. Because of the stochastic nature of the wind inflow, the generated wind fields do not match the time series of measurements, even when the statistical properties of the wind fields match well. Therefore, load validation performed utilising generated wind field models can only match the measured loads statistics while there can still be a large uncertainty in the inflow. Consequently, many observations and simulations are required to perform load validation of wind turbines.

With advancements in lidar technology, high-resolution measurements of the wind turbine inflow are possible now. Although characterising the wind turbulence is complex, the lidars still provide sufficient information about the wind inflow compared to other measurement devices such as anemometers. Dimitrov and Natarajan 2017, demonstrated a numerical methodology with six different lidar scanning patterns to perform inflow measurements for load simulations of a 10 MW turbine. They concluded that introducing lidar data to constrain turbulence fields reduced the statistical uncertainty of load signals such as

1

blade flapwise, tower fore-aft and yaw moments. The methodology was applied to field measurements from two lidar systems (Avent five-beam pulsed and a ZephIR cw lidar) in Dimitrov et al. 2019. The results indicated that load validation procedures with lidars provided load estimation uncertainties compared to the loads derived from mast-mounted cup anemometers. Conti et al. 2020, extended the study to perform load validation studies in waked conditions using a nacelle-mounted scanning lidar and highlighted the associated challenges such as the probe volume averaging effect and the assumptions necessary for flow modelling.

1.5 Inflow sensing lidars for optimising turbine operation

Turbine-mounted inflow measuring lidar systems can remotely scan the inflow wind fields upstream of the turbine. Traditionally, turbine control operate on a feedback basis, relying on wind speed and direction measurements from rotor speeds and to a lesser extent on nacelle-based measurements to control blade pitch, yaw angles and generator torque. So, in essence, the turbine only reacts to the wind disturbance already at the turbine. In addition, the wind measurements from the nacelle are perturbed by the presence of the rotor. Using lidar to sense the upstream inflow could improve turbine performance remotely. Lidarassisted feed-forward control (LAC) has been investigated extensively for more than ten years beginning with the work of Harris et al. 2007, who placed a lidar on the wind turbine nacelle and obtained preview information on wind gusts. Since then, a considerable amount of simulation-based studies have been performed aimed at various control objectives such as yaw control [Kragh et al. 2013; Mikkelsen et al. 2013; Schlipf et al. 2011], rotor speed control [Schlipf et al. 2013a; Wang et al. 2013], collective pitch control [Dunne et al. 2010; Schlipf and Kühn 2008; Schlipf et al. 2012a], individual pitch control [Dunne et al. 2011; Dunne et al. 2012; Unguran et al. 2019], cyclic pitch control [Sang et al. 2021; Schlipf et al. 2010], model predictive control [Laks et al. 2011a; Mirzaei et al. 2013a; Sinner and Pao 2018]. Figure 1.3 shows a typical control loop augmented with preview lidar measurements. In a feedback-only control system, the wind turbine is regulated by reactions of the turbine only. The analogy of driving a car blindfolded and reacting to how the car feels has been used to describe this process [Scholbrock et al. 2016]. Adding a lidar to preview the inflow allows the blindfold to be removed, allowing the controller to look ahead and perform a control actuation to a disturbance before the disturbance reaches the rotor plane. For a turbine-mounted lidar measuring a wind speed at a distance upstream of the turbine, a very simple advection assuming the Taylor's frozen turbulence hypothesis [Taylor 1938] would determine the time of impingement of the measured wind field on the wind turbine, excluding any wind evolution and induction zone effects. This effectively allows time to process the lidar measurements into control-ready inflow parameters and perform the necessary actuation to get the turbine ready for the inflow perturbation. However, due to the stochastic nature of the atmospheric boundary layer, terrain effects and the turbine's operation, the advection time between the measurement location and the rotor plane changes [Schlipf et al. 2015; Simley et al. 2014b]. Moreover, the type of lidar device and the data processing algorithms to obtain control relevant parameters heavily influence the effectiveness of any LAC strategy. Even though field testing of lidar-based control is still

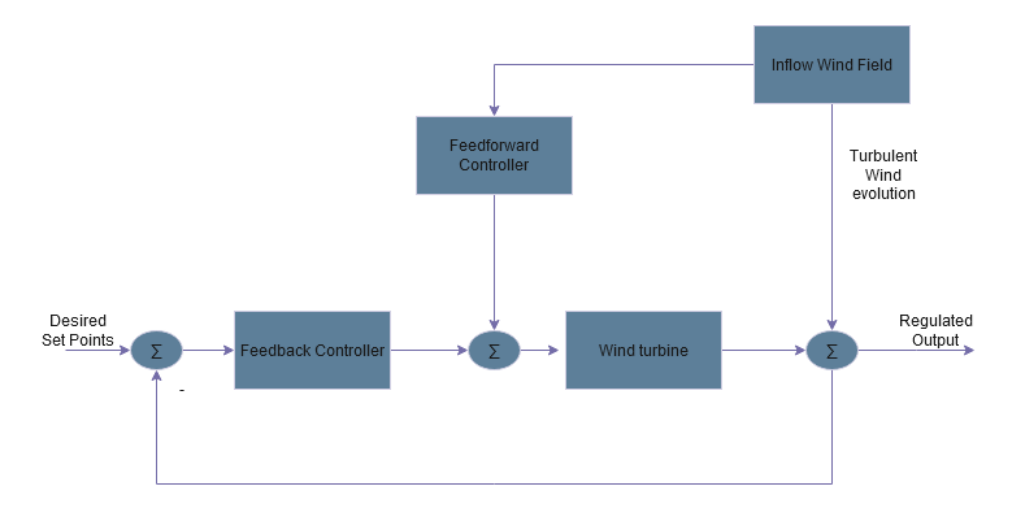


Figure 1.3: Block diagram of a typical combined feedforward-feedback mechanism with inflow sensing lidars.

relatively scarce, promising results in load reduction and increased power production were observed [Fleming et al. 2014; Schlipf et al. 2014; Scholbrock et al. 2013b].

Most LAC strategies have been investigated for use in the below-rated (region 2) and above-rated (region 3) conditions. In the below-rated region, LAC can be utilised to correct for yaw control [Kragh et al. 2013; Mikkelsen et al. 2013; Schlipf et al. 2011] or to increase the power capture [Bossanyi et al. 2014; Fleming et al. 2014; Schlipf et al. 2013b; Schlipf and Kühn 2008]. Field testing in [Fleming et al. 2014; Kragh et al. 2013] indicated that wind vane bias could be identified and corrected using lidar measurements that could potentially increase the turbine Annual Energy Production by a few percentage points. LAC in the below-rated regime has shown a slight increase in power capture. However, the power gains are potentially mitigated due to the increased torque and power fluctuations and therefore increased structural loads due to the tracking of the optimal tip speed ratio [Bossanyi et al. 2014; Schlipf et al. 2013b].

The potential for LAC in regulating rotor speed and reducing structural loads in region three has been established by collective pitch control (CPC) and individual pitch control (IPC) strategies. LAC-based CPC uses lidar measurements to estimate the rotor effective wind speed to regulate the rotor speeds by collectively pitching the blades, thereby reducing the loads [Bossanyi et al. 2014; Dunne et al. 2011; Schlipf et al. 2010]. IPC strategies can mitigate individual blade loads, which could be transferred to the non-rotating turbine components as well [Dunne et al. 2011; Dunne et al. 2012; Laks et al. 2011b]. IPC strategies can take advantage of the extensive lidar spatial coverage to estimate wind parameters such as vertical shear that can be utilised to reduce the once-per-revolution (1P) loads caused due to the horizontal and vertical shear.

More recent work on LAC has looked at the impact of turbulent wind evolution on the lidar measured wind fields its impact on the wind turbine. Chen et al. 2021 proposed a parameterised model for wind evolution following Simley et al. 2014b. The parameterised model provides information for the longitudinal coherence based on other observed variables.

1

Dong et al. 2021 evaluated the effectiveness of LAC under various turbulence characteristics from models specified in the IEC 61400-1 and determined that the benefits of LAC can depend on the turbulence models, the turbulence parameters, and the mean wind speed. In this work.,the lidar measurement coherence by the turbulence models is compared, assuming Taylor's frozen hypothesis. Guo et al. 2023 extended this study moving away from Taylors hypothesis and evaluating LAC performance with realistic wind evolution. This was possible due to improvements in turbulence simulation tools, such as the evoTurb by Chen et al. 2022 and the 4D Mann Turbulence Generator by Guo et al. 2022a, that have made it possible to integrate turbulence evolution into aeroelastic simulations. Further lidar assisted control applications include controller scheduling for reducing structural loads through turbulence intensity estimation [Schlipf et al. 2020] and lidar assisted wake control [Dhiman et al. 2020; Guo et al. 2022b; Lio et al. 2021] and lidar-assisted control for floating wind turbines [Guo and Schlipf 2023; Zalkind et al. 2022].

In a review paper of a joint industry-academia workshop, Simley et al. 2018 summarised the potential benefits and challenges associated with incorporating LAC strategies into wind turbines. Due to its direct impact on power production and load mitigation, LAC strategies have the highest potential of any lidar-based wind energy application in reducing the LCoE. Despite the challenges in integrating lidar measurements into a control system, LAC has received component certification, an essential milestone for technology acceptance. However, specific barriers exist before the full potential of LAC can be realised [Clifton et al. 2018]. The first identified barrier was the multi-disciplinary nature of LAC. Canet et al. 2021 approached this problem from a system-level perspective by integrating LAC concepts into the design phase of the turbine as suggested by Schlipf et al. 2018. Using literature reported LAC-based load reductions, they identified design drivers that LAC could relax and concluded that an LCoE improvement was by lifetime extension increasing AEP of up to 2 %. Similar studies in this direction include the work of Lio et al. 2022 who investigated lidar-assisted wind turbine retrofit control could provide fatigue load reductions and therefore opens possibilities to extend turbine lifetime. However, the study considered an ideal lidar system providing a perfect wind preview. In reality, obtaining a perfect wind preview is quite challenging.

1.6 OPEN QUESTIONS AND CHALLENGES

Looking at literature, a few open questions which would directly impact the effectiveness of utilising scanning lidar systems for measuring and characterising the wind turbine inflow can be identified and discussed briefly.

1.6.1 Evolution of scanning lidar technology

The design of a lidar-based application depends on how well the lidar device can measure the inflow and its variations. Two crucial requirements can therefore be identified. The lidar system should be enable to accurately measure rotor plane wind variations fast enough to capture the relevant spatio-temporal dynamics driving the turbine response. Due to the requirement of a high enough temporal refresh rate, cw lidars are advantageous over pulsed systems for LAC [Simley et al. 2014a]. However, for wind evolution studies, pulsed systems are beneficial due to their ability to measure simultaneously along the laser beam

12 1 Introduction

at several measurement locations. Recent studies indicate that pulsed systems may be beneficial for measuring flow fields in front of very large turbines [Soto Sagredo et al. 2024]. Due to the spatial limitations in the wind field sampling, the spatially varying line-of-sight measurements are combined alongside some flow assumptions to reconstruct wind parameters relevant for any lidar-assisted application. This process is called *wind field reconstruction*, and its accuracy is highly dependent on flow assumptions required for the reconstruction. Inspite of its limitations, simple lidar systems with a few probing beams have been applied successfully in the field for lidar-assisted control [Fleming et al. 2014; Scholpf et al. 2014; Scholbrock et al. 2013b].

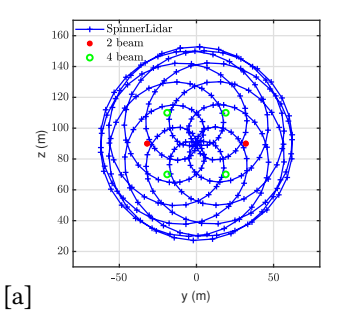




Figure 1.4: [a] Visualisation of the scanning patterns of the SpinnerLidar along with the scanning trajectory of a simpler 2 and 4 beam lidar system. [b] The SpinnerLidar at the University of Oldenburg.

The development of lidar systems with active wind scanning, such as the SpinnerLidar [Herges et al. 2017b; Kidambi Sekar and Kühn 2017; Mikkelsen et al. 2013; Pena et al. 2018] has opened up new opportunities for measuring the wind inflow at high spatio-temporal resolutions. These devices contrast the so-called fixed-beam systems consisting of a handful of laser beams staring consistently at a pre-defined spatial location. The SpinnerLidar is one such device capable of entire rotor plane scans with a high refresh rate (500 point measurements every second). Such a device could be installed directly into the turbine spinner and integrated with the control system to reduce the operational loads, allowing for lifetime extension. It is noted that the SpinnerLidar itself has been designed and suited only as a research device and was not intended to be used for LAC in a commercial application. In Fig.1.4 an illustration of the scanning possibilities afforded by the SpinnerLidar is shown against two commercially available fixed-beam lidar systems installed on a hypothetical NREL 5 MW turbine and scanning 126 m (1 D) ahead (scanning parameters obtained from Fu et al. 2022). The SpinnerLidar, due to its active beam steering (Fig. 1.4 [b]), is capable of measuring the entire swept area in contrast to relatively simple two and four beam systems. This allows possibilities to measure inflow in-homogeneities and follow coherent structures that drive the turbine response. Even though lidars can resolve not all small-scale inflow features, the large-scale atmospheric structures relevant for describing the turbine response can be measured.

At this juncture, obvious financial limitations exist, such as the high capital expenses (CAPEX), low robustness due to moving parts and corresponding high operational costs (OPEX). Moreover, some systems do not yet have dynamical scanning capabilities, i.e., the scanning system's ability to dynamically change scan parameters such as cone opening

angles in response to changing inflow conditions. Hence, it is imperative first to establish the advantages and limitations of scanning lidar systems in scanning the wind inflow and extracting wind parameters relevant to the turbine. Only after the benefits and limitations are established in detail can system-level investigations quantify the value added by utilising different lidar devices for lidar-assisted applications.

1.6.2 LIDAR WIND FIELD RECONSTRUCTION

As a single lidar system can only measure the wind velocities along the laser beam direction, reconstructing three-dimensional wind fields from nacelle-lidar measurements requires simplifying the incoming wind fields. Therefore, the development of data processing methods is necessary to convert lidar measurements into parameters useful for a particular use case, hereby termed wind field reconstruction.

van Dooren 2023 defines wind field reconstruction as "combining multiple line-of-sight measurements from one or multiple lidars to yield a specific wind field description suitable for a particular application". This definition is broad as it can be applied to any lidar data processing methodology such as finite parametrisation to obtain rotor-averaged wind quantities [Borraccino et al. 2017; Kapp and Kühn 2014], dual-Doppler reconstruction for resolution of two or three dimensional velocity components [Mikkelsen et al. 2020; van Dooren et al. 2017], velocity field reconstruction from temporally asynchronous scans [Beck and Kühn 2019; Towers and Jones 2016; van Dooren et al. 2016]. As LAC applications depend on a single lidar on the nacelle measuring the inflow, the parametrisation approach is taken to obtain relevant wind parameters for control. However, the reconstruction process is dominated by the limitations of wind field probing that influence the measurements. If the laser beam is not perfectly orientated with the local wind inflow, the lidar measures a radial or line-of-sight wind speed component, which is a projection of the actual wind speed onto the line-of-sight direction. This effect has been investigated in detail, where it was determined that small opening angles are ideal for estimating the rotor effective wind speeds. In contrast, large angles are preferred to resolve events such as vertical shear or yaw misalignment [Bossanyi et al. 2014]. These limitations create ambiguity in interpreting the extracted wind parameters [Kapp. S 2017; Schlipf 2016].

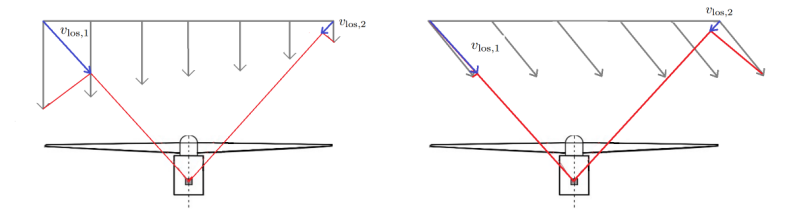


Figure 1.5: Wind field reconstruction ambiguity between a horizontal shear (left) and a misaligned direction (right).

Usual wind field assumptions include no vertical wind speed component and horizontally homogeneous flow. While the zero vertical component might be valid for simple terrain,

14 1 Introduction

the effect of atmospheric stability, such as the vertical upflow during convective conditions, renders this assumption invalid. Horizontal homogeneity implies equal wind speeds and directions at a certain height from the ground. Therefore, the extracted wind parameters could be ambiguous depending on the assumption taken for the wind field reconstruction. An example of this ambiguity is sketched in Figure 1.5. The sketch shows a two-beam lidar system measuring the radial wind speeds at a fixed focal distance. Here $v_{los,1}$ and $v_{los,2}$ are the line-of-sight velocity at the measurement points. In the first case, the wind field could be described as having a linear horizontal shear decreasing from right to left. Therefore, the left beam of the lidar measures a higher line-of-sight component compared to the right. The lidar would measure the same line-of-sight wind speeds in the second picture with the horizontal misalignment, even though the inflow situation is completely different. The argument can also be extended in the vertical direction. Therefore, depending on the assumptions required for a wind field reconstruction algorithm, it is possible to end up with widely conflicting information about the same inflow. This ambiguity potentially limits the application of inflow lidars. For example, lidar cannot be used for cyclic pitch control and yaw control with the same wind field reconstruction methodology as information about yaw misalignment and horizontal shear is necessary. To overcome this ambiguity, Kapp. S 2017 proposed combining the upstream measurements at two unique upstream locations to resolve direction and shear. However, the method assumes that the wind field remains frozen between the two measurement planes. Even assuming a perfectly flat terrain, due to the upstream blockage, the wind inflow is subject to deceleration and therefore contradicts Taylor's hypothesis.

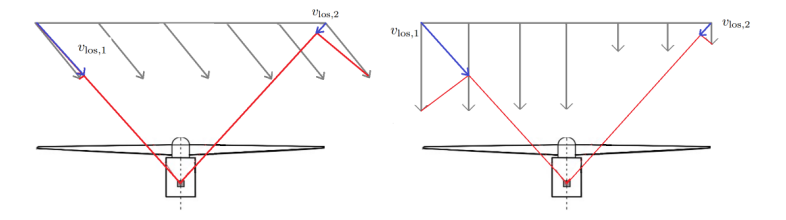


Figure 1.6: Wind field reconstruction ambiguity between directional misalignment (left) and a partial wake scenario (right).

In addition, these methods also have the issue that they cannot differentiate between undisturbed inflow and a waked inflow, a familiar situation for wind turbines in wind farms. This is illustrated in Figure 1.6. The horizontally misaligned flow will affect the line-of-sight measurements of the lidar in a similar way to that of a partially waked inflow. While other methods can identify the presence of wakes, such as by investigating the spectral broadening of the lidar backscatter signal [Held and Mann 2019a] or from the structural response [Bertelè et al. 2021; Bottasso et al. 2018; Schreiber et al. 2020], the application of wind field reconstruction methods to detect wakes would be biased.

Nacelle-based scanning lidars such as the SpinnerLidar overcome the limited spatiotemporal resolutions by providing distributed radial velocity measurements in two spatial dimensions overcoming the spatial scanning limits of simpler lidar systems. Therefore, applying classical wind field reconstruction methods would provide some rotor-averaged estimates of the wind inflow that do not use the full scanning capabilities of scanning systems. For scanning lidar-assisted operation of large turbines, there is a need for new wind field reconstruction models that can effectively capture the spatio-temporal in-homogeneities in the wind field. Therefore, the objective of the WFR methodology for a scanning nacelle-lidar should be to provide spatially varying radial velocity measurements in two spatial dimensions (2D), providing information on instantaneous changes in the wind inflow over the rotor area. This contrasts with the classical WFR definition for simple nacelle lidars that focus on extracting spatially averaged wind information. Furthermore, the large amounts of data collected by scanning lidar systems must be compressed into a few signals that retain the essential dynamical quantities in the inflow.

1.6.3 LIDAR MEASUREMENT AVAILABILITY

Availability for lidar systems is defined as the ratio of the time the lidar produces high-quality, usable data for any purpose to the total duration of the measurement campaign. For a nacelle-mounted lidar system, the availability is influenced by deterministic effects such as the rotation of the blades and stochastic effects like atmospheric conditions such as rain or fog, which reduce the available good data that can be processed [Davoust et al. 2014]. The deterministic data loss is influenced by factors such as lidar geometry, nacelle-mounting position and orientation, blade rotational speed and blade root geometry. Rotor (or) blade interference is the primary quantity affecting data availability for nacelle-mounted lidars. The rotation of the blades prevents the laser beam from focusing at the upstream location for cw lidars, while measurements of the time-of-flight of the return signal for pulsed lidar systems are affected. A simple method to eliminate the blade interference would be a spinner installation of the lidar systems. However, a spinner installation would require a more complicated and expensive mechanical retrofitting and integration while also increasing the complexity of the data processing and wind field reconstruction methodologies.

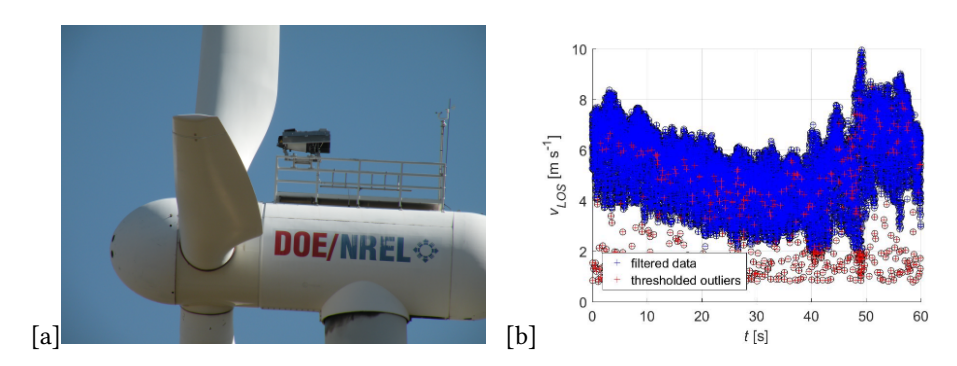


Figure 1.7: [a] A nacelle installation of the SpinnerLidar on the CART3 research turbine at the National Renewable Energy Laboratory. Photo credit: Marijn Floris van Dooren. [b] Distribution of the measured line-of-sight wind speeds from the SpinnerLidar for one minute.

Figure 1.7 illustrates a nacelle-installation of SpinnerLidar at the National Renewable Energy Laboratory. Also illustrated is a one-minute measurement period where the influence of

16 1 Introduction

1

the blades on the measurements can be visualised. The low line-of-sight wind speed measurements are the projection of blade rotational speed along the laser beam direction. While the data availability could be improved by installing the lidar further back on the nacelle and scanning with large beam angles, the directional bias limits the maximum beam scanning angle. In general, 30 %-40 % of data is lost for a nacelle-mounted scanning lidar system, which greatly impacts the estimated wind parameters. In other words, the availability of lidar measurements is a key parameter in determining the benefits of any lidar-based application like lidar-assisted control. Suppose the lidar cannot deliver confident estimates of the wind parameters. In that case, no benefits could be obtained, while the worst-case scenario would be that harmful actuation of the turbine control surfaces would worsen turbine performance over time. While several filtering methods have been investigated in literature [Alcayaga 2020; Beck and Kühn 2017; Gryning and Floors 2019; Herges and Keyantuo 2019], there is a lack of reconstruction methods for data points lost due to deterministic effects. Therefore, there is a need for wind field reconstruction methods that can reconstruct data points lost due to deterministic and stochastic effects and increase lidar data availability.

1.6.4 Flow evolution in the induction zone

The wind deceleration in the wind turbine induction zone is gaining more attention from researchers and industry alike due to its direct impact on the power production of a turbine. As the turbine extracts kinetic energy from the wind, the velocities upstream and downstream of the turbine are reduced compared to the undisturbed wind speed, i.e., the wind speed if no turbine was present. This effect is wind turbine blockage, while the affected region is called the induction zone. The flow deceleration is most substantial at the turbine but reduces in magnitude, moving away from the turbine into the undisturbed flow far upstream of the turbine. Industrial standards require that for power production assessment, the freestream wind speed should be at 2 to 4 rotor diameters in front of the rotor [IEC 2022] with 2.5 rotor diameters is normally recommended. Therefore, the wind deceleration in the induction zone is also a critical parameter to consider for LAC applications as the knowledge of when the upstream measurements would reach the turbine after considering the deceleration in the flow [Dunne et al. 2014]. This knowledge is critical for enabling the turbine to react dynamically and adapt to the incoming wind field. In addition, the non-zero radial wind speeds at the rotor tips due to the flow expansion around the turbine would affect the preview measurement quality of turbine-mounted lidar systems [Simley et al. 2014b].

Experimentally, the induction zone has been mapped using nacelle-based and ground-based lidars [Asimakopoulos et al. 2014; Mikkelsen et al. 2020; Simley et al. 2016; Slinger C et al. 2013]. The wind turbine induction zone is driven by the rotor induction and the interaction of the wind turbine with the wind inflow and its surrounding environmental features. In the former, the wind turbine's design and operation are influencing factors, while the latter is influenced by atmospheric conditions, terrain and neighbouring turbines. In wind farms, cumulative induction effects have been noticed and termed as wind farm blockage [Bleeg et al. 2018; Schneemann et al. 2021] where wind speed reductions of several percentage points have been seen through simulations and measurements. Furthermore, short turbine spacing inside tightly packed wind farms would create complex aerodynamic effects due

1

to the interaction of induction zones and wakes from neighbouring turbines. These effects were not considered by analytical models until the work of Branlard and Meyer Forsting 2020, who coupled vortex models with analytical wake models in FLOw Redirection and Induction in Steady State (FLORIS) [Gebraad et al. 2016].

More detailed methods for describing the blockage deceleration have been developed based on vortex theory [Branlard and Meyer Forsting 2020; Branlard et al. 2020; Medici and Alfredsson 2006; Sarmast et al. 2016; Segalini and Alfredsson 2013]. In these models, the flow around the wind turbine is modelled by treating the blades as vortex lines with constant circulation while the blade root and tip vortices are shed from the rotor. Evaluation and validation of these models is an important step toward implementing them to calculate the theoretical power output of a wind turbine or a wind farm. In the IEA Task 32 workshop held in 2019, induction zone models of varying fidelity were compared against nacelle-lidar measurements [N. G. Nygaard 2019]. While the induction zone deceleration could be observed in the field, a comparison of the engineering models indicated that the model outputs could not accurately capture the field data. This raised the possibility that certain physical phenomena influencing the induction zone deceleration, such as atmospheric stability, were not considered in the models. This issue is further compounded by complex aerodynamic interactions such as that of the near wake and induction zone and partial waked inflow situations which could affect the flow behaviour in the induction zone. Therefore, there is a need for high-resolution lidar measurements of the induction zone under various inflow conditions and operational states of the wind turbine that could help validate the induction models.

1.7 RESEARCH MOTIVATION AND GOALS

The motivation that led to the formulation of this thesis is fourfold. First, there is a fundamental question regarding the capability of scanning lidar systems in measuring the turbulent wind turbine inflow. This question is relevant to identifying the additional value provided by scanning systems for lidar-augmented turbine applications and leads to the formulation of the first research question:

1. How accurately can scanning lidars measure inflow wind fields, and what is the added value provided by continuously scanning devices like the SpinnerLidar compared to fixed-beam devices?

To fully utilise scanning lidar measurements, it is necessary to enhance or develop advanced wind field reconstruction methodologies that would exploit the detailed wind sensing capabilities of the scanning systems. This leads to the formulation of the second research question:

2. How can we develop dynamic line-of-sight wind field reconstruction methodologies that are ideally independent of flow assumptions and would take advantage of the high spatiotemporal resolutions offered by scanning lidar systems?

However, the ability of any wind field reconstruction method to accurately describe the inflow requires sufficient data availability to estimate the wind conditions with high 18 1 Introduction

1

confidence. This issue is particularly relevant for nacelle-mounted lidar systems, as data gaps due to blade passages is an inevitable result of such an installation.

3. How can we develop wind field reconstruction methods to compensate low-quality or even substitute missing data points and improve the data availability of scanning lidar systems?

Upstream measurements are performed with short-range continuous-wave lidar systems located within the turbine induction zone and are subject to flow deceleration and wind evolution. With the prevalence of wind farms, the interaction of flow between neighbouring turbines results in complex aerodynamic interactions. With the development of large wind farm arrays and the development of farm-level control strategies such as wake steering, it is crucial to characterise the behaviour of the induction zone for these highly complex flow conditions. This leads to the final research question:

4. How does the upstream induction zone of a utility-scale turbine behave during waked and unwaked inflow scenarios?

1.8 STRUCTURE OF THE THESIS

The thesis consists of an introductory chapter, four chapters dedicated to each research question and finally, a conclusion chapter.

Chapter 1 introduces the reader to lidar measurement principles, followed by an overview of different lidar measurement techniques focusing on nacelle-mounted and ground-based short-range lidars. An overview of state-of-art lidar-based applications is provided while also identifying the open research questions. Afterwards, the thesis objectives and the research questions are introduced.

In Chapter 2, the first research question is addressed. As it is quite challenging to investigate and quantify lidar capabilities based on field measurements due to lack of reference, the study is conducted inside high-resolution Large Eddy Simulations where lidars of different complexities are simulated. First, error quantification is performed based on various limitations of nacelle-based lidar measurements (volume averaging, directional bias, wind evolution, sampling limitations, measurement of turbulence spectra in different reference frames). Secondly, the sampling capabilities of the SpinnerLidar are evaluated against its fixed-beam counterparts by comparing metrics relevant to turbine control.

In Chapter 3, the second research objective is considered. A new dynamic line-of-sight velocity field reconstruction based on Proper Orthogonal Decomposition is developed and evaluated inside Large Eddy Simulations. This model is advantageous over normally used parameterisation-based reconstruction methods as it exploits the correlations within the measured $v_{\rm los}$ field to create a reduced order representation of the inflow. In addition, the method provides a way to extract and model dominant features in the inflow that drive the turbine dynamics. In this chapter, we test the $v_{\rm los}$ field reconstruction capabilities of a POD-based inflow model based on scanning lidar measurements in Large Eddy Simulations. In Chapter 4, a wind field reconstruction methodology is introduced based on a modified POD technique called Gappy-POD. The method exploits the spatio-temporal correlations in the inflow to reconstruct missing or erroneous data points. The reconstruction capability is

1

tested based on scanning lidar measurements of varying data qualities and inflow scenarios. Chapter 5 relates to the final research question. A highly instrumented measurement campaign at a two turbine wind farm with two synchronised short-range lidars is presented. Due to the very short spacing between the turbines, complex induction zone behaviour for the downstream turbine was expected for various operational states of the upstream turbine. Several measurement devices such as long-range lidars, eddy covariance stations, GPS devices, load measurements and SCADA data are used in conjunction with the short-range scanners yielding deeper insight into the flow characteristics and turbine reactions. Chapter 6 wraps up the thesis with conclusions and lays down avenues for future research.

2

EVALUATING SCANNING AND FIXED BEAM LIDAR SYSTEMS WITH HIGH FIDELITY SIMULATIONS

2.1 Introduction

Advancements in optical fibre technology based on telecommunications technology and remote wind sensing have continuously reduced the cost of lidar systems. However, lidar systems cannot measure the wind vector at the point of interest like anemometers and only measure the component of the wind vector projected in a volume of several meters along the laser beam direction.

Ideally, three linearly independent lidar measurements are required at a single point to resolve the full wind vector. However, implementing synchronised lidar scanning strategies is still a cumbersome endeavour. Therefore, to obtain parameters describing the inflow, wind field reconstruction strategies are employed along with flow simplification assumptions such as flow homogeneity, zero up-flow, or uniform wind direction, to name a few. Therefore, lidar measurement strategies have uncertainty sources inherent to the device itself, adversely impacting the measurement quality and the choice of the employed wind field reconstruction methodology. For any inflow-sensing lidar system, the most significant factors affecting the measurement quality are the directional bias [Schlipf and Kühn 2008], radial velocity averaging along the measurement volume [Sjöholm et al. 2009; van Dooren et al. 2022], wind evolution between the upstream measurement location and the rotor plane [Chen et al. 2021; Mann et al. 2018], upstream blockage deceleration [Schlipf et al. 2015; Simley et al. 2016].

Part of the contents presented in this chapter have been published as: A. P. Kidambi Sekar, M. F. van Dooren, A. Rott, and M. Kühn (2020). How much flow information can a turbine-mounted lidar capture?. In Journal of Physics: Conference Series (Vol. 1618, No. 3, p. 032050). IOP Publishing. DOI: 10.1088/1742-6596/1618/3/032050.

© 2020 by the authors. Reproduced in accordance with the Creative Commons Attribution 3.0 License.

In addition, the spatial and temporal coverage of the lidar is also a significant factor in capturing the relevant inflow dynamics. While large measurement distances are achievable through pulsed operation, relevant for very large wind turbines [Soto Sagredo et al. 2024], the continuous-wave (cw) type is advantageous for wind turbine applications due to their significantly larger sampling rates [Simley et al. 2012]. The spatial coverage is influenced by the beam-scanning strategy of the lidar device, while the temporal resolution depends on the lidar operating principle. Modern lidar systems are moving from fixed multi-beam systems toward steerable beams allowing active wind scanning. The development of the DTU SpinnerLidar [Mikkelsen et al. 2013] represents a new class of turbine-mounted scanning lidars that offer significantly higher wind field scanning rates compared to fixedbeam lidars. The SpinnerLidar is, however, a prototype research device with substantially higher costs and reduced robustness owing to moving parts compared to a fixed-beam lidar commonly utilised for Lidar-Assisted-Control (LAC) applications. Hence, it is relevant to revisit the applicability of these advanced lidar systems against fixed-beam devices: is it justified to use a scanning lidar over fixed-beam systems for lidar-assisted applications? Should the SpinnerLidar be considered for only specific applications such as load validation and turbulence assessment where high spatio-temporal resolutions are critical?

While full-field experiments can capture the spatio-temporal dynamics of the flow, it is not a trivial task to identify and quantify uncertainties due to the lack of a reliable reference. Therefore, estimating lidar effects such as directional bias or volume averaging is cumbersome, depending on the flow and environmental conditions. Lidar simulations provide a methodology to identify, verify and understand lidar capabilities and limitations. Simulating lidar systems inside a known wind field provides a reference domain for performance and quality assessment.

Identification of wind lidar limitations and its impact on measurement quality has been investigated before using numerical investigations to examine the performance of lidar-assisted control strategies [Laks et al. 2013; Simley et al. 2018; Simley et al. 2014b]. Similarly, lidar simulators have been developed for studying the accuracy of wind field reconstruction algorithms and quantifying the impact of measurement strategies [Lundquist et al. 2015; Raach et al. 2017; Rahlves et al. 2022a] or to study the limitations of the measurement principle [Churchfield et al. 2016; Meyer Forsting et al. 2017; Mirocha et al. 2015; Simley et al. 2012].

Some of these studies used stochastic wind fields commonly applied for aeroelastic load simulations that lack physics-based wind evolution models. As it is impossible to measure the flow around a turbine, in reality, accurately, no full-scale reference measurements from experimental campaigns are available. To bridge this gap, lidar simulations inside Large Eddy Simulations [Beck and Kühn 2019; Trabucchi 2020; van Dooren et al. 2016] can be performed as an alternative. Developments in parallel computing and computational modelling have resulted in LES models capable of accurately resolving the turbulent atmospheric flow [Maronga et al. 2015]. Consequently, these models represent the atmospheric flow making them an ideal reference for quantifying the lidar uncertainties.

The aim of this chapter is to provide a basis for gaining a deeper understanding of the lidar measurement technique and for evaluating measurement layout and scanning strategies for full-field measurements in a highly controllable virtual environment. This chapter quantitatively investigates capabilities and uncertainties associated with a turbine-mounted

inflow-scanning lidar system in high-fidelity Large Eddy Simulations based on and extending the previous work in Kidambi Sekar et al. 2020. To this aim, the chapter addresses two questions:

- 1. How do lidar uncertainties influence accurate measurements of inflow wind fields?
- 2. What are the advantages of using a scanning SpinnerLidar compared to fixed-beam devices?

To tackle the second question, we choose the characteristics of a few commercially available fixed-beam devices with different numbers of beams and orientations with a focus on cw devices. The ability of the different lidar systems to accurately represent the inflow is tested by applying wind field reconstruction techniques followed by an evaluation against the reference wind fields.

The chapter first beings with a description of the lidar measurement principle in Section 2.2. Chapter 2.3 describes methods where the Large Eddy Simulations and the lidar simulator are described in detail. In Chapter 2.4, the ability of lidar systems to measure the inflow is evaluated considering the measurement uncertainties. In Chapter 2.5, the performance of simple fixed-beam inflow scanning systems are evaluated against a suitable scanning lidar, i.e., the SpinnerLidar. Finally the Chapter is summarised with a short discussion in Chapter 2.6 and conclusions in Chapter 2.7.

2.2 The contineous-wave lidar measurement principles

In this section, an introduction to the measurement principle and associated uncertainties of cw lidars are discussed. While performing turbine-mounted lidar measurements, the following uncertainties have to be considered. Directional bias, range weighting and wind evolution are limitations common amongst all turbine-mounted lidar systems, while the beam-scanning strategy and the temporal resolution determine how well the lidar device measures the upstream rotor plane wind variations.

2.2.1 DIRECTIONAL BIAS

A lidar device can only measure the wind speed component projected along the direction of the laser beam. Hence, while performing turbine-mounted measurements, only a projection of the wind vector is measured by the lidar. The reconstruction of the longitudinal wind speed component, which is of most relevance for the wind turbine, can only be performed by making assumptions about the wind field. For a lidar, the line-of-sight $v_{\rm los}$ speed measurement at a point in space is expressed as a combination of the three wind components as described in Harris et al. 2007 and shown in Eq. (2.1).

$$v_{\text{los}} = \cos(\chi)\cos(\delta)u + \sin(\chi)\cos(\delta)v + \sin(\chi)w. \tag{2.1}$$

Here, χ is the azimuth and δ elevation angles of the focused laser beam. The movement of the turbine during operation will further impact the pointing angles of the laser beams. As a result, lidars are installed with a tilt to compensate for these changes. The three quantities u, v and w are the longitudinal, lateral and vertical wind components. For

turbine-mounted lidars, $u\gg v$, w and hence it is a reasonable assumption to set the lateral and vertical velocities to 0 in Eq. (2.1) to obtain the projected longitudinal component. However, the assumption of zero lateral and vertical velocities might not hold during conditions such as turbine yaw misalignment or during complex terrain or waked inflow. Moreover, the longitudinal velocity estimation error scales with the beam deflection angle. If the laser beam is misaligned with the u component, an error equal to the cosine of beam deflection is expected, along with the cross-contamination from the crossflow components. This directional bias introduces a source of error while using wind field reconstruction algorithms due to wind field assumptions such as flow homogeneity or assuming zero vertical and lateral velocities. The directional bias also introduces an ambiguity in resolving shear and directional parameters that could only be solved by performing measurements at two upstream locations or with two devices from different longitudinal positions [Kapp and Kühn 2014].

To analytically determine the directional bias on the estimation of the longitudinal wind speed component, we can utilise Eq. (2.1). By aligning the laser beam into the mean wind direction and assuming negligible lateral and vertical components (v, $w \approx 0$ in Eq. (2.1)) and no rotor axis tilt in case of a hub-mounted lidar, we can write:

$$\hat{u} = \frac{v_{\text{los}}}{\cos(\chi)\cos(\delta)},\tag{2.2}$$

where \hat{u} is the projection estimation of the longitudinal wind speed. Rearranging these equations by substituting Eq. (2.2) in Eq. (2.1), we obtain the error of the longitudinal velocity (ϵ_u) as:

$$\hat{u} - u = \epsilon_u = \tan(\chi)v + \frac{\tan(\delta)}{\cos(\chi)}w. \tag{2.3}$$

The partial derivative of the error estimation of the longitudinal wind speed as a function of the azimuth and elevation angles is calculated from Eq. (2.3).

$$\frac{\partial \epsilon_u}{\partial \chi} = \sec(\chi)(\upsilon \sec(\chi) + w \tan(\chi) \tan(\delta)) \qquad \text{and} \qquad \frac{\partial \epsilon_u}{\partial \delta} = w \sec(\chi) \sec^2(\delta). \quad (2.4)$$

The partial derivatives describes the change of error of the u component estimation with respect to the beam scanning angles and the effect of turbine roll and tilt during operation.

2.2.2 THE VOLUME AVERAGING EFFECT

When focused at a given focus point, the wind speed measurement of a cw lidar is not an accurate point measurement but a weighted average of the line-of-sight wind vector from projecting the local velocities on the laser beam direction. The radial wind speed $v_{\rm los}$ measured by a cw lidar focused at a point f in space can be shown as an integration of the wind speed projected along the beam direction.

$$v_{\text{los}} = \int_{-\infty}^{\infty} \phi_s \mathbf{n}_{\text{LOS}} \cdot \mathbf{u} ((s+f) \mathbf{n}_{\text{LOS}}) ds$$
 (2.5)

where n_{LOS} is the unit vector along the beam direction and ϕ_s is the spatial averaging function represented as a Lorenzian shaped weighing function described by Sonnenschein

and Horrigan 1971 as,

$$\phi_s = \frac{1}{\pi} \left(\frac{\Gamma}{s^2 + \Gamma^2} \right),\tag{2.6}$$

Where s is the distance along the laser beam from the focus point f and Γ is the half-width half maximum (HWHM), proportional to the Rayleigh length, which is an optical telescope property that also depends quadratically in size on the measurement focal distance. The probe length at a distance f can be expressed as $\Gamma = \frac{\lambda f^2}{\pi a^2}$ with λ as the laser wavelength, and a is the effective radius of the lidar telescope. The velocity contributions along the laser beam are distributed wider when focusing the laser beam further away from the lidar. Therefore, the low-pass filtering effect due to measurement volume averaging attenuates the measured wind turbulence.

This volume averaging property of a cw lidar increases with the square of the focus distance. It attenuates the turbulence fluctuations along the beam direction correspondingly due to weighing of the wind speeds along the probe volume [Angelou et al. 2012; Penã et al. 2017; Sjöholm et al. 2009]. Even though this effect is not critical for control and even advantageous in the estimation of rotor effective speeds due to rotor plane averaging [Bossanyi 2003], it leads to an under-prediction of turbulence estimates which are essential for determining turbine structural loads.

2.2.3 WIND EVOLUTION AND BLOCKAGE DECELERATION

An important aspect to consider while performing preview lidar measurements is the evolution of the wind turbulence and the induction slowdown between the position of measurement upstream of the turbine and the rotor plane. Wind evolution is the physical phenomenon of transforming the turbulence eddies over time while the fluid flow transports them spatially. This is denoted by the magnitude-squared coherence between wind speeds at two points separated by a distance in space with a certain time lag between them. To reduce wind evolution uncertainty, increasing the coherence bandwidth between the upstream measurement location and the rotor plane is desirable, providing more helpful information about the turbulence spectrum that translates to better controller performance [Dunne et al. 2014].

The stochastic evolution of the longitudinal component in freestream can be modelled based on many theories [Davenport 1962; Kristensen 1979; Panofsky and McCormick 1954; Pielke and Panofsky 1970; Ropelewski et al. 1973] based on longitudinal separation, wave-numbers and parameters related to the decay of coherent eddies. Simley et al. 2014a presented a simple coherence model dependent on the mean wind speed, turbulent kinetic energy and the integral length scales present in the flow:

$$\gamma_{x,K_{x_1},K_{x_2}}^2 = \exp\left(\left(-a_1 \frac{\sigma_{u_\infty}}{u_\infty} + a_2\right) \sqrt{\frac{f\Delta_x^2}{u_\infty}^2 + (b_1 L_u^{-b_2} \Delta x)^2}\right). \tag{2.7}$$

Equation (2.7) denotes the longitudinal coherence $\gamma_{x,K_{x_1},K_{x_2}}^2$ between two spatially separated points x_1 and x_2 as a function of the freestream wind speed u_{∞} , standard deviation $\sigma_{u_{\infty}}$, the integral length scale L_u and the spatial separation Δx distance itself. The constants a_1 , a_2 , b_1 , b_2 are defined by the wind field by defining an objective function which minimises 2

the integrated square error between the calculated coherence curve and the coherence modelled based on Eq. (2.7) at different longitudinal separation distances.

The presented longitudinal wind evolution model works under free inflow conditions where no turbine is present and no induction zone. Hence this model is not directly applicable in the induction zone as the wind speed slowdown is not modelled, leading to an over-estimation of coherence. Hence, we modify the coherence model derived in Simley et al. 2014a to include the induction wind speed reduction. In Eq. (2.7), the longitudinal coherence decreases with a reduced value of u_{∞} . A better wind evolution representation can be obtained by replacing this value of u_{∞} with a lower mean value, ideally equal to a reduced induction zone velocity. The reduced wind velocity in the induction zone u_{ind} could be measured either by refocusing the lidar in the induction zone and measuring the induction slowdown or by modelling the wind deceleration in the induction zone.

The induction zone slowdown as a function of the upstream distance from the rotor can be modelled as a function of the axial induction factor [Medici et al. 2011]. By applying the vortex sheet theory to the actuator disk model, the induction zone velocity u_{ind} of the rotor can be calculated as:

$$\frac{u_{\text{ind}}}{u_{\text{on}}} = 1 - a[1 + \xi(1 + \xi^2)^{-\frac{1}{2}}]. \tag{2.8}$$

Where $\xi = x/R$, where x is the distance along the symmetry axis (negative upstream), a is the axial induction factor of the turbine and R is the rotor radius. To model the wind speed slowdown in the induction zone along with the longitudinal wind evolution, Eq. (2.8) can be substituted into Eq. (2.7) resulting in:

$$\gamma_{x,K_{x_1},K_{x_2}}^2 = \exp\left(\left(-a_1 \frac{\sigma_{u_{\infty}}}{u_{\text{ind}}} + a_2\right) \sqrt{\frac{f\Delta_x^2}{u_{\text{ind}}^2} + (b_1 L_u^{-b_2} \Delta x)^2}\right). \tag{2.9}$$

This modified expression is one step towards combining the effect of wind evolution with the 1-D induction zone deceleration in the horizontal direction along the rotor axis. 2-D estimates of the combined induction and wind evolution could be obtained by combining 2-D induction zone deceleration models [Branlard et al. 2013; Troldborg and Meyer Forsting 2017] with wind evolution models.

2.2.4 Spatio-temporal limitations

The lidar measurement uncertainty is directly affected by the scanning trajectory and the number of points measured by a lidar during each scan. A lidar measuring a single point along the rotor axis will only return a single longitudinal wind speed. At least two points on a horizontal or vertical line are needed to calculate the shear or directional parameters [Mirzaei et al. 2013b; Simley et al. 2018]. While a scanning lidar system can measure a large number of points during every scan, this is a large amount of information for a controller which operates based on a few inputs and hence requires parameterisation based on wind field reconstruction models. For calculating turbulence characteristics relevant to loads, it is necessary to have a high temporal sampling rate. A reduced spatial coverage implies an incomplete rotor plane scan, thereby unable to sample the wind field in the rotational reference frames necessary to calculate fluctuating blade loads. Lidar measurements for

different control strategies require other wind field parameters as input; hence, there is not one scan pattern to satisfy the all possible control objectives. Here, we focus on the estimation of the rotor effective wind speed $u_{\rm eff}$, vertical shear $s_{\rm v}$, yaw misalignment $\delta_{\rm h}$ from the lidar measurements which are standard individual and collective pitch control (CPC, IPC) inputs. Here, vertical shear refers to the variation of the horizontal wind speed with height while yaw misalignment refers to the angular difference between the wind direction and the rotor orientation. The effective wind speed $u_{\rm eff}$ is calculated by averaging the velocities over the rotor area. The vertical shear is estimated as the power law exponent of the wind profile α while the yaw misalignment is calculated from the line-of-sight velocities assuming homogeneous flow over the rotor area.

Table 2.1: Overview of the scan patterns used to investigate the effects of spatial sampling.

ID	Scan	$u_{ m eff}$	$S_{ m V}$	$\delta_{\rm h}$
1	single Beam	X	-	-
2	2-Beam Vertical	X	X	-
3	2-Beam Horizontal	X	-	X
4	4-Beam	X	X	X
5	5-Beam	X	X	X
6	Horizontal Line	X	-	X
7	Vertical Line	X	\mathbf{X}	-
8	Circular Scan	X	\mathbf{X}	X
9	SpinnerLidar	X	x	X

Different lidar configurations are simulated to estimate spatial sampling effects by varying the position and number of beams. For this analysis, only an half opening angle of 30° is considered aiming at the points on the circumference of the rotor plane. While a shorter opening angle measuring around 75 % of the blade radius might be more representative for blade loads and power [Simley et al. 2014a], the objective here is to quantify the quality of the reconstructed wind parameters between the different investigated scan types. The SpinnerLidar measurements cover a spherical plane over the total swept rotor area. Different scan patterns are chosen from these measurements to represent typical commercially available fixed-beam lidars. These scan patterns are visualised in Figure 2.1 and tabulated in Table 2.1. The point measurement represents the simplest turbine-mounted lidar measurement without any beam steering mechanism staring along the rotor axis for spinner-mounted lidars. The two-beam horizontal and vertical scans have a maximum beam deflection angle of 30° from which the vertical shear s_v and the yaw misalignment δ_h can be estimated, respectively. The 4- and 5-beam lidar covers more spatial area than the two-beam devices and can simultaneously estimate the shear and the yaw misalignment. ID 8 represents the circular scanning lidar system which measures the circumference of the measurement circle with a beam deflection angle of 30°. All the fixed-beam scanning scenarios are performed at the upstream distances, and beam deflection angles are listed in Table 2.1. ID 9 represents the typical SpinnerLidar spherical plane measurement. To quantify the error in parameter estimation, we define standard and dynamic errors of the

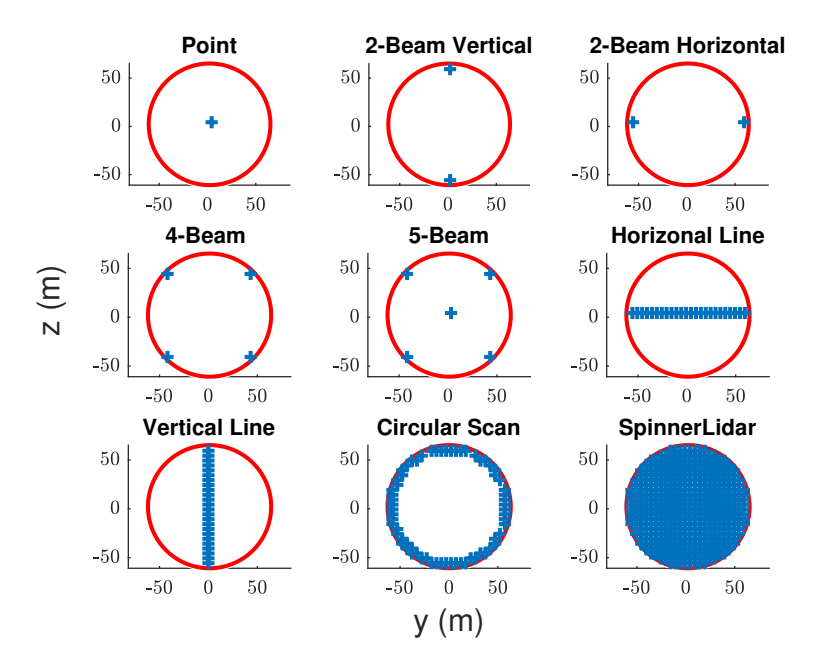


Figure 2.1: The investigated lidar scan patterns.

time series of wind field parameters $X \in \{u_0, s_v, \delta_h\}$,

$$\epsilon_{\text{std,X}} = \frac{\|X^{\text{lidar}} - X^{\text{LES}}\|_2}{\|X^{\text{LES}}\|_2}$$
 (2.10)

$$\epsilon_{\rm dyn,X} = \frac{\|(X^{\rm lidar} - \langle X^{\rm lidar} \rangle_t) - (X^{\rm LES} - \langle X^{\rm LES} \rangle_t)\|_2}{\|X^{\rm LES} - \langle X^{\rm LES} \rangle_t\|_2},\tag{2.11}$$

Here X^{lidar} is the set of wind field parameters estimated from the lidar scans, and X^{LES} are the results from the reference wind fields. ϵ_{std} represents the second norm of the time series, and the dynamic error is inspired by the idea that the fluctuations from the mean quantity $X(t) - \langle X \rangle_t$ are more critical for fatigue load calculations.

2.3 Methods

In this section, the scanning SpinnerLidar is introduced, followed by a description of the LES and the lidar simulator. As the analysis is carried out in a simulation environment, the results from the lidar simulator can be directly compared to the reference LES. With the lidar simulator, the lidar parameters can be controlled, providing an opportunity to test different operational parameters and isolate certain contributions to the total uncertainties.

2.3.1 Large-Eddy simulations

The LES wind fields were created with the PArallelised Large eddy simulation Model (PALM) [Maronga et al. 2015], which has been used extensively for studying the atmo-

2.3 Methods 29

spheric boundary layer. The code works based on solving the filtered, incompressible, non-hydrostatic Navier-Stokes equation using a Schumann volume averaging approach. The code utilises a central difference scheme to discretise the Boussinesq approximation of the 3-D Navier–Stokes equations on a structured Cartesian grid. To parameterise the subgrid scale turbulence, a 1.5th order closure based suggested by Deardorff 1980 is employed. All the simulations are performed using the default settings of PALM that include a 5th order scheme described in Wicker and Skamarock 2002 for solving advection terms and a 3rd order Runge-Kutta scheme for time marching. Periodic boundary conditions are used in the lateral boundaries, and no-slip conditions are applied to the lower boundary.

The wind turbine is modelled based on the Fatigue, Aerodynamics, Structures and Turbulence code (FAST) v8, developed by the National Renewable Energy Laboratory [Jonkman et al. 2005]. The FAST code, developed for horizontal wind turbines, models them as a combination of rigid and flexible bodies. The aerodynamic forces are calculated in the AeroDyn module, where the 3D flow around the blades is approximated into local 2D forces at cross-sections. Each blade is approximated as a line that rotates in time, with each line subdivided into sections. Both PALM and FAST simultaneously run in a direct loose two-way coupling [Krüger et al. 2022]. The velocity is sampled at the centre point of each section from the LES and passed into FAST. The AeroDyn model uses the pre-determined lift and drag tables to compute the aerodynamic force in each section. The forces are then transferred back into the structural dynamics module and also back to the LES solver. The LES solver applies the computed blade forces into the wind field, creating the induction zone and the turbine wake.

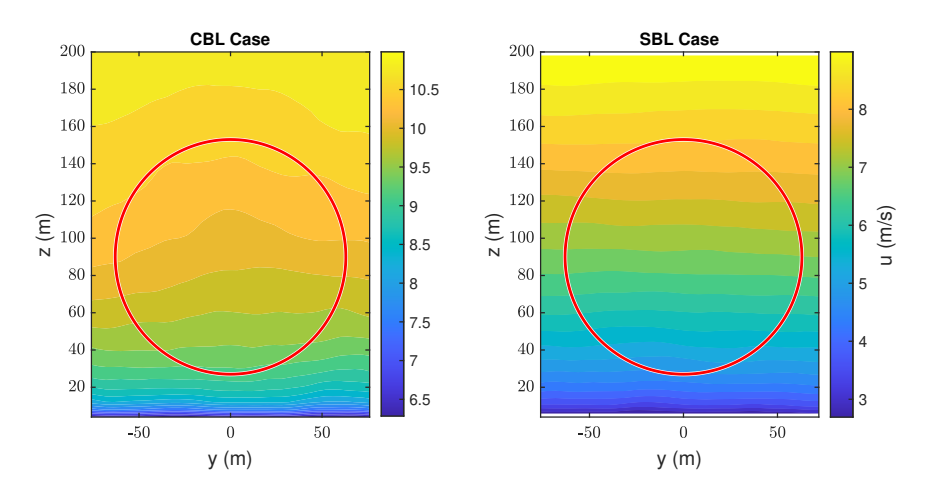


Figure 2.2: The mean longitudinal component *u* at a vertical plan 1 *D* upstream of the reference turbine for the CBL and SBL cases at the beginning of the main run. The red circle indicates the area covered by the rotor.

Two stationary and fully turbulent unsteady atmospheric boundary layers of unstable and stable stratification are generated first in a pre-run simulation without the wind turbine. For both cases, the large domain size ensures that the inflow of the turbine is not affected by the boundaries allowing for a homogeneous turbulent atmospheric boundary layer to develop after a pre-run of 25 hours. The instantaneous fields of the precursor simulation

are mapped onto the main simulation through turbulence recycling [Lund et al. 1998]. In the main run, the turbine is introduced into the wind field. The chosen turbine model is the NREL 5 MW reference turbine [Jonkman et al. 2009a] with a diameter of 126 m and a hub height of 90 m modelled as an actuator line with 63 blade sections. Essential details of the two simulations can be found in Table 2.2. Figure 2.2 depicts the averaged longitudinal component on a vertical plane 1 D upstream of the turbine at the beginning of the main simulation.

Table 2.2: The key parameters of the two PALM-FAST simulations.

Parameter	CBL Case	SBL Case
Domain size $L_x \times L_y \times L_z$	8188 x 4092 x 2048 m ³	2872 x 960 x 480 m ³
Grid mesh size $N_x \times N_y \times N_z$	2047 x 1023 x 512	718 x 240 x 120
Cell mesh resolution	$4 \times 4 \times 4 \text{ m}^3$	4 x 4 x 4 m ³
Wind turbine model	ALM	ALM
Number of blade elements	63	63
Atmospheric stability	Unstable	Stable
Geostrophic wind	$u = 11.85 \text{ ms}^{-1} \text{ and } v = -1.02 \text{ ms}^{-1}$	$u = 9.5 \text{ ms}^{-1} \text{ and } v = -5.17 \text{ ms}^{-1}$
Simulation sampling rate	5 Hz	5 Hz
Roughness length z_o	0.0175 m	0.1 m
Longitudinal wind speed at hub height	10.1 ms ⁻¹	7.2 ms ⁻¹
Longitudinal TI at hub height	11.91%	7.5%
Shear Exponent (α)	0.09	0.23
Integral length scale (m)	285	34
Wind veer over rotor (°)	0.8	9.3

2.3.2 THE SPINNERLIDAR

The SpinnerLidar [Herges et al. 2017b; Mikkelsen et al. 2013] is a turbine-mounted lidar capable of being installed on the nacelle or the spinner with the ability to scan the wind turbine inflow or the wake depending on its orientation. The device is a modified ZephIR-300 continuous-wave Doppler lidar system. The modification consists of a 2D scan head developed by the Technical University of Denmark and IPU P/S, Virum, Denmark that allows deflection of the laser beam in a pre-determined pattern unattainable by fixed-beam lidar systems. This modified scan pattern enables the measurement of radial wind speeds in the turbine inflow with an unprecedentedly high amount of spatial and temporal coverage (a maximum of 500 points per rotor scan and 1 s temporal update). Its scanhead consists of two rotating prisms capable of deflecting the focused lidar beam, each by a 15° deflection angle while rotating together with a fixed ratio of 7 to 13. The result is a scan pattern similar to a rosette figure that covers a large area with a very high spatial resolution. The maximum inclination of the laser beam found on the edges of the scan pattern is 30°. While operating the lidar with the full spatio-temporal resolution, it is possible to scan the inflow wind field with a cone of 60° every second with a scanning trajectory containing 500 points (see Fig 2.4). The lidar also includes a fast voice-coil-based focus motor capable of continuously re-focusing the laser beam at distances between 10 m to 150 m. The variation of the measurement probe volume as a function of focus distance for the SpinnerLidar is visualised in Fig. 2.5. The lidar can be installed in the spinner of a wind turbine, as the name implies, and on top of the nacelle just behind the rotor plane if a spinner installation is not feasible (in the latter case, measurements are then subject to blade interference).

2.3 Methods 31



Figure 2.3: The SpinnerLidar along with its mounting mechanism at the University of Oldenburg.

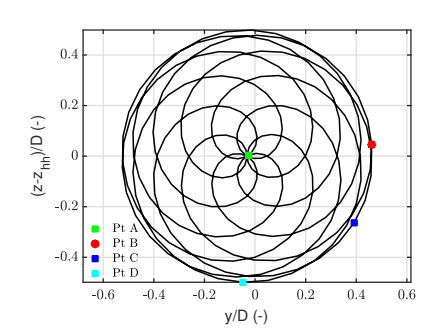


Figure 2.4: The visualisation of the rosette scan pattern performed by the SpinnerLidar seen in the *y-z*- plane.

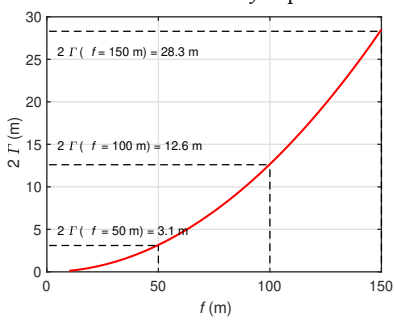


Figure 2.5: The variation of the measurement probe volume as a function of focus distance for the SpinnerLidar.

2.3.3 LIDAR SIMULATOR (LIXIM)

For simulating measurements from the LES, the integrated lidar simulation toolbox LiXim (Lidar Scanner Simulator) developed in Trabucchi 2020 is used. This lidar simulation tool can reproduce the operation of virtually any lidar system and facilitates its evaluation for different laser, operational and scanning settings. During the simulations, the yaw movement of the turbine is constrained, and the rotor axis tilt is not considered. The lidar simulator performs snapshot measurements of the wind field and interpolates between the LES grid points. LiXim also assumes no beam pointing uncertainties while no environmental effects are modelled. The lidar parameters can be modified in LiXim, allowing control over the laser beam properties and the optical trajectory. Lidar simulations are performed by modifying the upstream focus distance, opening angle and the sampling rate as tabulated in Table 2.3 for both the CBL and SBL cases totalling 100 simulations. The lidar's focal length varies from 30 m to 150 m, corresponding to 0.23 D to 1.2 D in front of the reference turbine. The half opening angle of the SpinnerLidar is modified between $\theta = 5^{\circ}$ to 22.5° equalling a maximum beam cone angle between 10° and 45°. For all simulations, 312 points are measured with the Rosette trajectory for every full 2D rotor scan (Fig. 2.4). The simulations are visualised in Fig. 2.6 (a) for the beam deflection angles and focal distances. The scans with different opening angles cover varying rotor areas. The SpinnerLidar is placed in the

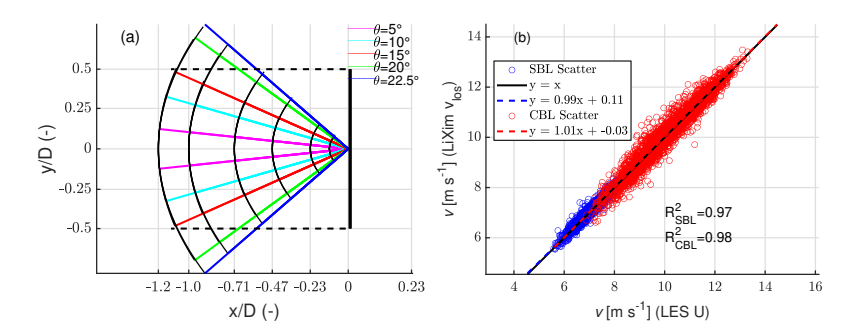


Figure 2.6: (a) Visualisation of the different scanning scenarios simulated for the study. The horizontal dotted lines indicate the width covered by the rotor. The black vertical lines show the different focus distances, and the coloured lines illustrate the different deflection angles of the SpinnerLidar, respectively. (b) The scatter plot between the LES u-component 1 D upstream of the turbine along the rotor axis against the corresponding SpinnerLidar v_{los} measurement for the CBL and SBL cases.

spinner of the NREL 5 MW reference turbine, shown as the vertical black line at x/D=0. For each set-up, LiXim simulates the lidar measurements from the LES with and without accounting for the volume averaging effect, i.e. normal and perfect point measurement. An interpolation scheme based on Delaunay triangulation is used to interpolate wind speeds at locations between two grid points.

For the validation of LiXim, a scatter plot between the $v_{\rm los}$ velocity at the centre of the rosette scan of the SpinnerLidar focused 1 D upstream of the turbine is plotted along with the corresponding LES u component taken at the closest point (Fig. 2.6 (b)). The centre point of the Rosette scan is chosen as the reference to eliminate any directional bias of line-of-sight velocities. A good fit is obtained for both the CBL and SBL cases indicating that the coupling between the LES and the LiXim simulations is plausible. The minor differences between the LES and the lidar can be attributed to the probe averaging effect (probe length of 19.6 m at a focus distance of 126 m) and LiXim interpolating between the LES grid points. Similarly, all the scan trajectories listed in Tab. 2.3 are simulated with LiXim and compared against each other and the reference wind field.

Table 2.3: Settings of the SpinnerLidar scenarios performed with the LiXim. The last row contains the normal operational parameters of the SpinnerLidar. The focus distance is normalised with the rotor diameter of the NREL 5 MW reference turbine.

Run	Focus distance (m)	Beam cone angle (°)	f_s (Hz)
1	30 (0.23 <i>D</i>)	10, 20, 30, 40, 45	1, 5
2	60 (0.47 <i>D</i>)	10, 20, 30, 40, 45	1, 5
3	90 (0.71 <i>D</i>)	10, 20, 30, 40, 45	1, 5
4	126(1.0 D)	10, 20, 30, 40, 45	1, 5
5	150 (1.19 <i>D</i>)	10, 20, 30, 40, 45	1, 5
Normal operation	10-150 (0.08 <i>D</i> - 1.19 <i>D</i>)	30	1

2.4 Results 33

2.4 RESULTS

First, to estimate the accuracy of lidar-based wind field measurements, the temporal sampling, directional bias and volume averaging limitations are investigated against the reference wind fields. Henceforth, for consistency, the results of the SpinnerLidar simulations with the volume averaging effect are referred to as a probe measurement and the simulations without the volume averaging as a point measurement (perfect lidar). Secondly, the wind field reconstruction capabilities of the SpinnerLidar against the fixed-beam devices are evaluated by direct comparison against the LES reference.

2.4.1 Effect of temporal sampling rate on the time series moments

To test the reproducibility of the statistical properties of turbulent flow from lidar measurements, we derive the spectral moments of the time series. The mean, variance, skewness and kurtosis of the SpinnerLidar simulations are plotted and compared against the reference LES in Figure 2.7. The moments are calculated at points taken from lidar measurements located on the rotor axis at different focal distances to neglect directional bias sampled at 1 Hz. The resulting $v_{\rm los}$ velocity, equivalent to the longitudinal wind speed, is compared against the longitudinal wind speed from the reference LES.

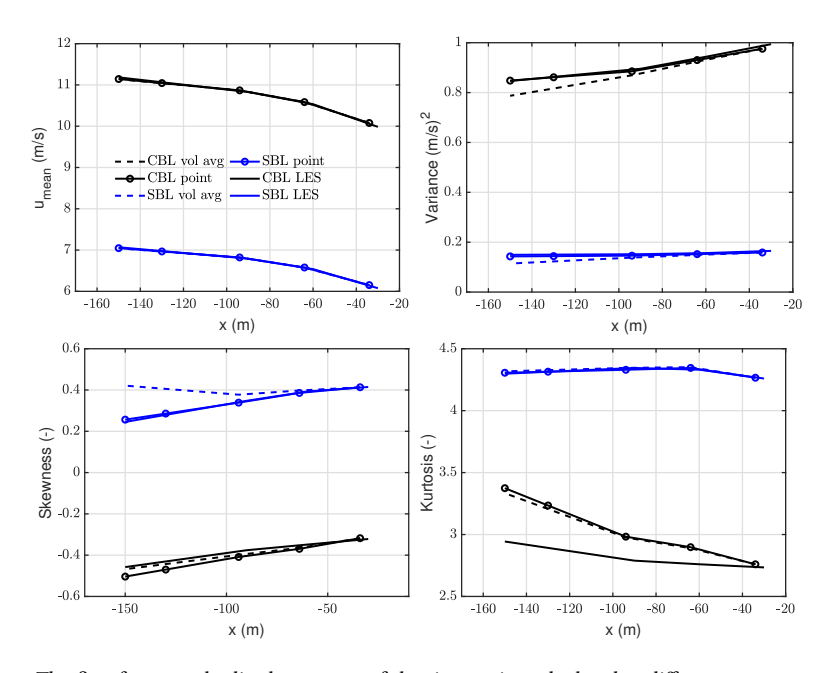


Figure 2.7: The first four standardised moments of the time series calculated at different upstream positions relative to the location of the turbine for the CBL and SBL cases. The dotted lines are the result of a lidar performing measuring with the influence of the probe volume and the circles are the results of the perfect lidar measurements without probe volume averaging. The solid lines are the results from the u-component velocity from the LES simulations at the nearest grid point.

The mean velocity decreases towards the turbine location at x = 0 m due to the induction zone blockage. Even with a 1 Hz sampling rate and the volume averaging effect, the mean value is captured with high accuracy compared to the LES. The slight variations in the wind speed reduction are due to the effect of the interpolation scheme used by the lidar simulator to integrate between grid points. The variance, which measures the fluctuations in the flow, behaves differently in comparison to the mean velocity. The volume averaging effect is visible at more considerable measurement distances attenuating lidar measured variance compared to the perfect lidar measurements. The lidar measured variance decreases in comparison to the point measurement at more considerable focal lengths, while the sampling rate has only a negligible effect. For the skewness and the kurtosis that define the measurement of the distribution symmetry and the shape, the sampling rate dominates over the volume averaging effect. The distribution's skewness becomes heavy-tailed compared to the LES, while the kurtosis is over-predicted for the CBL case and matches the SBL case quite well. The third and the fourth-order moments are affected by the temporal resolution of the scans, consequently affecting the results, especially at lower sampling rates.

The mean wind speed is independent of the sampling rate and volume averaging, while the variance is influenced by the larger probe volume at large focus distances, causing an underprediction of variance. The skewness and the kurtosis highly depend on the sampling rate and the total amount of samples but are not statistics required for control or load validation. A lidar measuring at 1 Hz is a standard setting for commercial devices and can estimate the mean wind speeds accurately, making it a suitable sampling rate for running lidars for control applications, as noted by Simley et al. 2018. As the turbulent fluctuations in the wind contribute most to the fatigue loading on the turbine, it is imperative to understand the volume averaging effect while using lidars for loads validation.

2.4.2 The volume averaging effect

The wind speed measurements of a cw lidar can be interpreted as a convolution of the wind speed time series and the Lorenzian weighing function that scales with the distance to the measurement point when the lidar beam is aligned with the wind direction.

The Lorenzian function introduces wind speed contributions from positions along the beam, effectively applying a low-pass filter to the measurements. The effect of the low-pass filtering can be seen in Fig. 2.8 for the CBL case, where the velocity time series at different upstream measurement locations are shown along with the reference data. At $f=30\,\mathrm{m}$, the probe volume is smaller than the resolved grid size leading to no differences in the time series measured by the SpinnerLidar and the reference. With an increase in focus distance, the low-pass filtering is more clearly visible and prominent at $f=126\,\mathrm{m}$, with the lidar unable to capture the small-scale velocity variations present in the LES.

To quantify the amount of Turbulent Kinetic Energy (TKE) attenuated by the lidar due to the volume-averaging effect, the total signal TKE ratio between the real lidar with the volume-averaging property and an ideal lidar performing a point measurement is plotted in Fig. 2.9. Henceforth, the lidar-measured TKE is defined as the kinetic energy of the line-of-sight measurements rather than the commonly used definition of TKE of the 3D wind field. The ratio is calculated by integrating the total area under the energy spectra. The focus distances at which the probe length is smaller than the grid resolution are marked

2.4 Results 35

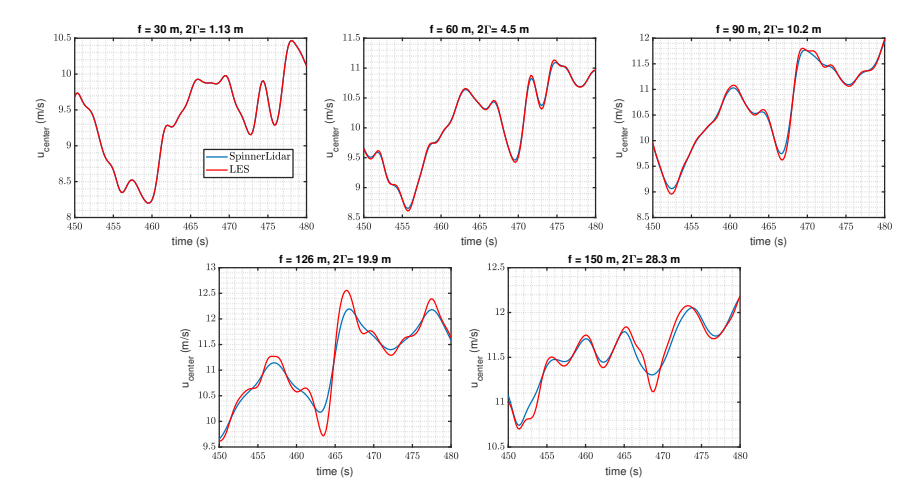


Figure 2.8: Time series of the line-of-sight wind velocities measured along the rotor axis for different focus distances compared against the longitudinal wind speed component from the reference LES at the same location. Only the CBL case is shown.

in red, while the black line shows a perfect lidar with no kinetic energy attenuation. For both the CBL and SBL cases, the lidar measured variance reduces at more considerable focal distances. At f=126 m, comparable to scanning one turbine diameter ahead of the NREL 5 MW reference turbine, the lidar measures approximately 5% and 15% lower turbulent kinetic energy due to the volume averaging effect for the CBL and SBL cases, respectively. For both cases, the lidar's attenuated TKE along the line-of-sight is highly negatively correlated to the probe length with a Pearson coefficient $\rho(\text{KE}_{\text{Ratio}}, 2\Gamma) \approx -1$. Hence, the amount of kinetic energy attenuated by the lidar shows a dependence on atmospheric stability.

2.4.3 Effect of directional bias

For turbine-mounted inflow lidars sensing along the rotor axis, the common assumption that the line-of-sight speed is the longitudinal u-component. This can be reasonable if the magnitude of the cross-wind components are pretty low, i.e. $u\gg v,w$ due to the lidar pointing directly into the wind. However, with a scanning setup, the estimation error of u depends on the angle between the laser beam and the wind direction.

Figure 2.10 illustrates the analytical error in the estimation of the longitudinal component ϵ_u as a function of the beam angles χ and δ for unity vertical and lateral speeds based on Eq. 2.4. When the lidar points into the wind, the beam angles are very small and the error induced by the lateral and the vertical wind speed components are low as the longitudinal wind speed component dominates the line-of-sight velocity. As this error increases with the beam angles, the cross-contamination from the lateral and the vertical components causes a higher error while back-projecting the line-of-sight wind speeds into the longitudinal component. The rate of change of the projection error as a function of the elevation angle δ exhibits symmetrical behaviour about the centre. In contrast, the derivative of the error as a function of χ is mirrored around the $\chi=0^\circ$ line. Inside the

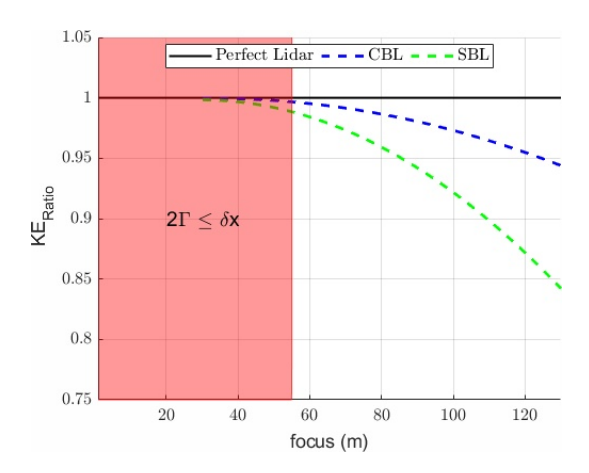


Figure 2.9: The ratio of the turbulent kinetic energy along the line-of-sight direction measured at the different upstream distances along the rotor axis for the lidar measurements with and without probe length averaging. Here $2\Gamma \le \delta x$ indicates the region where the probe volume is smaller than the LES grid resolution.

red circle which shows the SpinnerLidar maximum beam deflection angle, the pointing error reaches a maximum of 0.5 m/s. If the instantaneous yaw misalignment δ_h and up-tilt $\theta_{\rm up}$ of the turbine are taken into account, then the pointing error scales with $\chi + \delta_h$ and $\delta + \theta_{\rm up}$ in Eq. 2.4, which increases the projection error substantially at higher opening angles.

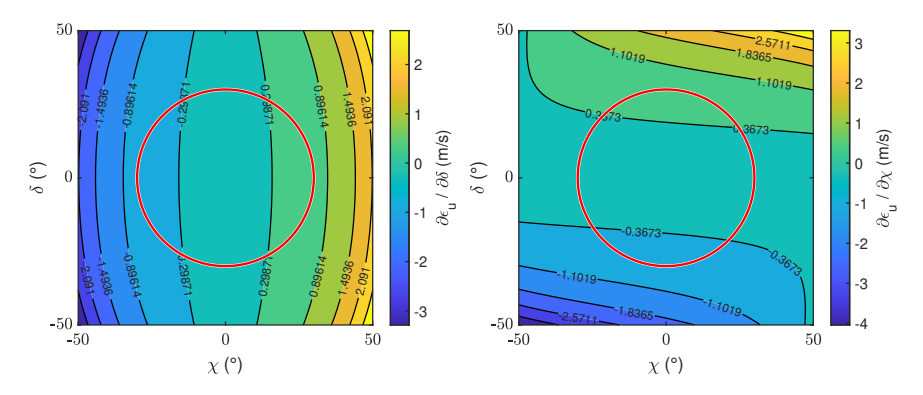


Figure 2.10: The error in estimation of the longitudinal component (ϵ_u) as a function of the elevation δ and azimuth χ angle for unity lateral and vertical wind speed in Eq. 2.4. The red circle indicates the \pm 30° opening angle of the SpinnerLidar.

Therefore, for turbine-mounted lidars, directional bias is easily the most significant error source in longitudinal velocity estimation, which is most relevant for the turbine. It is evident that for larger opening angles, the directional bias is dominating in comparison to volume averaging due to the increased cross-contamination from the crosswind components. It is estimated from Fig. 2.10 that the longitudinal component error will exceed more than \pm 0.5 m/s when the pointing angle exceeds 20° in either the horizontal or the vertical

2.4 Results 37

directions. This effect is more pronounced during turbine operation, yaw misalignment, or the typical rotor axis tilt.

2.4.4 Sampling the wind field in a stationary and rotating frame of reference

To calculate the turbine dynamic loading and the desired reduction through control actuation, it is essential to study the atmospheric turbulence impinging on the turbine. A wind turbine with a specified rotor speed will experience a wind field that varies spatially due to the atmospheric shear and turbulence. First, we investigate the spectra of a point taken at the centre of the SpinnerLidar scan at various distances upstream of the turbine to avoid directional bias. The fixed point turbulent spectra are calculated by estimating the power spectral densities (PSD) by splitting the time series into 20 blocks and applying a Hamming window with 50% overlap.

The results of the non-rotating spectrum for the two inflow cases at variable focus distances along the rotor axis are shown in Fig. 2.11 where the dotted lines indicate the real SpinnerLidar measurements with the volume averaging property and the solid lines indicate the measurements without the volume averaging property of the lidar. For the perfect lidar measurement, the spectra of both cases follow the inertial sub range part of the turbulent spectra given by the $-\frac{5}{3}$ Kolmogorov slope showing very close agreement with the reference LES spectrum. The distance dependency of the volume averaging effect is clear where the turbulent spectra of the real lidar measurements (dotted lines) show a drop-off from the $-\frac{5}{3}$ slope with the drop-off occurring earlier at larger focus distances. Hence, in a non-rotating spectrum, the lidar captures less energy at higher frequencies than the perfect measurements. Measuring upstream at 126 m (1 D), the spectral drop-off is pronounced at 0.1 Hz and 0.08 Hz for the CBL and SBL cases. The theoretical cut-off frequency based on Taylor's hypothesis defined as $f_{\text{cut-off}} = 0.5 \cdot u_{\text{mean}}/2\Gamma$, is not a good prediction indicator of the drop-off location as the volume averaging function of a cw lidar described by a Lorenzian function extends beyond the definition of the probe volume.

To investigate the directional bias on the measurement of stationary spectra, we calculate the spectra at a series of measurement points. For this purpose, a set of points are chosen from the SpinnerLidar trajectory at a fixed focus distance shown in Fig. 2.4 to cover a combination of beam angles. The analysis is done at a fixed upstream location f = 126 m to fix the probe volume to a constant value. The azimuth and elevation angles are both zero at Pt. A and are zero at Pt. D and Pt. B respectively, while Pt. C is located at = 26.1°, = -15.7°, respectively. In Figure 2.12, the PSD of the v_{los} and $u_{projected}$ velocities at each of the four points is normalised with the corresponding LES spectral density for the CBL and SBL cases. For Pt. A at the scan centre, free from directional bias, there are no differences between the projection and the line-of-sight speeds for the two cases. At points B, C and D, however, the projected velocities contain more energy than the radial speeds, with points B and C containing more energy than the u LES below the drop-off frequency. This increased energy content in the projected longitudinal velocity is due to the scaled variance induced due to multiplying the v_{los} time series with a scaling factor $\frac{1}{\cos y \cos \delta}$ in Eq. 5.1 while assuming $v, w \approx 0$. The presence of wind shear, especially in the SBL case, reduces the energies measured at Pt. D whose effect is reduced in Pt. B and C.

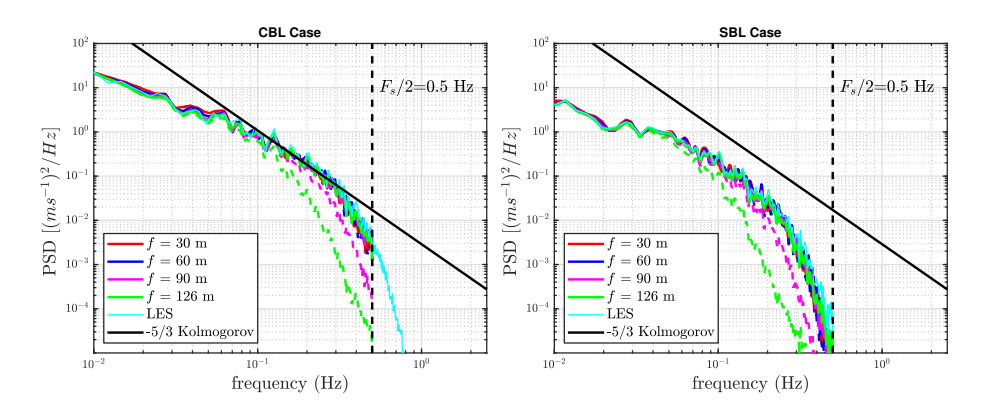


Figure 2.11: The non-rotating turbulent spectra of the line-of-sight velocities calculated from the SpinnerLidar simulations at a point located on the rotor axis at different upstream focus distances (f = 30 m, 60 m, 90 m, 126 m and 150 m). The solid lines show the results of a "perfect" lidar while the dotted lines show the results including the volume averaging effect while the dashed vertical line indicated the Nyquist cut-off frequency.

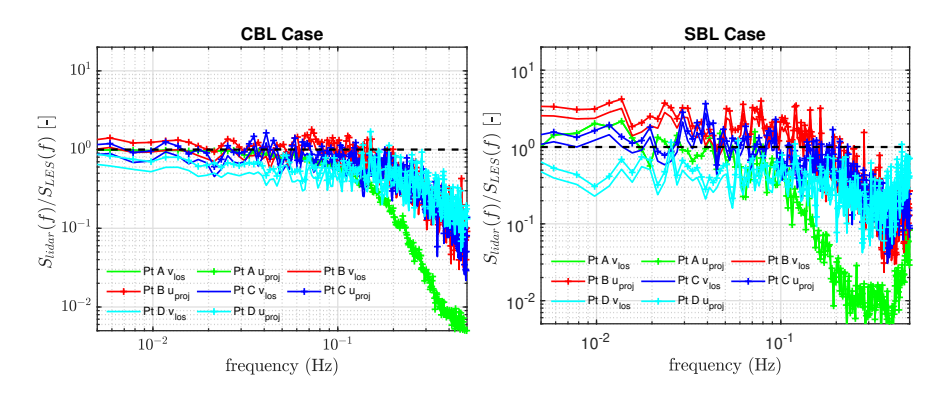


Figure 2.12: Power spectral density of the v_{los} and $u_{projected}$ velocities normalised with the PSD of the LES u velocity for the CBL and SBL cases. Points A, B, C, D lie are defined in Fig. 2.4.

The rotational spectrum can describe the loads the blades will experience as they rotate and slice through the wind field. The eddy slicing effect [Kristensen and Frandsen 1982] induces the accumulation of turbulent kinetic energy at the rotor speed frequency integers, described as 1P and 2P frequencies and so on. Fig. 2.13 shows the comparison of the rotationally sampled spectra of the line-of-sight and projected velocities measured by the SpinnerLidar at upstream distances $f=30~\rm m$, 60 m, 90 m and 126 m sampled at 1 Hz. The spectra are calculated by following a point located at 90% of the SpinnerLidar scan radius using the turbine's rotational speed obtained from the coupled aeroelastic simulations (11.88 rpm and 8.59 rpm, respectively). The reference LES spectrum is generated from the 3D LES wind field by tracing and following the point located at 90% of the blade radius at a distance of 126 m from the turbine. In the CBL case, the 1P frequency corresponds to 0.198 Hz and 0.145 Hz for the SBL case. Even with a sampling rate of 1 Hz, the SpinnerLidar can

2.4 Results 39

capture the first two harmonics for the CBL case and the first three harmonics for the SBL case.

These observations are in strong contrast to the results obtained from the non-rotational spectra in Fig. 2.11. For both cases, the PSD of longitudinal wind speed component 1 D upstream is reduced by factors 10 and 100 at 1P and 2P, respectively. The rotational spectra calculated at different upstream distances f=30 m, 60 m and 90 m also capture the eddy slicing effects quite well. For the SBL case, however, the measurements at shorter upstream distances under-predict the energy at the rotational harmonics as with a shorter focus distance, the variations due to the wind shear are not captured. Due to the Nyquist sampling limitation of the SpinnerLidar at $\frac{F_s}{2}=0.5$ Hz, the higher harmonics of the rotational spectra seen in the LES curve are not captured. The projected velocities contain higher energy content in the lower frequencies below 0.1 Hz due to the variance scaling seen in Fig. 2.12.

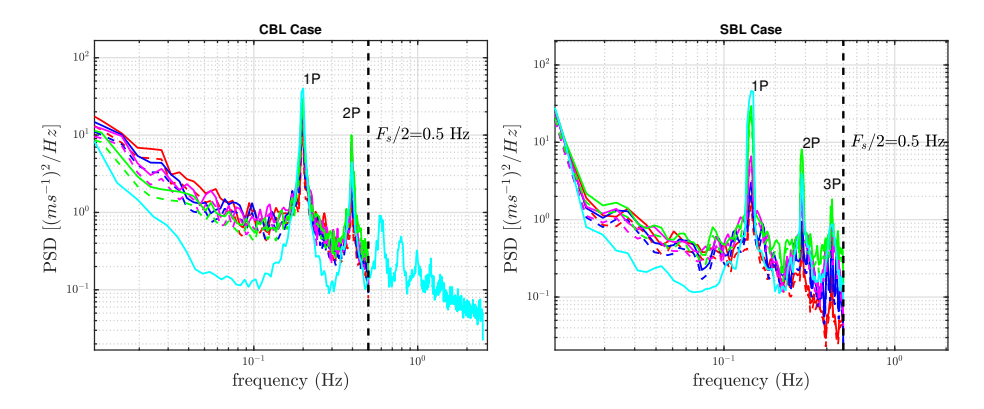


Figure 2.13: The rotational spectrum of the line-of-sight (dotted lines) and the projected velocities (solid lines) calculated by following a point located at 90% of the rotor radius for different upstream measurement distances following the legend in Fig. 2.11. The rotational speeds were ω_{CBL} = 11.8 rpm and ω_{SBL} = 8.59 rpm respectively. Legend similar to Figure 2.11.

2.4.5 The wind evolution and induction zone slowdown

The influence of the volume averaging property on wind evolution is visualised in Fig. 2.14 for the two cases where the longitudinal coherence between lidar measurements taken at an upstream reference point at f=150 m and the lidar measurements at f=60 m, 90 m and 126 m (corresponding $\Delta x=90$ m, 60 m and 24 m) are shown. The longitudinal coherence is calculated using the Matlab function *mscohere* with 20 blocks and applying a Hamming window with 50% overlap for points on the rotor axis to avoid directional bias.

The dotted and the solid lines indicate the measurements without and with the probe length averaging effect. As expected, at a particular frequency, there is a decrease in coherence with increasing horizontal separation Δx as the turbulent scales has more time to evolve between the two measurement points. The coherence drop-off at higher frequencies can be attributed to the small, turbulent structures evolving faster than the large-scale structures in the inflow. For the same separation distance, the coherence in the SBL case is higher than in the CBL case at frequencies below 0.1 Hz, after which there is a sharp drop-off. No

significant differences are observed between the coherence calculated for the ideal and the real lidar coherence curves. An analytical solution in Chen et al. 2021 assuming perfectly aligned inflow and Taylor's hypothesis valid within the probe volume also indicates the independence of the coherence-based wind evolution from the volume averaging. In other words, the large probe volume at f=150 m already low-pass filters the smaller turbulent structures moving towards the turbine, reducing the coherence at higher frequencies.

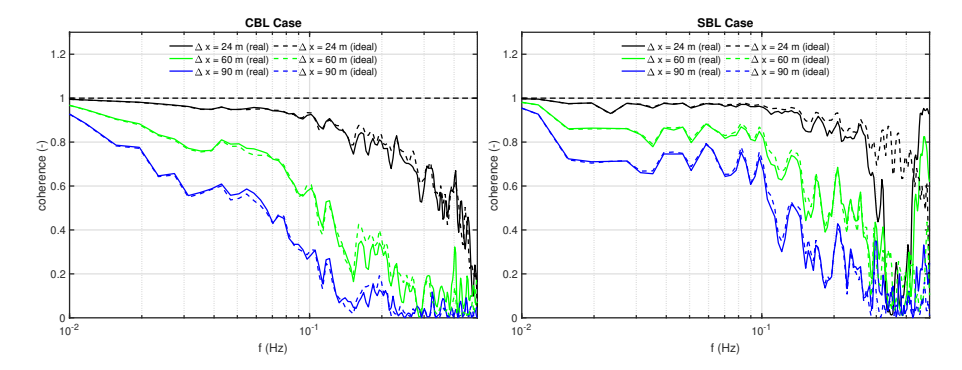


Figure 2.14: Coherence obtained between the reference upstream point located at f = 150 m in front of the turbine along the rotor axis from the LES simulations with ideal and real SpinnerLidar measurements at f = 30 m, 60 m and 90 m corresponding to $\Delta x = 120$ m, 60 m and 24 m for the CBL and SBL cases respectively.

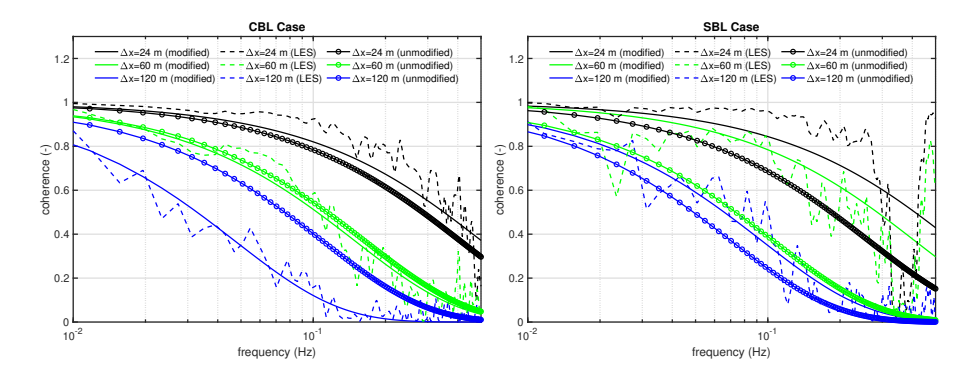


Figure 2.15: Coherence calculated between SpinnerLidar measurements for three different longitudinal separation distances along the rotor axis from the reference LES wind field and the coherence estimated by the unmodified longitudinal model and the modified coherence model taking into account the induction slowdown for the CBL and SBL cases.

The results of the induction-based wind evolution model presented in Eq. (2.9) can be found in Fig. 2.15 (b) indicated by the solid lines. The coherence curve obtained from the unmodified wind evolution model using the freestream wind speed in Eq. (2.7) is also seen along with the results from the actual coherence calculated from the LES wind field. It is immediately clear that the addition of the induction zone wind speed reduction reduces the

over-prediction of the coherence across all the frequency ranges while the effect becomes more pronounced at larger separation distances Δx where the induction zone slow down is severe close to the rotor. The slight differences in the coherence curves could be due to the error of lidar estimation bias of the integral length scale L_u used in Eq. (2.9) due to the volume averaging effect [Debnath et al. 2020]. The coherence bandwidth, defined as the frequency until the coherence remains above 0.5, is tabulated in Table 2.4. The modified wind evolution model performs much better than the unmodified model, especially at larger separation distances compared to the reference LES wind field.

Table 2.4: Coherence bandwidth for the modified (fb_{mod}) and the unmodified (fb_{unmod}) coherence models and the results from the reference LES wind field for the CBL and SBL cases.

$\Delta x(m)$	CBL			SBL		
	$\int b_{\rm LES}$ (Hz)	$f b_{\rm um}$ (Hz)	$f b_{\rm m}$ (Hz)	$f b_{\rm LES}$ (Hz)	$f b_{\rm um}$ (Hz)	$f b_{\rm m}$ (Hz)
24	0.34	0.28	0.35	0.31	0.17	0.30
60	0.11	0.12	0.11	0.23	0.07	0.12
120	0.02	0.08	0.03	0.066	0.04	0.06

2.5 EVALUATING FIXED BEAM AND SCANNING LIDAR SYSTEMS

2.5.1 Estimation of optimum scan location based on REWS

The rotor effective wind speed from the SpinnerLidar and the fixed-beam scan measurements are compared with the turbine estimated rotor effective wind speed to determine the ideal preview distance, beam opening angle and the corresponding coherence bandwidth. The rotor effective wind speed for the different devices are calculated as $u_{\text{eff}}(t) = \frac{1}{n} \sum_{i=1}^{n} u(x_i, t)$. The longitudinal velocity is estimated from the cosine projection with the assumption of zero lateral and vertical components (Eq. 2.2). Note that in this definition of REWS, there is no correction for the directional bias due to the turbine misalignment. Finally, a velocity deceleration correction is applied based on the turbine axial induction factor. The rotor effective wind speeds are calculated from the projected *u*-component at the measurement distance and the beam deflection angles. The calculated REWS are compared against the effective wind speed calculated from the turbine data by defining the normalised mean square error as $\frac{\|(u_{\text{eff}}^{lidar} - u_{\text{eff}}^{turbine})\|^2}{u_{\text{eff}}^{turbine}}$. The rotor effective wind speed from the turbine is calculated by means of the power balance estimator method [Soltani et al. 2013]. The method uses the entire rotor as an anemometer and calculates the wind speed experienced by the turbine by considering the turbine signals (power, rotational speed and pitch angle). The $u_{\rm eff}$ is estimated from the pitch angle β and the tip speed ratio λ from a pre-computed $C_P(\beta, \lambda)$ surface created from the output of the aeroelastic simulation. No blade passage effects are simulated as the lidar was simulated on the spinner of the reference turbine.

The normalised mean square error calculated between the REWS for different lidar scenarios and the REWS from the turbine is shown in Fig. 2.16 for the CBL and SBL cases. The impact of directional bias and wind evolution is visible in the REWS estimates obtained from the

lidar measurements. For opening angles greater than 30°, the SpinnerLidar measurements at points in the outer section of the scan trajectory have significant cross-contamination of the lateral and vertical components. Secondly, the error is dependant on focus distances and opening angles due to the wind evolution between the measurement and rotor planes. It is clear in Fig. 2.16 that the location of the optimum upstream measurement distance is influenced by atmospheric stratification. With a shorter focus distance, the effect of wind evolution could be reduced, but such a setup will require large beam deflection angles to capture the entire rotor plane, increasing the directional bias due to the cross-wind components with the opposite holding as well.

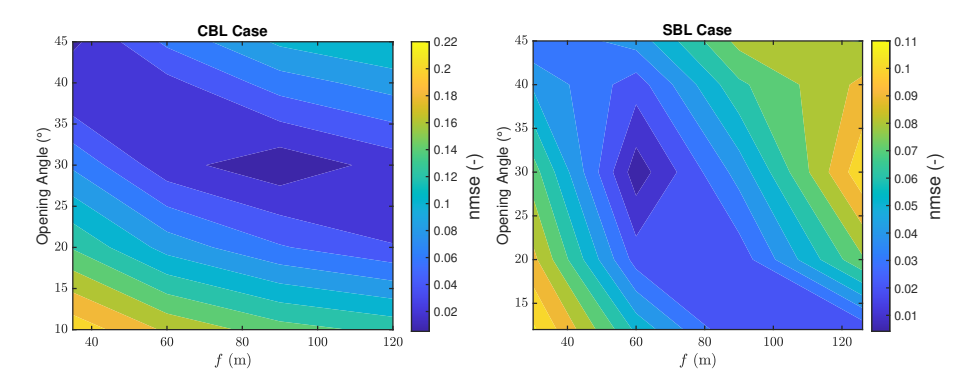


Figure 2.16: Normalised mean square error between the rotor effective wind speed calculated from the turbine and the lidar measured rotor effective wind speed as a function of focus distance and opening angle for SpinnerLidar measurements for the CBL and SBL cases.

In general, at large upstream distances and smaller opening angles (e.g., f = 126 m and θ = 5°, 10°), the projection error is relatively low, and most of the fluctuations in the rotor plane are captured leading to more minor errors. For the CBL case, the scan location optimised for the lowest error is estimated at an opening angle of 30° at a focus distance around 50 m to 110 m. In contrast, for the SBL case, the optimum scan distance lies between 60 m to 70 m with an opening angle of 30°. This is due to the significant shear present in the SBL inflow case, which requires large scanning angles to capture the wind variations in the rotor plane while wind evolution becomes dominant at more considerable focus distances.

To estimate the performance of the SpinnerLidar relative to the fixed-beam devices in Tables 2.5, 2.6, the optimal scan location is calculated for all scanning strategies by optimising for the highest coherence bandwidth. The coherence is calculated using the Matlab function *mscohere* with 20 blocks and applying a Hamming window with 50% overlap. The wavenumber is defined as $k = \frac{2\pi}{e_{\rm eddy}}$ and is the inverse of the smallest detectable eddy size $(e_{\rm eddy})$ with an accuracy of 50% assuming isotropy as defined in Held and Mann 2019b. While the optimum measurement distance and the opening angles for the same scanning strategy differ between the CBL and SBL cases, the optimal scan location for the fixed-beam scans is generally further upstream than the SpinnerLidar. Small θ reduces the directional bias for the fixed beam scans, but the optimal measurement position is situated upstream to scan a larger proportion of the rotor area. For the SpinnerLidar, the optimal

Table 2.5: CBL Case: The optimal focus distance and opening angle for the highest coherence bandwidth and corresponding measurable wave number for the rotor effective wind speeds calculated for the different scans.

ID	f _{opt} (m)	θ _{opt} (°)	$f b_{\text{opt}}$ (Hz)	k _{opt} (rad/m)
Point	30	-	0.0195	0.0122
2-Beam Vertical	126	20	0.0234	0.0146
2-Beam Horizontal	126	30	0.0234	0.0146
4-Beam	126	20	0.0313	0.0194
5-Beam	126	30	0.0313	0.0194
Horizontal Line	90	10	0.024	0.0149
Vertical Line	90	30	0.027	0.0168
Circular Scan	90	10	0.0508	0.0316
SpinnerLidar	90	30	0.1426	0.0887

Table 2.6: SBL Case: The optimal focus distance and opening angle for the highest coherence bandwidth and corresponding measurable wave number for the rotor effective wind speeds calculated for the different scans.

ID	$f_{\rm opt}$ (m)	θ _{opt} (°)	$f b_{\text{opt}}$ (Hz)	k _{opt} (rad/m)
Point	30	-	0.022	0.0194
2-Beam Vertical	90	30	0.037	0.0327
2-Beam Horizontal	126	20	0.039	0.0345
4-Beam	126	30	0.046	0.0407
5-Beam	126	30	0.050	0.044
Horizontal Line	30	20	0.032	0.0283
Vertical Line	126	10	0.039	0.0345
Circular Scan	90	45	0.056	0.0495
SpinnerLidar	60	30	0.111	0.0982

scan location is closer to the turbine reducing the wind evolution uncertainty that translates to a higher coherence bandwidth. The smallest detectable eddy size increases by 34% and 18% for CBL and SBL cases when moving from 2-beam to 4-beam devices, corresponding to the findings of Held and Mann 2019b. The measurable wave number is smaller for the horizontal and vertical line scans than for the 4-beam lidar due to the significantly reduced rotor coverage. In contrast, the circular scan offers better performance than all simple scanning strategies. The SpinnerLidar performs considerably better than all the fixed-beam devices, with the smallest measurable eddy size of 70.8 m and 64.9 m for the CBL and SBL cases, respectively. Only the SpinnerLidar is capable of measuring eddies smaller than 1 *D* indicating its potential for fatigue load reduction [Schlipf et al. 2018].

2.5.2 Effect of spatial sampling on three-parameter estimation

To estimate the performance of the beam scanning in comparison to fixed-beam devices, the standard and dynamic errors $\epsilon_{\rm std}$ and $\epsilon_{\rm dyn}$ defined in Eq. (2.10) and (2.11) are used. Three wind field parameters $u_{\rm eff}$, $\delta_{\rm h}$ and $s_{\rm v}$ are calculated for each of the scan patterns described in Tab. 2.5.2. The results of the different lidar scans are compared against the parameters

calculated from the LES at 1 D upstream of the turbine location to avoid the effects of wind evolution. For the various scan patterns performed, the following trends can be observed. For both cases, the static error associated with the estimation of u_{eff} is negligible for even a point measurement for the CBL case, but 0.06 for the SBL case as the single point cannot capture the spatial variations due to the strong shear present in the flow. The dynamic error of $u_{\rm eff}$ reduces from 0.28 to 0.03 and from 0.44 to 0.19 for the CBL and SBL cases moving from Scans 1-9. The estimation of the vertical shear is impossible for scan patterns 3 and 6, while the reconstruction of yaw misalignment is not possible for scan scenarios 2 and 7 as no wind variations in the horizontal and vertical directions are measured by these scans. For the 2-beam configurations, the static errors of δ_h and s_v are 0.45, 0.15 and 0.06 and 0.36 for the CBL and SBL cases, while a large dynamic error estimation of the yaw misalignment is noticed. The 4-beam and 5-beam configurations allow instantaneous shear and yaw estimation, with both configurations performing very similarly for the two cases. The $u_{\rm eff}$ estimation is slightly better for the 5-beam scan due to the presence of a centre beam. The dynamic shear and direction estimation based on horizontal and vertical line scans is better than its corresponding two-beam scenario due to higher spatial coverage. However, for the CBL case, the $\epsilon_{\rm dyn}$ for $\delta_{\rm h}$ is larger compared to the SBL case, presumably due to a comparatively large variance in the wind direction during convective conditions [Vollmer et al. 2016] which could be reduced by considering larger averaging intervals. The circular scan shows very low $\epsilon_{\rm std}$, $\epsilon_{\rm dyn}$ errors in $u_{\rm eff}$ estimation. The standard error estimation of δ_h and s_v are 0.18 and 0.56 while the dynamic error remains high at 0.98 and 0.25 respectively for the CBL case while for the SBL case returned values of 0.33, 0.10 and 0.22, 0.96 respectively. As expected, the SpinnerLidar providing more extensive spatial coverage substantially improves the static and dynamic estimation of the three parameters.

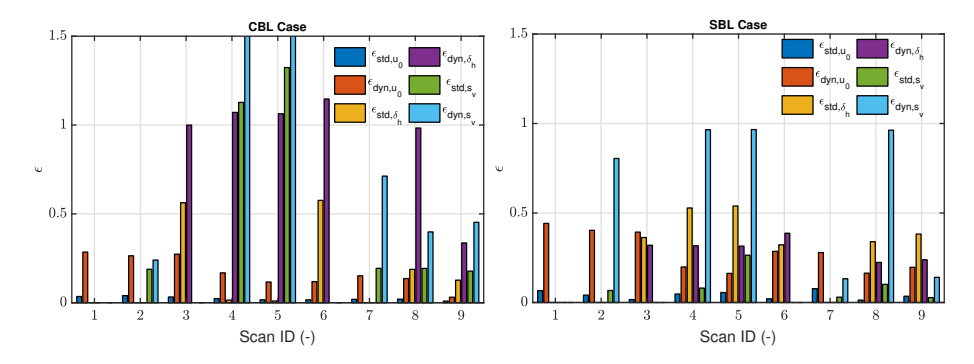


Figure 2.17: The standard and dynamic errors calculated for the different spatial samples for the CBL case and the SBL case.

In general, we note the following trends. The reconstruction accuracy of the wind parameters increases with increasing number of beams as the sizeable spatial coverage is more representative of the rotor area. The effective wind speed is captured very well with at least two beams as the single-beam lidar cannot capture the rotor plane variations such as sheared inflow. The dynamic error estimation reduces while performing line scans compared to 2-, 4-, 5- beam systems except for the dynamic estimation of δ_h for the CBL case.

2.6 Discussions 45

This behaviour further illustrates the need to consider the effects of atmospheric stability on the wind field parameterisation. Finally, scanning the inflow with the SpinnerLidar leads to meagre standard and dynamic estimation errors of the wind field parameters due to the complete rotor coverage.

2.6 Discussions

Performing turbine-mounted lidar measurements to optimise turbine performance requires knowledge about lidar capabilities and inherent uncertainties influencing the measurement quality. While a research-oriented prototype, like the SpinnerLidar, can measure the inflow with high spatio-temporal resolutions, the high costs could be prohibitive for commercial purposes. Large Eddy Simulations provide a suitable reference for analysing the different lidar systems' performance for different stratifications. Before discussing the results, the extent to which the lidar simulations can be considered appropriate must be addressed. As noted by Beck and Kühn 2019, the direct transferability of the results to the free field is not straightforward as the simulator performs step-and-stare measurements that neglect the volume averaging in the scanning direction. The simulator assumes maximum data availability as environmental factors such as fog or rain is not modelled. The uncertainty in beam pointing and the laser beam movement due to turbine or blade interference is also not modelled.

2.6.1 The limitations and capabilities of turbine-mounted li-

The capabilities and limitations of using a turbine-mounted SpinnerLidar for wind energy applications are discussed briefly. A lidar measuring at 1 Hz is a standard setting for commercial devices and can accurately estimate the mean wind information, making it suitable for using lidars for LAC. There is a negligible effect of the volume averaging on the estimation of mean wind parameters and it is even beneficial due to the more extensive rotor coverage. However, as the volume averaging effect acts as a low-pass filter at more considerable focus distances for cw lidars attenuating high-frequency fluctuations, it is essential to consider and model this effect for other lidar-based applications such as load validation.

Directional bias is the most significant error source while estimating the longitudinal wind speed that drives turbine response. It is evident that for larger opening angles typical for scanning lidars, the directional bias is dominant over volume averaging due to the increased cross-contamination from the crosswind components. The longitudinal component estimation is sensitive to beam pointing angles and dynamics changes during turbine operation (Fig. 2.10). The additional beam deflection due to the rotor axis tilt during operation can be countered by a slightly inclining the lidar during installation. Indeed, the directional bias effects could be avoided by using multi-lidar synchronised measurements, however impractical for LAC applications [Simley et al. 2016] or by utilising physics-based wind field reconstruction methods [Kidambi Sekar et al. 2018].

The spectral analysis in Fig. 2.11 points out the dominant effect of volume averaging measurements in a non-rotating reference frame, with the drop-off occurring at around 0.1 Hz. For the fixed point spectra at the outer scan edges, directional bias plays the most

dominant effect in scaling the time series and hence the variance (Fig. 2.12). The higher energy content in the turbulent spectra could lead to erroneous load predictions due to the scaled variance. However, the volume averaging effect does not affect the measurement in the rotating spectra where an accumulation of energy occurs at multiples of the rotor frequency. Even with a limited sampling rate of 1 Hz, SpinnerLidar captures the rotational harmonics due to the eddy slicing effect. This was made possible through the high spatial resolution that allows the lidar to capture the wind shear and spatial inflow variations. Accordingly, investigations of spatio-temporal characteristics of turbulent wind fields in a *fixed* frame of reference, e.g. done with the lidar mounted on the nacelle, should be executed only at shorter focal lengths. In contrast, the SpinnerLidar performs very well in the *rotating* frame of reference, i.e. when mounted in the rotating hub of the wind turbine while simpler lidar systems are limited due to the comparatively lower spatial scan resolution.

For modelling the wind evolution and induction slowdown, it is evident that the volume averaging effect at larger upstream distances already low-pass filters the high-frequency inflow turbulence. There are no differences in the coherences for various longitudinal separation distances between ideal lidar systems without and real lidar systems with the volume averaging effect (Fig. 2.14). Wind evolution is driven by the horizontal separation distance between the points and the induction factor of the turbine. By combining the longitudinal wind evolution model [Simley et al. 2014a] with a simple induction zone model [Medici et al. 2011], a better estimation of the coherence bandwidth is obtained. By widening the usable frequency range, more data from the turbulence spectrum can be utilised to filter out uncorrelated frequencies. This can prevent unnecessary control actions in wind preview-based controllers. The temporal sampling, volume averaging, directional bias and wind evolution constitute the significant error sources associated with turbine-mounted cw lidars.

2.6.2 On the evaluation of fixed-beam and scanning lidars for lidar-assisted control applications

The spatial resolution of the lidar is the deciding factor in the accurate estimation of the rotor averaged wind field parameters relevant for wind turbine control. For evaluating the scanning SpinnerLidar against fixed-beam systems, we perform inflow parameterisation for CPC and IPC strategies. For CPC, the dependence of the rotor effective wind speed on the upstream measurement distance and the beam angle is visualised in Fig. 2.16 for the SpinnerLidar. A smaller opening angle implies that the whole rotor area is not covered. At the same time, the directional bias becomes dominant at larger opening angles, introducing severe errors in calculating the rotor effective wind speed. Measurements taken further away from the rotor plane are also erroneous due to the wind evolution and induction deceleration between the measurement and the rotor plane. The effect of the directional bias is amplified during stable stratification and the associated stronger wind shear, which changes the optimum scan location. An optimisation was performed for the fixed-beam devices and tabulated in Tab. 2.5, 2.6. The optimum scan location of the SpinnerLidar depends on the atmospheric stability and varies between 70 m and 100 m (0.55 D to 0.8 D) and 60 m-70 m (0.4 D to 0.5 D) for the CBL and SBL cases respectively. The coherence bandwidth of the SpinnerLidar and the ability to resolve smaller eddies is

47

increased substantially due to the enhanced spatial coverage offered by the SpinnerLidar. Hence, by using a SpinnerLidar for CPC control, it is practical to scan closer to the rotor to enable a shorter preview time and associated lower wind evolution uncertainty. This would allow for a larger bandwidth to be processed for performing control actuation for which a minimum preview time is required [Dunne et al. 2014]. On a practical note, the presence of blade passage which reduces the measurement availability for nacelle-mounted lidars, has not been considered in our analysis. The loss in measurement data can lead to incorrect estimation of the spatially varying turbulence.

The performance of SpinnerLidar in comparison to fixed beam devices for IPC control is evaluated by calculating the standard and dynamic reconstruction errors associated with the effective wind speed, vertical shear and yaw misalignment. Figure 2.17 reveals that while estimating $u_{\rm eff}$, just a few measurement points are needed. The effective wind speed alone is captured pretty well even by relatively simple scan patterns, while a better estimation of the wind parameters is achieved while adding more beams. For turbinemounted lidars that experience undisturbed wind inflow, it is favourable to perform simple 4-beam scans to estimate the shear and direction simultaneously. The situation changes supposing dynamic changes in the shear or yaw, for instance, in the case of a turbine located in the downstream rows of a wind farm where a variety of partial wake situations are expected. In that case, it is sensible to scan more points to reduce the dynamic error. The circumferential scan performs similar to the 4-beam and 5-beam configurations but has the advantage that the rotational spectra useful for fatigue estimation are also captured. With inflow measurements from a SpinnerLidar, the parameter estimation is comparatively accurate as the scan covers the whole rotor plane. However, it is effective to scan only a minimum amount of points to reconstruct wind field parameters or to use model reduction techniques for dimensional reduction while retaining the necessary wind field information.

2.6.3 On the potential LCoE reductions

2.6 Discussions

While measuring the inflow using the SpinnerLidar shows clear benefits over fixed-beam counterparts, the high associated capital, operation and maintenance costs are essential factors to consider when selecting an appropriate lidar system. The SpinnerLidar comfortably outperforms the other investigated lidar systems in reconstructing wind inflow parameters required for all the chosen control concepts. However, such an analysis cannot give precise answers to the benefits of LAC as this would require many high-fidelity coupled LES and aeroelastic simulations with and without various LAC concepts with multiple lidar systems. System engineering studies such as the work of Canet et al. 2021 has explored the relation between LAC and LCoE reductions. However, the study was limited as only typical lidar augmented load reductions from literature could be used. However, the presented analysis was focused on identifying trends and the general applicability of a lidar system for a particular LAC concept. While prototype devices are usually associated with high associated capital costs and low reliability, adopting and integrating scanning lidar systems during the turbine design phase could reduce costs. With increasing turbine sizes consequently exposing the rotor to more extensive wind regimes in the atmospheric boundary layer, the large spatial resolution of the SpinnerLidar would be particularly useful in measuring spatial variations in the inflow allowing for the implementation of advanced control concepts such as 2P IPC or even individual flap control [Unguran et al. 2019].

2.7 Conclusions

Identification of the capabilities and limitations of turbine-mounted lidars for inflow-sensing is essential for achieving better performance of lidar-based applications like lidar-assisted control. In this chapter, the capabilities and uncertainties of a turbine-mounted lidar system were investigated with a focus on the prototype DTU SpinnerLidar using a lidar simulator inside two Large Eddy Simulations of different stratifications. The SpinnerLidar, a prototype research turbine-mounted scanning lidar, achieves higher spatio-temporal sampling rates than the more straightforward, cheaper, but more robust fixed-beam devices mounted on the nacelle. The performance of the SpinnerLidar against fixed-beam devices in extracting wind inflow information required for the realisation of lidar-assisted control concepts was evaluated. The lidar simulations were performed using a lidar simulator, granting an opportunity to isolate and investigate specific lidar limitations that cannot otherwise be performed in full-field experiments. The SpinnerLidar captures the rotational harmonics in a rotational frame of reference due to its high spatial coverage opening up opportunities for higher harmonic control.

Moreover, the SpinnerLidar also allows quick estimation of the dynamics of the controloriented wind inflow parameters such as the rotor effective wind speed, vertical shear and yaw misalignment compared to fixed-beam devices. However, the 3-parameter modelling of the inflow wind is limited due to the representation of the wind distribution in the rotor plane with just 3 parameters and the associated error in wind direction estimations in case of partially waked flows which were not fully covered in the two undistributed inflow simulations. While research-oriented scanning lidars such as the SpinnerLidar is may not be an ideal choice for LAC applications due to high capital, maintenance, and associated costs, a potential additional value could be to emulate simpler fixed-beam systems during LAC field tests.

3

LOWER ORDER DESCRIPTION AND RECONSTRUCTION OF SPARSE SCANNING LIDAR MEASUREMENTS OF WIND TURBINE INFLOW USING PROPER ORTHOGONAL DECOMPOSITION

Preview measurements of the inflow by turbine-mounted lidar systems can be used to optimise wind turbine performance or alleviate structural loads. However, nacelle-mounted lidars suffer data losses due to unfavourable environmental conditions and laser beam obstruction by the rotating blades. Here, we apply proper orthogonal decomposition (POD) to the simulated line-of-sight wind speed measurements of a turbine-mounted scanning lidar obtained from two large eddy simulations. This work aimed at identifying the dominant POD modes that can be used to subsequently derive a reduced-order representation of the turbine inflow. Secondly, we reconstructed the data points lost due to blade passage by using Gappy-POD. We found that only a few modes are required to capture the dynamics of the wind field parameters commonly used for lidar-assisted wind turbine control, such as the effective wind speed, vertical shear and directional misalignment. By evaluating turbine-relevant metrics in the time and frequency domain, we found that a ten-mode reconstruction could accurately describe most spatiotemporal variations in the inflow. Furthermore, a modal interpretation is presented by direct comparison with these wind field parameters. We found that the Gappy-POD method performs substantially better than spatial interpolation techniques, accurately reconstructing up to even 50 % of missing data. A POD-based wind field reconstruction offers a trade-off between wind field reconstruction techniques requiring flow assumptions and more complex physics-based representations, offers dimensional reduction and can overcome the blade passage limitation of nacelle-mounted lidar systems.

3.1 Introduction

With advances in lidar technology for wind energy applications, scanning the inflow of wind turbines has attracted greater attention. Turbine-integrated lidar systems can scan wind fields upstream of the turbine, allowing these measurements to be incorporated into turbine operation and control. Using preview lidar measurements as input, turbine performance can be improved in terms of alleviating structural loads, for example, by reducing blade and tower bending fatigue load damage or extreme loads by feed-forward lidar-assisted control [Schlipf et al. 2011; Simley et al. 2018]. Turbine-mounted lidar measurements can also be used for load validation [Conti et al. 2021; Dimitrov et al. 2019] and characterisation of turbulence [Penã et al. 2017].

The quality of wind field data extracted by lidar depends on the quality and beam scanning strategy of the lidar device itself. To date, commercial turbine-mounted lidar systems are limited to performing wind field measurements along fixed-beams, owing to their relatively simplistic but robust design [Borraccino et al. 2017; Held and Mann 2019b]. However, with the trend towards larger rotors, local wind field variations are affecting the turbine dynamics more strongly; hence, it is necessary to scan the entire rotor area rather than just a few fixed spatial locations. Next generation lidar systems with scanning capabilities could bridge this gap by performing very fast scanning measurements to capture the wind field in more detail. Such lidars are an improvement over fixed-beam systems commonly found in commercial applications, as they are instead outfitted with beam-steering mechanisms capable of moving and refocusing the laser beam to a predefined point or a scanning pattern in space. With such devices available, highly resolved measurements of the wind turbine inflow are possible [Herges et al. 2017a; Mikkelsen et al. 2013].

Due to the lidar's spatial sampling and line-of-sight limitations, wind field reconstruction (WFR) methods are required to extract even relatively simple parameters, such as rotor effective wind speed, direction and shear. Two types of WFR models can be found in the literature, i.e., static and dynamic WFR methods [Borraccino et al. 2017]. In the static approaches, wind fields are assumed to be stationary for a certain averaging period, and spatial flow assumptions such as Taylor's frozen turbulence Taylor 1938 are made to determine relevant wind field parameters [Borraccino et al. 2017; Kapp. S 2017]. These models are adequate for power performance measurements, as they well estimate the averaged wind characteristics but fall short while resolving inflow dynamics. Furthermore, the flow assumptions required for the reconstruction might not hold in the turbine induction zone and complex inflow situations.

In the dynamic reconstruction methodologies, both spatial and temporal variations of the wind fields are considered. A 3D-model based dynamic WFR technique was presented by Raach et al. 2014, combining the static model presented by Schlipf et al. 2012b with Taylor's frozen turbulence hypothesis. Towers et al. [Scholbrock et al. 2013a] introduced a dynamic

The contents presented in this chapter have been published as: (a) A. P. Kidambi Sekar, M. F. van Dooren, A. Rott, and M. Kühn. Lower Order Description and Reconstruction of Sparse Scanning Lidar Measurements of Wind Turbine Inflow Using Proper Orthogonal Decomposition. Remote Sensing, 14(11):2681, 6 2022. DOI: 10.3390/rs14112681.

© 2022 by the authors. Reproduced in accordance with the Creative Commons Attribution 3.0 License.

3.1 Introduction 51

reconstruction methodology to reconstruct two-dimensional horizontal wind fields at hub height from a pulsed lidar system with two fixed beams using an unscented Kalman filter. Guillemin et al. 2018 presented a method for extracting real-time wind field parameters, such as effective wind speeds, wind direction and shear, using a recursive weighted least-squares algorithm that was validated with simulated pulsed 4-beam lidar measurements. The performance of a fast Navier–Stokes physics-based solver to instantaneously reconstruct the local 3D velocity components from line-of-sight measurements of a scanning lidar upstream of the rotor was investigated in Kidambi Sekar et al. 2018. The performances of these models in reconstructing the dynamics of the wind inflow were found to be limited in situations where flow simplification assumptions are considered invalid [Raach et al. 2014], there is an assumption of simultaneous measurements at multiple beam locations [Scholbrock et al. 2013a] or there is insufficient spatial resolution for covering the total area swept by the rotor [Guillemin et al. 2018].

An alternative method is to accurately reconstruct the inflow without depending on strong assumptions concerning the wind field. As using high-resolution data directly as a control signal is not feasible, a crucial step towards a lidar-based wind field reconstruction is the reduction of the measurement data to a few key variables which still capture the most important spatio-temporal inflow variations. In fluid dynamics, proper orthogonal decomposition (POD) is a well used method for dimensional order reduction. POD describes a velocity field as a linear combination of modes containing spatial information about the flow and time-varying weighing functions defining the evolution of the flow field in time [Berkooz et al. 1993; Holmes et al. 2012; Sirovich 1987]. Mathematically, the POD method calculates deterministic orthogonal basis functions for representing a spatio-temporal field. The decomposition is unbiased because it does not look for prior information and the basis functions are obtained from the dataset itself, in contrast to other techniques. As the modes themselves are orthogonal, the method is suitable for reduced-order inflow reconstruction by truncating higher modes and rapidly reconstructing the wind field or using Galerkin projection to capture the dominant flow physics [Taira et al. 2017]. Therefore, a POD-based reconstruction would offer quick and reliable retrievals of the lidar-measured inflow simply by exploiting the redundancies in the data. Moreover, the dominant structures obtained via POD decomposition are representative of the coherent structures in the wind flow [Holmes et al. 2012]. For wind energy applications, POD has been used to develop and understand dynamic wake models [Andersen et al. 2017; Bastankhah and Porte-Agel 2017; Bastine et al. 2015]. Saranyasoontorn and Manuel 2005 used POD to investigate the wind turbine inflow based on stochastic wind field simulations.

Nacelle-mounted inflow sensing lidars experience data loss due to adverse atmospheric conditions, such as rain or fog, and more importantly, due to laser beam blockage by the rotating blades. The data loss is influenced by the blade root design, lidar mounting position and blade rotation [Davoust et al. 2014]. The reduced data availability increases the uncertainty while performing modal decomposition, and time and frequency domain analysis, which is critical for lidar-based wind turbine applications. For example, uncertainties in the estimated wind parameters could cause unnecessary and even harmful actuation of a lidar-based feed-forward control system. While spatial interpolation techniques could reconstruct missing points based on the information from the neighbouring points, these methods fail to capture localised events, such as partial gusts. As wind field dynamics

are of interest, ensemble averaging is disadvantageous, as small scale fluctuations are averaged out. One method for reconstructing spatio-temporal wind field gaps is using gappy proper orthogonal decomposition (Gappy-POD), first proposed by Everson and Sirovich 1995 and which has been adapted to solving experimental fluid flow problems with missing or false points [Gunes et al. 2006; Raben et al. 2012; Saini et al. 2016; Willcox 2006]. Gappy-POD uses a set of POD modes as a basis from which the missing data are estimated through an iterative process [Venturi and Karniadakis 2004]. However, this method breaks down while reconstructing empty snapshots or if certain data points are missing at all times. Reconstructing certain blind regions due to stationary hard targets, such as nacelle interference, could be potentially overcome with Kriging-based interpolation methods [Oliver and Webster 1990], but this lies outside of the scope of our work.

Herefore, there is no wind field reconstruction methodology that fully utilises scanning lidar measurements while accounting for the spatio-temporal inflow dynamics and affording the data compression necessary for control algorithms. Secondly, a data reconstruction method is required for accurately reconstructing spatio-temporal inflow variations from sparse scanning lidar measurements. The objective of this paper is twofold. Firstly, we introduce a dynamic wind field reconstruction methodology based on POD that requires no strong assumptions about the reconstructed wind field. We identify the dominant inflow spatial modes that can be used to obtain a reduced-order reconstruction of the inflow wind field measured with a turbine-mounted scanning lidar. We then assess the reconstruction quality based on metrics concerning the turbine inflow. Secondly, we investigate the performance of the Gappy-POD in reconstructing artificially removed measurement points. A modified Gappy-POD method is introduced to reduce the long solution times required for the iterative method. The accuracy of the reconstructed wind fields is evaluated by investigating inflow metrics and compared against the accuracies of spatial interpolation techniques.

The article is structured as follows: The methods, including the description of the POD and Gappy-POD procedures, are described in Section 3.2, along with descriptions of the reference large eddy simulations and the scanning lidar. The application of the POD method to simulated lidar measurements, POD-based reconstruction of the original line-of-sight velocity fields and quantitative analysis of the reconstructions based on wind field metrics are presented in Section 5.3, along with the results of the Gappy-POD reconstruction. Section 3.4 discusses the results, and Section 3.5 presents the conclusions.

3.2 Methods

Tailoring the methods of POD and Gappy-POD towards wind turbine inflow is introduced in Sections 3.2.1 and 3.2.2. The scanning lidar specifications and working principles are presented in Section 3.2.3. To obtain a realistic wind field dataset to investigate the inflow to a wind turbine, we employed virtual lidar data derived from high-fidelity large eddy simulations which are explained in Section 3.2.4, along with the virtual lidar simulator.

 $^{^1}$ The Proper Orthogonal Decomposition (POD) method in this chapter reconstructs the spatially varying line-of-sight velocity field (v_{los}) directly from scanning lidar measurements. This differs from a full 3D "wind field," as v_{los} represents only the wind component along the lidar beam within the scan plane

3.2 Methods 53

3.2.1 Proper Orthogonal Decomposition (POD)

POD is a powerful numerical technique applicable to identifying turbulent coherent structures from flow fields [Berkooz et al. 1993; Holmes et al. 2012; Sirovich 1987]. The decomposition provides a set of time-independent orthogonal spatial modes with respective time-dependent coefficients. The basic decomposition procedure is to sample the data, calculate the auto-covariance matrix and solve the corresponding eigenvalue problem, which can then be used to construct an orthogonal basis. Lidar systems can only sense the wind speed component along the line-of-sight direction. We perform POD analysis on the line-of-sight (v_{los}) measurements from a scanning lidar, as projection in the longitudinal flow direction would introduce geometrical errors in the reconstruction, especially at large scanning angles [Simley et al. 2014a]. Furthermore, the longitudinal velocity component is the dominant component in the line-of-sight measurements of a turbine-mounted lidar and the main driver of the dynamics of the turbine response. Moreover, wind field reconstruction algorithms [Borraccino et al. 2017; Kapp and Kühn 2014; Raach et al. 2014] also rely on the line-of-sight measurements to estimate wind field parameters. The practical application of this method to scanning lidar measurements is described in the following. The line-ofsight measurements of a turbine-mounted scanning lidar $\mathbf{v}_{los}(\mathbf{X}_i, \mathbf{t}_i)$, where $\mathbf{X}_i = [x_i, y_i, z_i]^T$, $j = 1 \cdots N$, $i = 1 \cdots n_s$ and $\mathbf{t} = (t_1, t_2, \dots, t_{n_s})$ and $\mathbf{X} = [\mathbf{X}_1, \mathbf{X}_2 \cdots \mathbf{X}_N]^T$, are organised in a snapshot matrix V defined as:

$$V(X,t) = [\mathbf{v}_{los}(\mathbf{X},t_1), \mathbf{v}_{los}(\mathbf{X},t_2) \cdots \mathbf{v}_{los}(\mathbf{X},t_{n_s})] = \begin{pmatrix} \mathbf{v}_{los}(\mathbf{X}_1,t_1) & \mathbf{v}_{los}(\mathbf{X}_1,t_2) & \cdots & \mathbf{v}_{los}(\mathbf{X}_1,t_{n_s}) \\ \mathbf{v}_{los}(\mathbf{X}_2,t_1) & \mathbf{v}_{los}(\mathbf{X}_2,t_2) & \cdots & \mathbf{v}_{los}(\mathbf{X}_2,t_{n_s}) \\ \vdots & \vdots & \vdots & \vdots \\ \mathbf{v}_{los}(\mathbf{X}_N,t_1) & \mathbf{v}_{los}(\mathbf{X}_N,t_2) & \cdots & \mathbf{v}_{los}(\mathbf{X}_N,t_{n_s}). \end{pmatrix}$$
(3.1)

where n_s is the number of snapshots and N is the total number of grid points in each snapshot. As our objective is to determine the dominant spatial modes, the application of the POD method to scanning lidar measurements is done a posteriori. Hence, all snapshots are available for the subsequent decomposition. It is common to subtract the mean value to obtain the fluctuating component $V'(X,t) = V(X,t) - \langle V(X,t) \rangle$. Here, $\langle V(X,t) \rangle$ denotes the spatial velocity field averaged over time. POD decomposes the wind field V'(X,t) into a linear superposition.

$$V'(X,t) = \sum_{j=1}^{N} Z_j(t)\phi_j(X),$$
(3.2)

where $\phi_j(X)$ are called the spatial POD modes optimal with respect to the flow turbulent kinetic energy, and $Z_j(t)$ are the time-evolving POD weighing coefficients. This solution is obtained by solving the eigenvalue problem of the covariance matrix $R = V'(X,t)V'(X,t)^T$:

$$R\phi_i = \lambda_i \phi_i, \tag{3.3}$$

resulting in a set of eigenvectors ϕ_j denoted as POD modes and a set of corresponding eigenvalues λ_j which can be ordered as $\lambda_1 \ge \lambda_2 \ge \lambda_3$ The flow field can now be denoted as a linear combination of N uncorrelated spatial modes:

$$V(X,t) = \langle V(X,t) \rangle + V'(X,t) = \langle V(X,t) \rangle + \sum_{j=1}^{N} Z_j(t)\phi_j(X), \tag{3.4}$$

where the jth weighing coefficient is obtained as:

$$Z_{j}(t) = \phi_{j}^{T}(X)V'(X,t). \tag{3.5}$$

 $Z_j(t)$ contains the temporal gains determining the development of the POD modes in time. A reduced-order representation of the flow field $\hat{V}(X,t) = \langle V(X,t) \rangle + \hat{V}'(X,t)$ can be obtained by truncating the higher modes and retaining only M < N modes where:

$$\hat{V}'(X,t) = \sum_{j=1}^{M} Z_j(t)\phi_j(X).$$
 (3.6)

For such a reduced-order approximation, the POD modes of Equation (3.3) are optimal with respect to the turbulent kinetic energy in the flow. Hence, they are a set of optimal modes with the least mean square error given by:

$$\langle ||V'(X,t) - \hat{V'}(X,t)||_2^2 \rangle$$
 (3.7)

The spatial modes $\phi_j(X)$ contain information about coherent structures, as the POD method can be seen as an energy filter that unravels the large spatial turbulent structures. However, it must be noted that these structures might not be actual physical structures present in the flow field, but merely a result of the mathematical operation. An important property of this method is that the POD modes are orthonormal, so their temporal gains are uncorrelated Holmes et al. 2012. With large flow matrices being common in fluid flow problems, the dimensions of the covariance matrix R become quite large, thereby making the application of classical POD very time-consuming. To avoid this, the method of snapshots [Sirovich 1987] is used, whereby the temporal covariance matrix V'^TV' is solved to obtain the same dominant spatial POD modes. Due to the reduced computational and memory resources needed, the snapshot method is a commonly used method for obtaining POD modes from flow data.

We can now apply the snapshot POD methodology to the line-of-sight velocity field obtained via scanning lidar measurements, truncating the higher modes and creating a reduced-order reconstruction of the flow. The order M of the reduced model in Equation (3.6) is crucial. Improper selection of M might lead to a dimensional reduction that is either very large or very small, and important flow field data may be lost.

3.2.2 THE GAPPY-POD

The Gappy-POD developed by Everson and Sirovich 1995 is an extension of the POD method that is capable of providing high accuracy approximations of missing or invalid data points. The method is based on an iterative POD implementation on the incomplete dataset, where the missing data points are initially replaced by a first guess, usually the temporal mean of the available data at that point. The output of every POD calculation is used as the input for the next iteration, where the number of modes is increased until a predefined convergence level is achieved. In other words, the initial guess is updated based upon an iterative POD approximation based on an increasing number of POD modes *P*. However, the optimum number of modes required to reconstruct the inflow differs based on the flow condition, i.e., the optimum number of modes required to accurately reconstruct

3.2 Methods 55

undistributed wind inflow, is lower compared to inflow reconstruction during partial or full wake conditions due to the higher wind field turbulence. This implies that if a large number of modes is chosen with a poor initial guess, then the data gaps will be filled with more details of the poor guess. Conversely, if only a small number of POD modes is chosen, then the finer details of the wind fields will not be captured.

Here, we follow the iterative Gappy-POD implementation proposed by Venturi and Karniadakis 2004, which has been shown to significantly improve the Gappy-POD accuracy [Gunes et al. 2006]. The iterative process is started based on an initial guess and a low number of modes $P_0 = 2$ from which a converged Gappy-POD approximation is obtained. This approximation is subsequently used as the next guess for the subsequent iterations $P_0 < P_1 < P_2 \ldots$, where the number of modes is increased and the process is continued until a certain convergence criterion is met. This results in a nested-loop implementation whereby POD convergence is evaluated for a given number of modes in the outer loop and the used number of modes P in the inner loop. The latter will be described as sub iterations (denoted by P), and the iterations based on the used number of modes P will be referred to as main iterations (denoted by P) from here on. The corresponding velocity field at every main and sub-iteration is denoted by P0. The Gappy-POD procedure to reconstruct the fluctuating component of velocity is as follows:

1. For the first main iteration n = 0, the initial guess for the velocity at the missing points is the temporal mean of all valid data available at that particular point, i.e.,

$$\overline{V}_{0,0}(X,t) = \begin{cases} V(X,t), & \text{if } X \in X_{d|t}, \\ \langle V(X) \rangle, & \text{if } X \in X_{g|t}. \end{cases}$$
(3.8)

Here, $X_{d|t}$ and $X_{g|t}$ are the locations of valid and invalid points, respectively. The mean is subtracted before performing POD, so $\langle V(X) \rangle$ is 0. For the n^{th} main iteration, the gappy field $V_{n,0}$ is filled with an initial guess to obtain an approximate filled field $\overline{V}_{n,0}$. Therefore, for the subsequent main iterations, this guess is the output from the previous main iteration $\overline{V}_{n,0} = \hat{V}_{n-1}$.

2. This is the first *sub-iteration* step. POD with P_n modes is performed on the filled wind field $\overline{V}_{n,s}$ to obtain an approximation

$$\tilde{V}_{n,s}(X,t) = \sum_{j=1}^{P_n} Z_j(t)\phi_j(X).$$
(3.9)

This uses a modification proposed by Gunes et al. 2006 which is computationally efficient and provides similar accuracy as solving the minimisation problem required for the Eversen–Sirovich method [Raben et al. 2012; Saini et al. 2016].

3. The data gaps are then filled using the POD reconstruction:

$$\overline{V}_{n,s+1}(X,t) = \begin{cases} V(X,t) & \text{if } X \in X_{d|t}, \\ \tilde{V}_{n,s}(X,t), & \text{if } X \in X_{g|t}. \end{cases}$$
(3.10)

- 4. The iterative process is repeated, whereby steps 2 and 3 are performed by increasing s until the calculated eigenvalue spectrum in step 2 reaches a predefined convergence level.
- 5. This is the final *sub-iteration* step. The approximated wind field is stored as \hat{V}_n and then passed on to the next main iteration.
- 6. For the subsequent main iterations, the number of POD modes used for the reconstruction is increased until the main iterations converge.
- 7. The final velocity field is now assembled by summing up the mean wind field and the iteratively reconstructed fluctuating part.

3.2.3 Turbine-mounted lidars for inflow scanning

For efficient optimisation of turbine performance, an advanced turbine-mounted lidar should be capable of measuring the total area swept by the rotor very regularly to sufficiently resolve the spatio-temporal dynamics. While the spatial resolution of a lidar depends on the beam-scanning strategy employed, the temporal resolution of a lidar system is given by the underlying measurement technique, i.e., pulsed or continuous operation. Although large measurement distances are achievable through pulsed operation, the continuous type is advantageous for the presented applications due to their significantly higher sampling rates achieved through continuous scanning [Simley et al. 2018].

Any lidar system can only provide wind speed measurements along the beam direction (so-called line-of-sight (v_{los}) wind speed): usually referred to as the "cyclops dilemma" in the literature [Schlipf et al. 2011]. The line-of-sight wind speed v_{los} is expressed as a projection of the three wind speed components along the line-of-sight, as described by Equation (5.1):

$$v_{\text{los}} = \cos(\chi)\cos(\delta)u + \sin(\chi)\cos(\delta)v + \sin(\delta)w. \tag{3.11}$$

where χ and δ are the azimuth and elevation angles of the horizontal and vertical directions of the focused laser beam, respectively. The quantities u, v and w are the longitudinal, lateral and vertical wind components, respectively.

Another important property of continuous-wave lidar measurements is the probe length averaging effect. The line-of-sight measurements of the lidar are not collected at a single point in space, but are a weighted averages over a thin cylindrical volume along the beam approximated as a Lorentzian function [Sjöholm et al. 2009], as the laser beam cannot be perfectly focused at an infinitesimally small point in space. The line-of-sight speed measured by the lidar can be expressed following Mann et al. 2009 as:

$$v_{los}(\mathbf{x}) = \int_{-\infty}^{\infty} \frac{1}{\pi} \left(\frac{\Gamma}{s^2 + \Gamma^2} \right) \mathbf{n} \cdot \mathbf{u} (s\mathbf{n} + \mathbf{x}) ds$$
 (3.12)

where \mathbf{x} is the centre of the measurement volume; $\mathbf{u}(\mathbf{x})$ is the velocity field; and the unit vector in the emission direction of the laser beam is denoted as:

$$\mathbf{n} = [\cos(\chi)\cos(\delta), \sin(\chi)\cos(\delta), \sin(\delta)]^{\mathrm{T}}.$$
 (3.13)

3.2 Methods 57

The probe length is considered to be twice the half-width at half maximum, which is the distance from the focal point at which the backscatter spectrum is reduced to half its peak power and depends quadratically on the focal distance. The probe length depends on the laser wavelength λ and the effective radius of the lidar's telescope a, which are fixed parameters [van Dooren 2021]. Most of the laser signal is reflected near the focal distance, but contributions from the vicinity of the focal point also exist. This results in an attenuation of measured turbulence.



Figure 3.1: The SpinnerLidar with its mounting platform mounted on the nacelle of the research turbine CART3 at the National Renewable Energy Laboratory (NREL), Colorado, USA. Photo courtesy of Marijn Floris van Dooren.

The SpinnerLidar [Herges et al. 2017a; Mikkelsen et al. 2013] is one high-resolution lidar device that satisfies the requirement of fast scanning of the rotor area. This research-based prototype lidar can perform 2D measurements of the radial line-of-sight wind speed on a spherical surface with very high spatial and temporal resolution. The lidar consists of a modified ZephIR-300 continuous-wave Doppler lidar with a 2D scan head developed by the Technical University of Denmark (Figure 3.1). The scan head consists of two rotating prisms deviating the lidar's focused beam by an angle of 15° while rotating at a fixed ratio of 7 to 13. The resulting scanning pattern movement creates a fast rosette trajectory covering a large area with a quasi-homogeneous spatial resolution. The lidar can sample up to a maximum of 500 radial line-of-sight measurement points distributed over each completed scan trajectory (Figure 3.2). The lidar is capable of providing 2D wind field scans at a temporal sampling rate of 1 Hz with a variable focal distance from 10 to 150 m (albeit with a constant opening angle of 30°). The probe length is 0.13 or 28.3 m at f=10 m and f=150 m, respectively.

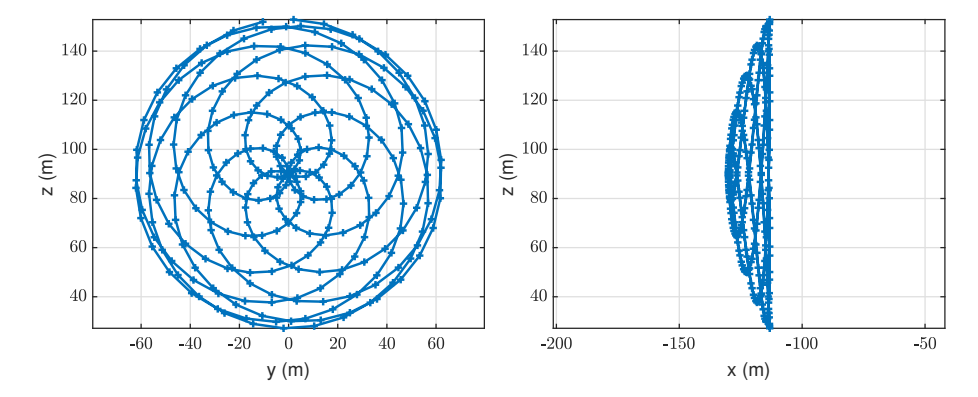


Figure 3.2: The rosette scanning pattern of the SpinnerLidar shown from two perpendicular perspectives.

3.2.4 Large-Eddy simulations (LES) and the lidar simulator (LiXim)

Wind turbines operate in the atmospheric boundary layer, which exhibits continuously varying flow characteristics. LES models can accurately resolve the turbulent kinetic energy in the atmosphere, making them suitable candidates for simulating realistic inflow conditions. Therefore, performing virtual lidar simulations inside the LES wind field provides a complete 3D reference wind field for comparison and quality assessment.

The LES data were obtained from simulations with the Parallelised Large Eddy Simulation Model (PALM) revision 3151. The PALM code is widely used for atmospheric boundary layer studies and works by solving the filtered, in-compressible, non-hydrostatic Navier–Stokes equations [Maronga et al. 2015]. PALM employs the Schumann volume averaging approach and uses central differences to discretize the non-hydrostatic and incompressible Boussinesq approximation of the 3D Navier–Stokes equations on a structured Cartesian grid. The simulations presented in this paper were performed using the PALM code in its default settings. The advection terms are solved by a fifth-order Wicker–Skamarock scheme. A third-order Runge–Kutta scheme is applied for the time integration. For cyclic horizontal boundary conditions, an FFT solver of the Poisson equation is used to ensure incompressibility. To model the effects of sub-grid scale turbulence on the resolved scale turbulence, a 1.5th order closure is employed [Deardorff 1980]. Monin–Obhukov similarity theory is used to obtain the turbulent fluxes between the surface and the first computational point on the model domain.

The turbine aeroelastic simulation was performed using the Fatigue, Aerodynamics, Structures and Turbulence code (FAST) v8, developed by the National Renewable Energy Laboratory (NREL) [Jonkman et al. 2005]. The code simulates the wind turbine as a combination of rigid and flexible bodies, and the aerodynamic forces are calculated via the AeroDyn module. Both PALM and FAST run simultaneously in an explicit loose two-way coupling [Krüger et al. 2022. The velocities from the LES field are transferred to FAST, which subsequently calculates the lift and drag on the blade segments based on look-up tables of the airfoil characteristics. Next, the relative velocities of the blades and their new positions are determined. This information is transferred back to PALM, where the forces are distributed back into the flow field, where the induction zone and the wake are generated, as visualised

in Figure 3.3b.

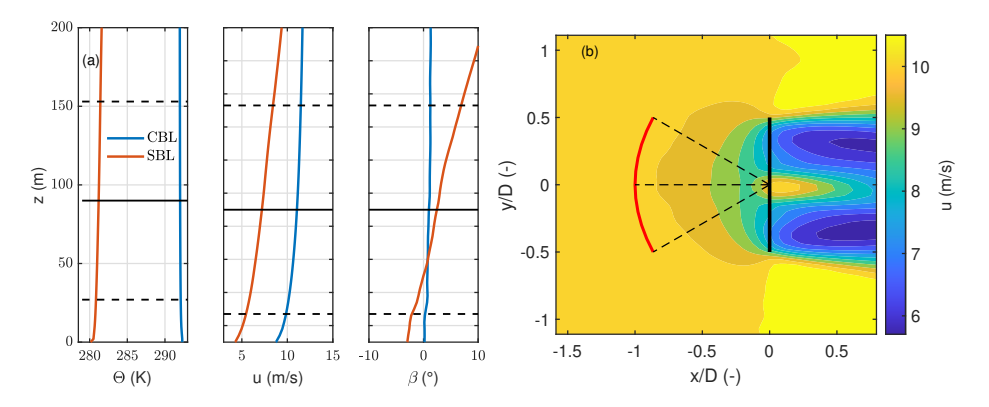


Figure 3.3: (a) Vertical profiles of the potential temperature, wind speed and wind veer at the end of the precursor run and (b) the averaged *u*-component at hub height extracted from the unstable LES wind field for the main run. The black vertical line indicates the position and size of the turbine rotor, and the red curve is the SpinnerLidar's measurement trajectory.

Two turbulent atmospheric boundary layers (ABL) of unstable and stable stratification, respectively, with a single turbine, were simulated using this framework. The wind turbine model was the actuator line implementation of the NREL 5 MW reference turbine [Jonkman et al. 2009b] with a rotor diameter of 126 m, a hub height of 90 m and 63 blade sections. To obtain a convective boundary layer (CBL), we performed a pre-run of 25 h to allow the boundary layer to develop and reach stationary flow. A roughness length $z_0 = 0.0175$ m was specified with a friction velocity $u_* = 0.52$ m/s, and the kinematic sensible heat flux at the surface was fixed at 0.023 K ms⁻¹. The surface potential temperature was 290 K. The instantaneous fields of the precursor simulation were mapped onto the main simulation via turbulence recycling Lund et al. 1998, where the turbine was introduced into the wind field. For simulating stable atmospheric conditions (SBL), a pre-run of 25 h was carried out, where the lowest grid cells were constantly cooled at a rate of 0.25 K/h. A roughness length of $z_0 = 0.1$ m was specified, and a temperature gradient of 1 K/100 m was specified. Similarly to the CBL case, the turbine was introduced in the main run, where the precursor simulation was mapped onto the main simulation. Important details of the precursor and the main run are summarised in Table 3.1. The dimensions of the simulation domain $L_{\rm x}, L_{\rm y}$ and $L_{\rm z}$ were normalised with the rotor diameter of the NREL 5 MW turbine. The mean longitudinal wind speed and turbulence intensity were defined as u_{hub} and TI_{hub}, respectively. The wind veer β was calculated between the top and bottom rotor tips, and α was the vertical shear exponent. z_0 was the roughness length, and the stability was characterised by the Obhukov length L.

Table 3.1: Setup of the two LES simulations and the results at the end of the precursor run.

Case	$L_x, L_y, L_z(D)$	u_{hub} (m/s)	TI_{hub} (%)	$\beta(-)$	α (-)	z_0 (m)	<i>L</i> (m)
CBL	$64.9 \times 32.4 \times 16.2$	10.1	11.9	0.8	0.09	0.0175	-452
SBL	$22.8\times7.6\times3.8$	7.2	7.5	9.3	0.23	0.1	114.3

To extract the SpinnerLidar measurements from the two LES wind fields, we used the integrated lidar simulation toolbox LiXim [Trabucchi 2020]. The SpinnerLidar was simulated in the LES using the LiXim simulator measuring at a focal distance of 126 m (1D) with a temporal resolution of 1 Hz for a total duration of 3700 s. The lidar simulator emulates the lidar measurements inside the LES wind field while considering the volume averaging effect and producing 312 measurement points distributed along the rosette scan pattern. The lidar simulator freezes the wind field for every measurement point and performs linear interpolation to obtain the projection in the direction of the laser beam. From the lidar properties and the focus distance, the length of the measurement volume is defined. The wind field is then interpolated over this volume, and the wind velocities along the line-of-sight are weighted based on the Lorentzian function. The lidar spatial averaging is described as a Lorentzian function for continuous-wave lidars [Sjöholm et al. 2009]. The effective probe length in terms of the FWHM of the SpinnerLidar when focused at a measurement range of 126 m (1D) is approximately 19 m. The simulated lidar device was assumed to have a horizontal orientation, and the rotor tilt was not considered. The measurements are then interpolated onto a uniform grid with a 3 m spacing resulting in 1261 grid points.

3.3 RESULTS

The performances of the POD-based reduced-order reconstructions were tested for virtual scanning lidar in the LES data. The simulations were used as a benchmark for comparing and quantifying the accuracy of the inflow based on various reconstruction metrics, such as the energy distributions, velocity field reconstruction, wind field parameterisation and turbulent spectra in the fixed and rotational frames of reference. Finally, the ability of the Gappy-POD method to reconstruct artificially removed measurement points was investigated for a range of data availabilities.

3.3.1 APPLICATION OF THE POD METHODOLOGY TO SCANNING LIDAR MEASUREMENTS

The eigenvalues and eigenvectors associated with the covariance matrix for the line-of-sight velocity fields of the two simulations were calculated based on Equation (3.3). The normalised magnitudes of the eigenvalues λ_j and the fraction of energy associated with each mode of the v_{los} measurements are shown in Figure 3.4. As expected, the eigenvalue magnitudes of the CBL modes contain more energy in general compared to the SBL modes due to the higher turbulence in the CBL. For the unstable case, the first POD mode contains 57.7% of the total measured energy; and the second, third, and fourth modes contribute 17.3%, 11.8% and 4.3%. For the stable case, the energy contributions of the first modes are 48.01%, 12.91%, 6.07% and 5.38%, respectively. It is clear from Figure 3.4b that the first ten modes contribute 96.6% and 87.7% of the measured turbulent kinetic energy (TKE); and the first 100 modes account for 99.95% and 99.99% for the CBL and SBL cases, respectively. Note that the total TKE measured by the lidar is not equivalent to that in the wind field due to volume averaging induced turbulence attenuation of the line-of-sight measurements.

²The lidar measured TKE is defined as the turbulent kinetic energy related only to the lidar measured line-of-sight velocities rather than the commonly used definition of the TKE for the whole 3D wind field.

3.3 Results 61

This may be surprising since, in a turbulent flow, energy is distributed over the different scales and its representation might usually require a large number of modes [Bauweraerts and Meyers 2020]. However, a lidar system acts as a low-pass filter for small scale turbulence due to its volume averaging property. Hence, the small scale turbulence is filtered out, and an accurate representation of the remaining lidar measured total TKE can be recovered with very few modes.

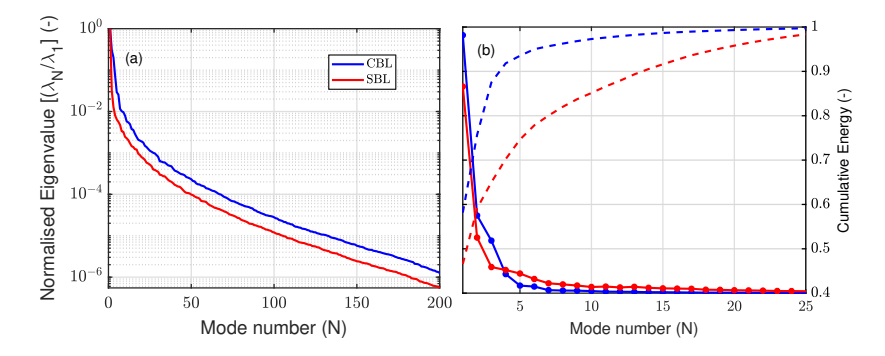


Figure 3.4: Eigen value distributions (a) and the energy contribution of each mode (b) for the unstable and stable cases.

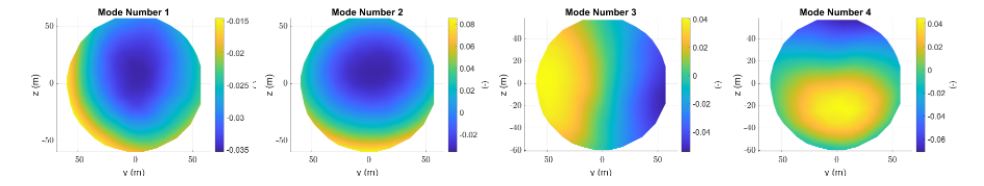


Figure 3.5: POD modes 1 to 4 of the line-of-sight (v_{los}) measurements for the CBL case.

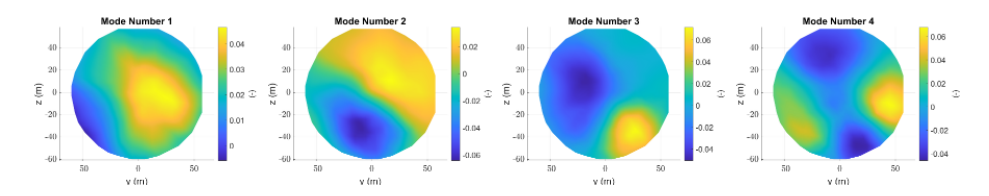


Figure 3.6: POD modes 1 to 4 of the line-of-sight ($v_{
m los}$) measurements for the SBL case.

The first four POD modes $\phi_j(X)$ for the CBL and SBL cases are illustrated in Figures 3.5 and 3.6, where well defined modes for both cases were obtained. For both cases, the modes exhibit clear structures that trend towards smaller scales with increasing mode number as the modes are sorted based on the energy content, and the kinetic energy decreases with scale. For the CBL case, modes 1 and 2 have similar mode shapes with different gradients, resulting from the variation in the line-of-sight velocities decreasing toward the edges of the scan pattern. The first two modes do not exhibit clear symmetry around the rotor axis

due to the slight wind shear present in the ABL. Modes 3 and 4 display variations in the horizontal and vertical directions, respectively. For the SBL case, the first mode shows a strong spatially localised shape related to the line-of-sight velocity distribution, and the second mode resembles a large gradient in the vertical direction, probably due to the strong vertical shear. The third mode displays variations in the horizontal direction, and the fourth mode shows a slightly more complex distribution. The asymmetry of the SBL modes could be explained by the larger surface roughness of the simulation ($z_0 = 0.1$ m) leading to a large effect of the ground on the inflow. Comparatively, the CBL was generated with less surface roughness ($z_0 = 0.0175$ m), thereby preserving weak statistical isotropy commonly observed in turbulent flows. As expected, the higher mode patterns became increasingly complex compared with the first few modes.

3.3.2 RECONSTRUCTION OF THE REDUCED VELOCITY FIELD

The extracted POD modes were used to reconstruct the velocity field based on Equation (3.6) by choosing increasing values of M (the number of modes used for reconstruction).

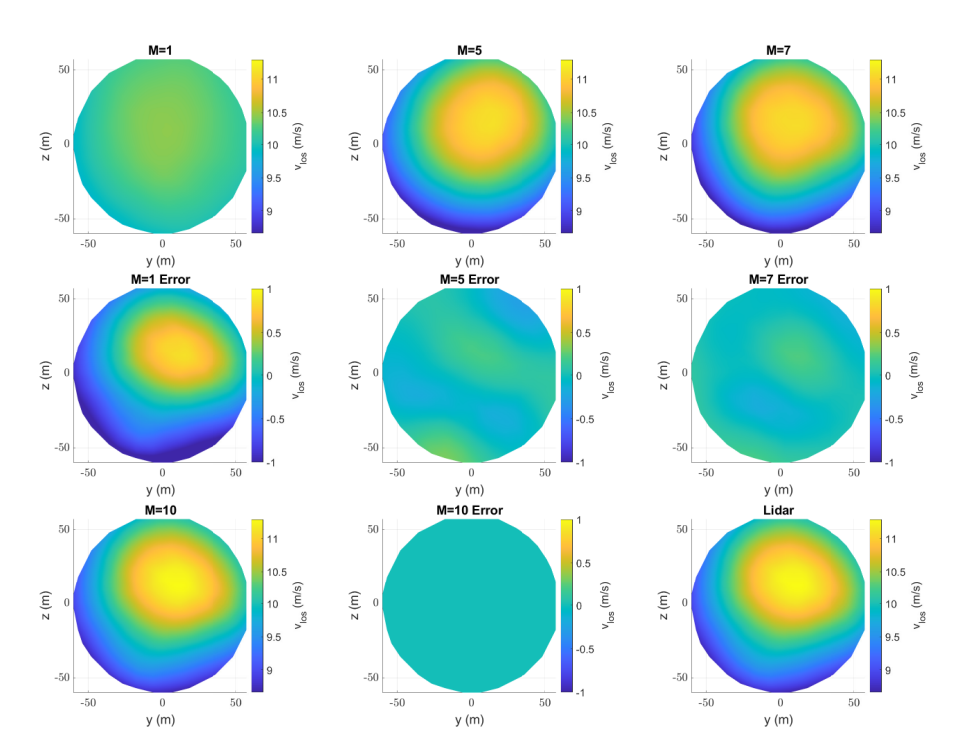


Figure 3.7: CBL case: Reconstruction of the line-of-sight (v_{los}) velocity snapshot at an arbitrary time instant t = 256 s with different numbers of modes (M = 1, 5, 7 and 10) and their corresponding errors with respect to full lidar measurements (bottom right-hand plot captioned as lidar).

A snapshot of the velocity field at an arbitrary time t = 256 s of the CBL inflow case was reconstructed and illustrated in Figure 3.7 for a different number of modes, along

3.3 Results 63

with its corresponding planar velocity reconstruction error in comparison to full lidar measurements. A more detailed wind field reconstruction was achieved while considering more modes for the reconstruction. For the reconstruction with M=1 (first mode alone), only the spatial variations in the line-of-sight measurements were obtained, as indicated by a constant velocity distribution over the whole measurement plane, which is also supported by the M=1 error plot with respect to the full lidar measurements. The addition of more modes into Equation (3.6) adds more localised wind field information, as the smaller wind field fluctuations which are contributed by the higher modes are taken into account. The velocity field reconstruction with ten modes shows close agreement with the untruncated full lidar measurements; reconstruction error is effectively reduced to almost zero throughout the measurement plane. The high recovery of kinetic energy in the first few modes, as discussed in Section 3.3.1, indicates that only a few modes are required to create a meaningful reduced-order model capturing all spatial variations in the wind field. For brevity, we only show the results of the CBL case, as the SBL also exhibited the same behaviour: the addition of more modes improving the spatial velocity reconstruction.

3.3.3 RECONSTRUCTION EVALUATION USING THE THREE-PARAMETER WIND FIELD MODEL

The main objective of any inflow sensing lidar is to capture the inflow, along with its variations that significantly impact the wind turbine. Thus, the quality of reconstruction should be evaluated with respect to wind field parameters that directly affect the turbine itself. For example, parameters such as the rotor effective longitudinal wind speed $u_{\rm eff}$, horizontal misalignment δ_h and vertical shear s_v are necessary to implement a standard individual pitch controller. The rotor effective wind speed quantity $u_{\rm eff}$ is related directly to the turbine's dynamic response and power output. This is the primary variable for selecting the operational condition of the turbine and input for collective pitch control. The horizontal misalignment δ_h and vertical shear s_v are essential for for determining the turbine's yaw setting and individual pitch control algorithms, whereby the controller compensates for asymmetric loading by pitching the blades individually. To extract the wind field parameters from the scanning lidar line-of-sight measurements, we used the threeparameter methodology from Kapp. S 2017. While the three-parameter methodology can be directly applied to the lidar data to obtain the relevant wind parameters, we calculated them from the reconstructed velocity fields to assess the reconstructed wind field's accuracy and provide a physical interpretation for the modes.

The three-parameter method proposes a parameterisation of the inflow wind field using three parameters to achieve the smallest possible deviation from the actual inflow field. At every *i*th measurement point, the lidar measures the line-of-sight speed $v_{los}(y_i, z_i)$ as a projection of the 3D wind components, following Equation (5.1). The measured line-of-sight speeds $v_{los}(y_i, z_i)$ in the spherical SpinnerLidar measurement plane could be fitted as a set of three parameters that is constant over the whole plane as:

$$\hat{v}_{los}(y_i, z_i) = (u_{eff} + s_v z_i) \begin{bmatrix} \cos(\delta_h) \\ \sin(\delta_h) \\ 0 \end{bmatrix} \cdot \boldsymbol{n}. \tag{3.14}$$

whereas n is the unit vector of the laser beam at point i, and y_i and z_i are the Cartesian coordinates of the point in the scanning plane. Grouping every point in the measurement plane results in a set of equations for every measurement point that could be solved in a least-square sense to determine the unknown parameters $Y = (u_{\text{eff}}, \delta_h, s_v)^T$:

$$\min_{\mathbf{Y}} \left(\sum_{i=1}^{N} \left(v_{\text{los}}(y_i, z_i) - \hat{v}_{\text{los}}(y_i, z_i) \right)^2 \right). \tag{3.15}$$

TIME SERIES RECONSTRUCTION OF THE THREE-PARAMETER MODEL

To quantify the reconstruction accuracy, inflow wind field parameters were extracted from the line-of-sight velocity distribution defined in Section 3.3.3. The results of the extracted wind field parameters from different reconstructions are compared with each other and with the full lidar measurements for the CBL and the SBL inflow cases. The three-parameter wind field model was applied to the SpinnerLidar simulations, which will henceforth be referred to as direct determination. Various reconstructions were created by truncation with M=1,2,3,5 and 10 modes, and the associated wind field parameters ($u_{\rm eff}$, $\delta_{\rm h}$ and $s_{\rm v}$) were calculated and compared with direct determination. For all the cases and parameters, there were negligible differences between the reconstructions with M=5 and M=10, and hence, only the reconstruction with M=5 is shown for brevity.

Figure 3.8 contains part of the time series of the three wind field parameters for different reconstructions with M = 1, 2, 3, 5 and 10 for the CBL and SBL cases, respectively. For the rotor effective wind speed u_{eff}, the time series of the different reconstructions overlap with each other well, even for reconstructions with few modes for the CBL and the SBL cases. The dynamic aspects of the rotor effective velocities calculated with different mode numbers are similar, there being only small variations between the reconstructions with M = 1 and M = 10 modes. The low-frequency characteristics of the u_{eff} time series were reproduced with reasonable accuracy with just one mode. The addition of more modes to the reconstruction introduced a few high-frequency variations to the time series. However, this was not the case for vertical shear or yaw misalignment. The reconstruction of s_v with one mode for the CBL case showed an average value of zero, whereas for the SBL case a value of 0.025 s⁻¹ was obtained, indicating that the first mode contained some vertical shear information. With the addition of the second and third modes to the reconstruction, we observed that the dynamics of the vertical shear were captured, albeit a little overpredicted for the CBL case. The horizontal misalignment reconstruction for CBL and SBL showed very similar behaviour. With the first mode alone, the basic dynamics of the time series were not captured. The addition of more modes to the reconstruction improved the estimation of both s_v and δ_h . For M=5 or higher, good agreement between the direct determination and the truncated reconstructions was obtained for all three parameters for both cases.

3.3 Results 65

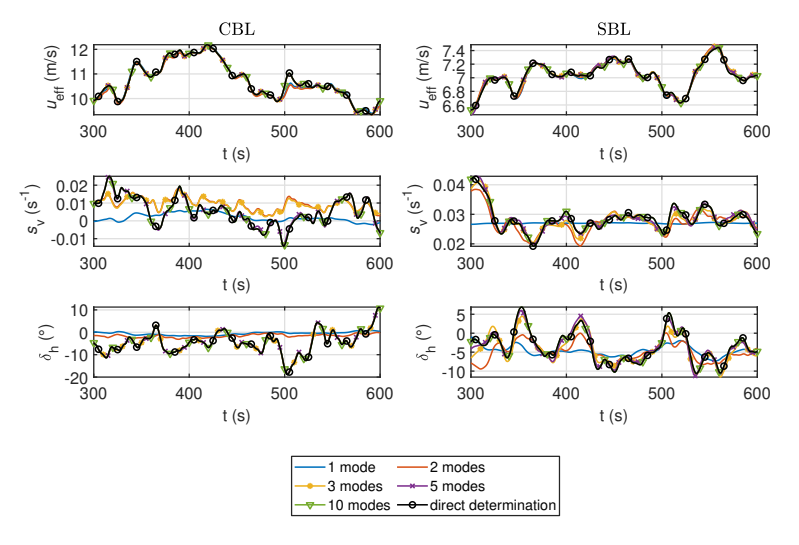


Figure 3.8: The time series of the wind field parameters $u_{\rm eff}$, $s_{\rm v}$ and $\delta_{\rm h}$ extracted at a sampling rate of 1 Hz for a duration of 300 seconds for different POD reconstructions for the CBL and SBL cases.

Accuracy of the three-parameter wind field reconstruction and an interpretation of the POD modes

To quantify the reconstruction error associated with these wind field parameters, we write

$$\mathbf{Y}(t) = \hat{\mathbf{Y}}\left(v_{\text{los}}(\mathbf{X}, t)\right),\tag{3.16}$$

where $\mathbf{Y}(t) = [u_{\rm eff}, \delta_{\rm h}, s_{\rm v}]^T$ is the set of rotor-averaged wind field parameters calculated by applying a three-parameter methodology $\hat{\mathbf{Y}}$ to the line-of-sight velocities. Similarly, the wind field parameters determined from the reduced-order reconstruction with M modes can be represented as:

$$\mathbf{Y}^{M}(t) = \hat{\mathbf{Y}}[v_{\text{los}}^{M}(\mathbf{X}, t)].$$
 (3.17)

The quality of the reconstructed wind field $v_{los}^M(X,t)$ and the corresponding wind field parameter $\mathbf{Y}^M(t)$ with M modes can be assessed by comparison to the original wind field parameters $\mathbf{Y}(t)$. To evaluate the reconstruction efficiency, two different error parameters are introduced. The errors associated with the reconstruction of the ith wind field parameter \mathbf{Y}_i are defined as:

$$\epsilon_{\text{std}}^{M}(\mathbf{Y}_{i}) = \sqrt{\left(\frac{\langle \mathbf{Y}_{i}^{M}(t)\rangle - \langle \mathbf{Y}_{i}(t)\rangle}{\max_{t}(\mathbf{Y}_{i}(t)) - \min_{t}(\mathbf{Y}_{i}(t))}\right)^{2}}$$
(3.18)

$$\epsilon_{\text{dyn}}^{M}(\mathbf{Y}_{i}) = \sqrt{\frac{\sqrt{\frac{\sum_{t=1}^{n_{s}}(\mathbf{Y}^{M}(t) - \langle \mathbf{Y}^{M}(t) \rangle)^{2}}{n_{s}}}}{\max_{t}(\mathbf{Y}_{i}^{M}(t)) - \min_{t}(\mathbf{Y}_{i}^{M}(t))} - \frac{\sqrt{\frac{\sum_{t=1}^{n_{s}}(\mathbf{Y}(t) - \langle \mathbf{Y}(t) \rangle)^{2}}{n_{s}}}}{\max_{t}(\mathbf{Y}_{i}(t)) - \min_{t}(\mathbf{Y}_{i}(t))}}^{2}}$$
(3.19)

where $\epsilon_{\rm std}$ and $\epsilon_{\rm dyn}$ represent the standard and dynamic error, respectively. These values quantify the respective mean error and the error associated with the fluctuations in the

wind field. The definition of the dynamic error was motivated by the fluctuation of wind field parameters having the largest effect on the loading and the fatigue of the turbine in contrast to the mean wind field parameters. To investigate the relationship between the POD temporal gains $Z_j(t)$ and the wind field parameter time series, the Pearson correlation coefficient ρ is used.

The standard and dynamic errors $\epsilon_{\rm std}$ and $\epsilon_{\rm dyn}$ were used to quantify the reconstruction quality for the CBL and SBL cases, as depicted in Figure 3.9a,b. The standard and dynamic errors exhibited similar trends for the CBL and SBL inflow cases. The standard error of reconstructed rotor effective wind speed $u_{\rm eff}$ remained less than 0.016 and 0.005 for the CBL and SBL cases for the reconstruction based on the first mode, indicating the first mode is highly correlated with the rotor averaged wind speed. For both cases, the standard reconstruction errors with one mode for s_v and δ_h were comparatively large but dropped when more modes were used. The standard errors for all the three wind field parameters decreased below 0.001 when considering the first five modes for the reconstruction. The standard error exhibited discontinuous behaviour for certain wind field parameters when certain modes were considered. The steep fall in the standard error magnitude with the addition of certain modes indicates that these modes are strongly correlated with these wind field parameters. The dynamic error for $u_{\rm eff}$ dropped below 0.002 for both cases when at least the first three modes were considered for the reconstruction. For both cases, the dynamic error of the three-parameter reconstruction also reduced below 0.001 while considering the first ten modes for reconstruction. Similar discontinuous behaviour was observed while considering specific modes. The discontinuous behaviour shown by the standard and dynamic errors occurring at identical mode numbers indicates a relationship between the particular mode and the corresponding wind field parameter.

3.3 Results 67

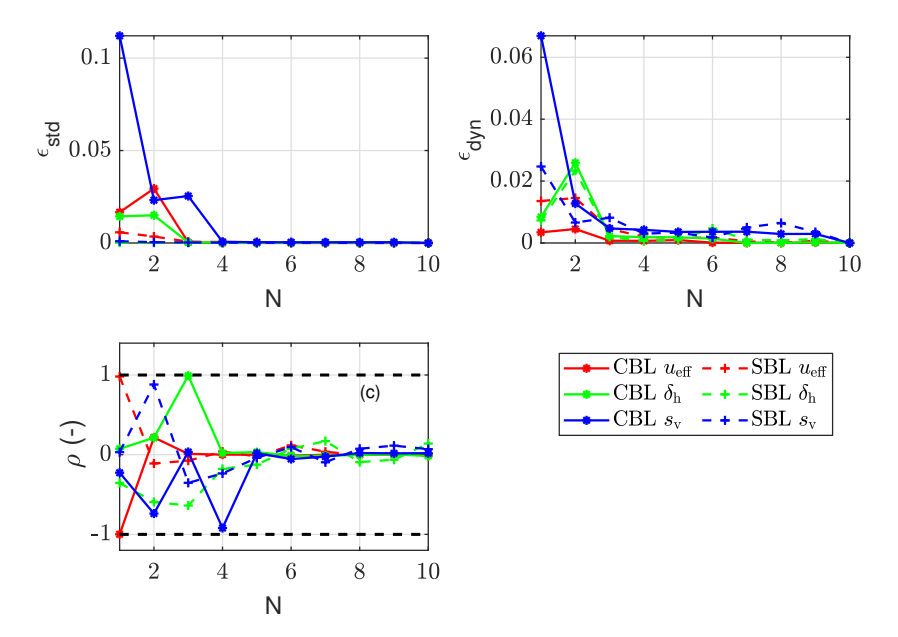


Figure 3.9: The standard ($\epsilon_{\rm std}$) and dynamic ($\epsilon_{\rm dyn}$) errors of the three-parameters calculated for reconstructions with various numbers of modes; correlations (ρ) between the time series of the reconstructed three-parameter wind field parameters; and the time evolution of the different POD modes $Z_{\rm i}(t)$.

The huge reductions in the standard and dynamic errors can be explained by the plots of correlation between the time series of the POD time coefficients $Z_i(t)$ and the wind field parameters Y(t), as visualised in Figure 3.9c. Confirming the hypothesis for the CBL case based on the time series reconstruction of the rotor effective velocity (Figure 3.8), the first mode is highly anti-correlated with spatial fluctuations in the wind field with $\rho(Z_1, u_{\text{eff}}) = -0.99$. The yaw misalignment (δ_h) is related to the third mode with $\rho(Z_3, \delta_h) = 0.99$. The vertical shear (s_v) is related to the second and the fourth modes $\rho(Z_2, s_v) = -0.72$ and $\rho(Z_4, s_v) = -0.91$. The argument of the relationship between the wind field parameters and the modes is also strengthened by the shapes of the POD modes (Figure 3.5): the third and fourth modes exhibit horizontal and vertical structures, whereas the first mode resembles the v_{los} variations. Similar arguments could be made for the SBL case, as the first mode is highly correlated with the spatial fluctuations in the effective wind speed: $\rho(Z_1, u_{\text{eff}}) = 0.98$. The vertical shear is highly correlated with the second mode, $\rho(Z_2, s_v) = 0.88$, and weakly anti-correlated with the fourth mode, $\rho(Z_4, s_v) = -0.36$. The yaw misalignment has the highest correlation with the third mode, $\rho(Z_3, \delta_h) = -0.63$, and also exhibits correlations with the first ($\rho(Z_1, \delta_h) = -0.36$) and second modes ($\rho(Z_2, \delta_h) = -0.59$). The second POD mode in Figure 3.6 exhibits a vertical distribution, and the third POD mode shows a horizontal distribution, further strengthening the argument that the POD modes are related to the properties of the inflow itself.

3.3.4 RECONSTRUCTION EVALUATION IN THE FREQUENCY DOMAIN

The dynamic loading induced on the turbine blades is determined by the wind fluctuations impinging on the blades and how quickly they rotate. As the blades move through the turbulent wind field, they perform a so-called "rotational sampling" of the turbulent structures, which differs from the velocities observed at a stationary point [Kristensen and Frandsen 1982]. To investigate this effect, we calculated the auto-spectral density of the longitudinal wind speed of the reduced-order reconstruction for the stationary hub centre and rotating reference frames for a radial position of 90% on the first blade only for the CBL case. The reconstructed spectra are evaluated with respect to the turbulent spectra directly determined by the lidar measurements and the reference LES (Figure 3.10).

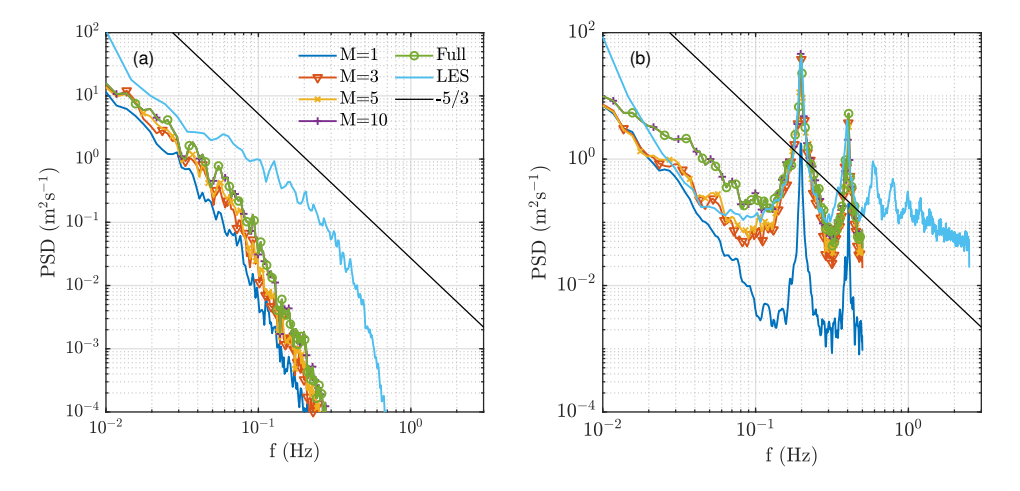


Figure 3.10: (a) Fixed point spectra of the $v_{\rm los}$ velocity on the rotor axis at an upstream measurement distance of 126 m with M=1,3,5 and 10 modes. (b) Rotational spectra of the $u_{\rm projected}$ velocities of the reduced-order reconstruction with M=1,3,5 and 10 modes. The results are shown only for the CBL case.

The spectra were calculated via Welch's modified periodogram method with a Hanning window, 300 s data segments and a 50% overlap between segments. For the hub centre point visualised in Figure 3.10a, the spectra of the different reconstructions exhibit very similar behaviour. LES in the figure refers to the spectrum calculated from the reference wind field sampled at 5 Hz, and the Kolmogorov slope is illustrated as a black line. The spectrum directly determined from the full lidar measurements is illustrated by the green line. The lidar measurements for all cases show a drop-off from the -5/3 Kolmogorov slope at 0.03 Hz, evident of the low-pass filtering effect of the lidar. The reconstructed spectrum with the first mode underpredicts the energy content by one order of magnitude, and the addition of more modes moves the spectrum upwards toward the full lidar measurements. The reconstructed spectra with ten modes and the full lidar measurements show no differences, indicating that with the first ten modes, almost all energy is recovered in comparison to the full lidar measurements.

However, completely different behaviour is observed when examining the rotationally sampled spectra of the projected longitudinal wind speed at an upstream measurement distance of 126 m sampled at 90% of the outer blade radius moving at 11.88 rpm, as

3.3 Results

shown in Figure 3.10b. The rotational spectra is calculated from the $u_{\text{projected}}$ velocities (by setting v = w = 0 in Equation (5.1), leading to $u_{\text{projected}} = v_{\text{los}}/(\cos(\chi)\cos(\delta))$. The light blue line shows the spectrum of the reference LES simulations sampled at 5 Hz. The 1P frequency (0.198 Hz) and the next five peaks of the higher harmonics are clearly visible. The reconstruction with M = 1 underpredicts and cannot capture the magnitude of the 1P and 2P peak, as the first mode only reconstructs the relatively weak radial asymmetry of the wind speeds over the wind field. With the addition of the second and third modes, the magnitudes of the 1P and 2P peaks are accurately reconstructed; adding more modes leads to marginally better predictions of these rotational harmonics. The higher harmonics seen in the rotational spectrum of the LES curve are not captured by the lidar due to the limited 1 Hz sampling rate yielding a corresponding Nyquist frequency of 0.5 Hz. The superior reconstructions in the rotational spectra in comparison to the fixed point spectra, even for $M \ge 3$ modes, can be attributed to the high spatial coverage of the lidar. Moreover, the fact that the dominating POD modes have clear relationships with the wind speed changes in the horizontal and vertical directions allows for better calculation of the rotational spectrum compared to the fixed frame. Note that the lidar measures more energy than the LES field at lower frequencies due to cross-contamination of the lateral and vertical components contributing to increased variance in the line-of-sight velocity.

3.3.5 Gappy-POD reconstruction of missing data points

Here, we present the results of using the Gappy-POD algorithm to reconstruct missing data points. We define total data availability over the entire dataset as the percentage of the average available wind field view allowed by the rotor. Gappiness is defined as:

$$G = 1 - \frac{|X_{d|t}|}{|X_{d|t} \cup X_{g|t}|} \tag{3.20}$$

where |.| denotes cardinality. The removal of points was based on defining a set of uniformly distributed pseudo-random integers consistent with the total number of measurement points using the Mersenne–Twister algorithm [Matsumoto and Nishimura 1998]. Different gappiness scenarios were created by randomly removing 10%, 20%, 30%, 40% and 50% of the data points from the CBL and SBL cases. Gappy-POD was applied to the gappy datasets, and the ability of the method to reconstruct missing points was evaluated. While removing measurement points, it was made sure that there were no data points with no data and no snapshot that was missing all measurements. Determining the convergence, i.e., the termination point of the iterative process, is necessary to achieve high accuracy. For this purpose, a convergence criterion based on the root mean square error (RMSE) was utilised only at the locations of the missing points; i.e., valid data points were ignored.

$$RMSE = \sqrt{\frac{\sum_{k=1}^{n_{g,t}} (v_{los,gappy,k} - v_{los,ref,k})^2}{n_{g,t}}}$$
(3.21)

where $v_{\rm los,gappy}$ represents the reconstructed data, $v_{\rm los,ref}$ represents the reference data with 100% availability and $n_{\rm g,t} = |X_{\rm g|t}|$ is the number of missing points. The sub-iteration convergence was investigated by inspecting the absolute normalised difference between the eigenvalue spectra between consecutive iterations. In this work, the value was chosen

as 0.05. If the convergence criteria was not satisfied, the guess for the missing data was updated using Equation (3.10) and the next sub-iteration was started. The variations in RMSE with the number of main iterations and for different gappiness G are plotted in Figure 3.11 for the CBL and SBL cases. The RMSE was normalised by the hub height wind speed to facilitate comparison between the two cases.

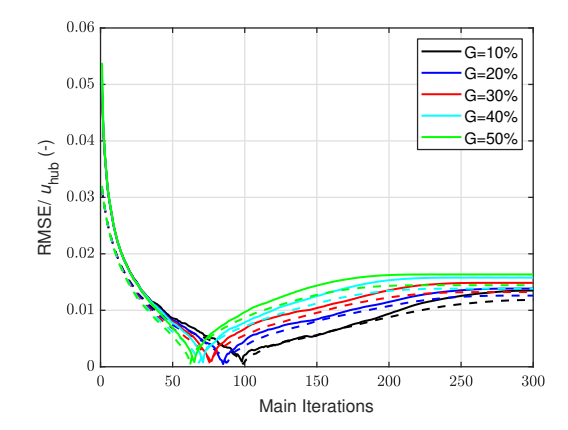


Figure 3.11: RMSE normalised with the hub height wind speed u_{hub} as a function of main iterations for the CBL case (solid lines) and the SBL case (dotted lines) for different gappiness percentages.

For all the cases, the normalised RMSE initially decreases, reaches a minimum and starts increasing again, a result of over-fitting. For both cases and all gappiness, the number of main iterations required to reach the minimum RMSE varies, but the optimum is found below 100 iterations. In general, the RMSE drops below 0.01 after 50 iterations for both cases and all availabilities. The SBL case converges slightly earlier and shows slightly reduced RMSE compared to the CBL case, presumably due to the lower turbulence. The motivation for performing the iterative implementation was that the optimum number of iterations for minimum RMSE was unknown. However, if the optimum number is known, the nested-loop algorithm can be modified by just repeating the sub-iterations alone (steps 2 to 4) in Section 3.2.2, drastically decreasing the required solution time. In the following, we also present the results of the henceforth named "direct Gappy" method, wherein the gappy procedure is performed by using the optimum number of modes obtained from Figure 3.11.

Figure 3.12a shows the optimum normalised RMSE of the three methods as functions of G. Here, natural interpolation refers to the C1 continuous triangulation-based natural neighbour interpolation method. As expected, both the direct and iterative gappy methods performed better than natural interpolation; a slight increase in RMSE was noticed with increasing G. The normalised RMSE of the natural interpolation on the CBL case ranged from 0.019 to 0.023; and the normalised RMSE ranged from 0.0008 to 0.0009 and 0.005 to 0.011 for the iterative and direct gappy implementations, respectively. For G = 30%, commonly observed in full-field measurements, the iterative and direct gappy procedures performed substantially better than spatial interpolation in reconstructing the missing points. In Figure 3.12b, the time required for the three methods is shown for reconstructing

3.3 Results 71

the whole dataset. The spatial interpolation method is the most robust, given solution times of less than 10 s; the solution time for the iterative solver increased with increasing G.

The computations were performed based on an un-optimised MATLAB code on a laptop running an Intel i7-4610M processor @ 3 GHz and 16 GB RAM. The iterative gappy solution requires the most processing time due to the time consuming nested loop implementation, whereas the direct gappy procedure is faster by 6 to 14 times depending on the availability. The reduced solution time for the direct gappy procedure is because only sub-iterations need to be performed until eigenvalue convergence, as the optimum number of modes is known.

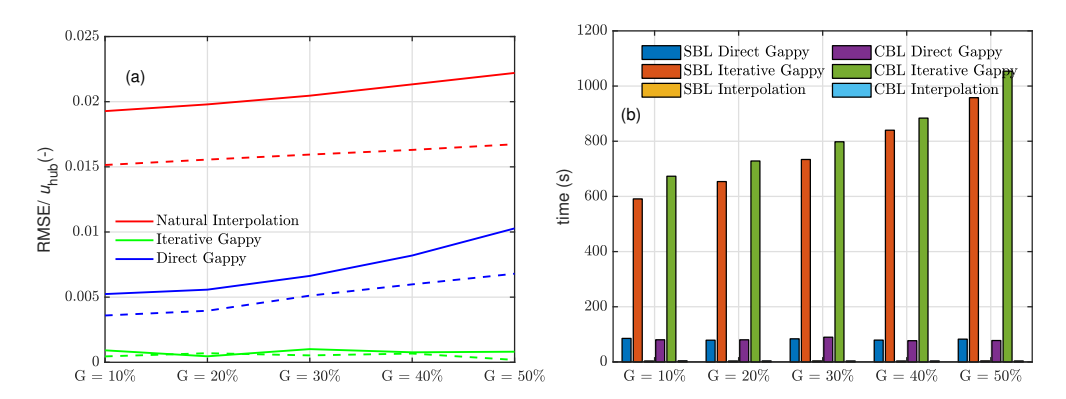


Figure 3.12: (a) Error comparison for the three methods. Solid and dotted lines indicate the CBL and SBL cases, respectively. (b) Comparison of the computational time taken for the three methods to reconstruct missing points.

RECONSTRUCTION OF SPATIAL WIND FIELD PARAMETERS

To quantify the accuracy of the reconstructed points, we calculated the wind field parameters (Section 3.3.3) from the filled wind field for the three methods and compared them against the reference dataset with 100% availability. As the reconstruction of the rotor effective wind speed is trivial for scanning lidars with high spatial resolution, we introduce a spatial turbulence intensity parameter to evaluate the reconstruction. The spatial TI is defined as:

$$TI_{Spatial}(t) = \frac{\sigma(v_{los}(X, t))}{\langle v_{los}(X, t) \rangle}$$
(3.22)

where $\sigma(v_{los})$ and $\langle v_{los} \rangle$ are the spatial standard deviation and the mean of the line-of-sight velocities calculated for each snapshot, respectively. The results of the reconstruction are plotted for the CBL case in Figure 3.13 and the SBL case in Figure 3.14.

For both cases, similar behaviour for the iterative and direct Gappy-POD methods can be observed: both methods perfectly reconstructed the wind parameters s_v and δ_h . Spatial interpolation of missing points led to very similar but slightly lower performance for s_v and δ_h in comparison to the two Gappy-POD methods. This was expected, as the vertical shear and directional misalignment's were averaged over the entire measurement plane, and hence small spatial fluctuations are averaged out. The reconstruction was comparatively poorer for the SBL case: the regression line is characterised by a larger slope in comparison

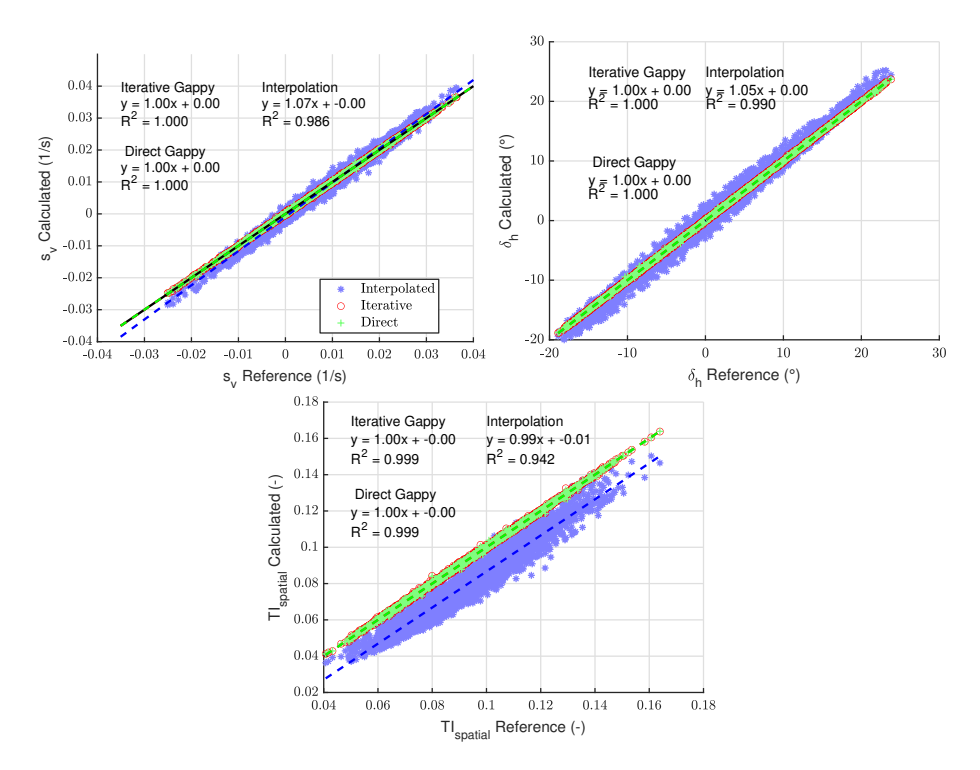


Figure 3.13: Comparison of s_v , δ_h and $TI_{Spatial}$ calculated from the reconstructed data for the CBL case with G=30%.

to the reference. However, the spatial TI estimated by interpolation has more scatter and offset in comparison to the reference: $R^2 = 0.942$ and 0.934, respectively, for the CBL and SBL cases. The estimated spatial TI of the two gappy methods agree better with the reference. There was almost no difference between the two methods ($R^2 \ge 0.99$ for both cases).

3.4 Discussion 73

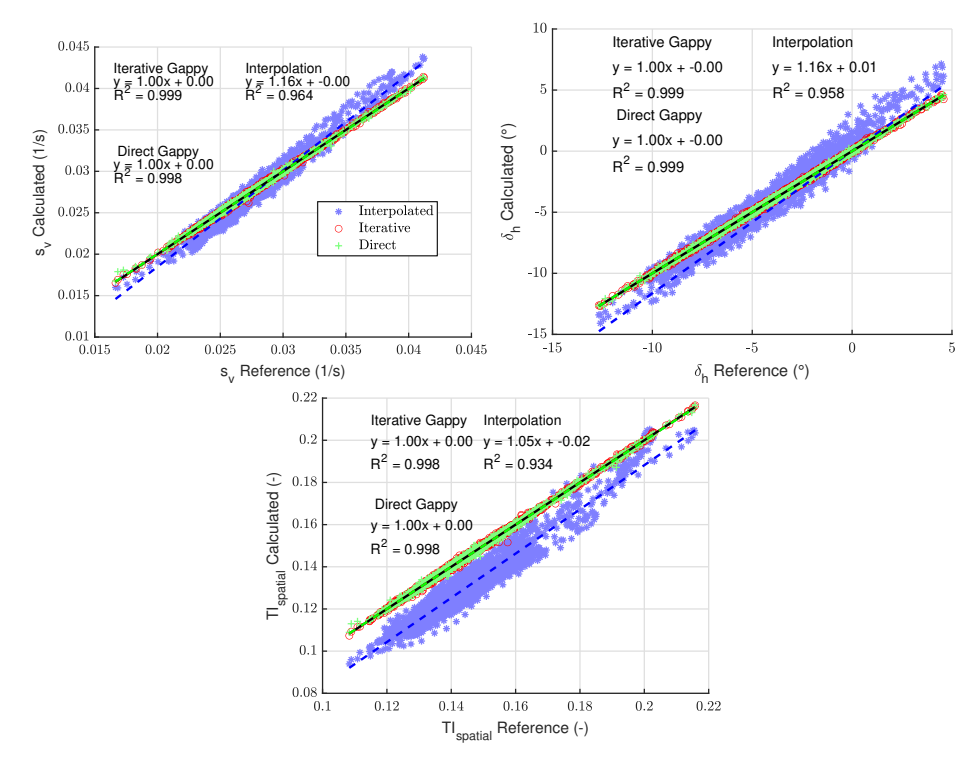


Figure 3.14: Comparison of s_v , δ_h and $\text{TI}_{\text{Spatial}}$ calculated from the reconstructed data for the SBL case with G=30%.

3.4 Discussion

We applied the POD methodology to reconstruct scanning lidar measured inflow data from two large eddy simulations of different inflow conditions. The first goal of this work was to apply POD to turbine-mounted scanning lidar measurements of the inflow and to identify the most energetic and dominating modes which can be used to create a reduced-order inflow reconstruction. Secondly, we tackled the problem of blade interference for nacelle-mounted lidars by using two Gappy-POD techniques to fill in missing data points and performed a comparison against spatial interpolation to quantify the reconstruction accuracy.

3.4.1 Towards POD-based reduced-order inflow modelling

The first goal of our work was to identify dominant modes that could yield strong dimensional reduction of the inflow while preserving the spatio-temporal dynamics. After such a dimensional reduction, the application of reduced-order modelling methods to scanning lidar measurements can be performed. Previously, analysis of the reduced-order descriptions of wind turbine inflows and wakes [Bastine et al. 2015; Saranyasoontorn and Manuel 2005] focused on the longitudinal velocity component due to its direct impact on the dynamical turbine response. While nacelle-lidar estimations of the longitudinal

velocity rely on the dominance of the longitudinal component over the lateral and vertical wind components $(u \gg v, w)$ in the line-of-sight direction, this is only an approximation with a certain error that depends on the orientation of the inflow in regard to the turbine and the beam direction itself, alongside effects of terrain, atmospheric stability, wind veer and turbine yaw setting. In accordance with our methodology, we did not impose strong wind field assumptions prior to the wind field reconstruction. Therefore, the methodology was applied directly to the line-of-sight measurements rather than projections in the longitudinal direction. Wind field reconstruction methods could be subsequently applied on the reduced line-of-sight wind field to extract wind parameters describing the turbine inflow. While estimating three-component velocity fields from line-of-sight measurements is a challenge in itself [Kidambi Sekar et al. 2018], a more detailed lower order inflow description could be potentially obtained by including all three velocity components. For quantifying the performance of a reduced-order reconstruction of the inflow, metrics related to the entire wind field were chosen. We see that with the first ten modes, most of the total lidar measured kinetic energy was recovered for both cases characterised by a sharp slope of the eigenvalue distributions (Figure 3.4). The majority of the lidar measured energy was concentrated in the first few modes, as the energy associated with the small scale turbulence was low-pass filtered due to the lidar volume averaging property. This lidar effect also nullifies the disadvantage of POD, whereby a large number of modes are generally required to capture small turbulent structures.

We observed that the dynamical behaviour of inflow characteristics relevant for turbinebased lidar applications was captured with high accuracy with just a few modes. The reconstruction accuracy further was quantified by calculating wind field parameters commonly used for turbine IPC control. The low-frequency characteristics of the rotor effective wind speed, vertical shear and horizontal misalignment can be captured by the first few modes alone (Figure 3.8); and the high-frequency fluctuations in the wind field parameters were reconstructed with high accuracy by taking the first ten POD modes. This indicates that simplified reduced-order dynamic models could be developed based on considering these dominant modes alone. Interestingly, the addition of certain modes to the reconstruction reduces the reconstruction errors substantially, suggesting that certain wind field parameters could be related to specific POD modes. From the high correlations between the modal time evolution and the wind parameters (Figure 3.9), it is clear that certain modes are related to certain wind field characteristics, providing a physical mode interpretation. We acknowledge that the modal interpretations with inflow parameters cannot be generalised and would vary depending on the inflow conditions, as seen from the varying correlation between the two considered LES fields. In addition, the reconstruction of turbulent spectra in fixed and rotating reference frames was investigated (Figure 3.10). For the stationary hub height spectra, 10-mode reconstruction offers good agreement with the lidar measured spectra. While reconstructing the rotational spectra necessary for modelling periodic blade loads, the eddy slicing effect (1P, 2P harmonics) is captured remarkably accurately with three or more modes.

Creating an inflow reconstruction with POD offers certain advantages over existing WFR methods. This method does not require strong assumptions about the wind field, unlike other WFR methods [Kapp. S 2017; Raach et al. 2014]. A POD-based inflow model also provides spatial wind information on a reduced basis, whereas parameterisation models

3.4 Discussion 75

only provide spatially constant wind parameters over the whole measurement plane. Hence, these models do not utilise the high spatial resolutions offered by scanning lidar systems such as SpinnerLidar, and events such as partial wakes and gusts are misinterpreted. Since the typical wind field characteristics for lidar-assisted 1P IPC are based on three parameters only, the effects of local flow details (partial wakes, gusts) are averaged out and are poorly represented in the wind field model. A POD reconstruction can represent significantly more wind field details, and hence can be used even for higher harmonics (e.g., 2P) in IPC or trailing edge flap control [Ungurán et al. 2019]. This would make a POD-based inflow model attractive for wind turbine control, as the dynamics of the non-homogeneous inflow can be described with a few modes and their weighing coefficients.

Creating a reduced-order dynamic inflow model can be achieved by Galerkin projection of the dominant POD modes onto the underlying Navier–Stokes equations governing the flow [Taira et al. 2017] or modelling the temporal dynamics of the weighing coefficients as a stochastic process Bastine et al. 2018], or by linearising the temporal dynamics of the weighing coefficients [Debnath et al. 2017; Iungo et al. 2015]. As wind turbines operate under conditions characterised by continuously changing states, special considerations must be given to dynamically adapt the ROM to changes in inflow states. This can be achieved either by determining the POD modes from a large dataset covering the majority of the inflow states, or by dynamically adapting the reduced-order model with state changes [Bergmann et al. 2005; Guo and Hesthaven 2019; Peherstorfer and Willcox 2015; Tadmor et al. 2011; Tallet et al. 2016].

To date, we have only investigated the quality of the reduced-order descriptions of the inflow dynamics based on two LES simulations. A general statement on the factors influencing our results cannot be derived without analysing a large enough dataset that considers variations in wind, atmospheric conditions and rotor sizes covering a variety of inflow and stability conditions that a turbine might experience during its lifetime. However, our simulations of two cases of typical atmospheric stratifications indicate that the majority of the energy was concentrated in the first ten dominant POD modes, and similar results were seen in free-field data as well. As most of the spectral energy in the flow are concentrated in the larger scales [Vollmer et al. 2016], the spatio-temporal flow variations would be captured in the first dominant POD modes, and the smaller scale structures would be filtered out due to the low-pass filtering of the measurements themselves. The effects of the larger scanning areas required for larger turbines and the representation of large atmospheric structures should be further analysed. However, for such an analysis, the optical parameters of the scanning lidar need to be modified to increase the measurement range and decrease the probe volume at large focal distances. As previously mentioned, the quality of the wind field reconstruction depends directly upon the lidar data quality and is thus subject to inaccuracies caused by the device's limitations. These shortcomings which are inherent device properties must be investigated in detail concerning their potential lidar-based relevance. In this study, the metrics for quantifying the accuracy of the model were chosen based on the inflow wind field itself. To further investigate the relationship between lidar measured wind fields and turbine dynamics, a detailed evaluation of the POD model could be performed by choosing quantities that describe the turbine's response.

3.4.2 RECONSTRUCTION OF MISSING DATA POINTS USING GAPPY-POD

We used Gappy-POD to reconstruct missing data points removed artificially to simulate blade interference. Gappy-POD utilises POD modes as a basis for the reconstruction of missing data points. The convergence of Gappy-POD was quantified using the root mean square error at the reconstructed points at every main iteration. Even up to a randomised gappiness of 50%, the RMSE dropped below 0.1% between 50 and 100 iterations. The Gappy-POD reconstruction algorithm was capable of reconstructing up to 50% missing data considerably better than spatial interpolation. This is because the spatio-temporal variations in the wind field are considered by Gappy-POD, whereas interpolation only uses the spatial information at neighbouring valid points. The reconstructed parameters with Gappy-POD agree better with the reference compared to spatial interpolation (Figures 3.13 and 3.14). To reduce solution times, a modified version of the Gappy-POD algorithm was presented where the iterative algorithm is replaced by direct solving using the optimum number of iterations (Figure 3.12). The direct Gappy implementation was able to achieve similar performance in reconstructing wind field parameters, with a 6 to 14 times reduction in solution times, depending on availability. However, the optimal number of modes required for reconstruction should be known in advance. Performing the direct calculations in a high-level programming language could reduce solution times to a few seconds, thereby making real-time reconstruction of missing points from wind fields possible. As the proposed method requires the time series of lidar measurements to estimate POD modes and iteratively reconstruct data points, a real-time implementation could be challenging. However, real-time reconstruction can be performed by estimating POD modes in an offline stage, which can be then subsequently used to reconstruct sparse data [Tong and Li 2020]. In [Venturi and Karniadakis 2004], it is shown that Gappy-POD would succeed even with random initial guesses but would require more iterations before arriving at a converged solution.

Before performing Gappy-POD, it is necessary that a robust outlier filter is applied to the dataset to detect blade interference and bad quality data due to environmental factors. As Gappy-POD is a data-driven method, the presence of invalid data points would introduce reconstruction errors which would propagate with every main or sub-iteration. It is also important to consider that by performing reconstruction based on lidar measured data, the missing point estimate would be optimised using the measured values. Hence, the reconstructed points will acquire at least the experimental uncertainty of the measurement data themselves [Murray and Seiner 2008]. For evaluating convergence in real experimental data, artificial convergence checking gaps can be introduced to the gappy data, over which the reconstruction error can be evaluated [Gunes et al. 2006].

3.5 Conclusions

Turbine-mounted lidar measurements can be used to derive information about the inflow to the wind turbine, which can subsequently be used for turbine control, load validation or turbulence characterisation. As lidar capabilities improve due to enhanced hardware and larger datasets, it is crucial to reduce the measurement data to a few variables that can still capture the spatio-temporal dynamics of the wind field. Here, we suggested a wind field reconstruction methodology for inflow measurements by a turbine-mounted scanning lidar, based on proper orthogonal decomposition (POD). It was tested in two LES

3.5 Conclusions 77

wind fields with different stratifications. Well defined inflow modes were obtained, and the majority of the lidar measured turbulent kinetic energy was captured with just the first ten POD modes for both cases. The data reduction was possible due to the volume averaging effect of the lidar filtering out smaller turbulent structures, thereby taking advantage of one of the lidar's limitations. The reconstructed velocity fields with the dominant modes agree well with the full lidar measurements and provide a method for extracting local spatial structures in the inflow.

The strong dimensional reduction and relationships between wind inflow parameters indicate that the development of simplified inflow models is possible. POD-based wind field reconstruction provides more information than classical methods; for instance, it captures the rotationally sampled wind field and the associated first and second harmonics, which dominate the dynamic blade loading. Furthermore, we used two Gappy-POD methods to fill in measurements lost due to blade passage and other factors that influence data availability, a significant problem for all nacelle-mounted lidars. Gappy-POD provides very good approximations with which to reconstruct data points lost to blade interference and other factors. Both Gappy-POD methods were found to reconstruct the missing data (up to 50%) with high accuracy in comparison to spatial interpolation, as spatio-temporal flow variations are taken into account. The wind field reconstruction method introduced applies to other scanning lidar systems with sufficiently high spatio-temporal resolution.

3

4

OVERCOMING BLADE INTERFERENCE: A GAPPY-POD DATA RECONSTRUCTION METHOD FOR NACELLE-MOUNTED LIDAR MEASUREMENTS

Nacelle-mounted lidar systems suffer data loss due to unfavourable atmospheric conditions such as rain or fog and most importantly the rotation of the blades that obstruct the laser beam from measuring upstream of the turbine. In this paper, we apply Gappy Proper Orthogonal Decomposition (Gappy-POD) to reconstruct incomplete flow fields from nacelle-mounted lidar measurements. For this purpose, two scanning nacelle-based SpinnerLidar simulations are performed inside a Large Eddy Simulation, one measuring the undisturbed wind inflow and the other in the wake of a reference turbine. Data loss of up to 90 % is simulated by artificially removing measurement points. The performance of Gappy-POD in reconstructing the wind fields is evaluated by comparing metrics such as effective wind speeds, vertical shear, yaw misalignment, wake deficit, wake meandering and the turbulent spectra in fixed and rotating frames of reference. We see that Gappy-POD is capable of accurately reconstructing missing data in comparison to normally used spatial interpolation techniques even in cases where 90 % of the data was missing. As a result, the dynamics of the reconstructed wind fields can be investigated based on highly accurate lidar-based wind field retrievals. The methodology can be used as a tool to develop effective wind field reconstruction techniques from sparse data.

4.1 Introduction

Flow measurements around wind turbines with lidar systems have gained more prominence in the last decade. Turbine-mounted lidar systems are capable of performing upstream measurements of the wind approaching the turbine, allowing for optimisation of turbine performance, i.e., reducing loads and extending the turbine lifetime [Simley et al. 2018]. Due to the increasing turbine size, it is meaningful to measure the whole rotor area to capture the spatio-temporal wind variations that drive the turbine response. For this purpose, scanning lidar systems have proven to be a reliable alternative to simple fixed-beam lidars due to their ability to steer and scan with the laser beam, providing a way to capture the entire rotor area. However, the performance of lidar-assisted wind turbine applications relies entirely on the measured data quality. The data quality from nacelle-mounted lidar measurements is negatively affected by the rotation of the blades during turbine operation which obstructs the laser beam from focusing on the pre-defined upstream measurement locations. In addition, this data loss is amplified by environmental factors such as the presence of rain or fog that reduce the quality of the backscattered signal. These effects result in local blind spots in the lidar measured wind fields. If these gaps are filled by ensemble averaging of scans, the fluctuations in the wind fields, which are highly relevant for the turbine dynamics are partially lost. An alternate approach would be to use the complete time series of lidar measured wind field snapshots obtained at high sampling rates to reconstruct the spatio-temporal data gaps. Gappy-POD is an extension of POD [Sirovich 1987] which is capable of providing accurate approximations for incomplete datasets. The objective of this paper is to introduce a data reconstruction method based on Gappy Proper Orthogonal Decomposition (Gappy-POD) [Willcox 2006] to reconstruct the incomplete measurements of a nacelle-mounted lidar following our work in [Kidambi Sekar et al. 2022. In this contribution, the Gappy-POD is tested in reconstructing missing data points in two inflow conditions (one in undisturbed inflow and the other in the wake) with a range of data availabilities in a high-resolution wind field obtained from a Large Eddy Simulation (LES) that is used as reference. To quantify the model performance, several metrics relevant for the turbine in the time and frequency domains are defined and evaluated.

4.2 METHODOLOGY

In this section, the LES simulation environment is described along with the lidar simulator used to simulate the lidar measurements. In addition, the POD and the Gappy-POD methods are explained.

4.2.1 Large-eddy simulations and scanning lidar simulations

The atmospheric boundary layer (ABL) is simulated using the Large Eddy Simulation model *PArallelised Large eddy simulation Model* (PALM) [Maronga et al. 2015]. A turbulent unstable ABL is simulated inside which an NREL 5 MW turbine is simulated with the actuator line coupled directly with the wind field [Krüger et al. 2022]. The coupling creates the turbine perturbation of the wind field, i.e., the induction zone and the wake. The

Measurements." Journal of Physics: Conference Series. Vol. 2265. No. 2. IOP Publishing, 2022. DOI: 10.1088/1742-6596/2265/2/022078.

^{© 2022} by the authors. Reproduced in accordance with the Creative Commons Attribution 3.0 License.

4.2 Methodology 81

unsteady ABL is generated with a roughness length $z_0 = 0.0175$ m, friction velocity of 0.52 m/s with a mean longitudinal speed of 10.1 m/s at hub height and corresponding turbulence intensity (TI) of 11.91% for a total duration of 3700 s which is sampled at 1 Hz. A more comprehensive description of the set-up and the statistics of the LES wind field is available in [Kidambi Sekar et al. 2020].

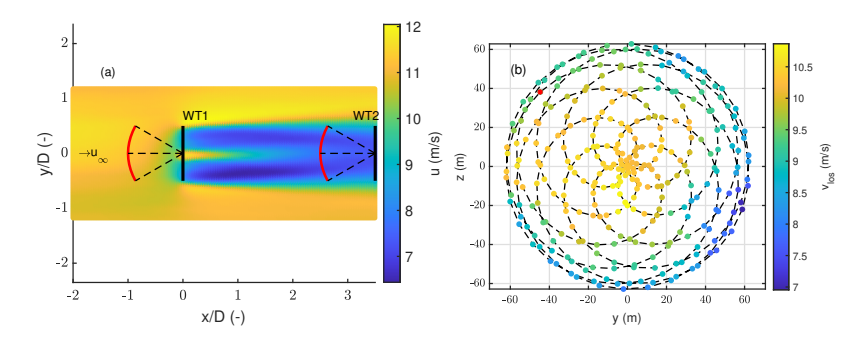


Figure 4.1: (a) The mean longitudinal wind velocity component (*u*) at a horizontal plane at hub height. The SpinnerLidar (red curve) is simulated at the hub height of the upstream turbine WT1 and the virtual downstream turbine WT2. (b) Exemplary instantaneous snapshot of the simulated SpinnerLidar measurement from WT1.

The SpinnerLidar, developed by DTU Wind Energy, is a scanning lidar capable of measuring a 2D wind field with a very high spatial and temporal resolution with a maximum value of up to 500 points distributed on a spherical measurement plane every second [Mikkelsen et al. 2013]. The SpinnerLidar measurements are simulated using the lidar simulator LiXim [Trabucchi 2020] which is capable of simulating the kinematic and optical properties of the SpinnerLidar. The SpinnerLidar measurements are simulated at two locations inside the LES wind field as visualised in Fig. 4.1. In the undisturbed inflow case, the SpinnerLidar is mounted on the nacelle of the simulated turbine (WT1) and is focused at an upstream distance of one turbine diameter 1 D corrosponding to 126 m. For the full wake scenario, the SpinnerLidar is mounted on a virtual turbine WT2 placed 3.5 D behind the first turbine and focused at an upstream distance of 1 D (and a corresponding 2.5 D downstream of the first turbine). For both cases, LiXim simulates the SpinnerLidar measurements with 312 points distributed on a rosette scanning pattern every second for the total simulation duration. The lidar simulator was programmed to perform snapshots of the wind field every second.

4.2.2 SpinnerLidar velocity snapshots with gaps

Consider a line-of-sight velocity matrix measured by the SpinnerLidar denoted as $V(\mathbf{X},t)$ where \mathbf{X} is a vector containing the x,y,z positions of the N measurement points at the time instant t. The snapshots are arranged in a matrix $V(\mathbf{X},t) = [\mathbf{v}_{los}(\mathbf{X},t_1)\mathbf{v}_{los}(\mathbf{X},t_2)\cdots\mathbf{v}_{los}(\mathbf{X},t_{n_s})]$ where each of the n_s columns denotes a snapshot with N line-of-sight velocities per snapshot. To simulate missing measurements, data was randomly removed from the velocity matrix. The points to be removed were chosen based on defining a set of uniformly distributed pseudo-random integers consistent with the total number of measurement

points using the Mersenne-Twister algorithm [Matsumoto and Nishimura 1998]. The percentage of missing data calculated over the number of snapshots can be expressed as:

$$G = \frac{1}{n_{\rm S}} \sum_{i=1}^{n_{\rm S}} \frac{n_{{\rm los, Gappy}, i}}{N}.$$
 (4.1)

Here, G describes the gappiness in the wind field, $n_{\log, \mathrm{Gappy}, i}$ denotes the total number of missing data points in snapshot t_i . For the analysis, 10 % to 90 % of the data is removed for each case resulting in average data availabilities of 90 % to 10 % for the whole datasets, respectively. The gaps are added such that no measurement point is missing on all snapshots and no single snapshot is missing all the measurement points as otherwise Gappy-POD would fail.

4.2.3 Proper Orthogonal Decomposition

Proper Orthogonal Decomposition (POD) is a data-based methodology that can provide lower order approximations of high-dimensional processes by exploiting the spatial correlations in the data. A detailed explanation of the theoretical framework behind the method can be found in [Berkooz et al. 1993; Holmes et al. 2012; Sirovich 1987] and in Chapter 3.2.1. In brief, POD decomposes a velocity flow field into a linear combination of modes and their temporal evolution which are calculated directly from the data in a certain least-squares optimal sense. The most dominant modes of the POD decomposition can then be chosen and used to build a reduced-order representation consisting of M modes $\hat{V}^{(M)}(\mathbf{X},t)$ of the lidar measured line-of-sight velocity fields $V(\mathbf{X},t)$, i.e.,

$$V(\mathbf{X},t) \approx \hat{V}^{(M)}(\mathbf{X},t) = \sum_{j=1}^{M} Z_j(t) \boldsymbol{\phi}_j(\mathbf{X}), \quad \text{where} \quad M \ll N.$$
 (4.2)

Here, $\phi_j(X)$ and $Z_j(t)$ are the spatial POD modes and their corresponding temporal evolutions which are obtained by solving the eigenvalue problem of the covariance matrix $R = V(X, t)^T V(X, t)$.

4.2.4 Gappy Proper Orthogonal Decomposition (Gappy-POD)

Everson and Sirovich [Everson and Sirovich 1995] first proposed using POD modes to reconstruct missing data. The Gappy-POD methodology provides high accuracy approximations of missing data points which starts from a certain initial guess and improves the guess in an iterative process. The core of the method consists of a minimisation problem of a function defined in the spatio-temporal domain where the velocity field is known. Modifications have been proposed to the Everson-Sirovich method which have proven to increase the accuracy of the guesses and reduce solution times [Gunes et al. 2006; Saini et al. 2016; Venturi and Karniadakis 2004]. Here, we follow the Gappy-POD algorithm proposed by [Gunes et al. 2006 and applied for scanning lidars [Kidambi Sekar et al. 2022]. The process begins with an initial simple guess of the missing points and a low number of POD modes (usually 2) used to obtain an approximation of the missing data. This approximation is passed on to the next iteration where the number of modes used for the reconstruction is increased and this process is repeated until a pre-defined convergence criteria is satisfied. This procedure results in a nested-loop implementation where the convergence is

83

4

evaluated for a given number of POD modes and the number of POD modes used for the reconstruction. As it is typical to remove the mean, Gappy-POD would reconstruct the velocity fluctuations at the locations of the missing points which is subsequently summed up with the mean to obtain the reconstructed wind field.

1. The velocity field with gaps is first written in a matrix form and a mask matrix:

$$V(X,t) = [m(X,t_1)v_{los}(X,t_1) \ m(X,t_2)v_{los}(X,t_2) \cdots m(X,t_{n_s})v_{los}(X,t_{n_s})]$$
(4.3)

Here $m(X, t_i)$ is the mask applied to the i^{th} snapshot in the form of a diagonal matrix that tracks the missing data and can be expressed as:

$$m(\mathbf{X}, t_i)\mathbf{v}_{\text{los}}(\mathbf{X}, t_i) = \begin{bmatrix} m_1 & & & \\ & m_2 & & \\ & & \ddots & \\ & & & m_N \end{bmatrix} \begin{bmatrix} \mathbf{v}_{\text{los}, 1, t_i} \\ \mathbf{v}_{\text{los}, 2, t_i} \\ \vdots \\ \mathbf{v}_{\text{los}, N, t_i} \end{bmatrix} = \begin{bmatrix} m_1 \mathbf{v}_{\text{los}, 1, t_i} \\ m_2 \mathbf{v}_{\text{los}, 2, t_i} \\ \vdots \\ m_N \mathbf{v}_{\text{los}, N, t_i} \end{bmatrix}$$
(4.4)

The diagonal element corresponding to each of the measurement points $j \in 1, \dots, N$ are:

$$m_j = \begin{cases} 1, & \text{if measurement at spatial location } j \text{ is available at the snapshot } t_i, \\ 0, & \text{if measurement at spatial location } j \text{ is unavailable at the snapshot } t_i. \end{cases}$$

$$(4.5)$$

- 2. The velocity field at any point on the Gappy-POD process is denoted as $V_{n,s}$ where V is the guess of the filled velocity field where n, s denote the main and sub iterations respectively.
- 3. M is the the number of modes which will be used for the reconstruction. Following Gunes et al. 2006 two modes (M = 2) are chosen for the first main iteration and is increased by 1 for every subsequent main iteration.
- 4. Let $\tilde{V}(\mathbf{X},t)$ be the filled-in wind field based on an guess at the locations of the missing points alone. For the first main iteration (n=0), the guess is usually the temporal mean $\langle V(\mathbf{X}) \rangle$ of all the available values at that location. For subsequent main iterations, the guess is the filled wind field from the previous main iteration. The POD method is applied to $\tilde{V}(\mathbf{X},t)$ resulting in a guess of the spatial modes $\phi_j(\mathbf{X})$ and their associated temporal evolution $Z_j(t)$:

$$\tilde{V}_{n,s}(\mathbf{X},t) = \sum_{j=1}^{M} Z_j(t) \boldsymbol{\phi}_j(\mathbf{X}). \tag{4.6}$$

5. According to the Everson - Sirovich method, a new set of temporal coefficients is calculated by minimising the error between the data at known locations and the POD approximation [Everson and Sirovich 1995], the following function is minimised to obtain an estimate of $Z_i'(t)$:

$$\min_{Z'_{j}(t)} \| \sum_{j=1}^{N} Z'_{j}(t) \phi'_{j}(\mathbf{X}) - \tilde{V}_{n,s}(\mathbf{X}, t) \|_{\text{Gappy}}^{2}$$
(4.7)

Here, the "Gappy" norm indicates that the minimisation is performed only on the spatio-temporal domain where $V(\mathbf{X},t)$ is known. While solving this minimisation problem would provide accurate estimates, it requires the inversion of large matrices which increases the required computational time. To avoid solving this computationally expensive minimisation problem (Eq. (4.7)), the approach described in [Gunes et al. 2006] is applied where $\tilde{V}_{n,s}(\mathbf{X},t)$ is used directly to estimate the missing data point, i.e., $Z_j'(t) = Z_j(t)$. Since no minimisation problem is necessary to obtain $Z_j'(t)$, this method is computationally less expensive than the Everson-Sirovich method but at the cost of slightly lower accuracy. In [Gunes et al. 2006], an average error of 0.2 % was reported for both the methods while reconstructing up to 50 % of missing data while similar results were obtained in [Raben et al. 2012; Saini et al. 2016].

6. The gaps in the data are then replaced by the guess, i.e.,

$$V_{n,s+1}(\mathbf{X},t) = \begin{cases} \tilde{V}_{n,s}(\mathbf{X},t), & \text{if } \mathbf{m}(\mathbf{X},t) = 0, \\ V(\mathbf{X},t), & \text{if } \mathbf{m}(\mathbf{X},t) = 1. \end{cases}$$
(4.8)

7. For *M* modes, steps (iv) to (vi) are iteratively performed and stopped based on convergence. The iteration with *M* modes constitutes the sub-iterations (*s*) and is continued until the obtained POD eigenspectrum does not change significantly anymore. The convergence criterion for the sub-iterations is defined on the eigenvalue convergence of the dominant modes between two sub-iterations:

$$\left|\frac{\lambda_{n,s,j} - \lambda_{n,s-1,j}}{\lambda_{n,s,i}}\right| < 0.05. \tag{4.9}$$

Here, $\lambda_{n,s,j}$ is the eigenvalue associated with the j^{th} POD mode and n and s are the main and sub-iteration numbers respectively. Now, the converged result of the current sub-iteration is used as an initial guess for the next iteration where the number of modes M used for reconstruction is increased by one and the next main iteration is started. The main iterative process is stopped when the optimum number of modes to accurately reconstruct the missing points is found.

4.3 RESULTS AND DISCUSSION

The performance of the Gappy-POD in reconstructing missing data for the two considered cases is tested and the results are discussed.

4.3.1 Convergence of Gappy-POD

As the Gappy-POD is an iterative process, it is important to know how many main iterations are necessary to obtain a high accuracy approximation of the missing data points. To quantify the convergence, the RMSE is calculated between the reference and the reconstructed wind fields at the locations of the missing points:

$$RMSE = \sqrt{\sum_{i=1}^{n_{los,Gappy}} \frac{(v_{los,Gappy,i} - v_{los,reference,i})^2}{n_{los,Gappy}}}$$
(4.10)

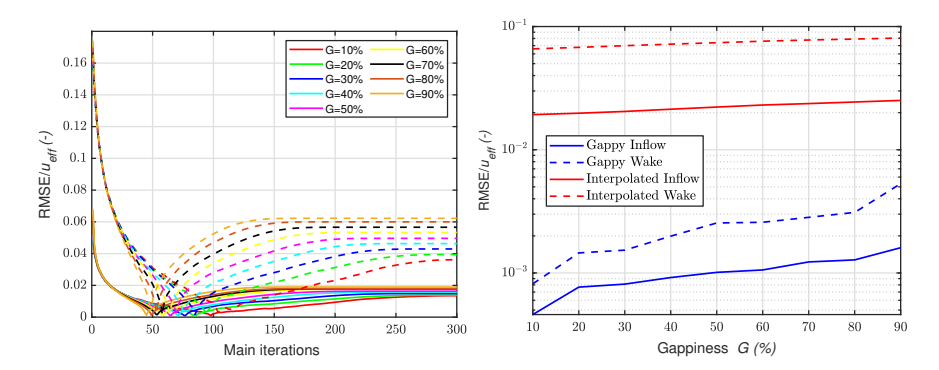


Figure 4.2: (a) The main iteration convergence for the undisturbed inflow and the full wake inflow cases for different gappiness percentages *G*. The solid and dotted lines denote the undisturbed inflow and the full wake case respectively. (b) The RMS error calculated for the Gappy-POD with optimum number of main iterations and the spatial interpolation estimation at the missing points for different gappiness percentages.

where $n_{\rm los,Gappy}$ denotes the total number of missing points over the entire time series. The RMSE is normalised by the mean hub height wind speed at the location of the lidar scan obtained from the LES for inter-comparison between the two cases.

Figure 4.2 (a) illustrates the error defined in Eq. (4.10) for the two inflow cases as a function of the number of main iterations and the gappiness percentage. All the curves exhibit the same trend: increasing the number of main iterations reduces the error. For the undisturbed inflow case, the normalised RMSE drops from 0.069 after the first iteration to below 0.001 and reaches an optimum minimum after 50 to 100 iterations depending on the gappiness percentages after which it slightly increases again. While it is expected that the error should decrease while more modes are added to the reconstruction, the monotonic error decrease is dependent on factors of the flow itself such as turbulence and noise. [Gunes et al. 2006; Saini et al. 2016] also reported non-monotonic behaviour of the reconstruction error where the error starts to diverge after a certain number of modes are used for the reconstruction. The wake case shows similar behaviour, with the error reducing from 0.16 to below 0.001 and reaching a minimum after approximately 50 to 100 iterations. The similar behaviour of the error curves for varying gappiness values is due to the identical temporal mean values used to fill the gaps during the first iteration. Due to the volume averaging property of the lidar whereby a few modes dominate the reconstruction and the first guess itself being the mean of the whole dataset, a very good approximation of the wind field is already obtained with the first sub-iteration itself.

It is remarkable that the Gappy-POD is capable of reconstructing even up to 90 % of missing points with a very low reconstruction error. Even though datasets with 90 % unavailability are quite extreme occurrences and were simulated solely to find the upper limit of the method itself, the method still provides reasonable approximations to missing points. For comparison, the RMSE is calculated for the Gappy-POD at its optimal minimum and shown against the RMSE obtained by performing triangulation-based natural-neighbour spatial interpolation to estimate the missing points in Fig. 4.2 (b). The Gappy-POD RMSE varies from 0.0005 to 0.0015 and 0.0008 to 0.004 for the inflow and wake cases respectively with increasing gappiness percentages. In contrast, the RMSE of the spatially interpolated wind

field is much higher and ranges from 0.02 and 0.09. We note that the optimum number of iterations that are required to obtain an accurate reconstruction would differ with different turbine operational states. Therefore, the optimum number of iterations required for Gappy-POD can be chosen based on the reconstruction accuracy required for a particular lidar based application. Looking at Fig. 4.2 (b), the RMSE of the Gappy-POD reconstruction drops below 0.02 and 0.08 for the undisturbed inflow and wake cases and already performs better than spatial interpolation after 25 iterations. Hence, if outperforming spatial interpolation is the goal, the Gappy-POD procedure can be stopped before reaching optimum minimum thus saving computational time.

4.3.2 Velocity field reconstruction

To visualise the Gappy-POD performance in reconstructing missing data, we plot the reconstructed line-of-sight velocity field in Fig. 4.3. A SpinnerLidar measurement at t=2266 s with a low snapshot data availability of 34 % makes it an ideal case to visually quantify Gappy-POD reconstruction and to provide a comparison against the natural interpolation method. The Gappy-POD reconstructed velocity field is shown after the optimum number of iterations with the lowest RMSE based on the minimum error definition in Fig. 4.2 (a).

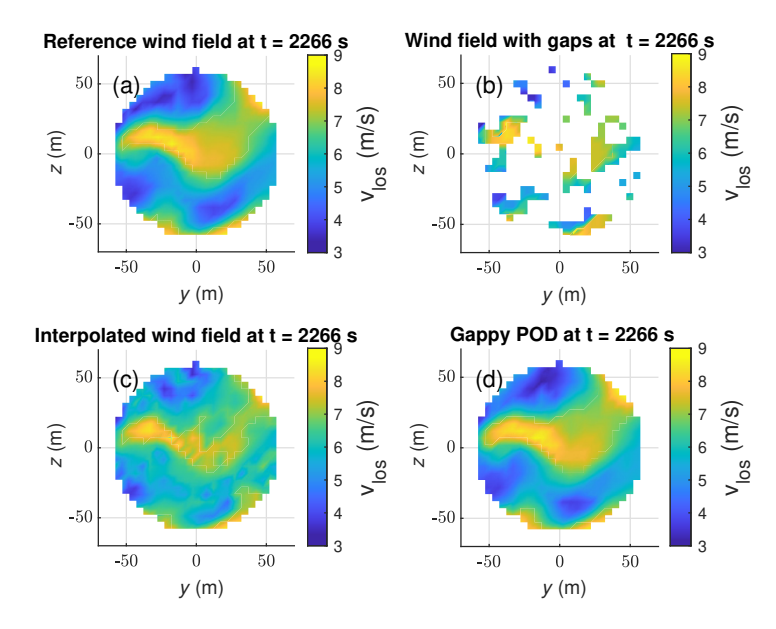


Figure 4.3: A snapshot of (a) the true reference wind field and (b) a gappy wind field with 66% gappiness at an arbitrary time t = 2266 s obtained from the undisturbed inflow case. The result of spatial interpolation of the gappy field is seen in (c) while (d) illustrates the reconstructed wind field obtained from the Gappy-POD algorithm after the optimum number of iterations.

A more accurate visual reconstruction of the missing data points is obtained from the Gappy-POD reconstruction in comparison to the spatial interpolation method. The high accuracy is achieved as spatio-temporal velocity variations are accounted for in the Gappy-

POD through the POD modes while natural interpolation only uses the spatial velocity information in the nearby points. Hence, the velocity magnitudes and the locations of localised structures in the wind field are captured better by Gappy-POD as compared to spatial interpolation. However, pure visualisation does not offer any insights into the wind parameters that are relevant for turbine operation and hence we define quantitative metrics to investigate the reconstruction performance.

4.3.3 RECONSTRUCTION OF WIND PARAMETERS FOR THE UNDISTURBED INFLOW CASE

We extract parameters relevant for the undisturbed turbine inflow from the reconstructed wind fields. For the sake of brevity, only the results of the two inflow cases with 30 % gappiness are shown as this value is the typical unavailability value for nacelle-mounted SpinnerLidar measurements based on experience from previous full-field experimental campaigns. We estimate the effective wind speed $u_{\rm eff}$, horizontal misalignment $\delta_{\rm h}$ and the vertical shear $s_{\rm v}$ from the reference SpinnerLidar measurements without any data gaps and the interpolated and the Gappy-POD reconstructions of the missing data. This parameterisation is performed based on the three-parameter model defined in Kapp. S 2017, which characterises the mean behaviour of the wind inflow in the 2-D lidar measurement plane based on the line-of-sight measurements. The effective wind speed is defined as the rotor equivalent wind speed in the measurement plane while the vertical shear is defined as the slope of the linearly increasing wind speed in the vertical direction. The horizontal misalignment $\delta_{\rm h}$ is an important parameter for determining the turbine's yaw setting. For the G=30 % case, a 200 s section of the 1 Hz time series of the three parameters is seen in Fig. 4.4.

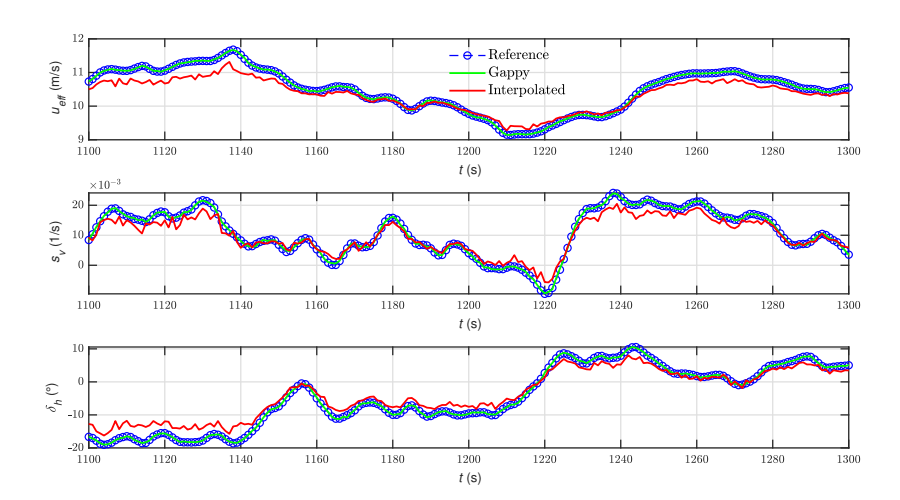


Figure 4.4: Time series of the three wind field parameters $u_{\rm eff}$, $s_{\rm v}$ and $\delta_{\rm h}$ at 1 Hz for a duration of 200 seconds.

The three parameters extracted from the Gappy-POD reconstructed wind fields show excellent agreement with the reference with almost no deviation. The parameters extracted from the interpolated wind field show a reasonable but not perfect agreement with the reference.

Table 4.1, contains the RMS error of the reconstructed three wind parameters through interpolation and Gappy-POD against the reference data. The Gappy-POD reconstruction exhibits a significantly lower RMS compared to the interpolated results.

Table 4.1: Root Mean Square Error (RMSE) for the calculated three inflow and wake parameters parameters for the Interpolated and gappy cases.

RMSE	Inflow			Wake				
	$u_{\rm eff}~({\rm m/s})$	$s_{\rm v} (1/{\rm s})$	$\delta_{ m h}$ (°)	$u_{\rm eff,wake}$ (m/s)	y_c (m)	z_c (m)		
Interpolated		8.5×10^{-6}		0.1588	0.64	0.39		
Gappy-POD	3.9×10^{-5}	4.03×10^{-8}	0.97	6.05×10^{-4}	0.0042	0.2366		

4.3.4 RECONSTRUCTION OF TURBULENT SPECTRA IN FIXED AND ROTAT-ING REFERENCE FRAMES

We calculated the turbulent spectra of the reconstructed wind fields in the fixed and rotating frames of reference (for the $G=30\,\%$ undisturbed inflow case). For the calculation of the fixed spectrum, the measurement point with the lowest availability over the total time series is chosen. The point is defined by the coordinates (-44.71 m, 38.18 m) situated in the upper left corner of the scan trajectory and is marked in Fig. 4.1 (b) with a red asterisk. The spectra is then calculated for the reference, interpolation and gappy schemes and visualised in Fig. 4.5 (a).

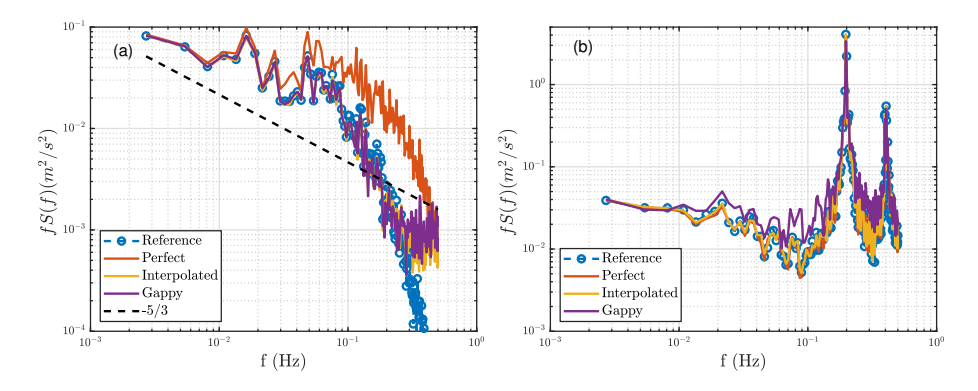


Figure 4.5: (a) Fixed point spectrum at the spatial point with lowest availability. Reference indicates the full lidar data with the volume averaging effect and Perfect refers to ideal lidar measurements without the volume averaging effect. Interpolated and Gappy refers to the spectra calculated from the missing point estimates through the Gappy-POD and spatial interpolation methods and -5/3 Kolmogorov slope is also indicated. (b) The rotational spectrum measured by following at point at 90% of the blade radius with a rotational speed of 0.19 Hz.

The spectra are calculated using the Welch's modified periodogram method with a Hanning window, 300 s segments and 50 % overlap between the segments. The spectra denoted by *perfect lidar* indicates the measurements of an ideal perfect lidar exactly focused at the measurement point. The black dotted line denotes the $\frac{-5}{3}$ Kolmogorov slope that indicates the decay of turbulence in the inertial sub-range. As expected, the reference lidar

measurement shows a drop-off from the perfect measurements around 0.03 Hz indicative of the lidar low-pass filtering effect. The spectra estimated for the interpolated and the Gappy-POD show a very good agreement with the reference except at very high frequencies. Both the methods deviate from the reference and exhibit constant power spectral density amplitudes at higher frequencies, resembling white noise. However, these deviations occur at f > 0.3 Hz much higher than the drop-off frequency. As spatial interpolation only uses wind information at the available spatial locations to guess the missing points, smaller structures where no data points are available are not resolved.

The Gappy-POD is capable of accurately reconstructing the localised wind fluctuations as the dynamics of the local wind variations are captured in the dominant POD modes used for the reconstruction. For the calculation of the rotational $v_{\rm los}$ spectrum in Fig. 4.5 (b), a point is chosen and followed at 90 % of the radius of the blade rotating at a constant rotational speed of 0.19 Hz. Due to the eddy slicing effect, turbulent energy is accumulated at multiples of the rotor RPM. The 1P and 2P harmonic peaks are estimated very well for both the interpolation and gappy methods. The SpinnerLidar can estimate the rotationally sampled wind fields more accurately than the fixed spectra as the large spatial coverage offered by the SpinnerLidar thereby capturing the wind shear and spatial wind variations that contribute to the periodic loading on the blades as it cuts through the atmospheric boundary layer [Kidambi Sekar et al. 2020].

4.3.5 Reconstruction of wind parameters for the full wake case

Following the spirit of subsection 4.3.3, we parameterise the fully waked inflow into quantities relevant for the turbine. The first metric is defined as the effective wake velocity $u_{\rm eff,wake}$ that is defined as the average projected longitudinal velocity over the measurement area. The projected longitudinal velocity at every measurement point is defined as:

$$u_{\text{projected}} = \frac{v_{\text{los}}}{\cos(\chi)\cos(\delta)}.$$
 (4.11)

Here, χ and δ are the azimuth and elevation angles of the focussed laser beam at the measurement point. To assess the dynamic behaviour of the wake and for wake tracking, we choose the dynamic meandering of the velocity deficit defined as the centre of energy of the deficit [Bastine et al. 2015], i.e.,

Here y_c and z_c are denoting the lateral and vertical location of the wake centre are chosen as the second and third metrics. The square of the projection of the line-of-sight velocity in the longitudinal direction is integrated over the scanning plane of the lidar. The wake deficit is an important parameter for determining the operating set point of the downstream turbine while tracking the wake center is important for implementing wake steering control algorithms. For the G=30 % case, a short 200 s reconstructed time series of the three metrics is shown in Fig. 4.6.

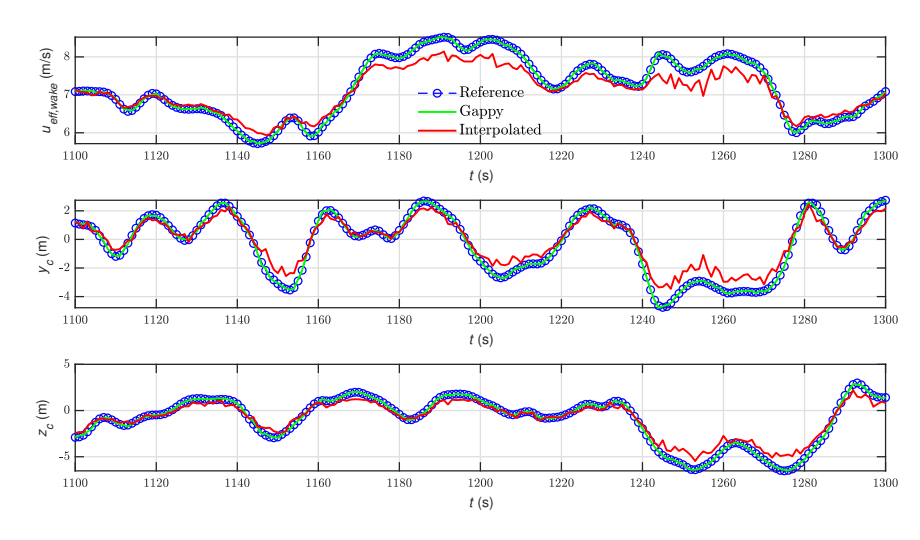


Figure 4.6: Time series of the three wind field parameters $u_{\rm eff,wake}$, $y_{\rm c}$ and $z_{\rm c}$ at 1 Hz for a duration of 200 seconds.

The time series of the reconstructed wake metrics exhibits similar behaviour as that of the inflow case. The Gappy-POD reconstructed metrics show very good agreement with the reference while the results from the interpolated scans exhibit deviations from the reference. The deviations from the reference are further quantified based on the RMS error (Tab. 4.1). Similar to the undisturbed inflow case, the Gappy-POD is capable of highly accurate reconstructions of missing data points.

4.4 Conclusions

This paper evaluates the performance of the Gappy-POD methodology for filling in missing measurement points lost due to blade interference and other factors that occur when using nacelle-mounted inflow measuring lidar systems. The methodology was tested inside a high resolution Large Eddy Simulation within which two SpinnerLidar measurements are emulated using a lidar simulator. Artificial data gaps were imposed by removing measurement points to consider data loss due to blade interference and other factors. The results indicate that the Gappy-POD method is capable of more accurately filling in missing points compared to triangulation-based natural-neighbour spatial interpolation methods. The method shows very good performance for both the undistributed inflow case and the full wake case even for extreme situations with 90 % missing data. The wind inflow metrics estimated from the reconstructed wind fields show very good agreement with the reference case even at a high SpinnerLidar sampling rate of 1 Hz. By reconstructing the gaps in the velocity fields, the dynamics of the wind field and their interaction with the turbine can be studied. This would not be possible to a similar extent while performing ensemble averaging of the snapshots whereby the highly fluctuating wind field information is averaged out. As the method requires the time series of the velocity measurements to build the POD modes and iteratively reconstruct missing points, a real-time implementation could be challenging. However, the iterative implementation could be skipped by directly

4.4 Conclusions 91

using the optimal number of modes to reconstruct the missing data points. This could significantly reduce solution times, provided that the optimal number of modes are known in advance [Kidambi Sekar et al. 2022].

It should be noted that the method first assumes that an appropriate outlier detection scheme is available which has accurately identified the erroneous data points. As the Gappy-POD is a data-based method, any erroneous data points that were missed during filtering could lead to larger estimation errors. Also, any uncertainties in the lidar measurements such as the volume averaging effect and directional bias would be propagated to the reconstructed wind fields. Future work includes extending the methodology to full-field measurements from different lidar systems.

4

5

SYNCHRONISED WINDSCANNER FIELD MEASUREMENTS OF THE INDUCTION ZONE BETWEEN TWO CLOSELY SPACED WIND TURBINES

Field measurements of the flow interaction between the near-wake of an upstream wind turbine and the induction zone of a downstream turbine are scarce. Measuring and characterising these flow features in wind farms at various operational states can be used to evaluate numerical flow models and design of control systems. In this paper, we present induction zone measurements of a utility-scale 3.5 MW turbine with a rotor diameter of 126 m in a two-turbine wind farm operating under waked and un-waked conditions. The measurements were acquired by two synchronised continuous-wave WindScanner lidars that could resolve longitudinal and lateral velocities by dual-Doppler reconstruction. An error analysis was performed to quantify the uncertainty in measuring complex flow situations with two WindScanners. This is done by performing a Large Eddy Simulation while using the same measurement layout, modelling the WindScanners sensing characteristics, and simulating similar inflow conditions observed in the field. The flow evolution in the induction zone of the downstream turbine was characterised by performing horizontal planar dual-Doppler scans at hub height. The measurements were conducted for undisturbed, fully waked and partially waked flows. Evaluation of the engineering models of the undisturbed induction zone showed good agreement along the rotor axis. In the full wake case, the measurements indicated a deceleration of the upstream turbine wake due to the downstream turbine induction zone as a result of the very short turbine spacing. During a wake steering experiment, the interaction between the laterally deflected wake of the upstream turbine and the induction zone of the downstream turbine could be measured for the first time in the field. Additionally, the analyses highlight the affiliated challenges while conducting field measurements with synchronized lidars.

5.1 Introduction

During operation, wind turbines create a reduced velocity region upstream due to rotor thrust, i.e. the induction zone. To account for the induction zone, the IEC 61400-12-1 [IEC 2022] standard recommends performing freestream velocity measurements more than 2 to 4 rotor diameters (D) upstream of the turbine. Wind turbines also create wakes, the main driver of unfavourable aerodynamic interactions in a wind farm where the downstream turbine extracts less power and is subject to higher structural loads due to reduced wind speeds and high wake turbulence. The near wake of a turbine extends $2.0\ D$ to $4.0\ D$ downstream and is highly influenced by rotor aerodynamics [Göçmen et al. 2016]. Therefore, for tightly packed wind farms, the induction zone of a downstream turbine can overlap with the near wake of an upstream turbine.

The upstream induction zone of a wind turbine has consequences for many wind power applications. The velocity deficit upstream of the turbine is responsible for the estimation bias in power curve measurements for isolated turbines [Slinger et al. 2020] and global blockage at the wind farm level [Schneemann et al. 2021]. Moreover, the flow slowdown and expansion around the turbine also affect lidar-based feedforward controllers, which require precise information on the velocity magnitudes and arrival times at the rotor [Dunne et al. 2014]. Several approaches have been previously followed to numerically [Branlard and Gaunaa 2015; Medici et al. 2011; Troldborg and Meyer Forsting 2017] and experimentally [Asimakopoulos et al. 2014; Mikkelsen et al. 2020; Simley et al. 2016] investigate the induction zone in free inflow conditions. The most detailed three-dimensional triple-synchronised lidar characterisation of the induction zone by [Simley et al. 2016] was performed around a Vestas V27 turbine with a diameter of 27 m, which is not representative of modern utility-scale multi-MW turbines.

Wind turbines operating in the downstream rows of wind farms are not always exposed to undisturbed inflow. Depending on the farm layout, wind direction, and wake effects such as meandering [Trujillo et al. 2011] and wake deflection strategies [Jiménez et al. 2009], the downstream turbines operate under partial or fully waked inflow. High-resolution measurements of the induction zone in partial and fully waked inflows are still limited. Engineering models of the induction zone have been developed to accurately estimate the annual energy yield and implement flow control strategies. Medici et al. 2011 presented a 1-D model for the induction zone using a vortex sheet method. [Branlard and Gaunaa 2015] developed a 2-D induction zone model based on a vortex cylinder implementation. Troldborg and Meyer Forsting 2017 presented a self-similar analytical 2-D induction zone model. Branlard and Meyer Forsting 2020 coupled these models with the wind farm simulation tool FLOw Redirection and Induction in Steady State (FLORIS) [NREL 2023] to provide flow estimations for wind farm control purposes. Although the coupling was evaluated against actuator disk simulations, a comparison with full-field data has not yet been performed because of the lack of high-quality field measurements.

Lidars are capable of measuring the velocity through the Doppler shift remotely and provide a way to measure the flow around wind turbines in the field [Werner and Streicher

The contents presented in this chapter have been published as: A. P. Kidambi Sekar, P. Hulsman, M. F. van Dooren, and M. Kühn. Synchronised WindScanner Field Measurements of the Induction Zone Between Two Closely Spaced Wind Turbines. Wind Energy Science, 2024, DOI: 10.5194/WES-9-1483-2024.

^{© 2024} by the authors. Reproduced in accordance with the Creative Commons Attribution 3.0 License.

5.1 Introduction 95

2005]. Field measurement campaigns using scanning lidars provide valuable data which can be used to characterise the induction zone behaviour for highly dynamic inflow conditions, atmospheric stabilities, and turbine interactions. However, conducting full-field measurements is challenging because of the complicated installation, highly dynamic inflow conditions, finite number of measurement sensors, and their associated limitations and uncertainties, which add complexity during post-processing. Multi-lidar systems such as WindScanners [Simley et al. 2016] can perform user-defined trajectories, whereby the laser beams are synchronised in space and time, enabling the resolution of two or three wind velocity components depending on the number of devices used. These devices have been used previously to map the induction zone [Simley et al. 2016], measure the flow around trees [Angelou et al. 2021], helicopter downwash [Sjöholm et al. 2014] and in the wind tunnel [Hulsman et al. 2022b; van Dooren et al. 2017; van Dooren et al. 2022]. Depending on the orientation and scan pattern, detailed two- or three-dimensional flow retrievals are possible. However, a thorough error and uncertainty assessment is required before interpreting the measurements, owing to the lidar measurement principle and scanning limitations, such as the volume averaging effect, assumptions on the vertical velocity for dual-Doppler reconstruction, scanning speeds, beam pointing, and intersection accuracies. Several studies have been conducted to estimate the measurement accuracy of scanning lidar retrievals. [van Dooren et al. 2017; van Dooren et al. 2022] presented an uncertainty analysis considering the lidar measurement uncertainty and the artificially added uncertainty of the dual-Doppler reconstruction for a two-lidar configuration. Giyanani et al. 2022 presented an uncertainty model to reconstruct a 3D wind vector considering the probe volume and the pointing accuracy for a three-lidar configuration. Emulating lidar measurement properties in high-fidelity CFD simulations provides a high-quality reference for error assessment and uncertainty quantification. Such approaches have been extensively utilised to understand long-range, pulsed scanning lidar measurements and their limitations [Bromm et al. 2018; Lundquist et al. 2015; Rahlves et al. 2022b; Robey and Lundquist 2022]. For continuous-wave systems, [Debnath et al. 2019; Kelley et al. 2018] used virtual-lidar in Large-Eddy Simulations (LES) approach to evaluate the accuracy of retrieving horizontal wind speeds for turbine-mounted wake scanning lidars considering effects such as probe volume averaging, assumption of zero vertical velocity and atmospheric effects such as stability. Meyer Forsting et al. 2017 utilised a virtual lidar technique to understand the influence of measurement averaging on wake measurements. They reported that the differences between lidar and point measurements are greatest at wake edges where the probe volume extends from the wake into the freestream reaching up to 30 % at 1 D downstream up to 60 % at 3 D downstream.

In this study, two synchronised ground-based continuous-wave WindScanner lidars were used to characterise the flow region between two 3.5 MW turbines, which were spaced $2.7\,D$ apart. The very short spacing creates an interaction between the near wake of the upstream turbine and the induction zone of the downstream turbine. During the measurement campaign, we implemented an active wake steering control on the upstream turbine. The near wake-induction zone interaction is of interest for wake steering control. Therefore, cases such as partial and full wake impingement with the induction zone are examined.

Considering the measurement campaign, the main objectives of the paper include:

- Demonstration of two-dimensional scanning of wind fields around utility-scale turbines with two synchronised WindScanner lidars.
- Identification and investigation of errors associated with performing ground-based synchronised scanning lidar measurements with two WindScanner in a controlled simulation environment.
- Characterisation of the two-dimensional induction zone behaviour and interaction between two closely spaced turbines for unwaked, waked and partial wake scenarios and evaluation of induction zone models.

The remainder of this paper is organised as follows. Section 5.2 describes the measurement and LES simulation setup. The results from the LES simulations and the full field measurements in Section 5.3. A discussion of the results and conclusions are presented in Section 5.4 and 5.5 respectively.

5.2 Methods

A description of the wind farm layout and the measurement setup is provided in Subsection 5.2.1. Subsection 5.2.2 contains information on the WindScanners, the programmed scan trajectories, and the data processing methods. The collected datasets are presented in Subsection 5.2.4. The setup of the Large-Eddy Simulation including the lidar simulator is explained in Subsection 5.2.5.

5.2.1 Test site description and inflow characterisation

The measurement campaign was conducted from November 2020 to June 2021 at a wind farm close to Kirch Mulsow in Northern Germany. The site has two eno126 turbines from eno energy systems GmbH with a rated wind speed of 11.4 m/s and power of 3.5 MW with a diameter D=126 m. The upstream and downstream turbines are abbreviated as WT1 and WT2 respectively.

5.2 Methods 97

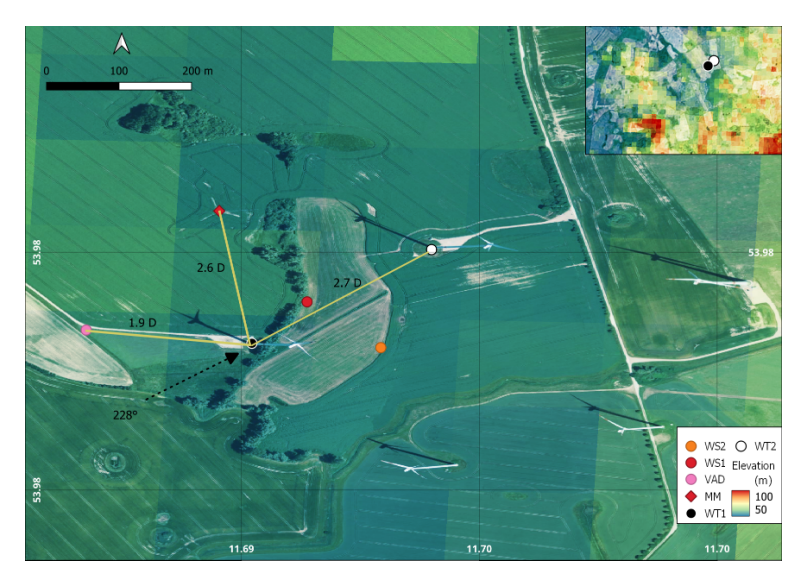


Figure 5.1: The wind park and measurement layout at Kirch Mulsow overlayed with elevation contours. A zoomed-out image of the site is shown in the top right corner illustrating the hills present upstream of the wind park. MM and VAD refer to the met mast and the inflow lidar while WS1 and WS2 refer to the two WindScanners. © Microsoft.

The layout of the site is illustrated in Fig. 5.1. The hub height of the downstream turbine at 137 m is 20 m higher than that of the upstream turbine at 117 m. The site itself is characterised as farmland with moderately rolling hills. The elevation data presented in Fig. 5.1 was obtained with a resolution of 200 m maintained by the German Ministry of Cartography and Geodesy. While the elevations at the turbine locations are approximately 52 m, abrupt changes in elevation are seen upstream notably the presence of a small hill with an elevation of 105 m, 22 D upstream of WT1 along the predominant wind direction of 228°. This creates a slope of 1.09° towards the two turbines. The village Garvensdorf was approximately 1200 m (9.5 D) upstream of WT1 along $\theta_{\rm wdir}$ = 228°. Furthermore, a treeline exists between WT1 and WT2 extending towards the met mast with a height of approximately 15 m to 20 m that can act as a windbreak and can cause perturbation to the wind flow [Counihan et al. 1974]. Other tree lines and clumps of forested areas are present at various upstream positions along $\theta_{\rm wdir}$ = 228°. During the measurement campaign, wake steering tests were performed on WT1 leading to partial wake scenarios at WT2. Additional information on the wake steering campaign is available in Hulsman et al. 2022a.

Inflow conditions were measured by a met mast placed 2.6 D north of WT1, equipped with two anemometers, Thies First Class Wind Transmitter anemometer of type 4.3352.00.400 at the lower tip of 54 m and close to the WT1 hub height of 116 m. A wind vane of type Thies First Class Wind Direction Transmitter of type 4.3151.00.212 is also installed at 112 m. All the instruments stored the data at a sampling rate of 50 Hz. To measure the atmospheric stability, an integrated CO_2/H_2O open-path gas analyser and 3D sonic anemometer (Irgason, Campbell Scientific) were also installed on the mast at a height of 6m on a boom oriented towards 136°. More details on the derivation of the Obhukhov length

from the Irgason are detailed in Bromm et al. 2018. The inflow measurements were further supported by a WindCube 200S lidar placed 1.9 D upstream of the WT1. The ground-based lidar was performing VAD scans with an elevation angle of 75° and with range gates set from 50 m to 840 m with a spacing of 5 m and a pulse length of 25 m. The accumulation times and angular speeds were 0.5 s and 30° s⁻¹, respectively. The data from the VAD scans were binned into 10-minute averages from which the wind shear and veer profiles were estimated. The turbine heading of WT1 and WT2 during operation was precisely measured using a differential GPS System of the type 3 Trimble ZephyrTM model. All the measurement devices were synchronised to the UTC time.

5.2.2 WINDSCANNERS

The WindScanners are continuous-wave (cw) scanning lidars with a steerable scanner head that users can program to perform any user-defined scan trajectory [Mikkelsen et al. 2017]. The steerable scanner head consists of two prisms connected to individual drives, which can be rotated independently, while a third motor is used to control the focal distance of the lidar. Each of the two prisms deflects the focused laser beam by $\pm 30^{\circ}$ to achieve a maximum measurement cone angle of 120° . In the present setup, the lidar can continuously sample line-of-sight speeds at a maximum sampling rate of 451.7 Hz. Two WindScanners were installed in the field in the region between the two turbines inside offshore containers for weather protection (Fig. 5.2 (a)).





Figure 5.2: (a) View of WS2 installed in a weatherproof container with WT1 in the background. The WindScanners were lifted through a hatch on the roof during operation using a hydraulic table. (b) The two laser beams from WS1 and WS2 simultaneously focused over a distance of approximately 200 m at WT2 onto a 5.3 cm by 8.6 cm laser beam detector card (white dots) after performing a steering calibration.

Both WindScanners synchronously provide a Doppler velocity spectrum for every measurement sample calculated from a discrete Fourier transform of the backscattered light

5.2 Methods 99

sampled at 120 MHz. The individual Doppler spectra are averaged to reduce noise, and the shot-noise-based mean background spectrum is removed to obtain the peak of the Doppler spectra. The line-of-sight velocity is estimated by determining the spectral peak through the median peak-finding method for continuous-wave lidars, as it is less sensitive to spurious noise than the centroid and maximum methods [Angelou et al. 2012].

A single lidar can only estimate the line-of-sight (v_{los}) speed along the laser beam direction that contains contributions from all three velocity components:

$$v_{\text{los}} = \cos(\gamma)\cos(\delta)u + \sin(\gamma)\cos(\delta)v + \sin(\delta)w, \tag{5.1}$$

where u,v and w are the longitudinal, lateral, and vertical wind velocity components, respectively, and χ and δ are the azimuth and elevation of the laser beam, respectively. By synchronising the two WindScanners in time and space, the WindScanners can estimate in the intersection point, the two dimensional wind speed component projected on the plane defined by the beams.

$$\begin{bmatrix} v_{\log,1} \\ v_{\log,2} \end{bmatrix} = \begin{bmatrix} \cos(\chi_1)\cos(\delta_1) & \sin(\chi_1)\cos(\delta_1) & \sin(\delta_1) \\ \cos(\chi_2)\cos(\delta_2) & \sin(\chi_2)\cos(\delta_2) & \sin(\delta_2) \end{bmatrix} \begin{bmatrix} u \\ v \\ w \end{bmatrix}$$
(5.2)

The u,v velocity components can be resolved by an additional assumption of the vertical flow component and combining the two v_{los} measurements by dual-Doppler wind field reconstruction by solving Eq. (5.2). Equation 5.2 can now be rewritten as:

$$u = \frac{\sin(\chi_2)\cos(\delta_2)(\upsilon_{\log,1} - \sin(\delta_1)w) - \sin(\chi_1)\cos(\delta_1)(\upsilon_{\log,2} - \sin(\delta_2)w)}{\cos(\delta_1)\cos(\delta_2)\sin(\chi_2 - \chi_1)}$$
(5.3)

$$\upsilon = \frac{\cos(\chi_1)\cos(\delta_1)(\upsilon_{\log,2} - \sin(\delta_2)w) - \cos(\chi_2)\cos(\delta_2)(\upsilon_{\log,1} - \sin(\delta_1)w)}{\cos(\delta_1)\cos(\delta_2)\sin(\chi_2 - \chi_1)}$$
(5.4)

In our measurements, the actual local value of the w component is unknown. Without generalisation, we assume that the vertical flow component to vanish in our case. The uncertainty associated with measuring three-dimensional flow events with two synchronous lidars is discussed in Section 5.2.3. Another important lidar measurement property is volume averaging, that is, the v_{los} measurements contain weighted contributions along a volume extending on either side of the focus point along the laser beam direction. The measured line-of-sight velocities of a cw lidar at the position $\mathbf{x} = (x, y, z)$, $v_{los}(\mathbf{x})$ can be mathematically expressed as the convolution of the wind vector $\mathbf{u}(\mathbf{x})$ projected along the laser beam direction and the volume averaging function:

$$v_{\text{los}}(\mathbf{x}) = \int_{-\infty}^{\infty} \phi(s) \mathbf{n} \cdot \mathbf{u}(s\mathbf{n} + \mathbf{x}) ds.$$
 (5.5)

Here, n is the unit vector along the line-of-sight direction and $\phi(s)$ is the spatial volume averaging function following Sonnenschein and Horrigan 1971 for cw lidars approximated as a Lorentzian function where s is the distance from the focal point along the laser beam. For cw lidars, the range weighting of line-of-sight speeds that occur along the laser beam direction at a point located at a distance f away from the lidar can be expressed as the Full

Width at Half Maximum (FWHM) of the focused laser beam $\Gamma=2\frac{\lambda f^2}{\pi a}$. Here, $\lambda=1.56~\mu m$ and a=56~mm are the laser wavelength and effective radius of the lidar's 6" aperture telescope, respectively. As the length of the measurement volume is related to f^2 , the measurement volume is quite large at large distances, and hence turbulent structures smaller than the measurement volume will be low-pass filtered by the lidar.

SCANNING PATTERNS

The region of interest within this work is the inflow of WT2. The WindScanners are programmed to perform spatially and temporally synchronised horizontal plane scans upstream of WT2. The measurement plane is at hub height and centred around the alignment of WT1 and WT2 at 228°. The WindScanners were not perfectly symmetrical to WT2 because of a tree line which prohibited symmetrical placement of WS1 with WS2 and WT2.

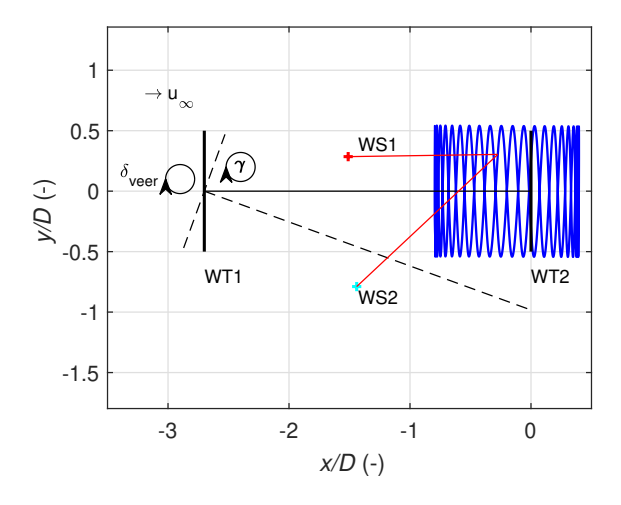


Figure 5.3: Illustration of the horizontal scanning pattern performed by the WindScanners, indicating the relative position of the two turbines and the two WindScanner with and without an intentional misalignment. The coordinate system is centred at the bottom of WT2.

The measurements are visualised in a global fixed reference frame centred at the bottom of WT2, where the x-axis is the connecting line between the two turbines, and the y- and z- axes are positive to the right looking towards WT2 and in an upward direction. The scan pattern was composed of a sinusoidal variation of the x-, y- coordinates of the focal point:

$$x(t) = A_{x} \sin\left(\frac{2\pi t}{T}\right) + x_{0} \qquad y(t) = A_{y} \sin\left(\frac{20 \cdot 2\pi t}{T}\right) + y_{0} \qquad z(t) = z_{0}. \tag{5.6}$$

Here $A_x = 0.60 D$, $A_y = 0.59 D$ are the amplitudes while $x_0 = -0.20 D$, $y_0 = 0 D$, $z_0 = 137.0 m$ are the offsets and T is the time period to complete each trajectory with each scan taking 29.6 s to complete. The horizontal scan plane at the hub height of WT2 extends from 0.8 D upstream of the turbine to 0.4 D downstream, with a width of 1.18 D as shown in Fig. 5.3. The offsets due to the terrain-induced height differences and the vertical offset of the

5.2 Methods 101

WindScanners inside the container mounting are included in Eq. (5.6), and are tabulated in Table 5.1.

Table 5.1: Relative and normalised distances from the bottom of WT2 and WS1, WS2 and WT1. The height offsets for WS1 and WS2 are calculated from the middle of the outer prism at the highest jacked-up position of the hydraulic table (Fig. 5.2 (a)).

	x (m)	y (m)	z (m)
WS1	-157.82 (1.25 <i>D</i>)	-112.37 (0.89 <i>D</i>)	-1.25
WS2	-54.04 (0.43 <i>D</i>)	-199.76 (1.59 <i>D</i>)	-0.60
WT1	-240.98 (1.91 <i>D</i>)	-234.04 (1.86 <i>D</i>)	-2.06
WT2	0	0	0

With a temporal sampling rate set at 451.7 Hz, each complete scan had approximately 13079 measurement points. In this sector, active wake steering was performed by toggling between two unique wake steering controllers and one greedy controller where no wake steering is performed, each operational for 35 minutes. The measurement campaign regarding the active wake steering is described in detail in Hulsman et al. 2022a. The WindScanner measurements are then subdivided into 35 min blocks, each representing a different operating state of the upstream turbine. All horizontal plane scans are grouped and averaged to obtain averaged profiles of the measured longitudinal and lateral velocities. For visualisation, the longitudinal and lateral velocities are interpolated using a cubic interpolation scheme onto a uniform grid with a spacing of 10 m. We rotated all measurements in the global reference frame into the main wind direction measured at the met mast at 1 m below WT1 hub height.

5.2.3 WINDSCANNER MEASUREMENT ERRORS AND UNCERTAINTIES

While performing synchronised WindScanner measurements, several errors affecting the measurement accuracy can be broadly divided into single- and dual-lidar errors. For this particular site and measurement setup, the various lidar errors, their impact and their analysis methodology are tabulated in Table 5.2.

Table 5.2: Summary of Dual-Doppler lidar measurement errors. Here, LES and SUP refers to Large Eddy Simulations and Standard Uncertainty Propagation methods that are described in the following sections.

Error	Source	Impact	LES	SUP
Single-Lidar				
$v_{\rm los}$ accuracy	Inaccuracy in estimation of radial wind speeds	Low		1
Probe volume averaging	Measurement volume variation during scanning	Medium	1	ĺ
Dual-Lidar				
Pointing accuracy	Imprecise pointing angles inherent to the lidar systems	Low		1
Dual-Doppler reconstruction error	Amplification of single-Doppler uncertainty due to dual-Doppler reconstruction	High	1	1
Statistical uncertainty	Flow turbulence combined with slow scanning times requires multiple scans	Medium	1	ĺ
Assumption of $w = 0$ m/s	Assumption for a dual-lidar setup	High	1	1

SINGLE-LIDAR ERRORS AND UNCERTAINTIES

First, we discuss the sources of the errors associated with single-lidar systems. For Wind-Scanners, the absolute measurement uncertainty of the lidar radial velocity estimation

was experimentally determined by Pedersen and Courtney 2021 to be less than 0.1% under nearly ideal conditions.

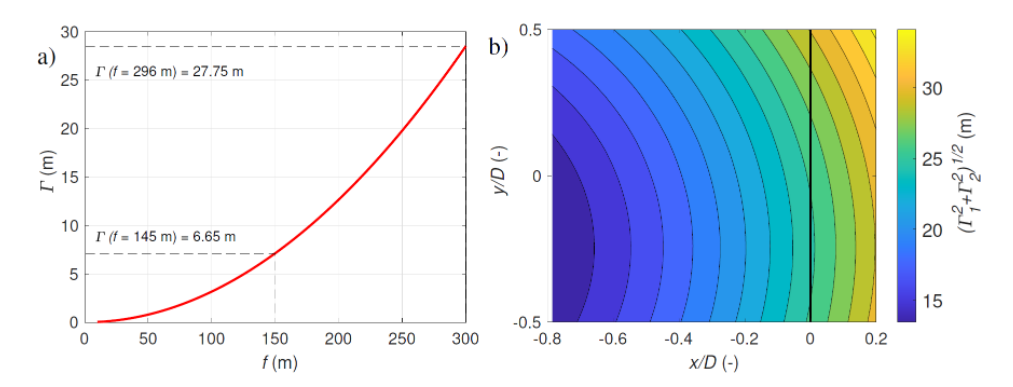


Figure 5.4: (a) The variation of the lidar measurement volume with focus distance. The dashed lines indicate the minimum and maximum measurement ranges, and (b) the variation in the effective lidar measurement volume within the scanning area.

While performing scanning cw lidar measurements, a variable measurement volume exists throughout the scan area. For the horizontal scans, the WindScanners measured at distances from 145 m to 296 m, corresponding to a probe volume ranging from 6.65 m (0.05 *D*) to 27.75 m (0.21 *D*), as shown in Fig. 5.4 (a, b). The WindScanners with their larger 6" aperture and shorter focus rods enabled the probe volume to remain below 30 m (0.24*D*) even at the maximum 300 m range in comparison to the previously used 3" WindScanners with smaller aperture [van Dooren et al. 2017]. The probe volume averaging effect is a significant source of uncertainty, especially at considerable focus distances, as it can lead to a measured wind speed bias in a sheared flow. This effect concerns our study as it is most severe for measurements at the wake edges, as the measurement volume extends from inside the wake to the freestream, and for measurements very close to the downstream turbine WT2, as the measurement volume would extend partially into the turbine wake. Due to range weighting, velocity measurements are subject to spatial filtering that attenuates the high-frequency wind information, which makes estimates of small-scale turbulence challenging at large focal distances.

DUAL-LIDAR ERRORS AND UNCERTAINTIES

Next, we discuss dual-Doppler pointing accuracy, which concerns the ability to steer the focused laser beam to a predefined point in space. To enable dual-Doppler wind field reconstruction, the laser beams from the two WindScanners must focus and be spatially and temporally synchronised with each other. The scanner orientation and levelling were thoroughly checked in a controlled laboratory. The final calibration of the steering motors was performed using the turbine tower and a rotating setup as hard targets, and by locating the laser beams using an infrared sensor card (Fig. 5.2 (b)). A pointing accuracy of 0.1° was determined in the field from the commanded and actual positions of the motors steering the prism. The temporal synchronisation of WindScanners was validated in a previous

5.2 Methods 103

wind tunnel campaign by van Dooren et al. 2022 and in the field by Giyanani et al. 2022. Giyanani et al. 2022 also estimated similar ranges for the pointing accuracy and calculated the effective intersection diameter at the intersection volume of laser beams to be in the order of 2 m to 5 m.

Due to the spatial and temporal variation in turbulence and the scanning strategy that requires a finite amount of time to complete each scan, the dominant flow features in the induction zone would not be revealed until multiple scans are collected and averaged. The chosen averaging period must allow the mean velocity measurements to converge while maintaining similar flow conditions throughout the scan duration. Simley et al. 2016 showed that for their measurements where each longitudinal scan took 10 seconds to complete, the dominant flow features were revealed after averaging for at least 3 minutes (18 scans) while the results were presented as 10-minute (60 scans) averages. In our setup, owing to the active toggling of the yaw controller on WT1, the inflow into WT2 changed every 35 minutes; hence, a maximum of only 71 complete scans were available for ensemble averaging over 35 minutes. The ability of WindScanners to capture salient flow features in the induction zone is further investigated in Section 5.3.1 through statistical uncertainty analysis.

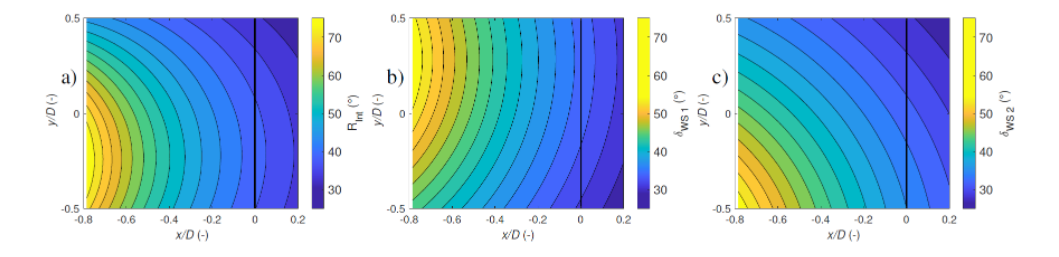


Figure 5.5: The variation of the beam intersection angle $R_{\rm int}$ (a) and the elevation angles, $\delta_{\rm WS1}$ (b), $\delta_{\rm WS1}$ (c) in the scanning area. WT2 is represented by a black vertical line at x/D=0.

The error in the dual-Doppler reconstruction is dependent on the relative alignment $R_{\rm int}$ of the laser beams to each other, which depends on the lidar position and measurement trajectory [Peña and Mann 2019; Stawiarski et al. 2013]. If the two laser beams are aligned with each other and with the main wind direction, the longitudinal wind component can be estimated accurately, whereas the orthogonal wind speed component cannot be accurately reconstructed. In other words, when the intersection angle tends towards 0° or 180°, the lateral component cannot be resolved. Figure 5.5 (a) illustrates the variation of $R_{\rm int}$ in the scan plane which decreases from 68° at x/D = -0.8 to 34° at x/D = 0.2.

The rotation in the wake of the upstream turbine induces a non-negligible vertical component in the flow. Therefore, the w = 0 m/s assumption to obtain Eq. (5.2) contributes to an error in dual-Doppler reconstruction. As the WindScanners are programmed to scan at the WT2 hub height (137 m), the corresponding elevation angles for WS1 (28° to 55°) and WS2 (25° to 56°) introduce a directional bias (Fig. 5.5 b, c). Hence in Eq. (5.1), the spatial variation of the non-zero vertical component and the corresponding $\sin(\delta)$ terms are a major error source, especially at measurement points with large elevation angles. While

installing the lidars closer to WT1 would reduce the required elevation angles, the lidar position was dictated and limited by the maximum achievable 300 m of range and available installation area.

Furthermore, we calculate the total uncertainty in the estimation of the longitudinal (e_u) and lateral (e_v) wind components by applying the Standard Uncertainty Propagation (SUP) method [Stawiarski et al. 2013; van Dooren et al. 2017] on Eqns. 5.3 and 5.4. Assuming small errors and zero correlation between them, the method considers the total propagated uncertainty in the dual-Doppler reconstruction due to beam intersection angles, pointing errors, and line-of-sight estimation errors due to neglecting the vertical flow component, and is described by the following equations:

$$e_{u} = \sqrt{\left(\frac{\partial u}{\partial v_{los,1}} e_{v_{los,1}}\right)^{2} + \left(\frac{\partial u}{\partial v_{los,1}} \sin(\delta_{1}) e_{w}\right)^{2} + \left(\frac{\partial u}{\partial v_{los,2}} e_{v_{los,2}}\right)^{2} + \left(\frac{\partial u}{\partial v_{los,2}} \sin(\delta_{2}) e_{w}\right)^{2} + \left(\frac{\partial u}{\partial \chi_{1}} e_{\chi_{1}}\right)^{2} + \left(\frac{\partial u}{\partial \chi_{2}} e_{\chi_{2}}\right)^{2} + \left(\frac{\partial u}{\partial \delta_{1}} e_{\delta_{1}}\right)^{2} + \left(\frac{\partial u}{\partial \delta_{2}} e_{\delta_{2}}\right)^{2}}$$

$$(5.7)$$

$$e_{v} = \sqrt{\left(\frac{\partial v}{\partial v_{los,1}} e_{v_{los,1}}\right)^{2} + \left(\frac{\partial v}{\partial v_{los,1}} \sin(\delta_{1}) e_{w}\right)^{2} + \left(\frac{\partial v}{\partial v_{los,2}} e_{v_{los,2}}\right)^{2} + \left(\frac{\partial v}{\partial v_{los,2}} \sin(\delta_{2}) e_{w}\right)^{2} + \left(\frac{\partial v}{\partial \chi_{1}} e_{\chi_{1}}\right)^{2} + \left(\frac{\partial v}{\partial \chi_{2}} e_{\chi_{2}}\right)^{2} + \left(\frac{\partial v}{\partial \delta_{1}} e_{\delta_{1}}\right)^{2} + \left(\frac{\partial v}{\partial \delta_{2}} e_{\delta_{2}}\right)^{2}}$$
(5.8)

where $e_{v_{los,1}}$, $e_{v_{los,2}}$ are line-of-sight errors, e_w is the error due to assumption of zero vertical velocity, i.e., the true value of w and e_{χ_1} , e_{χ_2} , e_{δ_1} and e_{δ_2} are lidar pointing errors. All the uncertainty terms in the paper are the 1.96 σ values of the corresponding error distributions; i.e. they are expected to include 95 % of all values. While SUP can be used to understand the influence of different aspects concerning measurement accuracy, not all errors can be studied in detail due to lack of references. Therefore, we also used additional lidar simulations to understand and quantify the different errors affecting the dual-Doppler reconstruction. The impact of the measurement volume, averaging times, lidar placement, and trajectory on the measurements is qualitatively investigated in Section 5.3.1 using a virtual lidar within LES.

5.2.4 MEASUREMENTS

As the region of interest was the zone between the two turbines, measurements were only performed when the turbines were aligned, i.e. when the wind direction was approximately 228°. We noticed that many measurements were also affected by unfavourable conditions such as rainfall and lower availability of aerosols to backscatter the laser beam. For operational safety reasons, the WindScanners were operated only with on-site personnel supervision. The measurements were further influenced due to the presence of the wind turbine nacelle and the rotating blades that would systematically reduce data availabilities in the scan region. We present exemplary measurements of four cases made during February 2021, which are summarised and tabulated in Table 5.3.

In Case 1, WT1 was switched off while WT2 was operational; hence, an undisturbed induction zone upstream of the turbine WT2 was expected. In Case 2, the two turbines were active and aligned, creating a full-wake inflow scenario for WT2. Cases 3 and 4 are measurements conducted while the wake steering control was active on the upstream turbine with averaged measured yaw offsets of 12.8° and -8.9°, respectively, creating a partial wake scenario at WT2.

5.2 Methods 105

Table 5.3: Overview of the measurement cases acquired in the field. Each case is characterised by its freestream wind speed u_{∞} , turbulence intensity (TI), integral length scale (T_i), mean θ_{wdir} and its standard deviation within the measurement period, stability parameter (z/L), stability, wind veer (γ), α_{shear} and the yaw offset of the turbines (γ_{WT}). Here the following abbreviations are used: Strong Stable (SS), Weakly Stable (WS) and Near Neutral (NN)

Case	Duration	u_{∞}	TI	$T_{\rm i}$	$\theta_{\text{wdir}} \pm \sigma_{\text{wdir}}$	z/L	Y	$\alpha_{ m shear}$	Status	∤WT1	YWT2
	(min)	(m/s)	(%)	(s)	(°)	(-)	(°)	(-)	WT1 /WT2	(°)	(°)
1	53	8.51	9.30	9.4	225.3 ± 9.1	0.040 (WS)	2.1	0.21	Off /On	3.7	0.9
2	35	9.60	7.68	10.5	225.3 ± 7.1	0.003 (NN)	19.8	0.38	On /On	-1.3	0.6
3	32	8.11	7.80	11.1	217.1 ± 9.8	-0.034 (NN)	13.3	0.23	On /On	12.8	2.2
4	26	8.68	5.39	9.1	227.2 ± 4.4	1.307 (SS)	19.4	0.49	On /On	-8.9	-1.1
LES	35 mins	7.77	6.7	4.5	228 ± 4.4	- (SS)	20.7	0.44	On /On	0	0

The freestream wind speed u_{∞} , turbulence intensity TI, wind direction θ_{wdir} and its standard deviation were calculated using the anemometer and wind vane at the hub height of WT1 placed on the met mast. The integral time scales $T_{\rm i}$ are calculated following Cheynet et al. 2016 by integrating the auto-correlation function till the first zero crossing. The atmospheric stability of the boundary layer can be characterised well by the Monin-Obhukov similarity theory [Barthelmie 1999; Monin and Obukhov 1954]. The Obhukov parameter (z/L) was measured by the eddy covariance station at a height of 6 m above the ground. The Monin-Obhukov length was calculated as:

$$L = \frac{-u_*^3 \theta_s}{kg(\overline{w'\theta'_s})},\tag{5.9}$$

where u_* denotes the friction velocity, k=0.4 denotes the von Kármán constant, g denotes the acceleration due to gravity, θ_s denotes the sonic temperature, and $\overline{w'\theta'_s}$ denotes the buoyancy flux. The friction velocity is estimated as $u_* = (\overline{u'w'}^2 + \overline{u'v'}^2)^{\frac{1}{4}}$. The stability classification of the Obhukov parameter z/L is performed for 30-minute averages based on Wyngaard 2010, January and further used in [Simley et al. 2016], where negative values indicate the presence of unstable conditions ($z/L \le -0.04$), positive values ($z/L \ge 0.4$) correspond to stable conditions, and values close to zero ($-0.04 \le z/L \le 0.04$) are related to neutral conditions.

The wind shear profile was also estimated from the VAD lidar by fitting a shear exponent $\alpha_{\rm shear}$ based on the power law between the top and bottom blade tips. The test site experienced larger than expected values of wind shear with an average value of 0.3 throughout the measurement campaign [Sengers et al. 2023]. The wind veer γ was calculated from the VAD lidar as the difference in wind direction between the top and bottom blade tips, and was clockwise positive. The actual yaw offset $\gamma_{\rm WT}$ was calculated by subtracting the GPS measured WT1 heading from the wind direction at the hub height measured from the met mast as follows:

$$\gamma_{\text{WT1}} = \theta_{\text{GPS},1} - \theta_{\text{wdir}}$$
 and $\gamma_{\text{WT2}} = \theta_{\text{GPS},2} - \theta_{\text{wdir}}$. (5.10)

A positive yaw misalignment was identified when the turbine was rotated clockwise looking from the top (Fig. 5.3). Data filtering for the field measurements was performed using a kernel density-based filter based on Beck and Kühn 2017 to identify and remove low-quality measurements. The method filters for the line-of-sight velocity and the Signal-Noise-Ratio

(SNR) in a bi-variate manner based upon the assumption of self-similarity of valid data. The method is applied on all the collected $v_{\rm vlos}$ measurements on the measurement plane and is capable of identifying hard targets such as the nacelle and blades through the clusters in the $v_{\rm vlos}$ - SNR space. The measurements are discretized and grouped into bins based on their $v_{\rm vlos}$ - SNR values. The frequency distribution of data points within each bin was then determined. Bins with frequencies exceeding 20 % of the most populated bin were retained for further analysis.

5.2.5 Numerical simulations of the experimental site

Before interpreting results, it is necessary to quantify the effect of lidar measurement error and uncertainties discussed in Section 5.2.3. To this end, we modelled the wind farm and inflow conditions in a simulation environment. The wind data are obtained from high-fidelity LES runs where the performance of two virtual WindScanners was assessed. The wind field was created using high-resolution LES performed with the Parallelised Large-Eddy Simulation Model (PALM). The PALM code is widely used for atmospheric boundary layer studies and works by solving the filtered, incompressible, non-hydrostatic Navier-Stokes equations. Further details of the model are available in Maronga et al. 2015. A single stably stratified LES run was performed and the two eno126 turbines are simulated with the actuator sector method using the Fatigue, Aerodynamics, Structures and Turbulence code (FAST) v8 [Jonkman et al. 2005], by the National Renewable Energy Laboratory (NREL) that is directly coupled with the LES [Krüger et al. 2022] allowing for the transfer of forces and velocities between the two simulations. The turbine FAST model was built using the aerodynamic properties, tower properties, and turbine controller provided by the farm operator. The eigenfrequencies of the FAST model of the two turbines are further tuned based on load data measured during the experiments. The WindScanners were simulated using the integrated lidar simulator (LiXim) developed by Trabucchi 2020 which can simulate lidar kinematic and optical properties. LiXim simulates the volume averaging property by discretising Eq. (5.5) in the LES while the uncertainty in beam pointing and environmental factors are not modelled.

An atmospheric boundary layer of stable stratification was simulated in a domain of dimensions 81 D x 20 D x 3.8 D with a uniform grid spacing of 5 m. Turbulence recycling [Lund et al. 1998] was applied at a distance of 15 D from the inlet, where the instantaneous wind fields of the precursor simulation are introduced into the main simulation. The potential temperature at the ground was set to 280 K. A potential temperature gradient of 1 K/100 m was prescribed from 100 m above the ground while the simulation was performed for 4800 s sampled at 5 Hz. For the analysis, the first 600 s of the simulation were removed to avoid transient effects, and only the final 35 simulation minutes were utilised to correspond with the field measurements. The terrain was modelled by prescribing a ground roughness length of 0.1 m. The simulated wind field has a mean wind speed at hub height u_{∞} = 7.77 m/s and a TI = 6.7%. The stable atmospheric boundary layer (ABL) is characterised by a strong shear exponent $\alpha_{\rm shear}$ = 0.44 and a wind veer of 20.7° between the top and bottom rotor tips. The virtual WindScanners are programmed to perform horizontal plane scans similar to the experimental setup following Eq. (5.6). The two operational turbines aligned in the prevailing wind direction in the LES resembled a full-wake scenario at WT2.

5.3 Results 107

5.3 RESULTS

This section is divided into two parts. In the first section, we show the results of the virtual WindScanner simulations in the LES and estimate the uncertainty associated with the dual-Doppler reconstruction. The results from the field measurements are presented in the second section. As the measurement plane extends 0.4 D downstream of WT2, laser beam blockage due to blade rotation was expected. During post-processing, it was discovered that the data quality for the measurements at $0.2 \le x/D \le 0.4$ was poor and hence was discarded for both LES and field measurements. A comparison against engineering models of the induction zone is shown only for the undisturbed induction case.

5.3.1 VIRTUAL WINDSCANNER EVALUATION IN LES

Line-of-sight simulations of the two WindScanners are performed using LiXim and the LES flowfield, after which a dual-Doppler reconstruction is applied to resolve the longitudinal and lateral wind fields.

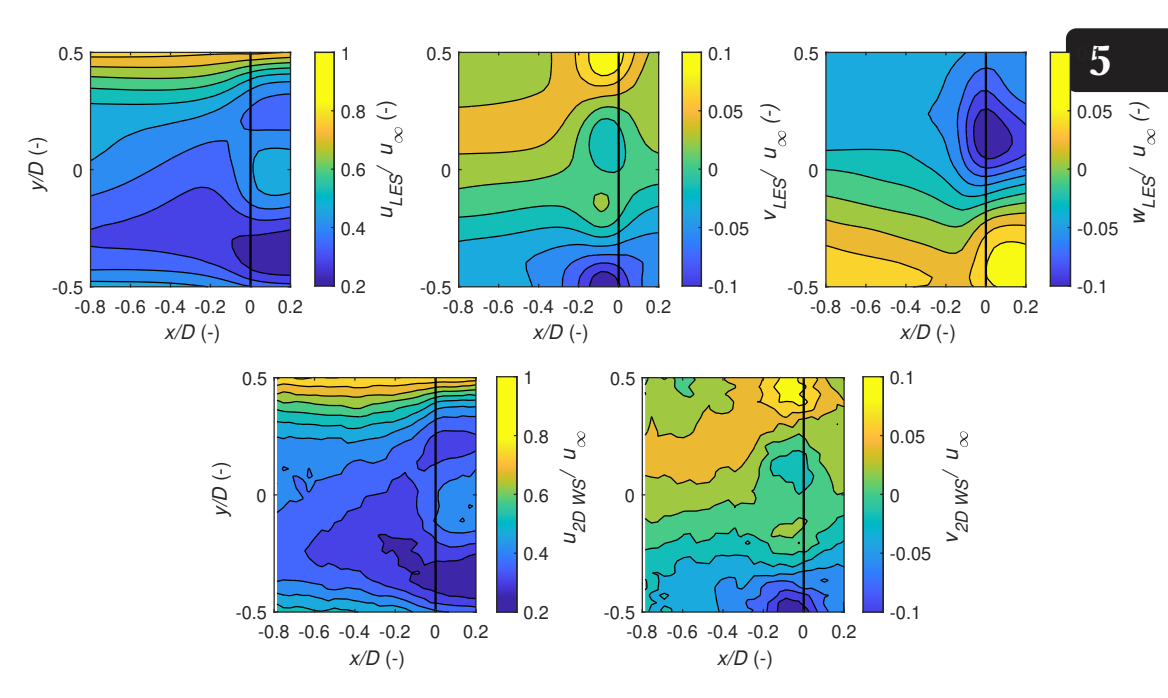


Figure 5.6: Longitudinal (u), lateral (v) and vertical (w) velocities on the horizontal plane from the LES (1st row) and the results of 2D WindScanner reconstruction inside the LES (2nd row) both averaged for the last 35 minutes of the simulation. The black vertical line at x/D = 0 is the rotor of WT2.

In Fig. 5.6, reconstructions of the WindScanner estimated 35-minute averaged longitudinal, lateral wind profiles are presented alongside the reference LES. A good qualitative agreement between the LES and the virtual WindScanner resolved u,v profiles is noted at most parts of the scanning area. The simulations reveal that the WindScanners can capture the spatial features in the flow such as the wake rotation and flow expansion at the

rotor tips. For the u profiles, the velocity profiles show deviations from the LES reference, presumably because of the directional bias induced by the large elevation angles and the probe volume extending through the shear layer and from the wake into the freestream. The lateral velocity profiles illustrating the wake rotation and flow expansion are captured well by the WindScanners. The profiles also indicate that the dominant flow structures in the induction zone are captured well for an average duration of 35 minutes when similar wind conditions are maintained for the scan duration.

STATISTICAL UNCERTAINTY

First, we discuss statistical uncertainty denoting the standard error of the mean. While the total propagated uncertainty regards the propagation of uncertainty of single variables through the dual-Doppler reconstruction, the statistical uncertainty quantifies the precision of the results from different scans with a higher number of scans typically reducing measurement noise from the statistical error. To quantify the statistical uncertainty, we use the margin of error estimated in the scanning area. It was calculated as $e_{\rm u,stat} = \frac{z_{\gamma}\sigma_{\rm u}}{\sqrt{N}}$ and $e_{\rm v,stat} = \frac{z_{\gamma}\sigma_{\rm v}}{\sqrt{N}}$. Here z_{γ} , the confidence level, is set to 1.96, denoting the 95 % confidence interval, $\sigma_{\rm u}$, $\sigma_{\rm v}$ are the standard deviations of the longitudinal and lateral velocity components in the scan plane obtained from the WindScanner simulations and N is the number of samples.

Application of these equations to calculate the statistical error requires a large number of uncorrelated samples. Therefore, the independence of the measurement samples is analysed by checking if the scanning time is long enough to ensure that the samples are separated by several multiples of integral length scales (Tab. 5.3). Tennekes and Lumley 2018 describe that, for statistical independence, sampling the wind once every two integral time scales is adequate. For our investigated cases, the scan time multiples of the integral length scale vary from 2.6 to 6.5. Therefore, while the measurements may not be entirely independent due to the relatively short integral time scale compared to the scanning time, they may still be treated as approximately independent.

We now calculate the statistical uncertainty using the $\frac{1.96\sigma}{\sqrt{N_s}}$ to estimate the statistical uncertainty where N_s is the number of independent samples. This effective sample size accounts for correlations in the turbulent flow, leading to a more accurate estimate of the error of the mean. The effective sample size is calculated based on Wilks 2019 as:

$$N_{\rm S} = N\langle \frac{1-r}{1+r} \rangle, \tag{5.11}$$

where r is the lag-1 auto correlation. Figure 5.7 shows the variation of the margin of error in the scanning area for the two reconstructed components. The margin of error for the longitudinal component varies in the scan area between 0.2 m/s to 0.4 m/s depending on the turbulence intensity in the wake. Similarly, for the v- component, the margin of error varies up to 0.21 m/s. The higher errors at scan edges could be attributed to the low amount of data points in these locations as a consequence of the scanning patterns. In the field, we expect that the margin of error would be slightly higher than in the idealised LES due to the filtering procedure reducing data availability in each scan.

5.3 Results 109

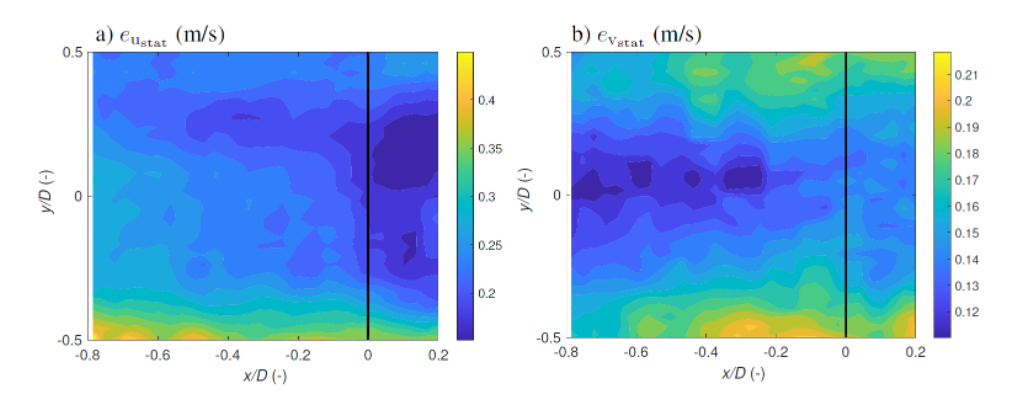


Figure 5.7: Statistical uncertainty estimated through the margin of error for the (a) u and (b) v components for the evaluated LES flow field.

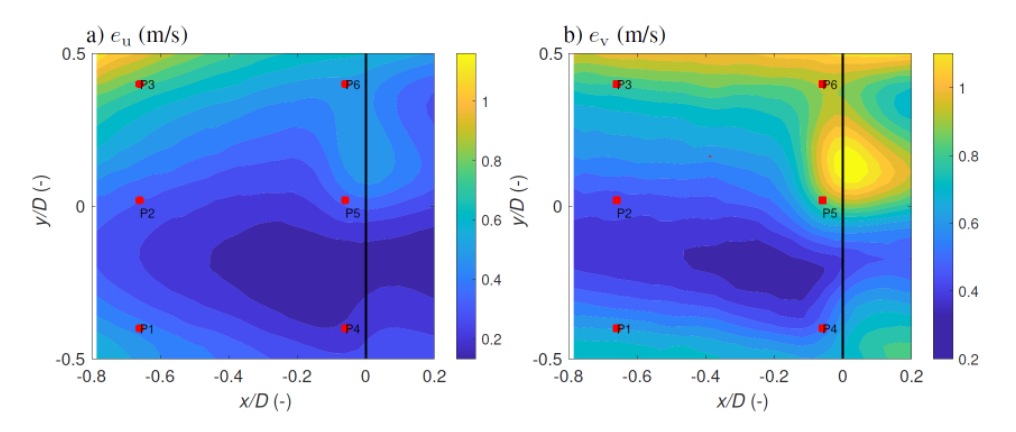


Figure 5.8: Dual-Doppler reconstruction error for (a) the longitudinal (e_u) and (b) the lateral (e_v) components for the evaluated LES flow field. The markers P1 - P6 indicate regions of interest.

DUAL-DOPPLER PROPAGATED UNCERTAINTY IN LES

Secondly, we discuss the total propagated uncertainties estimated through the SUP method. The total propagated errors in the estimation of the longitudinal and lateral wind speed components are performed based on Eqs. 5.7 and 5.8 and illustrated in Fig. 5.8. To study the influence of spatial velocity variation in the wake, the actual LES w component in Fig. 5.6 is used. The u component estimation error e_u varied between 0.2 m/s and 1 m/s. As expected, e_u is large at the WT2 rotor plane for the locations exhibiting higher w velocities. e_u is highest at the scan location closest to WS1 with the highest elevation angles whereby the lidars could only measure a small projection of the longitudinal wind speed. Similar behaviour is seen for the e_v as well ranging from 0.4 m/s to 1.1 m/s in the scanning area with the highest values seen where larger w velocities are present and at the scan area where the beam intersection angles are the lowest (Fig. 5.5).

Figure 5.9 illustrates the quadratic contributions of the different error terms in Eq. 5.7 and Eq. 5.8 and the total error for the respective flow component visualised for six locations

(P1, P2,... P6) as marked in Fig. 5.8. To analyse the contribution of certain measurement errors, the standard uncertainty propagation is evaluated for an error in $v_{\rm los}$ of 0.1 %, a pointing accuracy of 0.1° while the error introduced due to neglecting the vertical flow component is obtained from the local LES w component. The magnitude of the individual error contributions is normalised by the total error ($e_{\rm u}$, $e_{\rm v}$) to obtain the contribution of each term to the total error. For $e_{\rm u}$, the following trends are noticed. The line-of-sight error $e_{\rm vlos,i}$ contribution is almost negligible for all 6 points. The error due to the w component assumption $e_{\rm w,i}$ has a significant contribution to $e_{\rm u}$, especially at P4, P5 and P6 due to the large local w at these locations.

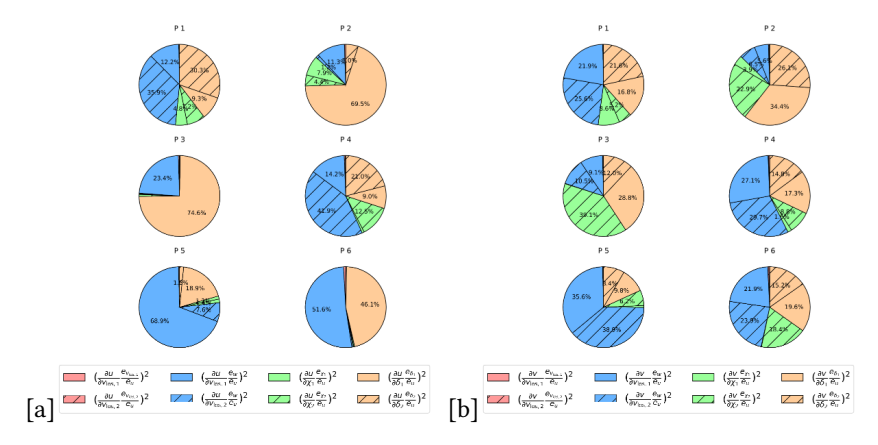


Figure 5.9: Quadratic contributions of the different error terms in the Standard Uncertainty Propagation (SUP) to the [a]] longitudinal (e_u) and [b] lateral (e_v) components at the marker

At P1, P2 and P3, e_{δ_i} has a large contribution due to the severe elevation angles required to scan at these points and the positive correlation between $\frac{\partial u}{\partial \delta}$ and δ . The varying contributions of $e_{w,i}$ at the points of interest can be explained by the relative alignment of the lidar with the wind direction. For a non-zero w component, an aligned lidar will contain a larger contribution of the w component projected onto its line-of-sight compared to the un-aligned case. At P1 and P4, the contribution of $e_{w,2}$ is the largest as WS2 is more aligned with the longitudinal wind component in comparison to WS1. Similarly, at P3, P5 and P6, WS1 is approximately aligned with the longitudinal wind speed component. So the errors at these points are dominated by the $e_{w,1}$, which is highest at P5 due to the large local w velocity in the LES field. For e_v , it is clear that the errors are preliminarily driven by the e_w while $e_{v\log_3 i}$ is almost negligible. However, the contributions of $e_{\chi,i}$ and $e_{\delta,i}$ are larger compared to that of e_u highlighting the sensitivity of the pointing angles for the lateral component reconstruction.

To visualise the reconstruction accuracy, horizontal velocity profiles are extracted at six upstream streamwise cross sections and compared against LES in Fig. 5.10. The shaded region illustrates the total measurement uncertainty where the statistical uncertainty and the propagated uncertainty are summed in quadrature assuming a perfectly calibrated lidar with no measurement bias and uncorrelated errors. This total combined uncertainty

5.3 Results 111

accounts for the statistical variability in the measured flow in addition to the variability due to the lidar limitations. The longitudinal velocity profiles measured by the virtual WindScanners at x/D < -0.63 exhibit deviations from the LES due to the large elevation angles required for scanning, while the estimation errors reduce towards WT2. Similarly, very close to the downstream turbine at x/D = -0.08, the WindScanner measured u profile is lower compared to the LES close to the rotor axis as the measurement volume extends behind the rotor while scanning very close to the rotor plane. At x/D = -0.8, the maximum u error is 11.6 %, while the error reduces in the downstream direction with a maximum error of 9.7 % at x/D = -0.63. The WindScanner-measured u velocity profiles at x/D = -0.56, x/D = -0.48, and x/D = -0.32 agree well with the LES. Moving further downstream, the difference in the intersection angles of the two lidars decreases. Therefore, the u component is estimated better on the scan's downstream side as the laser beams align with the prevailing wind direction with reducing elevation angles. While the intersection angle reduces towards WT2, the velocity profile at x/D = -0.08 shows slightly larger error bars due to a large vertical wind speed component resulting from local aerodynamic effects close to the rotor plane of WT2. The lateral velocity component profiles show a good agreement with the LES, with minor differences seen at the scan edges. The error bars around the vcomponent profiles are larger than the differences in the LES and WindScanner resolved profiles due to the inclusion of multiple error terms in the SUP. This indicates that the WindScanners can resolve the 2D velocity profiles with the current setup. While using the local w component in the SUP, it is seen that the observed velocity reconstruction errors are dependent on both the scanning strategy and the flow dynamics.

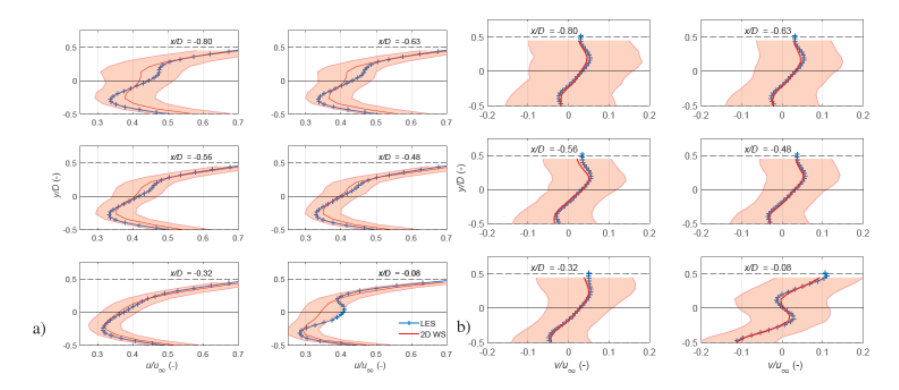


Figure 5.10: WindScanner estimated velocity profiles (red) of longitudinal (a) and lateral (b) velocities at six upstream cross sections compared against the reference LES (blue). The red shaded area indicate the total combined measurement uncertainty estimated through Eqn. 5.7 and Eqn. 5.8 using the local w velocity component.

5.3.2 Measurement results

This section illustrates and discusses the field measurements for the four measurement cases covering scenarios from undisturbed inflow to full and partial wake scenarios as described in Table 5.3. To calculate the propagated uncertainties using field data it is required to assume a constant w. For the full wake and partial wake cases, a value of w = 1 m/s is applied, similar to van Dooren et al. 2017. However, assuming a constant w

on the scanning area masks the velocity reconstruction error that is dependent on the flow dynamics, especially close to the rotor. Furthermore, this leads to a larger magnitude of e_u and e_v compared to the error when using the local w velocities directly.

THE UNDISTURBED INDUCTION ZONE

Figure 5.11 shows the averaged longitudinal and lateral wind velocities extracted from the WindScanner measurements of Case 1 in Tab. 5.3 with a mean wind speed of 8.51 m/s and a weakly stable stratification. The non-operating upstream turbine had an average yaw misalignment of 3.7° , whereas the downstream turbine had an average misalignment of 0.9° during the measurement period. The extent of the induction zone can be visualised by the *u*-component deceleration and is very strong within $-0.6 \le x/D \le 0$ upstream of WT2. This strong velocity deficit can be attributed to high axial induction and weakly stable stratification during the measurement period inhibiting vertical displacement of air particles further enhancing the blockage. The induction effect is strongest at the inboard blade stations and decreases towards the blade tips. The induction zone also exhibits a slightly asymmetrical distribution between the left (y/D > 0) and right sides (y/D < 0) of the rotor.

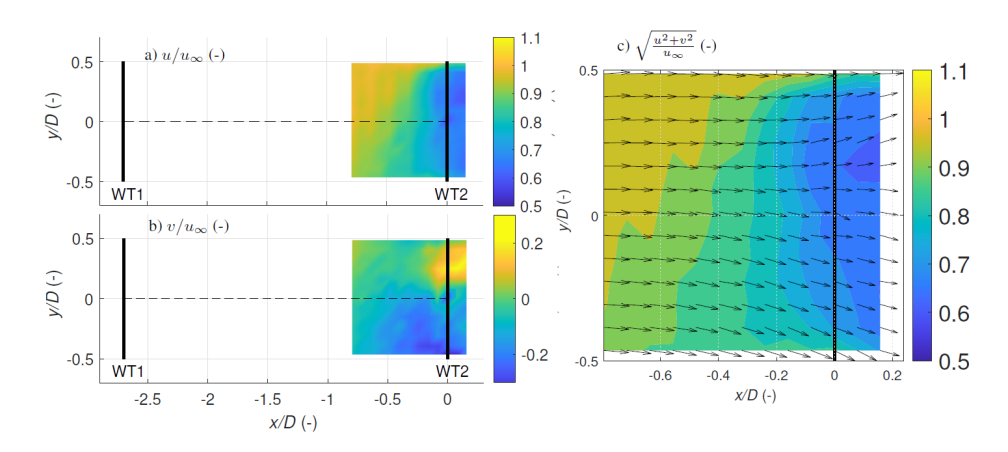


Figure 5.11: Case 1: Longitudinal (a) and lateral (b) velocities measured while WT1 was not operating and WT2 was operational. In (c), the quiver plot is based on the measured horizontal velocities.

Looking downwind, this slight asymmetry could be attributed to the presence of a tall treeline in-between WT1 and WT2 perturbing the flow by acting as a windbreak [Counihan et al. 1974; Tobin et al. 2017] and the strong vertical shear $\alpha_{\rm shear}=0.21$ that causes a vertical wind speed gradient varying the relative wind speed and the angle of attack of the blades during a rotation. Additionally, the induced velocities at the rotor plane are influenced by the counter-rotating wake creating a momentum transfer between the lower and upper rotor regions leading to a difference in flow magnitude between y/D > 0 and y/D < 0 [Madsen et al. 2012]. Hence, the blade sections would experience varying blade forces that vary the local thrust coefficient, and the corresponding deceleration. The lateral velocity component is non-zero close to the blade tips, indicating a flow expansion around

5.3 Results 113

the rotor. The large lateral velocities present close to the rotor plane can be attributed to the lower data availability due to blade passage, improper tracking of wind direction by WT2 influencing the induced velocities and neglecting vertical velocity in the dual-Doppler reconstruction. In Figure 5.11 (c), the u,v wind components within the scanning plane are combined to illustrate the wind direction behaviour in the scan plane, exhibiting an induction zone asymmetry and flow expansion around the WT2 rotor.

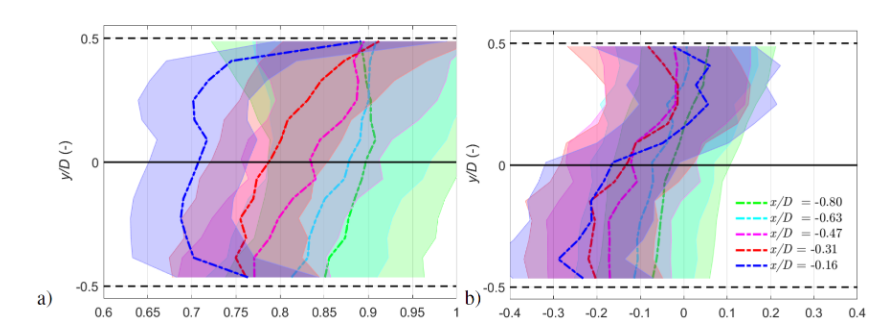


Figure 5.12: Case 1: Inflow longitudinal (a) and lateral (b) profiles extracted at various positions upstream of WT2. The shaded area represents the total combined measurement uncertainty calculated from the standard uncertainty propagation method (e_u) with w = 0.2 m/s, as WT1 was not operational.

In Fig. 5.12, horizontal inflow profiles at five upstream distances moving towards WT2 are plotted. The shaded regions indicate the total measurement uncertainty bounds calculated for the dual-Doppler reconstruction using Eq. (5.7), and Eq. (5.8). Here, a constant vertical component w=0.2 m/s is assumed, as no wakes are propagating from the non-operational upstream turbine and no direct measurements of the w component were available in the scanned area. The u component uncertainty due to the dual-Doppler reconstruction decreases moving toward the rotor. The horizontal profiles at $-0.8 \le x/D \le -0.31$ exhibit asymmetrical behaviour between the left (y/D>0) and right (y/D<0) blade tips, whereas at x/D=-0.16, the asymmetry disappears. The magnitude of the velocity deviations lies within the calculated uncertainty bounds. The lateral velocity profiles show a large magnitude very close to the rotor tips due to the flow expansion.

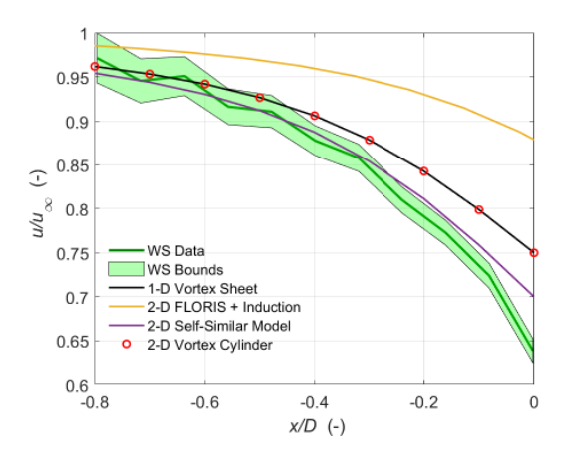


Figure 5.13: Case 1: Comparison of the velocity deceleration along the rotor axis against the predictions from different induction zone models. The green shaded area represents the upper and lower bounds of the total measurement uncertainty.

We compared the different induction zone models against the measurements along the rotor axis, as illustrated in Fig. 5.13. The upper and lower bounds of the WindScanner represent the propagated uncertainty bounds. Data availability between $0 \le x/D \le 0.2$ is reduced due to the presence of the nacelle and therefore excluded. Also plotted is the velocity deceleration predicted by the 1D vortex sheet theory [Medici et al. 2011] using the freestream velocity measured at the met mast extrapolated to WT2 hub height using the shear exponent and the axial induction factor of 0.23 estimated from the turbine thrust curve. The model-predicted velocity deceleration falls within the WindScanner bounds till x/D < -0.4 while the slowdown is under-predicted close to the rotor plane. Simley et al. 2016 also noted similar bias, the reasons for which were the model does not consider atmospheric stability nor the presence of the tower and nacelle-induced deceleration. The velocity deceleration predicted by the Vortex Cylinder model (VC model) [Branlard and Gaunaa 2015], FLORIS coupled with the Induction model (FLORIS+Induction) [Branlard and Meyer Forsting 2020] and the self-similar model [Troldborg and Meyer Forsting 2017] is also illustrated in Fig. 5.13 using the inflow conditions in Table. 5.3 as input parameters. Although these models can predict the upstream velocity deceleration in the horizontal plane, they do not consider the vertical shear. Therefore, only the deceleration along the rotor axis is displayed. The FLORIS+Induction model also utilises said VC method to predict the induction deceleration coupled with the Gaussian wake model in FLORIS accessed from Branlard 2019. As expected, the VC model shows excellent agreement with the 1D vortex sheet results but exhibits an under-prediction of the velocity decrease compared to the measurements. A similar under-prediction of the velocity decrease by the VC model was noted in Meyer Forsting et al. 2021 as no wake expansion is considered to affect the momentum balance between upstream and downstream of the rotor, which increases with increasing thrust coefficients, is included. Also shown in Fig. 5.13 are the results of the self-similar model proposed by Troldborg and Meyer Forsting 2017. Along the rotor axis, the model is similar to the VC model but contains an additional thrust-dependant scaling

5.3 Results 115

term to correct for the systematically underestimated axial induction. Applying their thrust correction factor, a better agreement with the WindScanner measurements is obtained until x/D < -0.4. The FLORIS+Induction model consistently under-predicts the magnitude of the velocity decrease along the centre line, with the effect becoming more severe towards the rotor. The axial induction and, therefore, the deceleration obtained from the FLORIS model were lower compared to the field measurements.

THE FULLY WAKED INDUCTION ZONE

This section presents the results of Case 2, with $u_{\infty}=9.60$ m/s, $\theta_{\rm wdir}=225.3^{\circ}\pm7.1^{\circ}$ and wind veer $\gamma=19.8^{\circ}$ in a near-neutral stratification. During the measurement period, the upstream turbine was operated by a greedy controller that introduced an average yaw misalignment of -1.3° , while WT2 was misaligned with an average of 0.6° with the prevailing wind direction. Hence, a full-wake scenario at WT2 is occurring. The WindScanners were programmed to perform horizontal scans at the hub height of WT2. This resulted in scans capturing the WT1 wake on a horizontal plane 0.16~D above the hub height of WT1 owing to the hub height difference.

Due to the downstream turbine operation, an induction zone deceleration is observed inside the wake between $-0.5 \le x/D \le 0$ upstream of the rotor, as shown in Fig. 5.14. The lateral velocity component is dominated by a lateral flow towards the left side (y/D > 0) of the rotor looking downstream. The flow expansion around the downstream turbine can be observed with stronger lateral velocities on the left side of the rotor (y/D > 0) looking downwind.

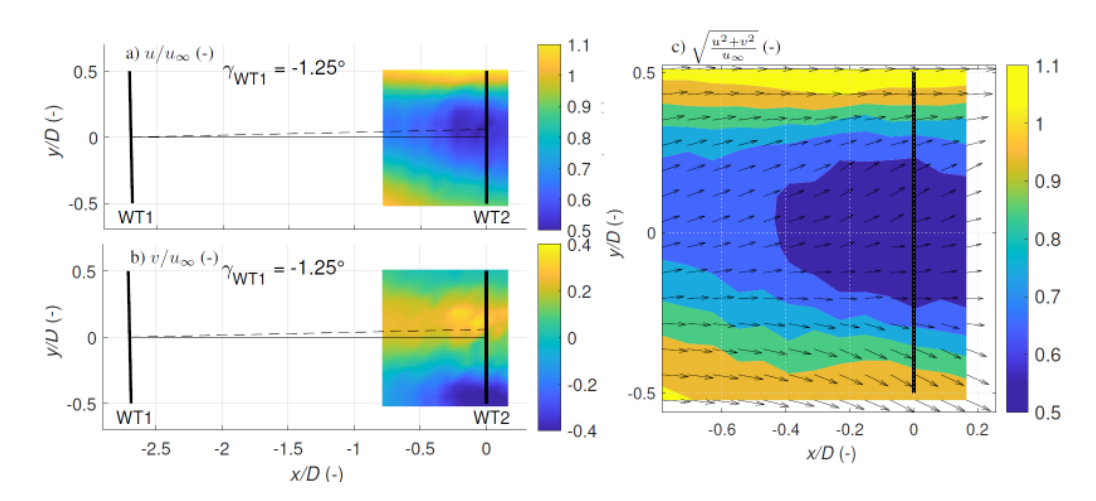


Figure 5.14: Case 2: Longitudinal (a) and lateral (b) velocities measured for the full wake case. The contour of the magnitude of the horizontal velocity and its vector field is plotted in (c).

In the region, $-0.8 \le x/D \le 0$ and $-0.1 \le y/D \le 0.3$, a strong cross-wind component is introduced to the wake that rotates in the opposite direction to that of the clockwise rotating rotor. By combining the u and v velocities, the local wind vector in the horizontal scan plane can be estimated. Plotted in Fig. 5.14 (c) is the total horizontal velocity magnitude U

superimposed with streamlines. A clear induction zone is visible centred around the rotor axis in the region $-0.5 \le x/D \le 0$ while the wake is expanded around the strong induction. Due to the proximity between the two turbines, an interaction between the induction zone of the downstream turbine with the wake of the upstream turbine is observed, while the wake deficit is further increased as the induction zone blocks and expands the flow around it.

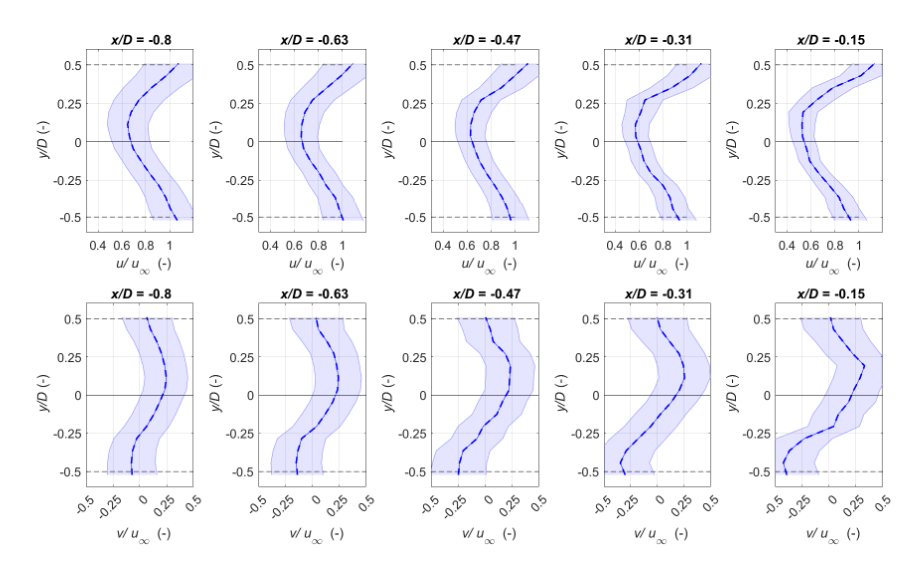


Figure 5.15: Case 2: Longitudinal and lateral velocities measured for the full wake case. The shaded area represents the total combined uncertainty calculated from the standard uncertainty propagation method (e_u) with w = 1 m/s, as WT1 was operational.

The horizontal flow profiles were plotted at five locations upstream of WT2, as shown in Fig. 5.15, to investigate the effect of WT2 induction on the wake profiles. As no measurements of the w component were available, a conservative value of 1 m/s has been utilised to estimate the upper and lower uncertainty bounds of the profiles. Instead of recovering, the longitudinal velocity profiles show a deceleration towards WT2. The effect of induction is strongest close to the rotor axis between $-0.2 \le \gamma/D \le 0.2$ where a velocity reduction of 27 % is observed between x/D = -0.8 and x/D = -0.15. The lateral velocity component shows a non-zero component between $-0.2 \le y/D \le 0.2$, indicating that the flow is pushed towards the blade tips and around the induction zone. The lateral velocity variations at the blade tips are due to the reduced data availability close to the blades ($x/D \ge -0.15$) due to blade passage and the yaw error of the downstream turbine. The turbine does not follow the wind direction perfectly; hence, time-varying yaw errors can be introduced, which would induce movement of the rotor within the scan area leading to erroneous estimates in the measurements. The lateral velocity profiles at different upstream positions exhibit a slight asymmetry. While terrain heterogeneity could explain some of the measured features, further differences with the undisturbed inflow case is expected due to the WT1 wake and differences in inflow conditions. For Case 2, the inflow is characterised by high shear and

5.3 Results 117

veer between the top and bottom rotor blade tips, in contrast to Case 1. This interaction of vertical shear with the wake can lead to an asymmetric velocity distribution as the wake rotation mixes the different layers of fluid in the vertically sheared flow [Abkar et al. 2018; Sezer-Uzol and Uzol 2013; Xie and Archer 2017]. At all five upstream positions, the wake at y/D < 0 exhibited stronger velocity reductions than the wake at y/D > 0, however, the magnitude of the velocity deviations are within the calculated uncertainty bounds.

THE PARTIALLY WAKED INDUCTION ZONE

Finally, we present the measurements of the induction zone upstream of WT2 during a partially waked condition shown in Fig. 5.16. The results for both positive and negative yaw offsets of WT1 are illustrated in Fig. 5.16. For a positive offset (Case 3: $\gamma_{WT1} = 12.8^\circ$), a wake deflection towards the left of the rotor (y/D > 0) is observed in the u component looking downstream, while the wake deflects to the right of the rotor (y/D < 0) for the negative offset (Case 4: $\gamma_{WT1} = -8.9^\circ$). For both cases, the partially waked inflow into WT2 is caused due to a combination of the yaw offset applied on WT1 and the misalignment of the wind direction with the orientation of the WT1-WT2 axis. For Case 3, the lateral velocity component is characterised by a flow towards the left side of the rotor (y/D > 0) due to a combination of the counter-clockwise wake rotation and the lateral force applied on the flow due to the intentional yawing of the turbine. The opposite effect is observed for Case 4, where a lateral flow towards the right side of the rotor plane is seen. The findings correspond to Fleming et al. 2018, where a stronger wake deflection for the positive yaw case is seen due to the aggregated effect of the wake rotation and counter-rotating vortices in comparison to the negative deflection case.

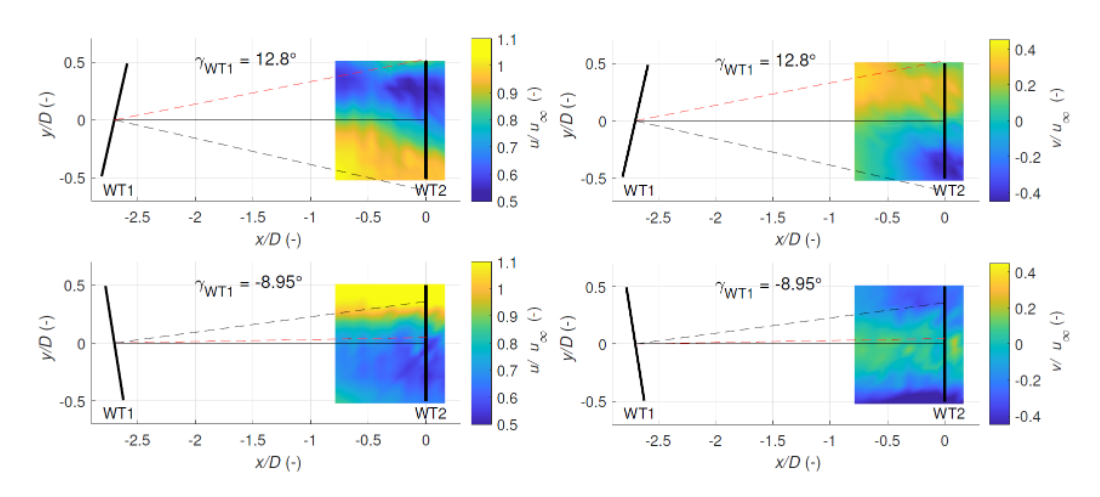


Figure 5.16: Cases 3 and 4: Longitudinal and lateral velocities measured for positive yaw offset (Case 3, 1^{st} row) and negative yaw offset (Case 4, 2^{nd} row). The red dashed line represents the average wind direction during the measurement period.

In both cases, the maximum magnitude of the lateral velocity inside the deflected wake is approximately 0.2 u_{∞} to 0.25 u_{∞} . The positive yaw offset case exhibits a comparatively more substantial lateral flow component compared to the negative yaw offset due to the 10°

misalignment between the turbine orientation and the wind direction as the lateral velocity would be increased by the projection of misaligned inflow into the defined coordinate system. As the measurements are in the near wake region of WT1, the lateral velocity would be additionally influenced by the aerodynamic effects of the rotor while the effect of yaw steering on the lateral component would be dominant further downstream. In both cases, the lateral component increases towards the blade tips to account for the flow expansion close to the downstream turbine. It is noted that for the positive offset case, the spatial distribution of the u component seems to move near the rotor axis instead of deflecting towards y/D > 0. This could be potentially attributed to the 10° misalignment between the wind direction and the turbine orientation direction in addition to the large variability of the wind direction from 208° to 223° which was the highest of all investigated cases.

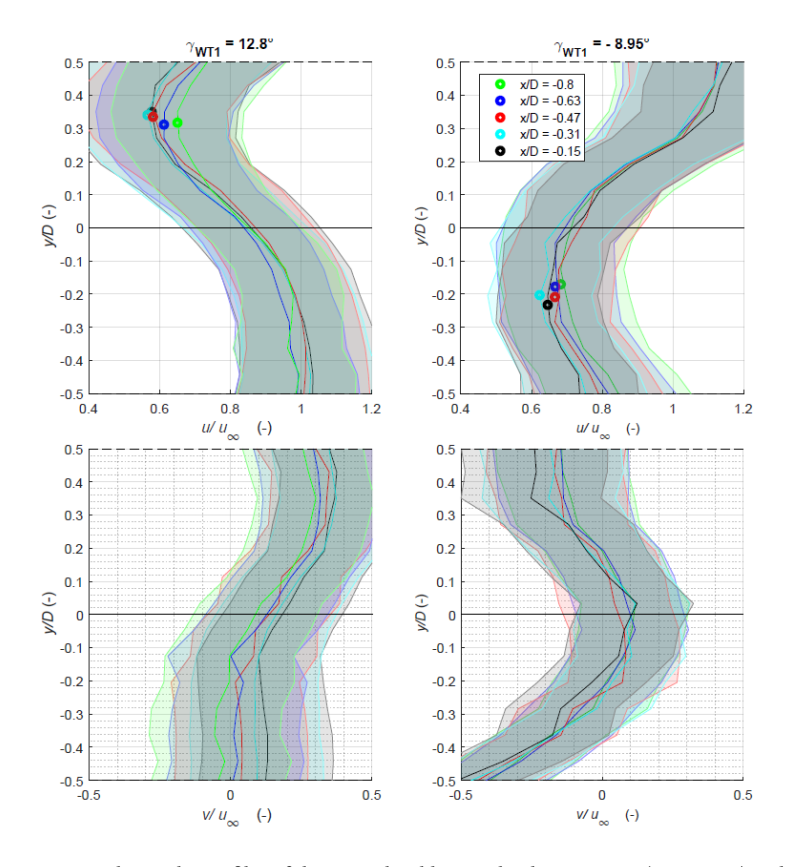


Figure 5.17: Cases 3 and 4: Wake profiles of the normalised longitudinal component (upper row) and the lateral velocity (lower row) extracted at various positions upstream of WT2 during active wake steering at WT1. The dots correspond to the wake centre at each location. The shaded area represents the total combined uncertainty calculated using the SUP method with $w=1~\mathrm{m/s}$.

Figure 5.17 illustrates the horizontal wake profiles of the longitudinal and lateral velocities

5.4 Discussion 119

at five distances upstream of WT2 for the two wake deflection cases. The dots correspond to the wake centre position determined by fitting a Gaussian through the measured wake profiles [Hulsman et al. 2022b]. For the positive offset γ_{WT1} = 12.8°, the wake centre deflects further to the left of the rotor to approximately y/D = 0.32. Similarly, the wake centre is deflected to the right to approximately y/D = -0.2 for negative offset γ_{WT1} = -8.9°. In both cases, the wake centre in the horizontal profiles does not exhibit significant lateral movement evidenced by the clustered wake centre locations in Fig 5.17. In both cases, a yaw-induced lateral flow is observed inside the deflected wake with a magnitude depending on the yaw offset and is present at the location of the maximum velocity deficit.

5.4 Discussion

We characterise the interaction of the near-wake and the induction zone between two closely spaced turbines with two synchronised scanning lidars. During the measurement campaign, yaw control is implemented on the upstream turbine. Hence, 2D characterisation of the induction zone of the downstream turbine is achieved for unwaked, waked and partial wake conditions.

Measurement campaigns require a comprehensive description of the measurement setup and appropriate uncertainty quantification to interpret results. As only two lidars were available for the experiment, an assumption on the vertical flow component, e.g. w = 0 m/s for the dual-Doppler reconstruction is necessary to extract two-dimensional horizontal flow fields. The location of the lidar and scanning trajectory have a significant impact on the measured velocity profiles. Therefore, to quantify the effect of the measurement setup and WindScanner limitations, we simulate the measurement scenario using a high-fidelity LES and a lidar simulator. Although such simulations might not completely capture the spatio-temporal dynamics observed in the field, they provide a complementary methodology for performance and quality assessment.

A comparison between the LES and the virtually simulated WindScanner indicates that the WindScanners can capture the main flow structures within a horizontal plane despite the used assumption (w = 0 m/s) and the inherent measurement principle limitations, such as directional bias and probe volume averaging. Analysis of the statistical and propagated uncertainties revealed that the former had in comparison a smaller uncertainty. For the longitudinal component, a maximum statistical uncertainty of 5 % and a maximum propagated uncertainty of 15 % relative to the mean wind speed was observed. A deeper analysis of the propagated uncertainties indicated that the main contribution to the uncertainty to estimate the u,v component was the w = 0 m/s assumption. Other important sources of the uncertainty were the probe volume averaging effect, the inaccuracy of the beamintersection angles and the beam-pointing errors.

The simulations highlight that spatial error variation also depends on the local vertical velocity distribution in the scanning area. This means that the reconstruction accuracy is not only lidar-dependent but also flow field dependent. Furthermore, the combination of the lidar-dependent errors and the vertical velocity increases the error, especially for a large elevation angle δ . Because no local vertical velocity measurements were available in the scanning area, a local vertical assumption was required to conduct the SUP. Therefore, the approach of van Dooren et al. 2016 was followed by assuming a conservative vertical

velocity of either 0.2 m/s (un-waked) or 1 m/s (waked) over the scanning area. This assumption masks the influence of the flow dynamics on the propagated errors and significantly increases the magnitude of the propagated errors. This complicates the analyses to determine significant flow features from field measurements, especially in waked cases. Further measurements with a third synchronised lidar are suggested to avoid the assumption of neglecting the vertical velocity and provide measurements with a lower uncertainty of the flow within the induction zone.

In the second part of this study, the full-scale experimental measurements using synchronised scanning lidar systems are analysed. Although accurate spatial and temporal synchronisation was achieved after careful calibration in the field, inherent uncertainties of the scanning lidar measurements need to be evaluated. The applied error of 0.1 % for $v_{\rm los}$ might be low for this measurement campaign. The work of Pedersen and Courtney 2021 suggested a 0.1% error in a highly controlled environment. van Dooren et al. 2022, used the same WindScanner lidars in a wind tunnel study and quantified the error against a hot wire anemometer with a mean average error metric less than 2 %. However, the probe lengths in their study were in the order of 13 cm. In the current field measurements, probe lengths in the order of 6.75 m to 27.75 m are measured increasing the expected error. Further measurements are required to obtain a representative e_{vlos} . This can be achieved by focusing the lidar next to a sonic anemometer to determine the impact of the probe volume effect on the line-of-sight measurements. Further WindScanner simulations indicated that the total propagated error was insensitive to a higher and more realistic 2 % line-of-sight error. An important aspect to consider during cw scanning measurements is the trade-off between spatial and temporal resolution. With a slower scan speed, the measurements cannot capture the fluctuating behaviour of the flow but only a fingerprint of the highly turbulent near wake. Moreover, the variable probe length during the scan causes a focal distance-dependent bias and therefore a variable low-pass filtering effect throughout the scan. Correcting for this effect is a challenging task and requires precise knowledge of the filtered and unfiltered spectra to either construct a transfer function or model [Angelou et al. 2012; van Dooren et al. 2022]. This was not performed in the current measurements. As expected, the measurements reveal the influences of the wake of WT1 on the induction zone of WT2. A longitudinal speed reduction towards the rotor plane is observed in the free inflow case. The lateral component shows a non-zero speed component towards the edges of the rotor, which indicates a flow expansion. An asymmetrical induction zone at hub height was also recorded and can be caused by multiple effects. This asymmetry can potentially be attributed to the dynamic interaction between the vertical shear and the rotating blades, which was noted by Bastankhah and Porte-Agel 2017 using wind tunnel measurements. Madsen et al. 2012 suggested that the induction zone at the rotor plane could be influenced by the counter-rotating wake creating a momentum transfer between the different rotor areas. Another possible effect of the observed asymmetry is the presence of a long and staggered treeline between the two turbines, which acts as a windbreak to the flow perturbing in the region between the two turbines [Counihan et al. 1974; Tobin et al. 2017]. Previous studies at the site (Hulsman et al. 2022a) have indicated the influence of a treeline on the met-mast measurements at 100 m elevation by comparing it against the ground-based lidar. A possible flow diversion by the treeline would indicate a larger vertical velocity component. This will lead to a larger uncertainty due to the necessary

5.5 Conclusions 121

assumption of w = 0 m/s to apply the dual-Doppler reconstruction. The magnitude of these terrain effects on the flow and the lidar measurements could not be quantified as no measurements were available when both turbines were non-operational. A high-resolution LES study incorporating the terrain and the treeline could be used to provide insights into the flow behaviour. However, the LES runs were intended to study the lidar measurement accuracy and therefore were only initialised with a similar roughness length to the terrain. An evaluation of various induction zone models is conducted, highlighting that the velocity deceleration modelled by the self-similar model [Troldborg and Meyer Forsting 2017] is in good agreement with the measurement data. More measurements covering more extensive operating and stability regimes would provide more insight. When both turbines were operational and aligned with the prevailing θ_{wdir} (fully waked), a clear overlap of the wake of WT1 and the induction zone of WT2 was observed. While vertical plane scans would have revealed the vertical shear and veer interaction with the wake, this was not investigated in the current study. The measurements during yaw steering show partial wake conditions impinging on either side of the rotor. It was expected that due to the partial wake inflow into WT2, the aerodynamic induction between the waked and unwaked parts of the rotor would differ impacting the distribution of induction zone deceleration over the rotor. However, these effects were not quantified in our study as the measured effects were within the uncertainty bounds of the measurements and therefore not significant enough. Additional measurements during partial wake conditions would be beneficial, especially with a third synchronised lidar, to study these interactions. While the hub height difference of 20 m between the two turbines would influence the measured induction zone and wake interaction, the effect could not be characterised as the presented study is specific to this two-turbine layout. The results of this study are based on four measurement cases containing 2-D flow within a horizontal scan performed at the hub height of the downstream turbine. However, future investigations should include measurements conducted with turbines at the same hub height and measure vertical planes or full rotor planes. This will aid in investigating the influence of atmospheric effects such as wind shear and veer. Multiple vertical plane measurements can also be performed to study the evolution of the flow field between the two turbines. A longer measurement campaign covering a range of shear and veer conditions including negligible veer and shear is suggested to investigate any possible correlations between atmospheric effects and the behaviour of the induction zone.

5.5 Conclusions

In this paper, results of a measurement campaign using two synchronised WindScanner lidars are presented which were used to capture the flow between two 3.5 MW utility-size turbines spaced 2.7 diameters ($D=126~\mathrm{m}$) apart. The lidar measurements were further supported by a ground-based lidar, a met mast and an eddy covariance station to accurately characterise the inflow. A detailed error analysis is performed by recreating the measurement procedure in a Large-Eddy Simulation where two virtual WindScanners were simulated to evaluate the dual-Doppler reconstruction accuracy. The reconstruction accuracy is influenced by the limitations of the measurement device, the reconstruction principle and the spatial variability of the vertical flow. The narrow turbine spacing and active wake steering on the upstream turbine allowed the characterisation of the induction

zone flow behaviour for free inflow, fully waked and partially wake scenarios. To the authors' knowledge capturing the 2-D flow both within the near wake and the induction zone during an intentional yaw misalignment in the field is measured for the first time. For a fully waked inflow, the impact of the induction zone on the wake was observed. This increased the wake deficit close to the rotor.

The study further highlights the challenges in conducting field measurements, and the additional considerations needed to characterise the induction zone behaviour. As field data is accepted as the ground truth and demanded for validating numerical models, a thorough characterisation of the site, the lidars, the measurements and their associated uncertainties are provided to ensure comprehensive traceability of the measurements. Further measurements, covering a larger range of inflow scenarios, preferably with a third synchronised lidar to avoid neglecting the vertical velocity in the dual-Doppler reconstruction, in conjunction with high-resolution simulations are suggested for further work to obtain a deeper understanding of the induction zone behaviour for various operational states of the turbine.

6

CONCLUSIONS AND OUTLOOK

High-resolution lidar measurements of the wind turbine inflow can be used to optimise turbine performance and reduce the levelised cost through load reduction, lifetime extension and enhanced power capture. This thesis's objective was to further understand the effectiveness of scanning lidars in measuring the inflow and develop novel wind field reconstruction algorithms capable of reconstructing spatio-temporal inflow dynamics from sparse data. Furthermore, the thesis also aimed at characterising the flow deceleration and evolution in the induction zone with synchronised scanning lidar systems, a critical aspect to consider while modelling the turbine inflow.

6.1 Conclusions

In the following the important outcomes of the identified research questions in Section 1.7 are summarised.

6.1.1 LIDAR MEASUREMENTS OF WIND TURBINE INFLOW

The temporal and spatial averaging of measurements as a consequence of the technological limitations is a concerning aspect while measuring the inflow with lidars. Therefore, the first part of the research (Chapter 2) was dedicated to understanding the lidar measurement principles and investigating the capability of lidars with fixed-beam and beam-scanning systems in accurately measuring the inflow. To this end, a virtual environment was used with high-fidelity physics-based wind field simulations based on Large Eddy Simulations. A lidar simulator to understand lidar measurement capabilities and uncertainties were utilised to simulate virtual lidars of different configurations. The highly customisable lidar setup combined with physics-based flow models allows investigating lidar performance for varying flow conditions. The results indicated that the ability of a lidar system to measure the inflow accurately depends on the measurement principle's limitations and the employed scanning strategy.

Directional bias is the most critical limitation affecting measurements due to the increased influence of the cross-wind components at large scanning angles. Combined with the larger effect of wind direction-turbine orientation alignment and the comparatively smaller

effect of the turbine operational tilt dynamics, this limitation would increase the angle between wind inflow and the laser beam, contributing to an even higher directional bias. Therefore, the estimation of longitudinal wind speed component through simple projection is sensitive to changes in the orientation of beam angles to the flow. While measurements of the stationary turbulent spectra are affected by the low-pass filtering due to the lidar volume averaging effect, modern scanning lidar systems like the SpinnerLidar can estimate the rotational spectra very well due to the extensive spatial coverage. This rotor area spatial coverage allows the lidar to capture effects such as vertical wind shear or partial gusts. In the rotating frame of reference of the blades such spatial inhomogeneties in the inflow lead to an accumulation of energy at multiples of the rotational frequency, ie., rotational sampling and eddy slicing effects. This extensive spatial coverage allows for advanced control strategies like correctional higher harmonics individual pitch control or trailing-edge flap control.

For cw lidar systems, the volume averaging effect does not significantly impact the estimation of wind evolution and is dominated by the upstream measurement distance and the atmospheric stability. A better estimate of the commonly used wind evolution coherence metric can be obtained by combining the upstream lidar measurements with a simple induction zone model to account for the flow deceleration. This allows the controller to utilise more information from the turbulent spectra, remove uncorrelated frequencies and avoid harmful actuation of the turbine control system.

The spatial resolution of the lidar is the deciding factor in the accurate estimation of the rotor averaged inflow parameters relevant for wind turbine control. For CPC and IPC strategies, scanning lidar systems can accurately estimate the rotor averaged wind quantities like rotor effective wind speeds and vertical shear. The coherence bandwidth and the smallest detectable eddy size are increased substantially due to the enhanced spatial coverage. However, the optimal upstream scan location is a variable quantity that also depends on atmospheric quantities like stability which can amplify the directional bias effects.

In general, with scanning lidar systems, the optimum scan location for scanning lidars for CPC control was much closer to the turbine than for fixed-beam devices, reducing the wind evolution uncertainty. Scanning systems are still comparatively expensive and unreliable as beam deflection mechanisms are required to steer the laser beam. In addition to the wind sensing capabilities, it is essential to include capital and operational expenses to estimate the value of integrating lidar systems into wind turbines for applications like control. However, as turbine loads scale over-proportionately with rotor size, the choice of scanning lidar systems could be attractive for larger turbines justifying the increased costs and being more economically viable.

6.1.2 Development of wind field reconstruction methods for scanning lidars

A line-of-sight velocity field reconstruction methodology based on Proper Orthogonal Decomposition was introduced in Chapter 3. The reconstruction performance was tested in two Large Eddy Simulations of different inflow conditions. In Chapter 4, the performance of the Gappy-POD was evaluated in reconstructing artificially removed measurement points simulating blade interference and non-ideal measurement conditions. To exploit the

6.1 Conclusions 125

capabilities of inflow measurements with scanning lidars, it was imperative that line-ofsight velocity field reconstruction methods fully utilise the provided high spatio-temporal resolutions.

With sufficiently high wind sensing rates, modal decomposition techniques such as POD could be applied to inflow lidar measurements. The application of POD to virtual SpinnerLidar measurements revealed the prospects of a reduced order description of the lidar measured inflow v_{los} fields with distinct spatial modes. The majority of the total energy was captured by a few dominant modes implying that reduced order models could be created just by considering these dominant modes alone. This data reduction is possible because of the probe length averaging property of the lidar that filters out the smaller turbulent structures. While the accurate representation of turbulent flows requires many modes, the measurements and the method appear synergistic. The entire two-dimensional spatially varying v_{los} wind field can be reconstructed with a very high level of accuracy in comparison to the existing wind field reconstruction models. An excellent agreement with the reference v_{los} wind fields is obtained while evaluating reconstruction accuracy based on various inflow metrics. This could be potentially advantageous while developing reduced order flow control strategies as the spatio-temporal dynamics of the measured wind field are effectively reduced to just a few signals. The spatial modes could be related to certain features in the wind inflow. However, the investigated LES cases are just two points in a vast parameter space. Therefore for the development of reduced order inflow models, changes in wind speeds, turbulence intensities, atmospheric conditions and the scenarios such as partial or full wakes or gusts must be considered along with the transition between these states. The reconstruction process is general because it can be applied to any lidar system with a high enough spatio-temporal resolution. Hence this method can be scaled with developments in scanning lidar systems' optical and mechanical capabilities. The Gappy-POD provided an efficient method to reconstruct missing or false data points providing a way to reconstruct low-quality measurements. The method overcomes a crucial problem with nacelle-mounted inflow lidars whose measurements are partially obstructed by the blades. A computationally efficient modification to the method allowed for reduced solution times to increase the feasibility of real-time implementation. By filling in missing measurement locations, the wind parameter estimation uncertainty due to data availability could be reduced, allowing for more confidence during actuating control surfaces for improving turbine performance. The method's effectiveness depends on the robust identification of the measurement locations with low quality/insufficient data. However, the reconstructed measurements with Gappy-POD would at least acquire the uncertainty of the measurements themselves.

6.1.3 CHARACTERISING THE INDUCTION ZONE WITH SYNCHRONISED LIDARS

A field measurement campaign was conducted where two synchronised scanning lidars were employed in a highly instrumented two turbine wind farm to characterise the inflow and the induction zone for waked and un-waked inflow scenarios.

With multiple synchronised lidar systems, it is possible to overcome the directional limitations and extract 2D or the whole 3D wind vector depending on the number of devices used. As only two synchronised scanners were available for this experiment, a lidar simulator in

LES based approach in a virtual environment was chosen to investigate the effectiveness of measuring the inflow with two scanners. Scanning lidar measurement campaigns require attention to tiny details such as effective steering calibration, scan head velocity and accelerations but provide valuable data to understand flow development around wind turbines. By methodically recreating the wind farm and the lidars and the employed scanning strategy within a simulation environment, it was possible to understand the effect of lidar limitations on the measurements. Therefore, virtual lidar simulations in LES was used to verify the methodology (measurement setup, scanning strategy, wind field reconstruction) and quantify the errors associated with the chosen methodology. Therefore, simulations and experiments can be complementary and should be used together during all phases of an experimental campaign.

Due to the large uncertainty in the measurements due to the limitations of the lidar and the wind farm layout, a detailed error analysis was conducted before the measurements could be interpreted. The measurements revealed that the induction zone of a wind turbine in undisturbed inflow, the induction zone is highly influenced by the terrain orography and wind shear. In the full-wake case, the measurements revealed a deceleration of the upstream turbine wake due to the downstream turbine induction zone due to short turbine spacing. During a wake steering experiment, the interaction between the laterally deflected wake of the upstream turbine and the induction zone of the downstream turbine could be measured for the first time in the field. While evaluating engineering models against measurements, it was noted that the models could not capture the asymmetrical induction zone deceleration as they do not consider vertical shear and did not model the terrain effects.

It was demonstrated that for wind parks with tight spacing, there was an interaction between the upstream turbine wake and the downstream turbine induction zone that blocked wake development and recovery. The measurements revealed an interaction between the partial wake and the induction zone for partial wake scenarios. A partial wake impinging on the weaker induction side of the rotor would decelerate slower than the stronger induction side of the rotor. However, this effect could not be clearly seen on the measurements due to the large uncertainty associated with the dual-Doppler reconstruction. If validated with future measurements, preferably with a third WindScanner to overcome the issue of the vanishing vertical velocity component in the dual-Doppler reconstruction, this could be potentially interesting for active wake steering, whereby deflecting the wake into the weaker induction area of the rotor would increase the rotor's effective wind speed, thus increasing the power output but presumably at the expense of higher asymmetrical rotor loads. Conversely, deflecting the wake into the stronger induction area of the rotor could reduce the asymmetrical rotor loads.

6.2 Outlook

This thesis focused on measurements of the wind turbine inflow with scanning lidar systems. A wind field reconstruction method based on Proper Orthogonal Decomposition for scanning lidars was developed and verified in a simulation environment. The wind field reconstruction methodology was further extended to reconstruct poor quality measurements and points lost due to blade rotation and interference for nacelle-mounted inflow sensing lidars. In addition, the induction zone was characterised using synchronised scanning lidar

6.2 Outlook 127

systems for undisturbed and waked inflows. Some next steps to extend the work are listed here.

In Chapter 2, the capabilities and advantages of utilising scanning lidar inflow measurements were discussed. As a next step, it could be advantageous to consider reconstructing turbulence parameters, such as Reynolds stresses, in the optimisation process, as explored in the study by Fu et al. 2023 to understand the capability of nacelle-mounted lidars to reconstruct both mean wind parameters and turbulence, simultaneously. As a next step, it would be beneficial to develop a simulation environment where system-level studies of integrating lidar systems into the turbine design phase could be performed. This would require, for example, an controller implementation into the virtual lidar, wind field and turbine framework. A thorough analysis could be performed where the actual value of implementing lidar systems could be determined. The results of such a study could be used to extend system engineering studies such as the work of Canet et al. 2021 who only could use typical lidar augmented load reductions from literature due to the lack of such a study. The results of such a study could be used to make informed decisions on the potential of scanning lidar technology in reducing the levelised cost of energy.

In Chapter 3, a lower order description of the wind turbine inflow was presented, and it was shown that a highly accurate representation of the inflow wind field could be obtained by choosing the most dominant spatial modes. As POD provides a systematic dimensional reduction by careful selection of modes, it should be possible to build very simple to highly complex inflow models by modelling the weighting coefficients of the selected modes. However, the selection of modes is highly dependent on the inflow quantities and the quantities relevant to the turbines. Therefore, it would be interesting to investigate if the modes chosen to represent the inflow could also be related to the turbine's response. Once this is established, truly dynamic inflow models with predictive capabilities could be developed through Galerkin projection to the underlying Navier-Stokes equations [Taira et al. 2017] or stochastic modelling [Bastine et al. 2018] or linearising [Debnath et al. 2017; Iungo et al. 2015] of the temporal dynamics of the weighing coefficients. Finally, applying the method to field data measured by scanning lidars would be very interesting. As more turbine operational states could be covered with long-term measurement data from field measurements, more detailed inflow models could be developed as higher order modes could be estimated more accurately. These combined reduced-order modelling approaches could be highly beneficial for developing new strategies in wind farm flow modelling, advanced control algorithms, and load prediction, exploiting the systematic dimensional reduction and dynamic inflow models built from carefully selected modes [Andersen and Murcia Leon 2022]. Due to the continuous improvements in the computational times and accuracy of machine-learning approaches, it may be beneficial to explore lidar wind field reconstruction methodologies utilising machine learning techniques [Wang et al. 2024]. Finally, it will be interesting to assess the performance of the developed reduced order model against the field data by using them in aeroelastic simulations to estimate the turbine response. Field validation of the Gappy-POD methodology described in Chapter 4 could not be performed due to a lack of reliable data. Therefore, field validation of the method could be beneficial in estimating the reconstruction accuracy, and the possibility of real-time implementation could also be evaluated.

More field measurement campaigns could be performed to understand the inflow behaviour

6

and the induction zone. The measurement campaign presented in Chapter 5 could not cover a large dataset covering a range of wind speeds, stabilities, and turbine operational states due to specific issues such as failure of measurement equipment, low measurement quality due to environmental conditions to name a few. Future measurements covering a more extensive range of inflow conditions will be precious in understanding the induction zone behaviour in wind farms. The virtual lidar in LES approach to model the wind park and the lidars provided a complementary methodology to investigate the errors and optimise trajectories for scanning lidar measurements. While the presented study focused on the characteristics of the mean wind fields, approaches to characterise the evolution of turbulence from scanning lidars similar to Puccioni et al. 2023 can be used to characterise the turbulent flow evolution in the induction zone.

The methodology can be extended, and digitisation of scanning lidar campaigns such as the work of Vasiljević et al. 2020 should be adopted in the campaign planning and the workflow. By creating Geographical Information System (GIS) layers, measurement constraints such as exclusion zones, laser beam blockage, and lidar range constraint maps could be utilised while determining optimal lidar placements for a particular envisaged measurement objective. The measurement campaign focused on the time-averaged wind fields, while the inflow dynamics were not the objective of the measurements. In future measurement campaigns, it would be interesting to measure the dynamical inflow behaviour in the induction zone due to abrupt changes in the inflow conditions such as wind direction change or partial gusts.

REFERENCES

- Abkar, M., Sørensen, J. N., & Porté-Agel, F. (2018). An Analytical Model for the Effect of Vertical Wind Veer on Wind Turbine Wakes. *Energies 2018, Vol. 11, Page 1838, 11*(7), 1838. https://doi.org/10.3390/EN11071838
- Adrian, R. J. (2005). Twenty years of particle image velocimetry. *Experiments in Fluids*, *39*(2), 159–169. https://doi.org/10.1007/s00348-005-0991-7
- Alcayaga, L. (2020). Filtering of pulsed lidar data using spatial information and a clustering algorithm. *Atmospheric Measurement Techniques*, 13(11), 6237–6254. https://doi.org/10.5194/AMT-13-6237-2020
- Andersen, S. J., Sørensen, J. N., & Mikkelsen, R. F. (2017). Turbulence and entrainment length scales in large wind farms. *Philosophical Transactions of the Royal Society A: Mathematical, Physical and Engineering Sciences, 375*(2091), 20160107. https://doi.org/10.1098/rsta.2016.0107
- Andersen, S. J., & Murcia Leon, J. P. (2022). Predictive and stochastic reduced-order modeling of wind turbine wake dynamics. *Wind Energy Science*, 7(5), 2117–2133. https://doi.org/10.5194/WES-7-2117-2022
- Angelou, N., Mann, J., & Dellwik, E. (2021). Scanning Doppler lidar measurements of drag force on a solitary tree. *Journal of Fluid Mechanics*, 917, A30. https://doi.org/10.1017/jfm.2021.275
- Angelou, N., Mann, J., Sjöholm, M., & Courtney, M. (2012). Direct measurement of the spectral transfer function of a laser based anemometer. *Review of Scientific Instruments*, 83(3), 033111. https://doi.org/10.1063/1.3697728
- Asimakopoulos, M, Clive, P, More, G, & Boddington, R. Offshore compression zone measurement and visualization. In: *European wind energy association 2014 annual event, barcelona, spain.* 2014.
- Barthelmie, R. J. (1999). The effects of atmospheric stability on coastal wind climates. Meteorological Applications, 6(1), 39–47. https://doi.org/10.1017/ S1350482799000961
- Bastankhah, M., & Porte-Agel, F. (2017). Wind tunnel study of the wind turbine interaction with a boundary-layer flow: Upwind region, turbine performance, and wake region. *Physics of Fluids*, *29*(6). https://doi.org/10.1063/1.4984078
- Bastine, D., Vollmer, L., Wächter, M., & Peinke, J. (2018). Stochastic wake modelling based on POD analysis. *Energies*, 11(3), 612. https://doi.org/10.3390/en11030612
- Bastine, D., Witha, B., Wächter, M., & Peinke, J. (2015). Towards a simplified dynamic wake model using POD analysis. *Energies*, 8(2), 895–920. https://doi.org/10.3390/en8020895
- Bauweraerts, P., & Meyers, J. (2020). Study of the energy convergence of the Karhunen-Loeve decomposition applied to the large-eddy simulation of a high-Reynolds-

- number pressure-driven boundary layer. *Physical Review Fluids*, *5*(11), 114603. https://doi.org/10.1103/PhysRevFluids.5.114603
- Beck, H., & Kühn, M. (2017). Dynamic Data Filtering of Long-Range Doppler LiDAR Wind Speed Measurements. *Remote Sensing*, 9(6), 561. https://doi.org/10.3390/rs9060561
- Beck, H., & Kühn, M. (2019). Temporal Up-Sampling of Planar Long-Range Doppler LiDAR Wind Speed Measurements Using Space-Time Conversion. *Remote Sensing 2019, Vol. 11, Page 867, 11*(7), 867. https://doi.org/10.3390/RS11070867
- Bergmann, M., Cordier, L., & Brancher, J. P. (2005). Optimal rotary control of the cylinder wake using proper orthogonal decomposition reduced-order model. *Physics of Fluids*, 17(9), 1–21. https://doi.org/10.1063/1.2033624
- Berkooz, G., Holmes, P., & Lumley, J. L. (1993). The proper orthogonal, decomposition in the analysis of turbulent flows. *Annual review of fluid mechanics*, *25*(1), 539–575. https://doi.org/10.1146/annurev.fluid.25.1.539
- Bertelè, M., Bottasso, C. L., & Schreiber, J. (2021). Wind inflow observation from load harmonics: initial steps towards a field validation. *Wind Energy Science*, *6*(3), 759–775. https://doi.org/10.5194/wes-6-759-2021
- Bleeg, J., Purcell, M., Ruisi, R., & Traiger, E. (2018). Wind Farm Blockage and the Consequences of Neglecting Its Impact on Energy Production. *Energies 2018, Vol. 11, Page 1609, 11*(6), 1609. https://doi.org/10.3390/EN11061609
- Bodini, N., Zardi, D., & Lundquist, J. K. (2017). Three-dimensional structure of wind turbine wakes as measured by scanning lidar. *Atmospheric Measurement Techniques*, 10(8), 2881–2896. https://doi.org/10.5194/amt-10-2881-2017
- Borraccino, A., Schlipf, D., Haizmann, F., & Wagner, R. (2017). Wind field reconstruction from nacelle-mounted lidar short-range measurements. Wind Energy Science, 2(1), 269-283. https://doi.org/10.5194/wes-2-269-2017
- Bossanyi, E. A. (2003). Wind turbine control for load reduction. *Wind Energy*, *6*(3), 229–244. https://doi.org/10.1002/we.95
- Bossanyi, E. A., Kumar, A., & Hugues-Salas, O. (2014). Wind turbine control applications of turbine-mounted LIDAR. *Journal of Physics: Conference Series*, *555*(1), 12011. https://doi.org/10.1088/1742-6596/555/1/012011
- Bottasso, C. L., Cacciola, S., & Schreiber, J. (2018). Local wind speed estimation, with application to wake impingement detection. *Renewable Energy*, 116, 155–168. https://doi.org/10.1016/j.renene.2017.09.044
- Branlard, E., & Gaunaa, M. (2015). Cylindrical vortex wake model: right cylinder. *Wind Energy*, 18(11), 1973–1987. https://doi.org/10.1002/WE.1800
- Branlard, E., Pedersen, A. T., Mann, J., Angelou, N., Fischer, A., Mikkelsen, T., Harris, M., Slinger, C., & Montes, B. F. (2013). Retrieving wind statistics from average spectrum of continuous-wave lidar. *Atmospheric Measurement Techniques*, *6*(7), 1673–1683. https://doi.org/10.5194/amt-6-1673-2013
- Branlard, E. (2019). Wiz, wake and induction zone model. https://github.com/ebranlard/wiz
- Branlard, E., & Meyer Forsting, A. R. (2020). Assessing the blockage effect of wind turbines and wind farms using an analytical vortex model. *Wind Energy*, *23*(11), 2068–2086. https://doi.org/10.1002/we.2546

Branlard, E., Quon, E., Meyer Forsting, A. R., King, J., & Moriarty, P. (2020). Wind farm blockage effects: comparison of different engineering models. *Journal of Physics:* Conference Series, 1618(6), 062036. https://doi.org/10.1088/1742-6596/1618/6/062036

- Bromm, M., Rott, A., Beck, H., Vollmer, L., Steinfeld, G., & Kühn, M. (2018). Field investigation on the influence of yaw misalignment on the propagation of wind turbine wakes. *Wind Energy*, *21*(11), 1011–1028. https://doi.org/10.1002/we.2210
- Brugger, P., Debnath, M., Scholbrock, A., Fleming, P., Moriarty, P., Simley, E., Jager, D., Roadman, J., Murphy, M., Zong, H., & Porté-Agel, F. (2020). Lidar measurements of yawed-wind-turbine wakes: characterization and validation of analytical models. Wind Energy Science, 5(4), 1253–1272. https://doi.org/10.5194/wes-5-1253-2020
- Canet, H., Loew, S., & Bottasso, C. L. (2021). What are the benefits of lidar-assisted control in the design of a wind turbine? *Wind Energy Science*, 6(5), 1325–1340. https://doi.org/10.5194/wes-6-1325-2021
- Chen, Y., Schlipf, D., & Wen Cheng, P. (2021). Parameterization of wind evolution using lidar. Wind Energy Science, 6(1), 61–91. https://doi.org/10.5194/wes-6-61-2021
- Chen, Y., Yu, W., Guo, F., & Cheng, P. W. (2022). Adaptive measuring trajectory for scanning lidars: proof of concept. *Journal of Physics: Conference Series*, 2265(2), 022099. https://doi.org/10.1088/1742-6596/2265/2/022099
- Cheynet, E., Jakobsen, J. B., Snæbjörnsson, J., Angelou, N., Mikkelsen, T., Sjöholm, M., & Svardal, B. (2017). Full-scale observation of the flow downstream of a suspension bridge deck. *Journal of Wind Engineering and Industrial Aerodynamics*, 171, 261–272. https://doi.org/10.1016/J.JWEIA.2017.10.007
- Cheynet, E., Jakobsen, J. B., Snæbjörnsson, J., Mikkelsen, T., Sjöholm, M., Mann, J., Hansen, P., Angelou, N., & Svardal, B. (2016). Application of short-range dual-Doppler lidars to evaluate the coherence of turbulence. *Experiments in Fluids*, *57*(12), 184. https://doi.org/10.1007/s00348-016-2275-9
- Churchfield, M., Wang, Q., Scholbrock, A., Herges, T., Mikkelsen, T., & Sjöholm, M. (2016). Using High-Fidelity Computational Fluid Dynamics to Help Design a Wind Turbine Wake Measurement Experiment. *Journal of Physics: Conference Series*, 753(3), 032009. https://doi.org/10.1088/1742-6596/753/3/032009
- Clifton, A., Clive, P., Gottschall, J., Schlipf, D., Simley, E., Simmons, L., Stein, D., Trabucchi, D., Vasiljevic, N., & Würth, I. (2018). IEA Wind Task 32: Wind lidar identifying and mitigating barriers to the adoption of wind lidar. *Remote Sensing*, 10(3), 406. https://doi.org/10.3390/rs10030406
- Conti, D., Dimitrov, N., & Peña, A. (2020). Aeroelastic load validation in wake conditions using nacelle-mounted lidar measurements. *Wind Energy Science*, *5*(3), 1129–1154. https://doi.org/10.5194/wes-5-1129-2020
- Conti, D., Dimitrov, N., Peña, A., & Herges, T. (2021). Probabilistic estimation of the Dynamic Wake Meandering model parameters using SpinnerLidar-derived wake characteristics. *Wind Energy Science*, 6(5), 1117–1142. https://doi.org/10.5194/wes-6-1117-2021

Counihan, J., Hunt, J. C., & Jackson, P. S. (1974). Wakes behind two-dimensional surface obstacles in turbulent boundary layers. *Journal of Fluid Mechanics*, 64(3), 529–564. https://doi.org/10.1017/S0022112074002539

- Davenport, A. G. (1962). The spectrum of horizontal gustiness near the ground in high winds. *Quarterly Journal of the Royal Meteorological Society*, 88(376), 197–198. https://doi.org/10.1002/qj.49708837618
- Davoust, S., Jehu, A., Bouillet, M., Bardon, M., Vercherin, B., Scholbrock, A. K., Fleming, P. A., & Wright, A. D. (2014). Assessment and Optimization of Lidar Measurement Availability for Wind Turbine Control (tech. rep. May). National Renewable Energy Lab.(NREL), Golden, CO (United States), No. NREL/CP-5000-61332.
- Deardorff, J. W. (1980). Stratocumulus-capped mixed layers derived from a three-dimensional model. Boundary-Layer Meteorology, 18(4), 495-527. https://doi.org/10. 1007/BF00119502
- Debnath, M., Brugger, P., Simley, E., Doubrawa, P., Hamilton, N., Scholbrock, A., Jager, D., Murphy, M., Roadman, J., Lundquist, J. K., Fleming, P., Porté-Agel, F., & Moriarty, P. (2020). Longitudinal coherence and short-term wind speed prediction based on a nacelle-mounted Doppler lidar. *Journal of Physics: Conference Series*, 1618(3), 032051. https://doi.org/10.1088/1742-6596/1618/3/032051
- Debnath, M., Doubrawa, P., Herges, T., Martínez-Tossas, L. A., Maniaci, D. C., & Moriarty, P. (2019). Evaluation of Wind Speed Retrieval from Continuous-Wave Lidar Measurements of a Wind Turbine Wake Using Virtual Lidar Techniques. *Journal of Physics:* Conference Series, 1256(1), 012008. https://doi.org/10.1088/1742-6596/1256/1/012008
- Debnath, M., Santoni, C., Leonardi, S., & Iungo, G. V. (2017). Towards reduced order modelling for predicting the dynamics of coherent vorticity structures within wind turbine wakes. *Philosophical Transactions of the Royal Society A: Mathematical, Physical and Engineering Sciences*, 375(2091), 20160108. https://doi.org/10.1098/rsta.2016.0108
- Dhiman, H. S., Deb, D., & Foley, A. M. (2020). Lidar assisted wake redirection in wind farms: A data driven approach. *Renewable Energy*, 152, 484–493. https://doi.org/10.1016/J.RENENE.2020.01.027
- Dimitrov, N., Borraccino, A., Peña, A., Natarajan, A., & Mann, J. (2019). Wind turbine load validation using lidar-based wind retrievals. *Wind Energy*, *22*(11), 1512–1533. https://doi.org/10.1002/we.2385
- Dimitrov, N., & Natarajan, A. (2017). Application of simulated lidar scanning patterns to constrained Gaussian turbulence fields for load validation. *Wind Energy*, *20*(1), 79–95. https://doi.org/10.1002/we.1992
- Dong, L., Lio, W. H., & Simley, E. (2021). On turbulence models and lidar measurements for wind turbine control. Wind Energy Science, 6(6), 1491–1500. https://doi.org/10.5194/WES-6-1491-2021
- Dunne, F., Pao, L. Y., Schlipf, D., & Scholbrock, A. K. Importance of lidar measurement timing accuracy for wind turbine control. In: 2014 american control conference. IEEE, 2014, 3716–3721. ISBN: 978-1-4799-3274-0. https://doi.org/10.1109/ACC.2014.6859337.

Dunne, F., Pao, L. Y., Wright, A. D., Jonkman, B., & Kelley, N. Combining standard feedback controllers with feedforward blade pitch control for load mitigation in wind turbines. In: 48th aiaa aerospace sciences meeting including the new horizons forum and aerospace exposition. 2010, 250. ISBN: 9781600867392. https://doi.org/10.2514/6.2010-250.

- Dunne, F., Pao, L., Wright, A., Jonkman, B., Kelley, N., & Simley, E. Adding Feedforward Blade Pitch Control for Load Mitigation in Wind Turbines: Non-Causal Series Expansion, Preview Control, and Optimized FIR Filter Methods. In: 49th aiaa aerospace sciences meeting. 2011, 1–17. https://doi.org/10.2514/6.2011-819.
- Dunne, F., Schlipf, D., Pao, L., Wright, A., Jonkman, B., Kelley, N., & Simley, E. Comparison of Two Independent Lidar-Based Pitch Control Designs. In: 50th aiaa aerospace sciences meeting including the new horizons forum and aerospace exposition. Reston, Virigina: American Institute of Aeronautics; Astronautics, 2012. ISBN: 978-1-60086-936-5. https://doi.org/10.2514/6.2012-1151.
- Everson, R., & Sirovich, L. (1995). Karhunen-Loève procedure for gappy data. *Journal of the Optical Society of America A*, 12(8), 1657. https://doi.org/10.1364/josaa.12.001657
- Fleming, P. A., Scholbrock, A. K., Jehu, A., Davoust, S., Osler, E., Wright, A. D., & Clifton, A. Field-test results using a nacelle-mounted lidar for improving wind turbine power capture by reducing yaw misalignment. In: *Journal of physics: Conference series. 524.*(1). IOP Publishing. 2014, 012002. https://doi.org/10.1088/1742-6596/524/1/012002.
- Fleming, P., Annoni, J., Churchfield, M., Martinez-Tossas, L. A., Gruchalla, K., Lawson, M., & Moriarty, P. (2018). A simulation study demonstrating the importance of large-scale trailing vortices in wake steering. *Wind Energy Science*, *3*(1), 243–255. https://doi.org/10.5194/wes-3-243-2018
- Frauhofer ISE. (2024). Electricity Generation | Energy-Charts. https://www.energy-charts.info/charts/energy_pie/chart.htm?l=en&c=DE&interval=year&year=2021
- Fu, W., Peña, A., & Mann, J. (2022). Turbulence statistics from three different nacelle lidars. Wind Energ. Sci, 7, 831-848. https://doi.org/10.5194/wes-7-831-2022
- Fu, W., Sebastiani, A., Peña, A., & Mann, J. (2023). Dependence of turbulence estimations on nacelle lidar scanning strategies. *Wind Energy Science*, 8(5), 677–690. https://doi.org/10.5194/WES-8-677-2023
- Gebraad, P. M. O., Teeuwisse, F. W., van Wingerden, J. W., Fleming, P. A., Ruben, S. D., Marden, J. R., & Pao, L. Y. (2016). Wind plant power optimization through yaw control using a parametric model for wake effects-a CFD simulation study. *Wind Energy*, 19(1), 95–114. https://doi.org/10.1002/we.1822
- Giyanani, A., Sjöholm, M., Rolighed Thorsen, G., Schuhmacher, J., & Gottschall, J. (2022). Wind speed reconstruction from three synchronized short-range WindScanner lidars in a large wind turbine inflow field campaign and the associated uncertainties. *Journal of Physics: Conference Series*, 2265(2), 022032. https://doi.org/10.1088/1742-6596/2265/2/022032

Glanemann, N., Willner, S. N., & Levermann, A. (2020). Paris Climate Agreement passes the cost-benefit test. *Nature Communications*, 11(1), 110. https://doi.org/10.1038/s41467-019-13961-1

- Göçmen, T., Laan, P. V. D., Réthoré, P. E., Diaz, A. P., Larsen, G. C., & Ott, S. (2016). Wind turbine wake models developed at the technical university of Denmark: A review. Renewable and Sustainable Energy Reviews, 60, 752–769. https://doi.org/10.1016/J.RSER.2016.01.113
- Gryning, S. E., & Floors, R. (2019). Carrier-to-Noise-Threshold Filtering on Off-Shore Wind Lidar Measurements. *Sensors 2019, Vol. 19, Page 592, 19*(3), 592. https://doi.org/10.3390/S19030592
- Guillemin, F., Nguyen, H.-N., Sabiron, G., Di Domenico, D., & Boquet, M. (2018). Real-time three dimensional wind field reconstruction from nacelle LiDAR measurements. *Journal of Physics: Conference Series, 1037(3), 032037. https://doi.org/10.1088/1742-6596/1037/3/032037
- Gunes, H., Sirisup, S., & Karniadakis, G. E. (2006). Gappy data: To Krig or not to Krig? *Journal of Computational Physics*, 212(1), 358–382. https://doi.org/10. 1016/j.jcp.2005.06.023
- Guo, F., Mann, J., Peña, A., Schlipf, D., & Cheng, P. W. (2022a). The space-time structure of turbulence for lidar-assisted wind turbine control. *Renewable Energy*, 195, 293–310. https://doi.org/10.1016/J.RENENE.2022.05.133
- Guo, F., & Schlipf, D. (2023). Assessing lidar-Assisted feedforward and multivariable feedback controls for large floating wind turbines. *Wind Energy Science*, 8(8), 1299–1317. https://doi.org/10.5194/WES-8-1299-2023
- Guo, F., Schlipf, D., & Cheng, P. W. (2023). Evaluation of lidar-Assisted wind turbine control under various turbulence characteristics. *Wind Energy Science*, 8(2), 149–171. https://doi.org/10.5194/WES-8-149-2023
- Guo, F., Schlipf, D., Zhang, Z., & Cheng, P. W. (2022b). Investigation on the wind preview quality for lidar-assisted wind turbine control under wake conditions. *Proceedings of the American Control Conference*, 2022-June, 3544–3549. https://doi.org/10.23919/ACC53348.2022.9867301
- Guo, M., & Hesthaven, J. S. (2019). Data-driven reduced order modeling for time-dependent problems. *Computer Methods in Applied Mechanics and Engineering*, 345, 75–99. https://doi.org/10.1016/j.cma.2018.10.029
- Harris, M., Bryce, D. J., Coffey, A. S., Smith, D. A., Birkemeyer, J., & Knopf, U. (2007). Advance measurement of gusts by laser anemometry. *Journal of Wind Engineering and Industrial Aerodynamics*, 95(12), 1637–1647. https://doi.org/10.1016/j.jweia.2007.02.029
- Held, D. P., & Mann, J. (2019a). Detection of wakes in the inflow of turbines using nacelle lidars. *Wind Energy Science*, 4(3), 407–420. https://doi.org/10.5194/wes-4-407-2019
- Held, D. P., & Mann, J. (2019b). Lidar estimation of rotor-effective wind speed An experimental comparison. *Wind Energy Science*, 4(3), 421-438. https://doi.org/10.5194/wes-4-421-2019
- Herges, T. G., & Keyantuo, P. (2019). Robust Lidar Data Processing and Quality Control Methods Developed for the SWiFT Wake Steering Experiment. *Journal of Physics*:

- Conference Series, 1256(1), 012005. https://doi.org/10.1088/1742-6596/1256/1/012005
- Herges, T. G., Maniaci, D. C., Naughton, B. T., Mikkelsen, T., & Sjöholm, M. High resolution wind turbine wake measurements with a scanning lidar. In: *Journal of physics:* Conference series. 854. (1). 2017. https://doi.org/10.1088/1742-6596/854/1/012021.
- Herges, T., Maniaci, D., Naughton, B., Hansen, K. H., Sjöholm, M., Angelou, N., & Mikkelsen, T. Scanning lidar spatial calibration and alignment method for wind turbine wake characterization. In: *35th wind energy symposium*, *2017*. 2017. ISBN: 9781624104565. https://doi.org/10.2514/6.2017-0455.
- Hill, C. (2018). Coherent focused lidars for Doppler sensing of aerosols and wind. *Remote Sensing*, 10(3), 466. https://doi.org/10.3390/rs10030466
- Holmes, P., Lumley, J. L., Berkooz, G., & Rowley, C. W. (2012). *Turbulence, Coherent Structures, Dynamical Systems and Symmetry* (2nd ed.). Cambridge University Press. https://doi.org/10.1017/cbo9780511919701
- Hong, J., Toloui, M., Chamorro, L. P., Guala, M., Howard, K., Riley, S., Tucker, J., & Sotiropoulos, F. (2014). Natural snowfall reveals large-scale flow structures in the wake of a 2.5-MW wind turbine. *Nature Communications*, 5(May). https://doi.org/10.1038/ncomms5216
- Hulsman, P., Sucameli, C., Petrović, V., Rott, A., Gerds, A., & Kühn, M. (2022a). Turbine power loss during yaw-misaligned free field tests at different atmospheric conditions. *Journal of Physics: Conference Series, 2265(3), 032074. https://doi.org/10.1088/1742-6596/2265/3/032074
- Hulsman, P., Wosnik, M., Petrović, V., Hölling, M., & Kühn, M. (2022b). Development of a curled wake of a yawed wind turbine under turbulent and sheared inflow. *Wind Energy Science*, 7(1), 237–257. https://doi.org/10.5194/wes-7-237-2022
- IEC 61400-50-3 (tech. rep.). (2022). International Electrotechnical Commission. https: //webstore.iec.ch/publication/59587
- IEC. (2022). Wind turbines, Part 12-1: Power performance measurements of electricity producing wind turbines, *International Electrotechnical Commission*, 2005, 179.
- Iungo, G. V., Santoni-Ortiz, C, Abkar, M, Porté-Agel, F, Rotea, M. A., & Leonardi, S. (2015).
 Data-driven Reduced Order Model for prediction of wind turbine wakes. *Journal of Physics: Conference Series*, 625(1), 012009. https://doi.org/10.1088/1742-6596/625/1/012009
- Iungo, G. V., Wu, Y. T., & Porté-Agel, F. (2013). Field measurements of wind turbine wakes with lidars. Journal of Atmospheric and Oceanic Technology, 30(2), 274–287. https://doi.org/10.1175/JTECH-D-12-00051.1
- Jiménez, Crespo, A., & Migoya, E. (2009). Application of a LES technique to characterize the wake deflection of a wind turbine in yaw. *Wind Energy*, *13*(6), 559–572. https://doi.org/10.1002/we.380
- Jonkman, J., Butterfield, S., Musial, W., & Scott, G. (2009a). *Definition of a 5-MW Reference Wind Turbine for Offshore System Development* (tech. rep.). National Renewable Energy Laboratory (NREL). Golden, CO. https://doi.org/10.2172/947422

Jonkman, J. M., Buhl Jr, M. L., & others. (2005). FAST user's guide. *National Renewable Energy Laboratory, Golden, CO, Technical Report No. NREL/EL-500-38230.*

- Jonkman, J., Butterfield, S, Musial, W, & Scott, G. (2009b). Definition of a 5-MW reference wind turbine for offshore system development (tech. rep. February). National Renewable Energy Lab.(NREL), Golden, CO (United States). http://tethys-development.pnnl.gov/sites/default/files/publications/Jonkman_et_al_2009.pdf
- Kaimal, J. C., Wyngaard, J. C., & Haugen, D. A. (1968). Deriving Power Spectra from a Three-Component Sonic Anemometer. Journal of Applied Meteorology, 7(5), 827–837. https://doi.org/10.1175/1520-0450(1968)007<0827: dpsfat>2.0.co;2
- Kapp. S. (2017). Lidar Based Reconstruction of Wind Fields And Applications for Wind Turbine Control (Doctoral dissertation). Carl von Ossietzky Universität Oldenburg. Oldenburg.
- Kapp, S., & Kühn, M. A five-parameter wind field estimation method based on spherical upwind lidar measurements. In: *Journal of physics: Conference series. 555.* (1). IOP Publishing. 2014, 12112. https://doi.org/10.1088/1742-6596/555/1/012112.
- Kelberlau, F., Neshaug, V., Lønseth, L., Bracchi, T., & Mann, J. (2020). Taking the Motion out of Floating Lidar: Turbulence Intensity Estimates with a Continuous-Wave Wind Lidar. *Remote Sensing 2020, Vol. 12, Page 898, 12*(5), 898. https://doi.org/10.3390/RS12050898
- Kelley, C. L., Herges, T. G., Martinez, L. A., & Mikkelsen, T. (2018). Wind turbine aerodynamic measurements using a scanning lidar. *Journal of Physics: Conference Series*, 1037(5), 052014. https://doi.org/10.1088/1742-6596/1037/5/052014
- Kidambi Sekar, A. P., & Kühn, M. (2017). Lower Order Modeling of Wind Turbine Inflow with Short-Range Lidars. *Wind Energy Science Conference, Lyngby, Denmark, 270617-1340-S10, 26-29 June.*
- Kidambi Sekar, A. P., Rott, A., Van Dooren, M. F., & Kühn, M. (2020). How much flow information can a turbine-mounted lidar capture? *Journal of Physics: Conference Series*, 1618(3), 32050. https://doi.org/10.1088/1742-6596/1618/3/032050
- Kidambi Sekar, A. P., Van Dooren, M. F., Mikkelsen, T., Sjöholm, M., Astrup, P., & Kühn, M. (2018). Evaluation of the LINCOM wind field reconstruction method with simulations and full-scale measurements. *Journal of Physics: Conference Series*, 1037(5), 52008. https://doi.org/10.1088/1742-6596/1037/5/052008
- Kidambi Sekar, A. P., van Dooren, M. F., Rott, A., & Kühn, M. (2022). Lower Order Description and Reconstruction of Sparse Scanning Lidar Measurements of Wind Turbine Inflow Using Proper Orthogonal Decomposition. *Remote Sensing*, *14*(11), 2681. https://doi.org/10.3390/rs14112681
- Kragh, K. A., Fleming, P. A., & Scholbrock, A. K. (2013). Increased power capture by rotor speed-dependent yaw control of wind turbines. *Journal of Solar Energy Engineering*,

- Transactions of the ASME, 135(3), 1-7. https://doi.org/10.1115/1.4023971
- Krishnamurthy, R., Choukulkar, A., Calhoun, R., Fine, J., Oliver, A., & Barr, K. S. (2013). Coherent Doppler lidar for wind farm characterization. *Wind Energy*, 16(2), 189–206. https://doi.org/10.1002/WE.539
- Kristensen, L. (1979). On Longitudinal Spectral Coherence. *Boundary-Layer Meteorology*, 16(3), 145–153. https://doi.org/10.1007/BF03335363
- Kristensen, L., & Frandsen, S. (1982). Model for power spectra of the blade of a wind turbine measured from the moving frame of reference. *Journal of Wind Engineering and Industrial Aerodynamics*, 10(2), 249–262. https://doi.org/10.1016/0167-6105(82)90067-8
- Krüger, S., Steinfeld, G., Kraft, M., & Lukassen, L. J. (2022). Validation of a coupled atmospheric–aeroelastic model system for wind turbine power and load calculations. *Wind Energy Science*, 7(1), 323–344. https://doi.org/10.5194/WES-7-323-2022
- Laks, J., Pao, L., Simley, E., Wright, A., Kelley, N., & Jonkman, B. (2011a). Model Predictive Control Using Preview Measurements From LIDAR. https://doi.org/10.2514/6.2011-813
- Laks, J., Pao, L., Simley, E., Wright, A., Kelley, N., & Jonkman, B. (2011b). Model Predictive Control Using Preview Measurements From LIDAR. https://doi.org/10. 2514/6.2011-813
- Laks, J., Simley, E., & Pao, L. A spectral model for evaluating the effect of wind evolution on wind turbine preview control. In: *Proceedings of the american control conference*. 2013, 3673–3679. ISBN: 9781479901777. https://doi.org/10.1109/acc.2013.6580400.
- Lio, W. H., Larsen, G. C., & Thorsen, G. R. (2021). Dynamic wake tracking using a cost-effective LiDAR and Kalman filtering: Design, simulation and full-scale validation. *Renewable Energy, 172, 1073–1086. https://doi.org/10.1016/J.RENENE.2021.03.081
- Lio, W. H., Meng, F., & Larsen, G. C. (2022). On LiDAR-assisted wind turbine retrofit control and fatigue load reductions The Science of Making Torque from Wind (On LiDAR-assisted wind turbine retrofit control and fatigue load reductions. *TORQUE 2022*) *Journal of Physics: Conference Series*, 2265, 32072. https://doi.org/10.1088/1742-6596/2265/3/032072
- Lund, T. S., Wu, X., & Squires, K. D. (1998). Generation of Turbulent Inflow Data for Spatially-Developing Boundary Layer Simulations. *Journal of Computational Physics*, 140(2), 233–258. https://doi.org/10.1006/jcph.1998.5882
- Lundquist, J. K., Churchfield, M. J., Lee, S., & Clifton, A. (2015). Quantifying error of lidar and sodar doppler beam swinging measurements of wind turbine wakes using computational fluid dynamics. *Atmospheric Measurement Techniques*, 8(2), 907–920. https://doi.org/10.5194/AMT-8-907-2015
- Maas, H. G., Gruen, A., & Papantoniou, D. (1993). Particle tracking velocimetry in three-dimensional flows Part 1. Photogrammetric determination of particle coordinates. *Experiments in Fluids*, 15(2), 133–146. https://doi.org/10.1007/BF00190953

Madsen, H. A., Riziotis, V., Zahle, F., Hansen, M. O., Snel, H., Grasso, F., Larsen, T. J., Politis, E., & Rasmussen, F. Blade element momentum modeling of inflow with shear in comparison with advanced model results. In: *Wind energy. 15.* (1). John Wiley; Sons Ltd, 2012, 63–81. https://doi.org/10.1002/we.493.

- Mann, J. (1994). The spatial structure of neutral atmospheric surface-layer turbulence. *Journal of Fluid Mechanics*, 273, 141–168. https://doi.org/10.1017/ S0022112094001886
- Mann, J. (1998). Wind field simulation. *Probabilistic Engineering Mechanics*, 13(4), 269–282. https://doi.org/10.1016/S0266-8920(97)00036-2
- Mann, J., Cariou, J.-P. C., Parmentier, R. M., Wagner, R., Lindelöw, P., Sjöholm, M., & Enevoldsen, K. (2009). Comparison of 3D turbulence measurements using three staring wind lidars and a sonic anemometer. *Meteorologische Zeitschrift*, 18(2), 135–140. https://doi.org/10.1127/0941-2948/2009/0370
- Mann, J., Penã, A., Troldborg, N., & Andersen, S. J. (2018). How does turbulence change approaching a rotor? *Wind Energy Science*, 3(1), 293–300. https://doi.org/10.5194/wes-3-293-2018
- Maronga, B., Gryschka, M., Heinze, R., Hoffmann, F., Kanani-Sühring, F., Keck, M., Ketelsen, K., Letzel, M. O., Sühring, M., & Raasch, S. (2015). The Parallelized Large-Eddy Simulation Model (PALM) version 4.0 for atmospheric and oceanic flows: model formulation, recent developments, and future perspectives. *Geoscientific Model Development*, 8(8), 2515–2551. https://doi.org/10.5194/gmd-8-2515-2015
- Matsumoto, M., & Nishimura, T. (1998). Mersenne twister. *ACM Transactions on Modeling and Computer Simulation*, 8(1), 3–30. https://doi.org/10.1145/272991.272995
- Medici, D., & Alfredsson, P. H. (2006). Measurements on a wind turbine wake: 3D effects and bluff body vortex shedding. *Wind Energy*, 9(3), 219–236. https://doi.org/10.1002/we.156
- Medici, D., Ivanell, S., Dahlberg, J.-, & Alfredsson, P. H. (2011). The upstream flow of a wind turbine: blockage effect. *Wind Energy*, 14(5), 691–697. https://doi.org/10.1002/we.451
- Meyer Forsting, A. R., Troldborg, N., & Borraccino, A. (2017). Modelling lidar volume-averaging and its significance to wind turbine wake measurements. *Journal of Physics: Conference Series*, 854(1), 012014. https://doi.org/10.1088/1742-6596/854/1/012014
- Meyer Forsting, A, Rathmann, O., Laan, M. v. d., Troldborg, N, Gribben, B, Hawkes, G, & Branlard, E. (2021). Verification of induction zone models for wind farm annual energy production estimation (2019 J. Phys.: Conf. Ser. 1934 012023). *Journal of Physics: Conference Series*, 1934(1), 012024. https://doi.org/10.1088/1742-6596/1934/1/012024
- Mikkelsen, T., Angelou, N., Hansen, K., Sjöholm, M., Harris, M., Slinger, C., Hadley, P., Scullion, R., Ellis, G., & Vives, G. (2013). A spinner-integrated wind lidar for enhanced wind turbine control. *Wind Energy*, *16*(4), 625–643. https://doi.org/10.1002/we.1564

Mikkelsen, T., Sjöholm, M., Angelou, N., & Mann, J. (2017). 3D WindScanner lidar measurements of wind and turbulence around wind turbines, buildings and bridges. *IOP Conference Series: Materials Science and Engineering, 276*(1), 012004. https://doi.org/10.1088/1757-899X/276/1/012004

- Mikkelsen, T., Sjöholm, M., Astrup, P., Peña, A., Larsen, G., van Dooren, M. F., & Kidambi Sekar, A. P. (2020). Lidar Scanning of Induction Zone Wind Fields over Sloping Terrain. *Journal of Physics: Conference Series*, 1452(1), 012081. https://doi.org/10.1088/1742-6596/1452/1/012081
- Mirocha, J. D., Rajewski, D. A., Marjanovic, N., Lundquist, J. K., Kosović, B., Draxl, C., & Churchfield, M. J. (2015). Investigating wind turbine impacts on near-wake flow using profiling lidar data and large-eddy simulations with an actuator disk model. *Journal of Renewable and Sustainable Energy*, 7(4), 043143. https://doi.org/10.1063/1.4928873
- Mirzaei, M., Soltani, M., Poulsen, N. K., & Niemann, H. H. (2013a). Model predictive control of wind turbines using uncertain LIDAR measurements. *Proceedings of the American Control Conference*, 2235–2240. https://doi.org/10.1109/ACC.2013.6580167
- Mirzaei, M., Soltani, M., Poulsen, N. K., & Niemann, H. H. (2013b). Model predictive control of wind turbines using uncertain LIDAR measurements. *Proceedings of the American Control Conference*, 2235–2240. https://doi.org/10.1109/acc.2013.6580167
- Monin, A. S., & Obukhov, A. M. (1954). Basic laws of turbulent mixing in the surface layer of the atmosphere. *Originally published in Tr. Akad. Nauk SSSR Geophiz. Inst, 24*(151), 163–187.
- Murray, N. E., & Seiner, J. M. The effects of Gappy POD on higher-order turbulence quantities. In: 46th aiaa aerospace sciences meeting and exhibit. 2008. ISBN: 9781563479373. https://doi.org/10.2514/6.2008-241.
- N. G. Nygaard. Wind Field Reconstruction in the Induction Zone A Round Robin Exercise. In: *Wind energy science conference 2019*. Cork, 2019.
- NREL. (2023). FLORIS. Version 3.4. https://github.com/NREL/floris
- Newman, J. F., & Clifton, A. (2017). An error reduction algorithm to improve lidar turbulence estimates for wind energy. Wind Energy Science, 2(1), 77–95. https://doi.org/10.5194/WES-2-77-2017
- Oliver, M. A., & Webster, R. (1990). Kriging: A method of interpolation for geographical information systems. *International Journal of Geographical Information Systems*, 4(3), 313–332. https://doi.org/10.1080/02693799008941549
- Panofsky, H. A., & McCormick, R. A. (1954). Properties of spectra of atmospheric turbulence at 100 metres. *Quarterly Journal of the Royal Meteorological Society*, 80(346), 546–564. https://doi.org/10.1002/qj.49708034604
- Pedersen, A. T., & Courtney, M. (2021). Flywheel calibration of a continuous-wave coherent Doppler wind lidar. *Atmospheric Measurement Techniques*, 14(2), 889–903. https://doi.org/10.5194/amt-14-889-2021
- Peherstorfer, B., & Willcox, K. (2015). Dynamic data-driven reduced-order models. Computer Methods in Applied Mechanics and Engineering, 291, 21–41. https://doi.org/10.1016/J.CMA.2015.03.018

Peña, A., Bechmann, A., Conti, D., & Angelou, N. (2016). The fence experiment – full-scale lidar-based shelter observations. *Wind Energy Science*, 1(2), 101–114. https://doi.org/10.5194/WES-1-101-2016

- Peña, A., & Mann, J. (2019). Turbulence Measurements with Dual-Doppler Scanning Lidars. *Remote Sensing*, 11(20), 2444. https://doi.org/10.3390/rs11202444
- Penã, A., Mann, J., & Dimitrov, N. (2017). Turbulence characterization from a forward-looking nacelle lidar. *Wind Energy Science*, 2(1), 133–152. https://doi.org/10.5194/wes-2-133-2017
- Pena, A., Sjöholm, M., Mikkelsen, T., & Hasager, C. B. Inflow characterization using measurements from the SpinnerLidar: The ScanFlow experiment. In: *Journal of physics: Conference series. 1037.* (5). Institute of Physics Publishing, 2018. https://doi.org/10.1088/1742-6596/1037/5/052027.
- Pielke, R. A., & Panofsky, H. A. (1970). Turbulence characteristics along several towers. Boundary-Layer Meteorology, 1(2), 115–130. https://doi.org/10.1007/BF00185733
- Puccioni, M., Moss, C., & Iungo, G. V. (2023). Coupling wind LiDAR fixed and volumetric scans for enhanced characterization of wind turbulence and flow three-dimensionality. *Wind Energy*. https://doi.org/10.1002/WE.2865
- Raach, S., Schlipf, D., & Cheng, P. W. (2017). Lidar-based wake tracking for closed-loop wind farm control. *Wind Energy Science*, 2(1), 257–267. https://doi.org/10.5194/wes-2-257-2017
- Raach, S., Schlipf, D., Haizmann, F., & Cheng, P. W. (2014). Three dimensional dynamic model based wind field reconstruction from lidar data. *Journal of Physics: Conference Series*, 524(1), 12005. https://doi.org/10.1088/1742-6596/524/1/012005
- Raben, S. G., Charonko, J. J., & Vlachos, P. P. (2012). Adaptive gappy proper orthogonal decomposition for particle image velocimetry data reconstruction. *Measurement Science and Technology*, 23(2). https://doi.org/10.1088/0957-0233/23/2/025303
- Rahlves, C., Beyrich, F., & Raasch, S. (2022a). Scan strategies for wind profiling with Doppler lidar An large-eddy simulation (LES)-based evaluation. *Atmospheric Measurement Techniques*, *15*(9), 2839–2856. https://doi.org/10.5194/AMT-15-2839-2022
- Rahlves, C., Beyrich, F., & Raasch, S. (2022b). Scan strategies for wind profiling with Doppler lidar An large-eddy simulation (LES)-based evaluation. *Atmospheric Measurement Techniques*, 15(9), 2839–2856. https://doi.org/10.5194/AMT-15-2839-2022
- Robey, R., & Lundquist, J. K. (2022). Behavior and mechanisms of Doppler wind lidar error in varying stability regimes. *Atmospheric Measurement Techniques*, 15(15), 4585–4622. https://doi.org/10.5194/AMT-15-4585-2022
- Ropelewski, C. F., Tennekes, H., & Panofsky, H. A. (1973). Horizontal coherence of wind fluctuations. *Boundary-Layer Meteorology* 1973 5:3, 5(3), 353–363. https://doi.org/10.1007/BF00155243

Saini, P., Arndt, C. M., & Steinberg, A. M. (2016). Development and evaluation of gappy-POD as a data reconstruction technique for noisy PIV measurements in gas turbine combustors. *Experiments in Fluids*, 57(7), 1–15. https://doi.org/10.1007/s00348-016-2208-7

- Sang, L. Q., Li, Q., Cai, C., Maeda, T., Kamada, Y., Wang, X., Zhou, S., & Zhang, F. (2021). Wind tunnel and numerical study of a floating offshore wind turbine based on the cyclic pitch control. *Renewable Energy*, 172, 453–464. https://doi.org/10.1016/J.RENENE.2021.03.027
- Saranyasoontorn, K., & Manuel, L. (2005). Low-dimensional representations of inflow turbulence and wind turbine response using Proper Orthogonal Decomposition. Journal of Solar Energy Engineering, Transactions of the ASME, 127(4), 553–562. https://doi.org/10.1115/1.2037108
- Sarmast, S., Segalini, A., Mikkelsen, R. F., & Ivanell, S. (2016). Comparison of the near-wake between actuator-line simulations and a simplified vortex model of a horizontal-axis wind turbine. *Wind Energy*, 19(3), 471–481. https://doi.org/10.1002/we.1845
- Sathe, A., & Mann, J. (2013). A review of turbulence measurements using ground-based wind lidars. *Atmospheric Measurement Techniques*, 6(11), 3147–3167. https://doi.org/10.5194/AMT-6-3147-2013
- Sathe, A., & Mann, J. (2012). Measurement of turbulence spectra using scanning pulsed wind lidars. *Journal of Geophysical Research: Atmospheres*, 117(D1), 1201. https://doi.org/10.1029/2011JD016786
- Schlipf, D. (2016). *Lidar-assisted control concepts for wind turbines* (Doctoral dissertation). University of Stuttgart. Stuttgart. https://doi.org/http://dx.doi.org/10.18419/opus-8796
- Schlipf, D., Cheng, P. W., & Mann, J. (2013a). Model of the correlation between lidar systems and wind turbines for lidar-assisted control. *Journal of Atmospheric and Oceanic Technology*, 30(10), 2233–2240. https://doi.org/10.1175/JTECH-D-13-00077.1
- Schlipf, D., Fischer, T., Carcangiu, C. E., Rossetti, M., & Bossanyi, E. A. (2010). Load Analysis of Look-Ahead Collective Pitch Control Using LIDAR. *Proceedings of the 10th German Wind Energy Conference (DEWEK)*, 2, 1–4. https://doi.org/http://dx.doi.org/10.18419/opus-3902
- Schlipf, D., Fleming, P., Haizmann, F., Scholbrock, A., Hofsäß, M., Wright, A., & Cheng, P. W. (2014). Field Testing of Feedforward Collective Pitch Control on the CART2 Using a Nacelle-Based Lidar Scanner. *Journal of Physics: Conference Series*, 555(1), 012090. https://doi.org/10.1088/1742-6596/555/1/012090
- Schlipf, D., Fleming, P., Kapp, S., Scholbrock, A., Haizmann, F., Belen, F., Wright, A., & Cheng, P. W. (2013b). Direct Speed Control using LIDAR and turbine data. *Proceedings of the American Control Conference*, 2208–2213. https://doi.org/10.1109/ACC.2013.6580163
- Schlipf, D., Fürst, H., Raach, S., & Haizmann, F. (2018). Systems Engineering for Lidar-Assisted Control: A Sequential Approach. *Journal of Physics: Conference Series*, 1102(1), 012014. https://doi.org/10.1088/1742-6596/1102/1/012014

Schlipf, D., Guo, F., & Raach, S. (2020). Lidar-based Estimation of Turbulence Intensity for Controller Scheduling. *Journal of Physics: Conference Series*, 1618(3), 032053. https://doi.org/10.1088/1742-6596/1618/3/032053

- Schlipf, D., Haizmann, F., Cosack, N., Siebers, T., & Cheng, P. W. (2015). Detection of wind evolution and lidar trajectory optimization for lidar-Assistedwind turbine control. *Meteorologische Zeitschrift*, 24(6), 565–579. https://doi.org/10.1127/metz/2015/0634
- Schlipf, D., Kapp, S., Anger, J., Bischoff, O., Hofsäß, M., & Kühn, M. (2011). Prospects of Optimization of Energy Production by LIDAR Assisted Control of Wind Turbines. *EWEA 2011 conference proceedings*, 1–10. http://elib.uni-stuttgart.de/opus/volltexte/2013/8585/
- Schlipf, D., & Kühn, M. (2008). Prospects of a Collective Pitch Control by Means of Predictive Disturbance. *9th Ger. Wind Energy Conf. DEWEK*, (Figure 2), 1–4.
- Schlipf, D., Pao, L. Y., & Cheng, P. W. Comparison of feedforward and model predictive control of wind turbines using LIDAR. In: *Proceedings of the ieee conference on decision and control*. IEEE. 2012, 3050–3055. https://doi.org/10.1109/CDC.2012.6426063.
- Schlipf, D., Rettenmeier, A., Haizmann, F., Hofsass, M., Courtney, M., & Cheng, P. W. (2012b). Model based wind vector field reconstruction from lidar data. https://doi.org/http://dx.doi.org/10.18419/opus-8136
- Schneemann, J., Rott, A., Dörenkämper, M., Steinfeld, G., & Kühn, M. (2020). Cluster wakes impact on a far-distant offshore wind farm's power. *Wind Energy Science*, 5(1), 29–49. https://doi.org/10.5194/wes-5-29-2020
- Schneemann, J., Theuer, F., Rott, A., Dörenkämper, M., & Kühn, M. (2021). Offshore wind farm global blockage measured with scanning lidar. *Wind Energy Science*, 6(2), 521–538. https://doi.org/10.5194/wes-6-521-2021
- Scholbrock, A., Fleming, P., Fingersh, L., Wright, A., Schlipf, D., Haizmann, F., & Belen, F. Field Testing LIDAR-Based Feed-Forward Controls on the NREL Controls Advanced Research Turbine. In: 51st aiaa aerospace sciences meeting including the new horizons forum and aerospace exposition. 2. (1). IEEE. Reston, Virigina: American Institute of Aeronautics; Astronautics, 2013, 5–28. ISBN: 9781624101816. https://doi.org/10.2514/6.2013-818.
- Scholbrock, A., Fleming, P., Fingersh, L., Wright, A., Schlipf, D., Haizmann, F., & Belen, F. (2013b). Field testing LIDAR-based feed-forward controls on the NREL controls advanced research turbine. 51st AIAA Aerospace Sciences Meeting including the New Horizons Forum and Aerospace Exposition 2013. https://doi.org/10.2514/6.2013-818
- Scholbrock, A., Fleming, P., Schlipf, D., Wright, A., Johnson, K., & Wang, N. Lidar-enhanced wind turbine control: Past, present, and future. In: 2016 american control conference (acc). 2016-July. IEEE, 2016, 1399–1406. ISBN: 978-1-4673-8682-1. https://doi.org/10.1109/ACC.2016.7525113.
- Schreiber, J., Bottasso, C. L., & Bertelè, M. (2020). Field testing of a local wind inflow estimator and wake detector. *Wind Energy Science*, 5(3), 867–884. https://doi.org/10.5194/wes-5-867-2020

Segalini, A., & Alfredsson, P. H. (2013). A simplified vortex model of propeller and windturbine wakes. *Journal of Fluid Mechanics*, 725, 91–116. https://doi.org/ 10.1017/jfm.2013.182

- Sengers, B. A. M., Steinfeld, G., Hulsman, P., & Kühn, M. (2023). Validation of an interpretable data-driven wake model using lidar measurements from a field wake steering experiment. *Wind Energy Science*, 8(5), 747–770. https://doi.org/10.5194/wes-8-747-2023
- Sezer-Uzol, N., & Uzol, O. (2013). Effect of steady and transient wind shear on the wake structure and performance of a horizontal axis wind turbine rotor. *Wind Energy*, 16(1), 1–17. https://doi.org/10.1002/WE.514
- Simley, E., Angelou, N., Mikkelsen, T., Sjöholm, M., Mann, J., & Pao, L. Y. (2016). Characterization of wind velocities in the upstream induction zone of a wind turbine using scanning continuous-wave lidars. *Journal of Renewable and Sustainable Energy*, 8(1), 013301. https://doi.org/10.1063/1.4940025
- Simley, E., Fürst, H., Haizmann, F., & Schlipf, D. (2018). Optimizing lidars for wind turbine control applications-Results from the IEA Wind Task 32 workshop. *Remote Sensing*, 10(6). https://doi.org/10.3390/rs10060863
- Simley, E., Pao, L. Y., Frehlich, R., Jonkman, B., & Kelley, N. (2014a). Analysis of light detection and ranging wind speed measurements for wind turbine control. *Wind Energy*, 17(3), 413–433. https://doi.org/10.1002/we.1584
- Simley, E., Pao, L. Y., Gebraad, P., & Churchfield, M. Investigation of the impact of the upstream induction zone on LIDAR measurement accuracy for wind turbine control applications using large-Eddy simulation. In: *Journal of physics: Conference series. 524.* (1). IOP Publishing. 2014, 12003. https://doi.org/10.1088/1742-6596/524/1/012003.
- Simley, E., Pao, L. Y., Kelley, N., Jonkman, B., & Frehlich, R. LIDAR wind speed measurements of evolving wind fields. In: 50th aiaa aerospace sciences meeting including the new horizons forum and aerospace exposition. 2012. https://doi.org/10.2514/6.2012-656.
- Sinner, M. N., & Pao, L. Y. (2018). A Comparison of Individual and Collective Pitch Model Predictive Controllers for Wind Turbines. *Proceedings of the American Control Conference*, 2018-June, 1509–1514. https://doi.org/10.23919/ACC.2018.8431598
- Sirovich, L. (1987). Turbulence and the dynamics of coherent structures. I. Coherent structures. Quarterly of Applied Mathematics, 45(3), 561–571. https://doi.org/10.1090/qam/910462
- Sjöholm, M., Angelou, N., Hansen, P., Hansen, K. H., Mikkelsen, T., Haga, S., Silgjerd, J. A., & Starsmore, N. (2014). Two-Dimensional Rotorcraft Downwash Flow Field Measurements by Lidar-Based Wind Scanners with Agile Beam Steering. *Journal of Atmospheric and Oceanic Technology*, 31(4), 930–937. https://doi.org/10.1175/JTECH-D-13-00010.1
- Sjöholm, M., Mikkelsen, T., Mann, J., Enevoldsen, K., & Courtney, M. (2009). Spatial averaging-effects on turbulence measured by a continuous-wave coherent lidar. *Meteorologische Zeitschrift*, 18(3), 281–287. https://doi.org/10.1127/0941-2948/2009/0379

Slinger C, Leak M, Pitter M, & Harris M. Relative power curve measurements using turbine mounted, continous-wave lidar. In: *Proceedings of the european wind energy assosciation*. 2013.

- Slinger, C. W., Harris, M, & Pitter, M. (2020). Wind speed measurement for absolute power curve determination from induction zone lidar measurements. *Journal of Physics:* Conference Series, 1618(3), 032027. https://doi.org/10.1088/1742-6596/1618/3/032027
- Smalikho, I. N., Banakh, V. A., Pichugina, Y. L., Brewer, W. A., Banta, R. M., Lundquist, J. K., & Kelley, N. D. (2013). Lidar investigation of atmosphere effect on a wind turbine wake. *Journal of Atmospheric and Oceanic Technology*, *30*(11), 2554–2570. https://doi.org/10.1175/JTECH-D-12-00108.1
- Soltani, M. N., Knudsen, T., Svenstrup, M., Wisniewski, R., Brath, P., Ortega, R., & Johnson, K. (2013). Estimation of rotor effective wind speed: A comparison. *IEEE Transactions on Control Systems Technology*, *21*(4), 1155–1167. https://doi.org/10.1109/TCST.2013.2260751
- Sonnenschein, C. M., & Horrigan, F. A. (1971). Signal-to-Noise Relationships for Coaxial Systems that Heterodyne Backscatter from the Atmosphere. *Applied Optics*, 10(7), 1600. https://doi.org/10.1364/ao.10.001600
- Soto Sagredo, E., Hannesdóttir, Rinker, J. M., & Courtney, M. (2024). Reconstructing turbulent wind-fields using inverse-distance-weighting interpolation and measurements from a pulsed mounted-hub lidar. *Journal of Physics: Conference Series*, 2745(1), 012017. https://doi.org/10.1088/1742-6596/2745/1/012017
- Stawiarski, C., Traumner, K., Knigge, C., & Calhoun, R. (2013). Scopes and challenges of dual-doppler lidar wind measurements-an error analysis. *Journal of Atmospheric and Oceanic Technology*, 30(9), 2044–2062. https://doi.org/10.1175/ JTECH-D-12-00244.1
- Tadmor, G., Oliver, L., Noack, B. R., Cordier, L., Delville, J., Bonnet, J. P., & Morzyński, M. (2011). Reduced-order models for closed-loop wake control. *Philosophical Transactions of the Royal Society A: Mathematical, Physical and Engineering Sciences,* 369(1940), 1513–1524. https://doi.org/10.1098/rsta.2010.0367
- Taira, K., Brunton, S. L., Dawson, S. T., Rowley, C. W., Colonius, T., McKeon, B. J., Schmidt, O. T., Gordeyev, S., Theofilis, V., & Ukeiley, L. S. (2017). Modal analysis of fluid flows: An overview. *AIAA Journal*, *55*(12), 4013–4041. https://doi.org/10.2514/1.J056060
- Tallet, A., Allery, C., & Leblond, C. (2016). Optimal flow control using a POD-based reduced-order model. *Numerical Heat Transfer, Part B: Fundamentals, 70*(1), 1–24. https://doi.org/10.1080/10407790.2016.1173472
- Taylor, G. I. (1938). The Spectrum of Turbulence. *Proceedings of the Royal Society of London.*Series A Mathematical and Physical Sciences, 164(919), 476–490. https://doi.org/10.1098/rspa.1938.0032
- Tennekes and Lumley. (2018). A First Course in Turbulence. The MIT Press. https://mitpress.mit.edu/9780262536301/a-first-course-in-turbulence/

Tobin, N., Hamed, A. M., & Chamorro, L. P. (2017). Fractional Flow Speed-Up from Porous Windbreaks for Enhanced Wind-Turbine Power. *Boundary-Layer Meteorology*, 163(2), 253–271. https://doi.org/10.1007/s10546-016-0228-8

- Tong, Z., & Li, Y. (2020). Real-Time Reconstruction of Contaminant Dispersion from Sparse Sensor Observations with Gappy POD Method. *Energies 2020, Vol. 13, Page 1956*, 13(8), 1956. https://doi.org/10.3390/EN13081956
- Towers, P., & Jones, B. L. (2016). Real-time wind field reconstruction from LiDAR measurements using a dynamic wind model and state estimation. *Wind Energy*, 19(1), 133–150. https://doi.org/10.1002/WE.1824
- Trabucchi, D. (2020). Lidar Measurements and Engineering Modelling of Wind Turbine Wakes (Doctoral dissertation). Carl von Ossietzky Universitat Oldenburg. https://www.shaker.de/de/content/catalogue/index.asp?lang=de&ID=8&ISBN=978-3-8440-7516-8
- Troldborg, N., & Meyer Forsting, A. R. (2017). A simple model of the wind turbine induction zone derived from numerical simulations. *Wind Energy*, *20*(12), 2011–2020. https://doi.org/10.1002/we.2137
- Tropea, C. (1995). Laser doppler anemometry: Recent developments and future challenges. Measurement Science and Technology, 6(6), 605-619. https://doi.org/10. 1088/0957-0233/6/6/001
- Trujillo, J. J., Bingöl, F., Larsen, G. C., Mann, J., & Kühn, M. (2011). Light detection and ranging measurements of wake dynamics. Part II: Two-dimensional scanning. *Wind Energy*, 14(1), 61–75. https://doi.org/10.1002/we.402
- Unguran, R., Petrovic, V., Boersma, S., Van Wingerden, J. W., Pao, L. Y., & Kuhn, M. (2019). Feedback-feedforward individual pitch control design for wind turbines with uncertain measurements. *Proceedings of the American Control Conference, 2019-July*, 4151–4158. https://doi.org/10.23919/acc.2019.8814757
- Ungurán, R., Petrović, V., Pao, L. Y., & Kühn, M. (2019). Uncertainty identification of blade-mounted lidar-based inflow wind speed measurements for robust feedback-feedforward control synthesis. *Wind Energy Science*, 4(4), 677–692. https://doi.org/10.5194/wes-4-677-2019
- Valldecabres, L., Nygaard, N. G., Vera-Tudela, L., von Bremen, L., & Kühn, M. (2018). On the Use of Dual-Doppler Radar Measurements for Very Short-Term Wind Power Forecasts. *Remote Sensing 2018, Vol. 10, Page 1701, 10*(11), 1701. https://doi.org/10.3390/RS10111701
- van Dooren, M. F., Trabucchi, D., & Kühn, M. (2016). A methodology for the reconstruction of 2D horizontal wind fields of wind turbinewakes based on dual-Doppler lidar measurements. *Remote Sensing*, 8(10), 809. https://doi.org/10.3390/rs8100809
- van Dooren, M. F. (2021). Doppler Lidar Inflow Measurements. Handbook of Wind Energy Aerodynamics, 1–34. https://doi.org/10.1007/978-3-030-05455-7 $\{_\}$ 35-1
- van Dooren, M. F. (2023). *Doppler Lidar Measurement, Modelling and Wind Field Reconstruction* (Doctoral dissertation). University of Oldenburg. Oldenburg.

van Dooren, M. F., Campagnolo, F., Sjöholm, M., Angelou, N., Mikkelsen, T., & Kühn, M. (2017). Demonstration and uncertainty analysis of synchronised scanning lidar measurements of 2-D velocity fields in a boundary-layer wind tunnel. *Wind Energy Science*, 2(1), 329–341. https://doi.org/10.5194/wes-2-329-2017

- van Dooren, M. F., Kidambi Sekar, A. P., Neuhaus, L., Mikkelsen, T., Hölling, M., & Kühn, M. (2022). Modelling the spectral shape of continuous-wave lidar measurements in a turbulent wind tunnel. *Atmospheric Measurement Techniques*, *15*(5), 1355–1372. https://doi.org/10.5194/amt-15-1355-2022
- Vasiljević, N., Vignaroli, A., Bechmann, A., & Wagner, R. (2020). Digitalization of scanning lidar measurement campaign planning. *Wind Energy Science*, *5*(1), 73–87. https://doi.org/10.5194/WES-5-73-2020
- Veers, P. S. (1988). *Three-dimensional wind simulation* (tech. rep.). United States.
- Venturi, D., & Karniadakis, G. E. (2004). Gappy data and reconstruction procedures for flow past a cylinder. *Journal of Fluid Mechanics*, *519*, 315–336. https://doi.org/10.1017/S0022112004001338
- Vollmer, L., Steinfeld, G., Heinemann, D., & Kühn, M. (2016). Estimating the ake deflection donstream of a ind turbine in different atmospheric stabilities: An les study. *Wind Energy Science*, 1(2), 129–141. https://doi.org/10.5194/wes-1-129-2016
- Wagner, R., Courtney, M., Gottschall, J., & Lindelöw-Marsden, P. (2011). Accounting for the speed shear in wind turbine power performance measurement. *Wind Energy*, 14(8), 993–1004. https://doi.org/10.1002/we.509
- Wagner, R., Pedersen, T. F., Courtney, M., Antoniou, I., Davoust, S., & Rivera, R. L. (2014). Power curve measurement with a nacelle mounted lidar. *Wind Energy*, 17(9), 1441–1453. https://doi.org/10.1002/we.1643
- Wang, L., Chen, M., Luo, Z., Zhang, B., Xu, J., Wang, Z., & Tan, A. C. (2024). Dynamic wake field reconstruction of wind turbine through Physics-Informed Neural Network and Sparse LiDAR data. *Energy*, 291, 130401. https://doi.org/10.1016/ J.ENERGY.2024.130401
- Wang, N., Johnson, K. E., & Wright, A. D. (2013). Comparison of strategies for enhancing energy capture and reducing loads using LIDAR and feedforward control. *IEEE Transactions on Control Systems Technology*, 21(4), 1129–1142. https://doi.org/10.1109/TCST.2013.2258670
- Werner, C., & Streicher, J. (2005). Lidar: Range-Resolved Optical Remote Sensing of the Atmosphere (C. Weitkamp, Ed.). *102*.
- Wicker, L. J., & Skamarock, W. C. (2002). Time-Splitting Methods for Elastic Models Using Forward Time Schemes. *Monthly Weather Review*, 130(8), 2088-2097. https://doi.org/10.1175/1520-0493(2002)130<2088:TSMFEM>2.0.CO; 2
- Wilks, D. S. (2019). Statistical Methods in the Atmospheric Sciences, Fourth Edition. Statistical Methods in the Atmospheric Sciences, Fourth Edition, 1–818. https://doi.org/10.1016/C2017-0-03921-6

Willcox, K. (2006). Unsteady flow sensing and estimation via the gappy proper orthogonal decomposition. *Computers and Fluids*, 35(2), 208–226. https://doi.org/10.1016/j.compfluid.2004.11.006

- Würth, I., Valldecabres, L., Simon, E., Möhrlen, C., Uzuno glu, B., Gilbert, C., Giebel, G., Schlipf, D., & Kaifel, A. (2019). Minute-Scale Forecasting of Wind Power—Results from the Collaborative Workshop of IEA Wind Task 32 and 36. *Energies 2019, Vol.* 12, Page 712, 12(4), 712. https://doi.org/10.3390/EN12040712
- Wyngaard, J. C. (2010, January). *Turbulence in the Atmosphere*. Cambridge University Press. https://doi.org/10.1017/CBO9780511840524
- Xie, S., & Archer, C. L. (2017). A Numerical Study of Wind-Turbine Wakes for Three Atmospheric Stability Conditions. *Boundary-Layer Meteorology*, 165, 87–112. https://doi.org/10.1007/s10546-017-0259-9
- Zalkind, D., Abbas, N. J., Jasa, J., Wright, A., & Fleming, P. (2022). Floating wind turbine control optimization. *Journal of Physics: Conference Series*, 2265(4), 042021. https://doi.org/10.1088/1742-6596/2265/4/042021
- Zhan, L., Letizia, S., & Iungo, G. V. (2020a). Optimal tuning of engineering wake models through lidar measurements. *Wind Energy Science*, 5(4), 1601–1622. https://doi.org/10.5194/WES-5-1601-2020
- Zhan, L., Letizia, S., & Valerio Iungo, G. (2020b). LiDAR measurements for an onshore wind farm: Wake variability for different incoming wind speeds and atmospheric stability regimes. *Wind Energy*, *23*(3), 501–527. https://doi.org/10.1002/WE.2430

LIST OF PUBLICATIONS

PUBLICATIONS ON WHICH THIS THESIS IS BASED

Publications in Journals

1. Kidambi Sekar, A. P., van Dooren, M. F., Rott, A., Kühn, M. (2022b). Lower Order Description and Reconstruction of Sparse Scanning Lidar Measurements of Wind Turbine Inflow Using Proper Orthogonal Decomposition. Remote Sensing, 14(11), 2681. https://doi.org/10.3390/rs14112681

This publication serves as Chapter 3 in the dissertation.

A.P.K. designed the research, developed the methodology, performed the LES simulations, performed the data analysis and wrote the paper. M.v.D developed the analysis toolbox for the SpinnerLidar together with A.P.K, implemented the three-parameter WFR method and thoroughly reviewed the manuscript. A.R and M.K contributed with intensive discussions on the scientific content and thoroughly reviewed the manuscript. M.K supervised the research. All authors have read and agreed to the published version of the manuscript.

2. Kidambi Sekar, A. P., Hulsman, P., van Dooren, M. F., & Kühn, M. (2024). Synchronised WindScanner field measurements of the induction zone between two closely spaced wind turbines. Wind Energy Science, 9(7), 1483–1505. https://doi.org/10.5194/wes-9-1483-2024

This publication serves as Chapter 5 in the dissertation.

APK and PH prepared and installed the WindScanner setup of the experiment and jointly measured the data. APK focused on the measurements in a horizontal plane of the induction zone. APK and PH analysed the measurement data obtained by the WindScanner, the met mast and the two turbines. APK performed the virtual WindScanner simulations, extended the uncertainty quantification methodology and wrote the manuscript, while PH calibrated the turbine model and executed the LES runs. APK interpreted the WindScanner results with regard to the induction zone. PH analysed and prepared the VAD data for further use. MvD assisted during the design and execution of the measurement campaign, helped interpret the data and supported in the uncertainty quantification methodology. MK was involved in the design of the measurement campaign, provide extensive reviews and had a supervisory role. All authors contributed to fruitful discussions and reviewed the manuscript.

150 List of Publications

PEER REVIEWED CONFERENCE PUBLICATIONS

1. Kidambi Sekar, A. P., Rott, A., Van Dooren, M. F., Kühn, M. (2020). How much flow information can a turbine-mounted lidar capture? Journal of Physics: Conference Series, 1618(3), 32050. https://doi.org/10.1088/1742-6596/1618/3/032050. [Contents of this paper has been extended in Chapter 2]

An extended version of this publication serves as Chapter 2 in the dissertation.

A.P.K. designed the research, developed the methodology, performed the LES simulations, performed the data analysis and wrote the paper. M.v.D developed the analysis toolbox for the SpinnerLidar together with A.P.K and thoroughly reviewed the manuscript. A.R and M.K contributed with intensive discussions on the scientific content and thoroughly reviewed the manuscript. M.K supervised the research.

2. Kidambi Sekar, A. P., van Dooren, M. F., Kühn, M. (2022a). Overcoming Blade Interference: A Gappy-POD Data Reconstruction Method for Nacelle-Mounted Lidar Measurements. Journal of Physics: Conference Series, 2265(2), 022078. https://doi.org/10.1088/1742-6596/2265/2/022078

This publication serves as Chapter 4 in the dissertation.

A.P.K. designed the research, developed the methodology, performed the LES simulations, performed the data analysis and wrote the paper. M.v.D and M.K contributed with intensive discussions on the scientific content and thoroughly reviewed the manuscript. M.K supervised the research.

FURTHER PUBLICATIONS

Publications in Journals

- van Dooren, M.F., A. P. Kidambi Sekar, Neuhaus, L., Mikkelsen, T., Hölling, M. and Kühn, M., 2022. Modelling the spectral shape of continuous-wave lidar measurements in a turbulent wind tunnel. Atmospheric Measurement Techniques, 15(5), pp.1355-1372. https://doi.org/10.5194/amt-15-1355-2022
- Hulsman, P., Simley, E., A. P. Kidambi Sekar, Sucalemi, C., Petrovic, V., Steinfeld, G., Steinbruck, S., Lukkason, L., Gerds, A. and Kühn, M., 2024. Impact of atmospheric conditions and yawmisalignment on the wake behaviour and nacelle-mounted anemometers. Journal of Wind Engineering and Industrial Aerodynamics, (under preparation).

PEER REVIEWED CONFERENCE PUBLICATIONS

- 1. A. P. Kidambi Sekar, van Dooren, M. F., Mikkelsen, T., Sjöholm, M., Astrup, P., Kühn, M. (2018, June). Evaluation of the LINCOM wind field reconstruction method with simulations and full-scale measurements. In Journal of Physics: Conference Series (Vol. 1037, No. 5, p. 052008). IOP Publishing. https://doi.org/10.1088/1742-6596/1037/5/052008
- 2. Mikkelsen, T., Sjöholm, M., Astrup, P., Peña, A., Larsen, G., Van Dooren, M.F. and A. P. Kidambi Sekar, 2020. Lidar Scanning of Induction Zone Wind Fields over Sloping Terrain.

List of Publications 151

- In Journal of Physics: Conference Series (Vol. 1452, No. 1, p. 012081). IOP Publishing. https://doi.org/10.1088/1742-6596/1452/1/012081
- Lehnhoff, S., A. P. Kidambi Sekar, Van Dooren, M.F., Kühn, M. and Seume, J.R., 2020, September. Full scale rotor blade deformation measurements in comparison with aeroelastic simulations based on measured high-resolution wind fields. In Journal of Physics: Conference Series (Vol. 1618, No. 5, p. 052036). IOP Publishing. https://doi.org/10.1088/1742-6596/1618/5/052036

Presentations and Posters at Conferences

- 1. A. P. Kidambi Sekar, M. Kühn,2017. Lower Order of Wind Turbine Inflow with Short-Range Lidars, Wind Energy Science Conference 2017, 26-29 June 2017, Lyngby, Denmark.
- A. P. Kidambi Sekar, M. F. van Dooren, M. Kühn; "Analysis of Correlation Between Lidar Measured Wind Fields and Wind Turbine Response", Wind Energy Science Conference, 17-20 June 2019, Cork, Ireland
- 3. A. P. Kidambi Sekar, M. F. van Dooren, A. Rott, M. Kühn; "How much flow information can a turbine-mounted lidar capture?.", The Science of Making Torque from Wind Conference, 2020, Delft, Netherlands
- 4. A. P. Kidambi Sekar, P. Hulsman, M. F. van Dooren, M. Kühn; "Synchronised WindScanner Measurements Between Two Closely Spaced Wind Turbines", Wind Energy Science Conference, 25-28 May 2021, Hannover, Germany
- A. P. Kidambi Sekar, M. F. van Dooren, M. Kühn; "Overcoming Blade Interference: A Gappy-POD Data Reconstruction Method for Nacelle-Mounted Lidar Measurements", Wind Energy Science Conference, The Science of Making Torque from Wind Conference, 2022, Delft, Netherlands

CURRICULUM VITÆ

Anantha Padmanabhan Kidambi Sekar

Personal

Place of birth Karamana, India

EDUCATION

Jul. 2009 - May. 2013	Bachelor of Engineering in Mechanical Engineering, Thiagarajar	
	College of Engineering, Anna University	
Sep. 2013 - Feb. 2016	Master of Science in Aerospace Engineering, Delft University	
	of Technology	
	Thesis: Numerical and wind tunnel investigation of root spoilers	
	on horizontal axis wind turbines	

EXPERIENCE

Aug 2014 - Dec 2014	Graduate Student Intern, University of Washington, Fluid Imag-
	ing Diagnostics Lab, Seattle, USA
Jan 2015 - Oct 2015	Graduate Thesis Student, Energy Research Centre of the Nether-
	lands (now TNO), Petten, Netherlands
May 2016 - Jun 2022	Researcher at ForWind - University of Oldenburg, Oldenburg,
	Germany
Aug 2017 - Oct 2017	Visiting Researcher at DTU National Laboratory for Sustainable
	Energy, Risø, Denmark
Sep 2022 - Dec 2024	Senior Consultant at Offshore Wind Consultants (OWC), Ham-
	burg, Germany
Jan 2025 - Present	Energy Yield and Site Assessment Expert at EDF Renewables
	Deutschland, Hamburg, Germany

EIDESSTATTLICHE ERKLÄRUNG

Hiermit versichere ich, die vorliegende Arbeit selbstständig verfasst, keine anderen als die angegebenen Quellen und Hilfsmittel verwendet und die Leitlinien guter wissenschaftlicher Praxis der Carl von Ossietzky Universität Oldenburg befolgt zu haben.

Die Arbeit hat weder in ihrer Gesamtheit noch in Teilen einer anderen Hochschule zur Begutachtung in einem Promotionsverfahren vorgelegen und im Zusammenhang mit dem Promotionsvorhaben wurden keine kommerziellen Vermittlungs- oder Beratungsdienste in Anspruch genommen.

Teile der Arbeit sind bereits veröffentlich.

Ananth Kidambi

Anantha Padmanabhan Kidambi Sekar Hamburg 07.10.2024